

INFORMATION TO USERS

This material was produced from a microfilm copy of the original document. While the most advanced technological means to photograph and reproduce this document have been used, the quality is heavily dependent upon the quality of the original submitted.

The following explanation of techniques is provided to help you understand markings or patterns which may appear on this reproduction.

1. The sign or "target" for pages apparently lacking from the document photographed is "Missing Page(s)". If it was possible to obtain the missing page(s) or section, they are spliced into the film along with adjacent pages. This may have necessitated cutting thru an image and duplicating adjacent pages to insure you complete continuity.
2. When an image on the film is obliterated with a large round black mark, it is an indication that the photographer suspected that the copy may have moved during exposure and thus cause a blurred image. You will find a good image of the page in the adjacent frame.
3. When a map, drawing or chart, etc., was part of the material being photographed the photographer followed a definite method in "sectioning" the material. It is customary to begin photoing at the upper left hand corner of a large sheet and to continue photoing from left to right in equal sections with a small overlap. If necessary, sectioning is continued again -- beginning below the first row and continuing on until complete.
4. The majority of users indicate that the textual content is of greatest value, however, a somewhat higher quality reproduction could be made from "photographs" if essential to the understanding of the dissertation. Silver prints of "photographs" may be ordered at additional charge by writing the Order Department, giving the catalog number, title, author and specific pages you wish reproduced.
5. PLEASE NOTE: Some pages may have indistinct print. Filmed as received.

University Microfilms International

300 North Zeeb Road
Ann Arbor, Michigan 48106 USA
St. John's Road, Tyler's Green
High Wycombe, Bucks, England HP10 8HR

78-8676

GERGELY, John Steven, 1949-
DYE LASER SYSTEM FOR MONITORING ATMOSPHERIC
MOLECULAR POLLUTANTS.

City University of New York,
Ph.D., 1978
Engineering, electronics and electrical

University Microfilms International, Ann Arbor, Michigan 48106

© 1977

JOHN STEVEN GERGELY

ALL RIGHTS RESERVED

DYE LASER SYSTEM FOR MONITORING ATMOSPHERIC
MOLECULAR POLLUTANTS

by

JOHN S. GERGELY

A dissertation submitted to the
Graduate Faculty in Engineering
in partial fulfillment of the
requirements for the degree of
Doctor of Philosophy, The City
University of New York

1977

This manuscript has been read and accepted for the Graduate Faculty in Engineering in satisfaction of the dissertation requirement for the degree of Doctor of Philosophy.

12/30/77
date


Chairman of Examining Committee

1/30/78
date


Executive Officer

Professor Samir Ahmed

Professor Robert Alfano

Professor John Cooney

Professor George Eichmann

Professor Morris Ettenberg

Professor Carl Shulman
Supervisory Committee

The City University of New York

PLEASE NOTE:

This dissertation contains
color photographs which will
not reproduce well.

UNIVERSITY MICROFILMS INTERNATIONAL.

Abstract

DYE LASER SYSTEM FOR MONITORING ATMOSPHERIC MOLECULAR POLLUTANTS

by

John S. Gergely

Adviser: Professor Samir Ahmed

A laser radar (LIDAR) system was designed, built, and successfully operated to measure ambient NO_2 concentrations in the atmosphere. The LIDAR system operated by measuring the differential absorption of scattered energy (DASE) of two laser signals emitted at wavelengths corresponding to a maximum and minimum in the absorption spectrum of NO_2 . As will be shown, the use of this approach greatly increases the sensitivity and range for the detection of NO_2 .

The LIDAR system was designed to be capable of operation in two basic modes. In the first mode, the outputs at the two required wavelengths, on and off resonance absorption of NO_2 , are obtainable in rapid sequence, with frequency selection by an electromagnetically-driven diffraction grating from a flashlamp-pumped organic-dye laser. In the second mode, an intra-cavity dielectric-interface polarizing beam-splitter is used to obtain simultaneously the pair of close-lying independently-tunable wavelengths required from the dye laser. This is the first reported successful use of a DASE LIDAR system operating in the simultaneous mode. In this mode of operation, errors due to scintillation effects and particle and aerosol drift are effectively reduced.

The system developed for both sequential and simultaneous operation incorporated an automatic calibration feature which allowed for the variations in bandwidth which inevitably occur with dye lasers. Experimental results are presented which show the necessity and advantages of this automatic calibration approach. The calibration system operates by monitoring each wavelength for each outgoing laser pulse, and automatically allows for the variations in laser bandwidths, and hence determines the effective NO₂ absorption cross sections each time the laser is fired. This is the first reported use of this automatic calibration approach which we believe to be essential to the successful operation of LIDAR systems of this type.

With the errors in the system minimized through the use of simultaneous two-wavelength operation, measurements were made with the LIDAR transmitter and associated telescope receiver directed out the laboratory window across the upper East Side of Manhattan. Several readings were obtained for various times during the day to observe changes in pollution levels over areas of heavy vehicular traffic located over one kilometer from the LIDAR site. As expected, the pollution levels peaked at rush hour times and leveled off thereafter.

To examine the possibility of an integrated LIDAR system capable of monitoring several pollutants simultaneously, experiments were carried out on energy transfer processes in dye mixtures. Simultaneous two and three wavelength laser action was obtained in dye mixtures at several widely separated spectral regions for the first time, including simultaneous outputs at the three primary colors. Experimental results indicate that the energy transfer was by a radiative process.

The work reported demonstrates potential for practical LIDAR

systems operating on the DASE principle to be used for the effective monitoring of ambient molecular pollution.

ACKNOWLEDGEMENTS

I wish to express my gratitude to all the members of my doctoral committee. In particular, I wish to thank my mentor, Professor Samir Ahmed, for his insight, guidance, and confidence in my work. The helpful discussions with Professor Robert Alfano are much appreciated. I am also thankful to Mr. Dave Pressman for his help in constructing various sections of the LIDAR system, and to Mr. Frank Barone for his help in aligning the receiver system.

I wish also to express my appreciation for the partial support of this work to the City University of New York under grant numbers 10224, 01626, and 01266, to the EPA under grant numbers R803109-01-0, R803109-02-0, and R803109-03-0, and to the Army under grant number DAAA15-74-C-0247.

I am also thankful to my parents for their continuous encouragement. Lastly, I am most grateful to my wife, Debbie, whose patience and bright outlook toward the future encourage me to attain goals which at times seem unreachable.

TO
DEBBIE

TABLE OF CONTENTS

<u>Chapter</u>		<u>Page</u>
1	INTRODUCTION AND BACKGROUND	1
	1.1 The Need for Effective Pollution Monitoring	1
	1.2 Background	2
	1.2.1 Introduction	2
	1.2.2 Raman	2
	1.2.3 Resonance Raman	4
	1.2.4 Long Path Absorption	4
	1.2.5 Resonance Fluorescence	5
	1.2.6 Differential Absorption of Scattered Energy (DASE)	7
	1.3 Summary and Outline of This Study	7
2	LIDAR TECHNIQUES	10
	2.1 Introduction	10
	2.2 Atmospheric Scattering Mechanisms	10
	2.2.1 Raman Scattering	10
	2.2.2 Resonance Raman Scattering	13
	2.2.3 Absorption and Fluorescence Scattering	14
	2.2.4 Rayleigh Scattering	14
	2.2.5 Mie Scattering	14
	2.3 Atmospheric Parameters	15
	2.4 Lidar Schemes: A Comparative Analysis	18
	2.4.1 Introduction	18
	2.4.2 NO ₂ Absorption Spectrum	19
	2.4.3 General Formulation	19
	2.4.4 Differential Absorption of Scattered Energy (DASE)	22

2.4.4.1	Basic Theory	22
2.4.4.2	Evaluation of Required System Parameters for Detection of NO ₂	27
2.4.4.2.1	Received Signal Requirements	27
2.4.4.2.2	Transmitted Power Requirements	28
2.4.4.2.3	Pump Depletion	29
2.4.5	Resonance Fluorescence	30
2.4.5.1	Basic Theory	30
2.4.5.2	Evaluation of Required System Parameters for Detection of NO ₂	30
2.4.6	Raman and Resonance Raman	33
2.4.6.1	Basic Theory	34
2.4.6.2	Evaluation of Required System Parameters for Detection of NO ₂	34
2.4.7	Long Path Absorption	38
2.4.7.1	Basic Theory	38
2.4.7.2	Evaluation of Required System Parameters for Detection of NO ₂	42
2.5	Summary	42
3	THE LIDAR SYSTEM	45
3.1	Introduction	45
3.2	Optical Receiver	45
3.3	The Dye Laser	50
3.3.1	The Laser Head	50
3.3.2	Dye Laser Mechanism--Brief Description	56
3.3.3	Intra-Cavity Grating for Wavelength Selection	58
3.4	Experimental Arrangement for Sequential Operation	60
3.5	Simultaneous Two-Wavelength Operation	60
3.5.1	The Need for Simultaneous Two-Wavelength Operation	60

	3.5.2	Cavity Design	65
	3.5.2.1	Introduction	65
	3.5.2.2	Dielectric-Interface Polarizing Beam-Splitting Cube	68
	3.5.2.3	Air-Spaced Glan-Taylor Prism	71
	3.6	Calibration	75
	3.6.1	The Need for Calibration	75
	3.6.2	The Calibration System	89
	3.6.3	Tuning Technique	94
4		NO ₂ MEASUREMENTS	118
	4.1	Introduction	118
	4.2	Results of Field Tests	118
	4.2.1	Sequential Measurements	118
	4.2.1.1	Factors Affecting Accuracy	119
	4.2.2	Simultaneous Two-Wavelength Measurements	124
	4.3	Error Analysis	142
5		SIMULTANEOUS MULTIWAVELENGTH OUTPUTS FROM ENERGY-TRANSFER DYE-MIXTURE LASERS	146
	5.1	Introduction	146
	5.2	Energy Transfer Mechanisms	147
	5.2.1	Introduction	147
	5.2.2	Radiative and Nonradiative Energy Transfer	149
	5.3	Multiwavelength Laser Action in Dye Mixtures-- Experimental Results	154
	5.4	Energy Transfer Mechanisms--Experimental Results	159
	5.4.1	Radiative Energy Transfer	159
	5.4.2	Nonradiative Energy Transfer	165
6		SUMMARY AND CONCLUSIONS	180

REFERENCES

182

LIST OF TABLES

<u>No.</u>	<u>Caption</u>	<u>Page</u>
2.4:1	Tabulated Comparison of Monostatic LIDAR Schemes	44
4.2:1	Range, Resolution, NO ₂ Pollution Concentration, and Uncertainties for Various Times During the Day	140

LIST OF FIGURES

<u>No.</u>	<u>Caption</u>	<u>Page</u>
2.2:1	The Raman Process	12
2.4:1	NO ₂ Absorption Curve	20
2.4:2	Obtainable Depth Resolution for Backscatter LIDAR Schemes	21
2.4:3	The DASE Scheme	23
2.4:4	The Resonance Fluorescence Scheme	31
2.4:5	The Raman Scheme	35
2.4:6	The Long Path Absorption Scheme	39
3.1:1a	The LIDAR System for Sequential Operation	46
3.1:1b	Photographs of the LIDAR System for Simultaneous Operation	47
3.2:1	Fresnel Lens	48
3.2:2a	The Optical Receiver System for Simultaneous Operation	51
3.2:2b	Photographs of the Optical Receiver System For Simultaneous Operation	52
3.3:1a	Coaxial Arrangement of the Flashlamp-Pumped Dye-Laser Head	53
3.3:1b	Photographs of the Laser Head Situated in the LIDAR System	54
3.3:2	Typical Flashlamp-Pumped Dye-Laser Output Pulse	55
3.3:3	Energy Levels of Organic Dye Molecules	57
3.3:4	Dispersion of Grating and Effective Aperture Created by the Laser Head	59
3.4:1	The Overall Transmitting System with Calibration Setup for Sequential Operation	61
3.5:1	Beam Spreading	63
3.5:2	Beam Steering	63

3.5:3	Beam Scintillation	64
3.5:4a	Optical Arrangement for Simultaneous Two-Wavelength Output	66
3.5:4b	Photographs of the Optical Arrangement for Simultaneous Two-Wavelength Output	67
3.5:5	Dielectric-Interface Polarizing Beam-Splitting Cube	69
3.5:6	Spectrometer Photograph of the Simultaneous Two-Wavelength Output Utilizing the Dielectric-Interface Polarizing Beam-Splitting Cube	70
3.5:7	Air-Spaced Glan-Taylor Prism	72
3.5:8	Spectrometer Photograph of the Simultaneous Two-Wavelength Output Utilizing the Air-Spaced Glan-Taylor Prism	74
3.5:9	Spectrometer Photograph of the Simultaneous Two-Wavelength Output Utilizing the Air-Spaced Glan-Taylor Prism for Equal Output Energies in Each Lasing Line	76
3.6:1a	Experimental Setup for Monitoring Laser Frequency Shifts and Bandwidth Changes	78
3.6:1b	Photographs of the Experimental Setup for Monitoring Laser Frequency Shifts and Bandwidth Changes	79
3.6:2	Spectrometer Photograph of the 4478.5 Å Laser Line for Sequential Operation	81
3.6:3	Spectrometer Photograph of the 4478.5 Å Laser Line for Simultaneous Two-Wavelength Operation	81
3.6:4	Spectrometer Photograph of the 4500 Å Laser Line for Sequential Operation	82
3.6:5	Spectrometer Photograph of the 4500 Å Laser Line for Simultaneous Two-Wavelength Operation	82
3.6:6a	Spectrometer Photograph of the Simultaneous Two-Wavelength Output, Bias Voltage = 20 KV, First Shot	83
3.6:6b	Bias Voltage = 20 KV, Second Shot	93
3.6:6c	Bias Voltage = 20 KV, Third Shot	84
3.6:6d	Bias Voltage = 20 KV, Fourth Shot	84

3.6:6e	Bias Voltage = 19 KV, First Shot	85
3.6:6f	Bias Voltage = 19 KV, Second Shot	85
3.6:6g	Bias Voltage = 19 KV, Third Shot	86
3.6:6h	Bias Voltage = 19 KV, Fourth Shot	86
3.6:6i	Bias Voltage = 18 KV, First Shot	87
3.6:6j	Bias Voltage = 18 KV, Second Shot	87
3.6:6k	Bias Voltage = 18 KV, Third Shot	88
3.6:6l	Bias Voltage = 18 KV, Fourth Shot	88
3.6:7a	The Calibration Setup	90
3.6:7b	Photographs of the Calibration Setup	91
3.6:8a	Calibration Signals for Simultaneous Two-Wavelength Operation for the 4478.5 Å Laser Line with N ₂ in the Calibration Cell	95
3.6:8b	Calibration Signals for Simultaneous Two-Wavelength Operation for the 4500 Å Laser Line with N ₂ in the Calibration Cell	96
3.6:9a	Calibration Signals for Simultaneous Two-Wavelength Operation for the 4478.5 Å Laser Line with NO ₂ -N ₂ Mixture in the Calibration Cell	97
3.6:9b	Calibration Signals for Simultaneous Two-Wavelength Operation for the 4500 Å Laser Line with NO ₂ -N ₂ Mixture in the Calibration Cell	98
3.6:10	Experimental Setup Used for Fine Frequency Tuning	101
3.6:11a	Spectrometer Photograph of the Simultaneous Two-Wavelength Output to Get 5 Å Bandwidths in Each Line--4478.5 Å	104
3.6:11b	--4500 Å	104
3.6:11c	--the 4478.5 Å and 4500 Å Laser Lines	105
3.6:11d	--the 4478.5 Å and 4500 Å Laser Lines	105
3.6:11e	--the 4478.5 Å and 4500 Å Laser Lines	106
3.6:11f	--the 4478.5 Å and 4500 Å Laser Lines	106

3.6:11g	--the 4478.5 Å and 4500 Å Laser Lines	107
3.6:11h	--the 4478.5 Å and 4500 Å Laser Lines	107
3.6:11i	--the 4478.5 Å and 4500 Å Laser Lines	108
3.6:12a	The Initial Fine Tuning Signals for Simultaneous Two-Wavelength Operation for Obtaining Frequency Coincidence for the 4478.5 Å Laser Line	109
3.6:12b	The Final Fine Tuning Signals for Simultaneous Two-Wavelength Operation for Obtaining Frequency Coincidence for the 4478.5 Å Laser Line	110
3.6:13a	The Initial Fine Tuning Signals for Simultaneous Two-Wavelength Operation for Obtaining Frequency Coincidence for the 4500 Å Laser Line	111
3.6:13b	The Final Fine Tuning Signals for Simultaneous Two-Wavelength Operation for Obtaining Frequency Coincidence for the 4500 Å Laser Line	112
3.6:14	Spectrometer Photograph of the Simultaneous Two-Wavelength Output with Laser Frequencies Fine Tuned to 4478.5 Å and 4500 Å with Approximately 5 Å Bandwidths	113
3.6:15	Spec. Sheet 3.6:1	114
4.2:1	Typical LIDAR Return Signal	120
4.2:2	Typical LIDAR Return Signal with Chimneys Below Beam Path	120
4.2:3a	Sequential LIDAR Return Signals at 4478.5 Å and 4500 Å	121
4.2:3b	Sequential Calibration Signals at 4478.5 Å and 4500 Å	122
4.2:4a	Simultaneous LIDAR Return Signals at 4478.5 Å and 4500 Å, Time: 8:45 A. M.	125
4.2:4b	Simultaneous Calibration Signals for 4478.5 Å and 4500 Å, Time: 8:45 A. M.	126
4.2:4c	Simultaneous LIDAR Return Signals at 4478.5 Å and 4500 Å, Time: 9:00 A. M.	127
4.2:4d	Simultaneous Calibration Signals for 4478.5 Å and 4500 Å, Time: 9:00 A. M.	128

4.2:4e	Simultaneous LIDAR Return Signals at 4478.5 Å and 4500 Å, Time: 9:30 A. M.	129
4.2:4f	Simultaneous Calibration Signals for 4478.5 Å and 4500 Å, Time: 9:30 A. M.	130
4.2:4g	Simultaneous LIDAR Return Signals at 4478.5 Å and 4500 Å, Time: 5:30 P. M.	131
4.2:4h	Simultaneous Calibration Signals for 4478.5 Å and 4500 Å, Time: 5:30 P. M.	132
4.2:4i	Simultaneous LIDAR Return Signals at 4478.5 Å and 4500 Å, Time: 6:00 P. M.	133
4.2:4j	Simultaneous Calibration Signals for 4478.5 Å and 4500 Å, Time: 6:00 P. M.	134
4.2:4k	Simultaneous LIDAR Return Signals at 4478.5 Å and 4500 Å, Time: 6:30 P. M.	135
4.2:4l	Simultaneous Calibration Signals for 4478.5 Å and 4500 Å, Time: 6:30 P. M.	136
4.2:4m	Simultaneous LIDAR Return Signals at 4478.5 Å and 4500 Å, Time: 8:00 P. M.	137
4.2:4n	Simultaneous Calibration Signals for 4478.5 Å and 4500 Å, Time: 8:00 P. M.	138
4.2:4o	Simultaneous Calibration Signals for 4478.5 Å and 4500 Å for Normalization (with N ₂ in Cell)	139
4.3:1	Experimental Setup for Determination of LIDAR-Reading Uncertainties	143
4.3:2	Error Plot for Determination of LIDAR-Reading Uncertainties	144
5.2:1	Donor-Acceptor System of Two Organic Dyes with Overlapping Fluorescence and Absorption Bands	148
5.2:2	Donor-Acceptor System of Four Organic Dyes with Overlapping Fluorescence and Absorption Bands	150
5.2:3	Donor-Acceptor System with Overlapping Absorption Bands	151
5.2:4	Donor and Acceptor Energy Levels	153
5.3:1	Absorption and Fluorescence Spectra of the Three Dyes at Optimum Concentrations from Which Simultaneous Laser Outputs Were Obtained in the Three Primary Colors	155

5.3:2	Absorption and Fluorescence Spectra of the Three-Dye Mixture at Optimum Concentrations from Which Simultaneous Laser Outputs Were Obtained in the Three Primary Colors	157
5.3:3	Experimental Setup for Obtaining Fluorescence and Absorption Spectra	158
5.3:4	Optical Arrangement for Obtaining Simultaneous Three-Color Outputs in the Three Primary Colors	160
5.3:5	Absorption and Fluorescence Spectra for Simultaneous Two-Wavelength Output	161
5.3:6	Optical Arrangement for Obtaining Two Pairs of Wavelengths Simultaneously	162
5.4:1	Experimental Setup for Obtaining Fluorescence and Absorption Spectra	164
5.4:2	Overlap Integral of Dichlorofluorescein (Donor) and DODC (Acceptor)	166
5.4:3	Overlap Integral of Dichlorofluorescein (Donor) and Rhodamine B (Acceptor)	167
5.4:4	Fluorescence Quantum Yield of DODC in the Mixture with Dichlorofluorescein	168
5.4:5	Fluorescence Quantum Yield of Rhodamine B in the Mixture with Dichlorofluorescein	169
5.4:6	Experimental Setup for Obtaining Fluorescence Spectra	171
5.4:7	Fluorescence Quantum Yield of 7-Diethylamino-4 Methyl Coumarine Versus Concentration	173
5.4:8	Fluorescence Quantum Yield of 7-Diethylamino-4 Methyl Coumarine (Donor) in Mixtures with DODC (Acceptor, 1×10^{-4} M/l) Versus Donor Concentration	174
5.4:9	Fluorescence Quantum Yield of DODC (Acceptor, 1×10^{-4} M/l) in Mixtures with 7-Diethylamino-4 Methyl Coumarine (Donor) Versus Donor Concentration	175
5.4:10	Normalized Fluorescence Quantum Yield of DODC (Acceptor, 1×10^{-4} M/l) in Mixtures with 7-Diethylamino-4 Methyl Coumarine (Donor) with Respect to the Fluorescence Quantum Yield of Pure Solution of the Donor Versus Donor Concentration	176

5.4:11 Normalized Fluorescence Quantum Yield of DODC
(Acceptor, 1×10^{-4} M/l) in Mixtures with
7-Diethylamino-4 Methyl Coumarine (Donor) with
Respect to the Fluorescence Quantum Yield of the
Donor in the Same Mixture Versus Donor Concentration 177

CHAPTER 1 INTRODUCTION AND BACKGROUND

1.1 The Need for Effective Pollution Monitoring

The adverse effects of pollution on health are well known, and hence the need for effectively monitoring such pollution in heavily populated areas is apparent.¹

The use of lasers for atmospheric pollution monitoring has received considerable attention.^{2-5,19} The potential advantages of using lasers for this purpose are simple in essence.

Existing methods for monitoring air pollution utilize fixed-site chemical stations. However, to effectively cover a large metropolitan area, such as that of New York City, very many fixed-site stations are required with attendant expenses. In addition, such stations only provide information in their immediate vicinity and not in the air between or above them.

Optimally, the intelligent planning of selective and more localized pollution control measures, which would be less disruptive than general ones, would require a three-dimensional pollution map of the area. Moreover, it should ideally, instantaneously reflect changes in conditions. An additional desirable goal would be the ability to track moving clouds of pollutants.

Greatly increasing the number of fixed-site monitoring stations and using aircraft sample collections would be prohibitively expensive methods for attaining these goals. It is for these reasons that laser monitoring schemes, with their potential ability to instantaneously and remotely determine pollutant concentration and spatial distribution,

1.2 Background

1.2.1 Introduction

LIDAR, an acronym for Light Detection and Ranging, was given to laser ranging systems. The first recorded backscattered echoes from the atmosphere were reported in 1963 by Ficco and Smullin, and by Ligada, who measured backscattered signals from haze.^{6,7} Since then, research and development have concentrated on developing LIDAR into an effective method for air pollution monitoring.

1.2.2 Raman

Raman scattering was first used to detect molecular constituents of the atmosphere in 1967 by Leonard, Cooney, and Melfi.⁸⁻¹⁰ Later, Inaba and Kobayashi discussed the possibility of pollution detection by Raman scattering, and subsequently remotely detected SO₂ and CO₂ in the atmosphere.^{11,12} Unfortunately, the pollution detection sensitivity that the Raman scheme offers is not adequate for trace contaminant measurements typically found in polluted urban areas. However, considerable effort has been directed to monitor water vapor and major atmospheric constituents using the Raman scattering method.¹³⁻¹⁵

An advantage of the Raman scheme is that a single frequency laser can be used as a source to obtain the Raman backscatter from the constituents of interest. On the other hand, Raman schemes are greatly limited in their attainable sensitivities by the relatively small Raman scattering cross sections.

Using a nitrogen laser operating at 3371 Å at 20 KW peak power 10 ns halfwidth at 50 HZ, Kobayashi and Inaba (1971) have detected Raman sig-

nals from clear air and from an oil smoke plume.³ The receiving system consisted of a 30 cm diameter telescope followed by an f 8.5 half meter grating monochromator and spectral interference filter. They were able to show the presence of H₂O, CH₄, H₂S, CO, NO, and SO₂ in the oil smoke plume at a distance of 30 m.

Progress in laser sources led to improvement in Raman detection systems. Thus, in 1973 Hirschfeld described a system using a frequency doubled Ruby laser transmitter with a 3 m aperture telescope as the receiver.¹⁶ This was used in field tests to detect CO₂, H₂O, and SO₂ over a 200 m range. Concentrations of approximately 10⁴ ppm of water vapor, 310 ppm of CO₂, and 300 ppm of SO₂ were detectable. The SO₂ was dispersed in controlled amounts to create detectable plumes for monitoring. The SO₂ concentration is of course much higher than those present in ambient conditions.

The 2 j, 2 HZ Ruby laser source was doubled in KDP with 8 percent efficiency and the returned signal was processed by photon counting techniques referenced against the nitrogen system and probably represents the state of the art for sensitivity and range.^{17,18}

The advent of tunable dye lasers opened possibilities for other LIDAR pollution detection methods with inherent advantages over the Raman scheme.² The four LIDAR schemes for which tunable dye lasers are particularly important and that presently appear to be the most promising for the detection of molecular pollutants with resonant absorption in the visible and near ultraviolet are: resonance Raman, long path absorption, resonance fluorescence, and differential absorption of scattered energy (DASE).

1.2.3 Resonance Raman

Observations of resonance Raman scattering in gases have been very few. Bernstein (1973) measured resonant Raman enhancements in gaseous Cl_2 , Br_2 , and I_2 . He obtained intensities of 10 to 1000 times stronger than the normal Raman effect.⁷²

Rosen (1975) estimated the feasibility of using resonance Raman scattering for the remote detection of pollutants.⁷³ He estimated that for 10^4 pulses of 0.05 mJ each, 100 ppm of NO_2 and 10 ppm of SO_2 could be detected at 1 km at night, and 100 ppm of NO could be detected during daytime. These are for a signal to noise ratio of 10. These concentrations are 3 to 4 orders of magnitude higher than ambient pollution concentrations encountered.

1.2.4 Long Path Absorption

Hanst (1968) described the measurement of average pollutant concentration along a laser beam path by laser resonance absorption.^{20,21} More recently, Zaromb (1969), Nakahara and Ito (1970), Inomota and Igarashi (1972), and Hodgeson, McClenney and Hanst (1973), suggested the long path absorption scheme for determining average pollutant densities.²²⁻²⁵ Kidal and Byer have given a detailed analysis of the doubled-ended long path absorption method.² This analysis was later extended to the single ended absorption method using topographical targets by Byer and Garbuny.²⁶

To determine the average pollutant density along a laser beam path, absorption measurements have been carried out using low power diode lasers by Hinkley (1970).²⁷⁻²⁹ Using a $\text{Pb}_{0.88}\text{Sn}_{0.12}\text{Te}$ diode laser mounted onto a cold-finger of a cryogenic Dewar, concentrations ranging

from 74 to 1000 ppm of C_2H_4 in N_2 were detected in a laboratory in a sample chamber 30 cm long. Similar experiments were carried out by Snowman using a CO_2 laser.³⁰

More recently, O'Shea and Dodge (1974) measured NO_2 absorption coefficients for the most prominent argon-ion laser lines.³¹ Measurements using the long path absorption of argon-ion lines by NO_2 in an urban atmosphere were carried out. A corner cube reflector was positioned 3.54 km from the laser site to reflect the laser signal back to the receiver. Integrated pollutant concentrations ranging from 0.05 ppm to 0.15 ppm of NO_2 were detected.

The topographical single ended absorption method was first demonstrated by Henningsen, Garbuny and Byer in 1974.³² The transmitter consisted of a CaLaSOAP:Nd laser source electro-optically Q-switched and operated in a TEM_{00} mode with 10 mj/pulse output energy at 1.06 μm .

The 1.06 μm output from the laser was frequency doubled in a 2 cm long CDA crystal with an efficiency of 25 percent. The output from the frequency doubler was focused into a temperature-tuned $LiNbO_3$ parametric oscillator. An etalon within the laser cavity was fine tuned piezo-electrically which allowed the infrared frequency to be tuned on and off a resonance peak of CO.

Using a wooded area as a topographical target a concentration of 47 ppm of CO was detected at a range of 107 m. The CO was released from containers situated below the laser beam path.

1.2.5 Resonance Fluorescence

In 1969, Bowman, Gibson and Sandford used a flashlamp-pumped dye

laser tuned by a tilted Fabry-Perot interferometer to obtain nighttime measurements of sodium in the upper atmosphere.³³ The output of the dye laser was used to induce fluorescence from sodium at altitudes up to 150 km. Concentrations ranging from $1.8 \times 10^{14} \text{ m}^{-2}$ to $9 \times 10^{12} \text{ m}^{-2}$ were detected at altitudes of 80 to 100 km.

By 1970, regular measurements were being made of the sodium double layer at 90 km altitude.³⁴ Since that time, observations of the sodium layer have been numerous.³⁵⁻³⁹ In 1972, Gibson and Sandford extended the use of the resonance fluorescence scheme into daytime operation by using a narrow band optical receiver.^{40,41}

The use of resonance fluorescence backscattering for probing the troposphere has been limited. However, the method has been extensively analyzed by Kidal and Byer, and by C.M. Penny.^{2,42} Resonance backscattering also has been discussed by ourselves, Kobayashi and Inaba, and Measures and Pilon.^{44,3,43}

In 1972, Gelbwachs utilized resonance fluorescence of NO_2 excited by an argon-ion laser to detect NO_2 locally with a sensitivity of one part per billion.⁴⁵ The laser excitation was at 4480 \AA and the fluorescence was monitored at 7000 to 8000 \AA . Local Los Angeles air, drawn through filters, was monitored, and NO_2 variations measured over a period of a few hours showed concentrations ranging from 0.03 ppm to 0.1 ppm. Filtering was necessary to eliminate interfering fluorescence from particulates in the air.

The increased sensitivity of resonance fluorescence backscattering makes it appear useful as a remote monitoring method compared to the Raman method. As will be shown later, the sensitivity of the resonance

fluorescence scheme is greatly surpassed by the differential absorption of scattered energy method (DASE).

1.2.6 Differential Absorption of Scattered Energy (DASE)

The DASE method was first suggested by Schotland in 1964 using a searchlight as a source.⁴⁶ The method was recently extended to LIDAR pollution monitoring by Ahmed and Gergely, Igarashi, and others.^{47,50,2,26,43,48,49}

The earliest experimental work was performed by Schotland who used a temperature tuned Ruby laser to measure the water vapor vertical profile by the DASE method.⁴⁶ DASE measurements in the atmosphere were first reported by ourselves and by Igarashi.^{47,50} DASE measurements also were later reported by Rothe, Brinkman and Walther of Cologne, Germany.^{51,53} Calibration measurements of the differential absorption method were made by Grant et al.⁵² Using a flashlamp-pumped dye laser operating near 4450 Å at 4 to 8 mj pulse energy, they measured NO₂ of known concentration in a sample chamber.

The DASE system with its superior operating capabilities is the topic of interest in this work and a detailed theoretical comparison between the aforementioned LIDAR schemes is given in Chp. 2.

1.3 Summary and Outline of This Study

The tasks accomplished are summarized below:

1. The basic laser radar system was designed built and tested. It consists of a flashlamp-pumped dye laser and an optical receiver with a 15 inch Fresnel lens.

2. The optical arrangements of the dye laser system were designed for two alternate modes of operation. In one mode, outputs at the two required wavelengths, on and off the resonance absorption of the pollutant, are obtainable in rapid sequence, with frequency selection by an electromagnetically driven grating. In the second mode of operation, an intracavity polarizing-prism beam splitter is used to obtain simultaneously a pair of close-lying independently tunable wavelengths.
3. Field tests of the LIDAR system were carried out from City College and extended over the upper East Side of Manhattan. In these tests ambient levels of NO_2 concentrations were measured. These measurements showed that ambient levels below 0.2 ppm could readily be detected at ranges of more than 1 km.
4. The LIDAR system makes use of a calibration cell containing the pollutant gas to be monitored, so that a calibration signal is automatically available with each outgoing pulse. This makes the system independent of the slight variations in laser output characteristics that occur from pulse to pulse.
5. To improve flashlamp-pump laser output and efficiency, and to obtain simultaneously laser outputs at wavelengths suitable for monitoring NO_2 and other pollutants whose absorptions lie within the visible band, experiments were also carried out on energy transfer processes in dye mixtures. In this work, simultaneous outputs were successfully obtained at desired wavelengths. An investigation of the excitation energy transfer indicates an optical process. This work led to the first tunable three-color dye

mixture laser spanning the visible spectrum.⁷⁷

The following is a chronological listing of the material presented in this work:

1. In Chp. 1, the need for an effective method of pollution monitoring is explained, and the historical development of LIDAR systems is given. Finally, an outline of this thesis is presented.
2. In Chp. 2, atmospheric scattering mechanisms are presented, first in a qualitative manner, then scattering relationships are detailed under Atmospheric Parameters. Towards this end, the four LIDAR schemes, Raman and resonance Raman, long path absorption, resonance fluorescence, and differential absorption of scattered energy (DASE) are described, and a comparison of operating parameters is given in Table 2.4:1.
3. In Chp. 3, the LIDAR system developed in this work, is described in detail. Sequential mode of operation is described first, then the necessity and operating characteristics of Simultaneous Two-Wavelength operation is presented. Experimental results showing the fluctuations in output beam quality, including bandwidth changes, indicate a strong need for calibrated output signals.
4. In Chp. 4, results of field tests are given along with uncertainties associated with the LIDAR readings.
5. In Chp. 5, theoretical and experimental results are given on energy transfer processes in dye mixtures.
6. In Chp. 6, a summary and conclusions are presented on the work reported.

CHAPTER 2 LIDAR TECHNIQUES

2.1 Introduction

All laser radar techniques depend upon atmospheric scattering mechanisms for their operation. Possible techniques for pollution monitoring include the following:

1. Raman and resonance Raman (Raman backscatter),
2. long path absorption (resonance absorption),
3. resonance fluorescence (resonance fluorescence backscatter),
and
4. differential absorption of scattered energy (DASE) (Rayleigh and Mie backscatter).

In the following section, the atmospheric scattering mechanisms are explained qualitatively, then scattering relationships are detailed in Sect. 2.3 under Atmospheric Parameters. A comparison of the LIDAR schemes is made in Sect. 2.4 which shows the superior operating characteristics of the DASE system.

2.2 Atmospheric Scattering Mechanisms

2.2.1 Raman Scattering

The Raman effect consists of the appearance of displaced lines in the spectrum of monochromatic light scattered by molecules. The degree of displacement, $\Delta\nu$, is characteristic of the molecules causing the scattering. The intensity of the spectral line is proportional to the density of scattering molecules.

The Raman effect is essentially a detail of the Rayleigh scattering

process. In the Rayleigh process, incident light on a molecule is virtually absorbed and immediately re-emitted. The absorbed light does not raise the molecule to an excited energy level, as in classical resonance absorption. Instead, after absorption, the molecule is in a virtual excited state. This has two consequences. First, the molecule re-emits the energy in a very short time--about 10^{-12} sec. Second, the absorption and scattering cross sections are very small. It has been estimated that, for a typical liquid irradiated at 6328 \AA , 1 part in 10^4 of the incident light will be scattered in a path length of 1 cm.^{60,61} Gases have fewer molecules per unit volume, and the fraction of light will obviously be much less.

A small portion of the molecules excited (10^{-2} to 10^{-6} or less) will emit (Raman) light of a slightly different wavelength than the incident light.^{60,61} This phenomenon is known as Raman scattering. The process is shown in Fig. 2.2:1. Light is absorbed by molecules in the ground state, and for some molecules Raman light is re-emitted, with these molecules returning not to the ground state, but to an excited vibrational level. The emitted light is naturally of a lower energy or frequency than the incident light. The difference in frequency is equal to one of the natural vibrational frequencies of the molecule. Several such shifted lines are usually observed in a Raman spectrum. Each molecule has its own set of vibrational frequencies and therefore its unique Raman spectrum, which can thus be used to uniquely identify the scattering (or re-emitting) molecule.

A few molecules initially absorb light while they are in an excited vibrational state and decay to a lower energy level, so that their Raman scattered light has a higher frequency. Therefore, the complete

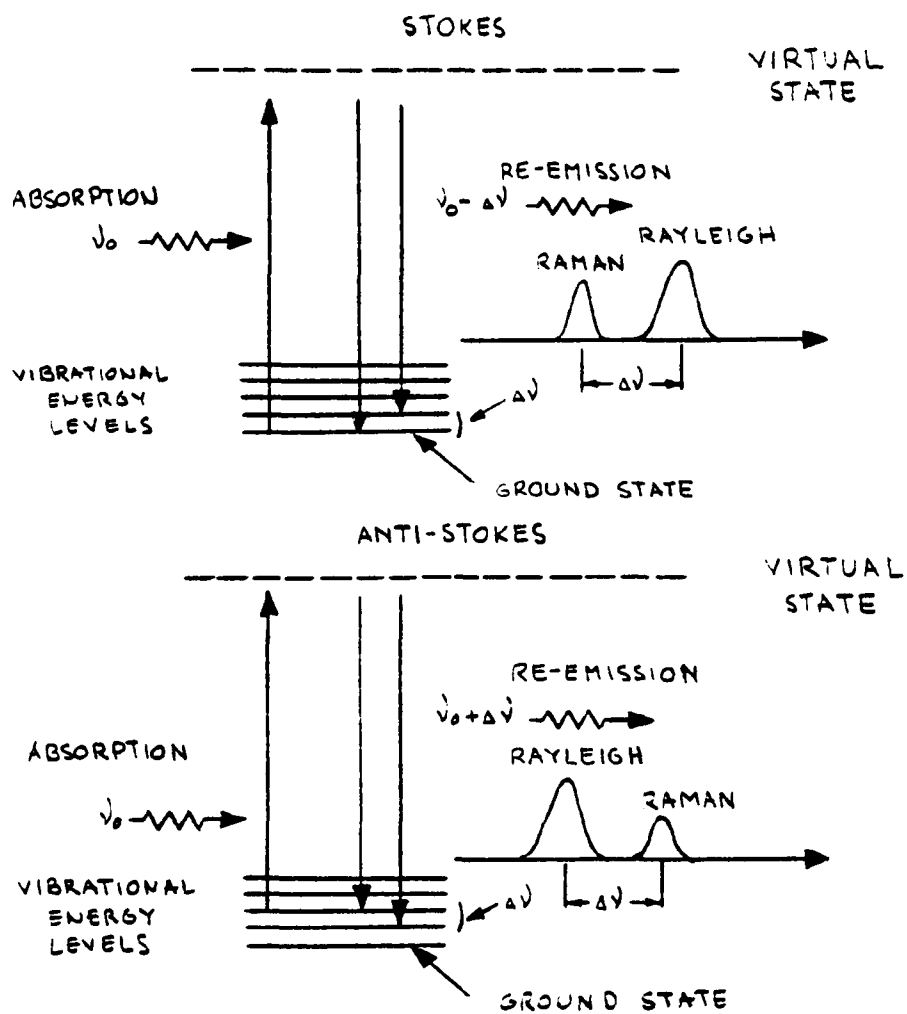


FIGURE 2.2:1 THE RAMAN PROCESS

scattering spectrum is made up of the Rayleigh scattering (predominant) at the same frequency as the incident light and the two components of the Raman spectrum, the Stokes lines (which are shifted to a lower frequency), and the anti-Stokes lines (which are shifted to a higher frequency). The Stokes lines are more intense because under most circumstances most molecules are in the ground energy level. To summarize, the typical Rayleigh scattering ratio is 1 in 10^4 (for a 1 cm liquid path).^{60,61} Of this 10^{-4} , only 1 in 10^2 to 10^4 of the scatterings exhibits the displaced wavelengths characteristic of Raman scattering. For atmospheric gases, the Raman scattering ratio is much less. For N_2 at atmospheric pressure, this scattering ratio is approximately 1 in 10^{10} for a 1 cm path length.¹⁸

The Raman cross section determines the fraction of an incident light beam which will be scattered at Raman wavelengths. It is a critical piece of information needed for determining pollutant detectabilities and necessary for quantitative measurements. The cross section is a function of the fourth power of the frequency of the incident radiation, and it may be enhanced by resonance effects.

2.2.2 Resonance Raman Scattering

The resonance Raman effect can best be explained if the first step in scattering is considered to be the quasi-absorption of the incident light. As the light is scanned in frequency and approaches an absorption band, the fraction of the light absorbed increases, and the fraction of the scattered light increases proportionally, thus a larger apparent cross section results.

2.2.3 Absorption and Fluorescence Scattering

Absorption and fluorescence scattering is in actuality a description of the classical resonance absorption and fluorescence mechanisms. As an example, when monochromatic light propagates through the atmosphere and encounters a species of molecules whose absorption band coincides with the propagation frequency of the transmitted light, a portion of the light is absorbed. Subsequently, some of the absorbed monochromatic radiation will be re-emitted by the molecules over a wide spectrum characteristic of the absorbing species. The fluorescence scattered will be in all directions, shifted toward the longer wavelength end of the spectrum and will resemble the absorption spectrum of the molecules.

2.2.4 Rayleigh Scattering

Scattering from atoms or molecules for which the particle diameter is small compared to the wavelength of the incident light is called Rayleigh scattering. The scattered light is directional and is of the same frequency of the incident radiation. In the atmosphere, Rayleigh scattering is due to molecules normally present in the air, such as, N_2 , O_2 , H_2O , and CO_2 .^{2,18,58}

Rayleigh scattering occurs because molecules, for example, react to nonresonant radiation. When incident radiation passes over molecules, a general vibration is set up within the molecules, not at the resonance frequency, ω_0 , but at the frequency, ω , of the field. The vibrating molecules are the sources of the scattered radiation.

2.2.5 Mie Scattering

Scattering from particles for which the particle diameter is large

compared to the wavelength of incident light is called Mie scattering. In this process, the scattered light is of the same frequency of the incident radiation. In the atmosphere, Mie scattering is due to particulates and aerosols.^{2,18,58}

The DASE scheme makes use of both Rayleigh and Mie scattering. The next section details scattering relationships which are then used in Sect. 2.4 in a comparison of the four types of LIDAR schemes that have potential for use as pollution monitoring systems.

2.3 Atmospheric Parameters

The atmosphere attenuates a transmitted light beam by elastic (Rayleigh, Mie) scattering and by absorption.

The propagation of a light beam of intensity I_0 through the atmosphere may be expressed by:

$$I = I_0 \exp(-\alpha_A r), \quad (2.3:1)$$

where,

I = the transmitted intensity over a distance r ,

α_A = the atmospheric volume extinction coefficient which is composed of a sum of terms:

$$\alpha_A = \alpha_R + \alpha_M + \alpha_{ABS}. \quad (2.3:2)$$

where,

α_R , α_M , α_{ABS} are respectively the Rayleigh, Mie, and absorption extinction coefficients.

The Rayleigh extinction coefficient is due to molecular scattering and can be calculated as a function of altitude for known atmospheric molecular densities. Mie scattering is due to particulates and aerosols

in the atmosphere and is highly variable in both particulate size, wavelength, and particle distribution. For identical molecules of density N , the volume extinction coefficient can be written in terms of a cross section $\alpha = \sigma N$ where, σ is the total cross section (cm^2) for the optical interaction with the molecule or particle.

In general, the scattering of light from molecular or particulate matter is not isotropic. The cross section is then specified by the differential cross section $\sigma(\theta, \varphi) = d\sigma/d\Omega$ where, θ is the scattering angle and φ is the polarization angle.⁵⁴ For isotropic scattering, the scattering cross section per unit solid angle is $d\sigma/d\Omega = \sigma/4\pi$. For backscattering ($\theta = \pi$) the volume backscatter coefficient $\beta = N\sigma(\pi)$.⁵⁴

For molecular Rayleigh scattering, the differential cross section is:⁵⁴

$$\frac{d\sigma_R}{d\Omega} = \frac{\pi^2(n^2 - 1)^2}{3\lambda^4 N^2} (\cos^2 \theta \cos^2 \varphi + \sin^2 \varphi), \quad (2.3:3)$$

where,

n = the refractive index,

N = the density of molecules, and

λ = the wavelength of incident light.

For unpolarized light, the angular factor averaged over φ reduces to $(\cos^2 \theta + 1)/2$. Finally, for backscattering ($\theta = \pi$), the Rayleigh backscatter coefficient is uniquely given by:⁵⁴

$$B_R = \frac{8\pi N \sigma_R(\pi)}{3}. \quad (2.3:4)$$

In the above discussion, the Raman volume extinction coefficient has been neglected since it is at least two orders of magnitude less than the Rayleigh extinction coefficient. However, the Raman differ-

ential cross section is given by:^{2,55,56}

$$\frac{d\sigma_{\text{RAM}}}{d\Omega} = \left(\frac{1}{2\pi\epsilon_0 c^2} \right)^2 \omega_1 \omega_2 r^2 \alpha^2, \quad (2.3:5)$$

where,

ω_1 = the pump frequency,

ω_2 = the Raman frequency, and

$r\alpha$ = the Raman polarizability.

The two frequencies differ by the vibrational mode frequency, ω_v , so that $\omega_2 = \omega_1 - \omega_v$.

The large variation in size, density distribution and properties of atmospheric aerosols preclude an accurate calculation of the Mie scattering cross section. However, a useful empirical relation relating the Mie scattering coefficient is given below:^{2,57,58}

$$B_M = \frac{3.91}{V} \left[\left(\frac{0.55}{\lambda} \right)^{0.585(V^{1/3})} \right] \text{ km}^{-1}, \quad (2.3:6)$$

where,

λ = the wavelength of incident light in μm , and

V = the visibility in km.

This empirical expression is an approximation which has been found experimentally to hold under normal visibility conditions when ambient particulate concentrations are relatively low.¹⁸

The final parameter in the atmospheric volume extinction coefficient is absorption. Atmospheric absorption is not serious for wavelengths longer than 2500 Å. Below 2500 Å, absorption due to atmospheric oxygen becomes important with an absorption coefficient reaching 1 km^{-1} at 2450 Å.²

Now, having discussed both the atmospheric scattering mechanisms

and atmospheric parameters, a comparative analysis can be made of the four types of pollution monitoring schemes mentioned in Chp. 1, namely:

1. differential absorption of scattered energy (DASE),
2. resonance fluorescence,
3. Raman and resonance Raman, and
4. long path absorption.

From the discussion which follows, it will be seen that the DASE approach has inherent advantages over the other pollution monitoring schemes.

2.4 LIDAR Schemes: A Comparative Analysis

2.4.1 Introduction

For all four schemes, except the Raman, laser sources are needed at wavelengths that match the resonance absorption of the pollutants of interest. Dye lasers are now available with outputs tunable over the entire near ultraviolet and visible spectral ranges. They are capable of narrow band operation, less than 1 \AA , with good frequency stability.⁵⁹ Pulse energies of over 1 j (per pulse) are typically available from flashlamp-pumped dye lasers. If coaxial flashlamps and appropriate discharge circuitry are utilized, these energies are available in pulses only a few hundred nanoseconds in duration, as is required for obtaining desired depth resolution in LIDAR applications. Several of the important commonly encountered pollutants have absorption spectra in the visible and near ultraviolet due to electronic transitions. These pollutants include NO_2 , NO , SO_2 , and O_3 . This work centers on a pollution monitoring scheme to detect trace contam-

inant levels of NO_2 in the atmosphere.

2.4.2 NO_2 Absorption Spectrum

As can be seen in Fig. 2.4:1, NO_2 has a clearly structured absorption spectrum in the blue, with well defined peaks and troughs.⁹⁵

2.4.3 General Formulation

The backscattered signal from a target at range R is given by:¹⁸

$$P_r(R) = \left(\frac{\rho}{\pi}\right) K P_0 \frac{A}{R^2} \exp\left(-2 \int_0^R \alpha_A(r) dr\right), \quad (2.4:1)$$

where,

$P_r(R)$ = the received power from range R ,

P_0 = the transmitted power,

K = the optical system efficiency,

A = the area of the receiving telescope,

$\frac{\rho}{\pi}$ = the effective reflectivity of the remote target, and

$\alpha_A(r)$ = the volume extinction coefficient at range r .

The transmitted radiation interacts with the pollutant molecules through the atmospheric volume extinction coefficient, α_A , as defined in Eq. 2.3:1. The portion of the returned signal due to Raman and fluorescence scattering is taken into account in the effective reflectivity term ρ/π . The depth resolution attainable by backscatter methods is shown schematically in Fig. 2.4:2. The depth resolution is given by

$$\Delta R = \frac{ct}{2}, \quad (2.4:2)$$

where,

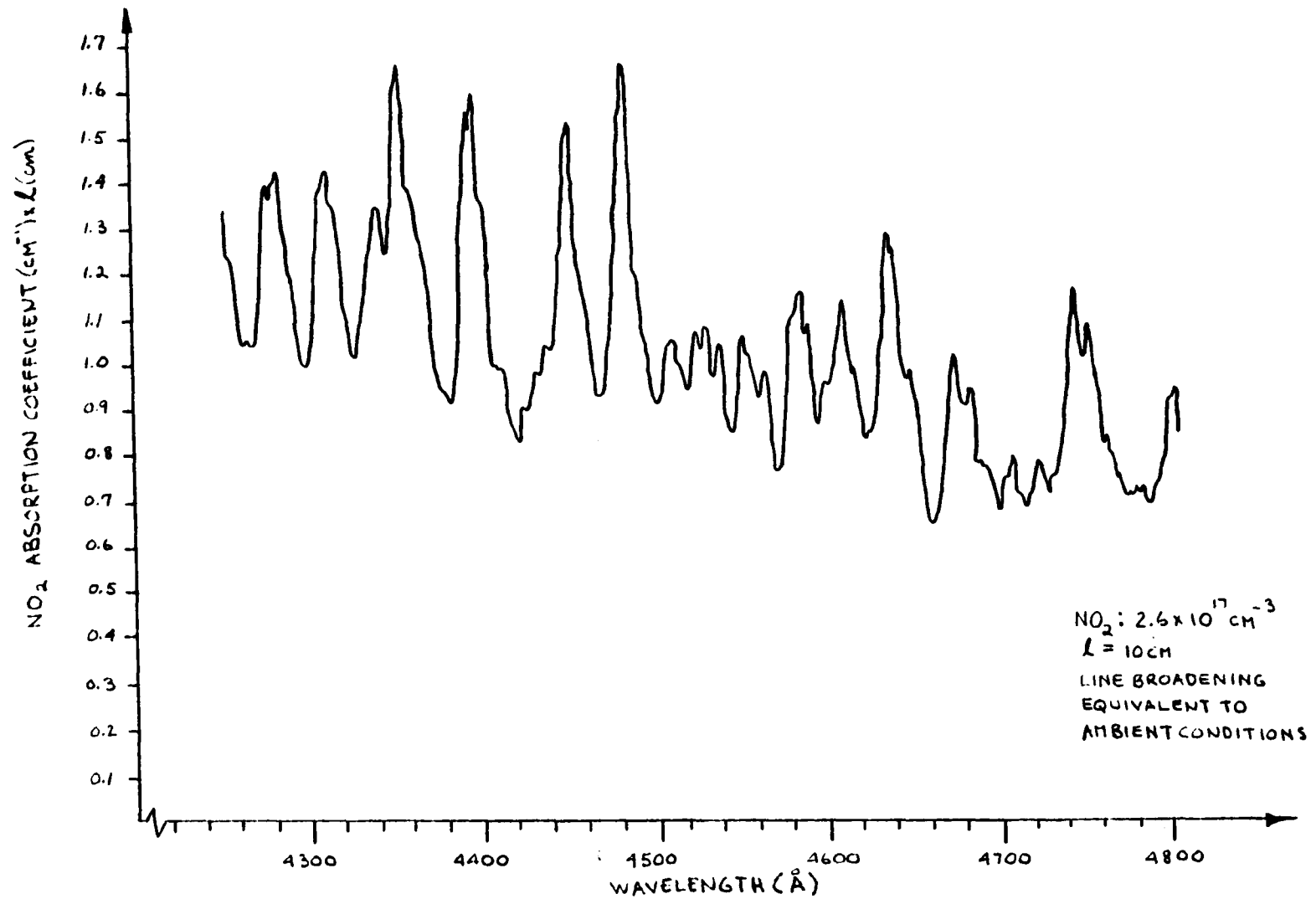


FIGURE 2.4:1 NO_2 ABSORPTION CURVE

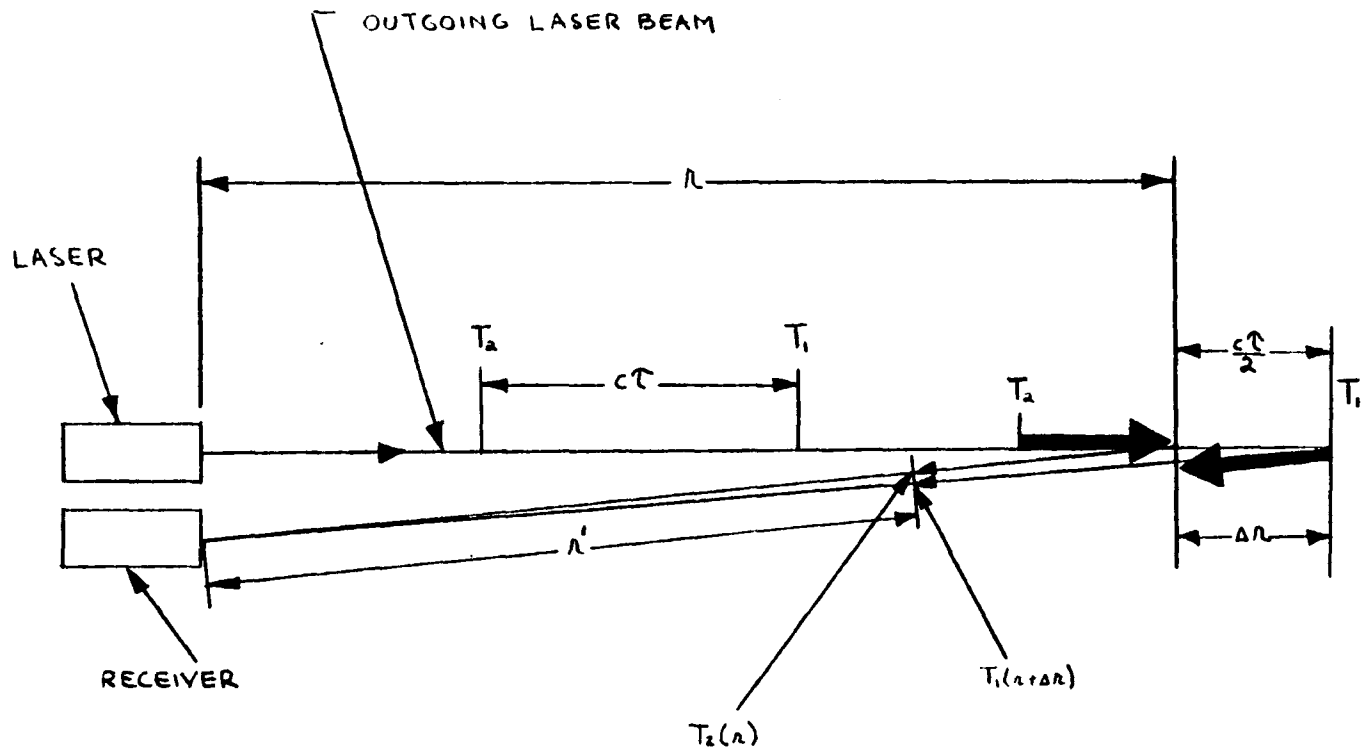


FIGURE 2.4:2 OBTAINABLE DEPTH RESOLUTION FOR BACKSCATTER LIDAR SCHEMES

$\tau = \tau_p + \tau_D + \tau_F$, the sum of the laser pulse width τ_p , the detector integration time, τ_D , and the molecular fluorescence time, τ_F (τ_F only comes into effect in the resonance fluorescence backscatter scheme).

In the discussion that follows, a comparison among the DASE, resonance fluorescence, Raman and resonance Raman, and long path absorption schemes is made. For the purpose of comparison the DASE LIDAR system developed here were used as a basis.

2.4.4 Differential Absorption of Scattered Energy (DASE)

2.4.4.1 Basic Theory

In its simplest form, this scheme determines the concentration of a pollutant at an arbitrary point, distance r in space, by measuring the optical resonance absorption due to the pollutant across an incremental path length, Δr . This is shown schematically in Fig. 2.4:3. The absorption across Δr is obtained from the relative attenuation of two collinear laser beams at close-lying wavelengths, λ_1 and λ_2 , respectively on and off the resonance absorption of the pollutant molecule in question. The relative attenuation is determined from comparisons (at the receiver) of the Rayleigh and Mie atmospheric elastic backscatter from the two laser beams as they traverse Δr . Appropriate temporal resolution at the receiver permits determination of r and Δr , the range and spatial resolution of the pollutant distribution.

Several features of this scheme should be noted at this stage:

1. As mentioned earlier, dye lasers are now capable of narrow band operation, less than 1 \AA , with good frequency stability. Since

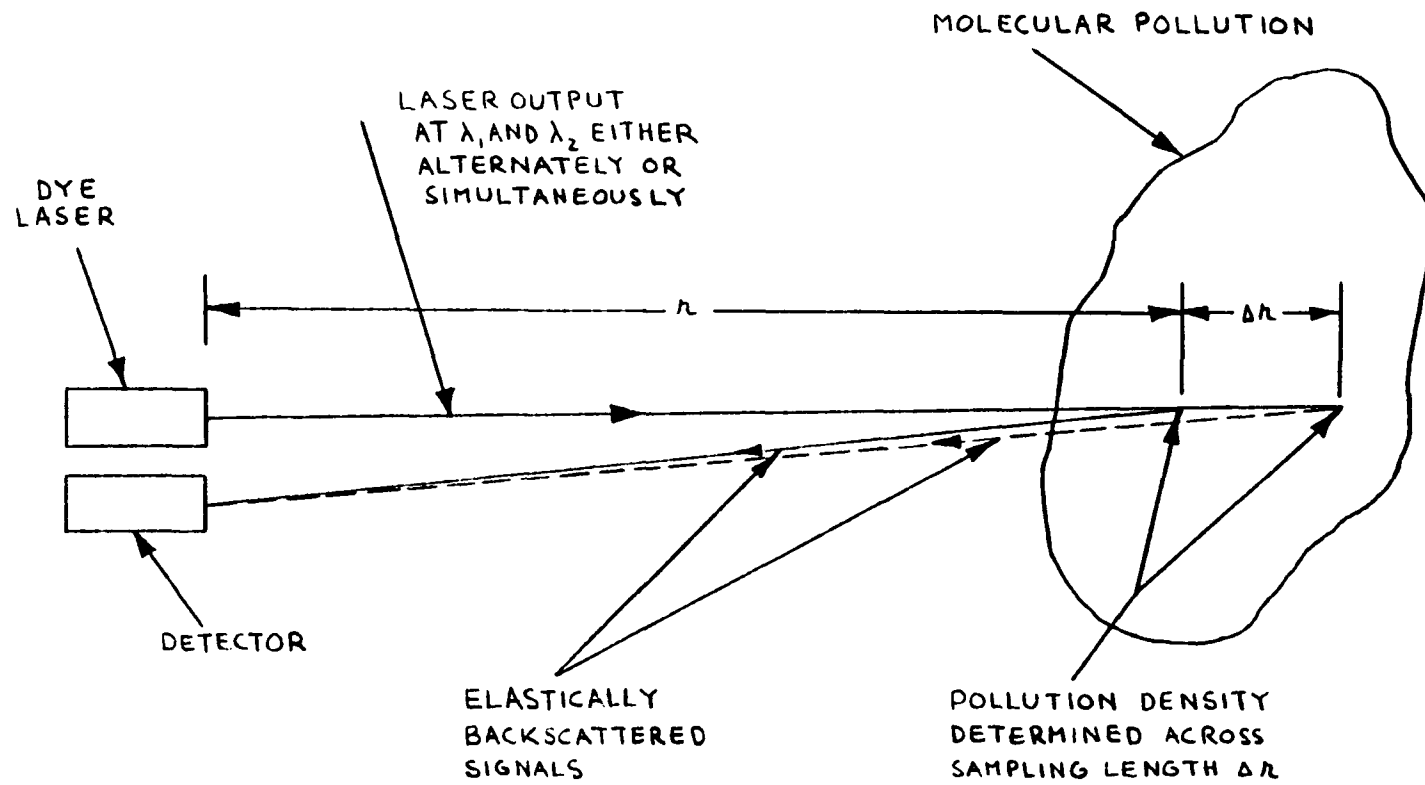


FIGURE 2.4:3 THE DASE SCHEME

the receiver signal is simply the elastic backscattered component of the transmitted signal, this permits the use of very narrow bandwidth receivers (if possible, down to the bandwidth of the transmitted signal). This is an important factor in reducing undesirable background noise and the limitations that it places on LIDAR monitoring schemes.

2. The received signal that is due to the elastic scattering from the atmosphere is relatively large and thus easily detected.
3. Since this scheme determines the pollutant concentration by an absorption method, the achievable detection sensitivity is high even where the required spatial resolution is high (or equivalently, where the sampling lengths are small).

The backscattered power observed by a LIDAR system with collinear transmitting and receiving optical axes is given by Eq. 2.4:1. For the DASE case the effective reflectivity of the atmosphere is given by:¹⁸

$$\frac{p}{\pi} = \frac{ct_p}{2} [\beta_R(R, \lambda) + \beta_M(R, \lambda)], \quad (2.4:3)$$

where,

c = the speed of light,

t_p = the laser pulse length,

$\beta_R(R, \lambda)$ = the Rayleigh backscatter coefficient, and

$\beta_M(R, \lambda)$ = the Mie backscatter coefficient.

Substituting this relation into Eq. 2.4:1 yields,

$$P_r(R, \lambda) = \frac{ct_p}{2} [\beta_R(R, \lambda) + \beta_M(R, \lambda)] K P_0(\lambda) \frac{A}{R^2} \exp \left\{ -2 \int_0^R [\alpha_{SC}(R, \lambda) + \sigma_{ABS}(R, \lambda) N_r] dr \right\}, \quad (2.4:4)$$

where,

$\alpha_{SC}(R, \lambda) = \alpha_R(R, \lambda) + \alpha_M(R, \lambda)$, the atmospheric volume scattering coefficient without absorption,

$\alpha_R(R, \lambda)$ = the Rayleigh volume scattering coefficient, and

$\alpha_M(R, \lambda)$ = the Mie volume scattering coefficient. The other parameters were previously defined.

An expression for \bar{N}_r , averaged over a distance ΔR can be obtained from Eq. 2.4:4 by forming the difference of the logarithm of $P_r(R)$ evaluated at R and $R + \Delta R$ for both a frequency on the absorption peak (λ_1) and to the absorption trough (λ_2). These equations are shown below:

$$\begin{aligned} \ln P_r(R, \lambda_1) - \ln P_r(R + \Delta R, \lambda_1) = & -2\frac{\Delta R}{R} + \ln[\beta_R(R, \lambda_1) + \\ & \beta_M(R, \lambda_1)] - \ln[\beta_R(R + \Delta R, \lambda_1) + \beta_M(R + \\ & \Delta R, \lambda_1)] + 2\bar{\alpha}_{SC}(\lambda_1)\Delta R + 2\sigma_{ABS}(\lambda_1)\bar{N}_r\Delta R, \end{aligned} \quad (2.4:5)$$

$$\begin{aligned} \ln P_r(R, \lambda_2) - \ln P_r(R + \Delta R, \lambda_2) = & -2\frac{\Delta R}{R} + \ln[\beta_R(R, \lambda_2) + \\ & \beta_M(R, \lambda_2)] - \ln[\beta_R(R + \Delta R, \lambda_2) + \beta_M(R + \\ & \Delta R, \lambda_2)] + 2\bar{\alpha}_{SC}(\lambda_2)\Delta R + 2\sigma_{ABS}(\lambda_2)\bar{N}_r\Delta R. \end{aligned} \quad (2.4:6)$$

An expression for \bar{N}_r , the value of N_r averaged for the depth resolution ΔR at range r can be obtained from Eqs. 2.4:5 and 2.4:6 as:

$$\bar{N}_r = \frac{1}{2\Delta\sigma\Delta R} \left[\frac{\ln \frac{P_r(R, \lambda_1)}{P_r(R + \Delta R, \lambda_1)}}{S} - \frac{\ln \frac{P_r(R, \lambda_2)}{P_r(R + \Delta R, \lambda_2)}}{S'} \right] + \quad (2.4:7)$$

where,

$$S = -2[\bar{\alpha}_{SC}(\lambda_1) - \bar{\alpha}_{SC}(\lambda_2)]\Delta R, \quad (2.4:8)$$

$\bar{\alpha}_{SC}(\lambda) = \bar{\alpha}_R(\lambda) + \bar{\alpha}_M(\lambda)$, the total volume scattering coefficient neglecting absorption, averaged over ΔR , and

$\Delta\sigma = \sigma_{ABS}(\lambda_1) - \sigma_{ABS}(\lambda_2)$, the difference in absorption cross

sections.

$$S' = \ln \left[\frac{\beta_R(R + \Delta R, \lambda_1) + \beta_M(R + \Delta R, \lambda_1)}{\beta_R(R, \lambda_1) + \beta_M(R, \lambda_1)} \right] - \ln \left[\frac{\beta_R(R + \Delta R, \lambda_2) + \beta_M(R + \Delta R, \lambda_2)}{\beta_R(R, \lambda_2) + \beta_M(R, \lambda_2)} \right]. \quad (2.4:9)$$

In order to evaluate Eq. 2.4:7, it is necessary to know the magnitudes of S and S' . These quantities are, in general, unknown. However, if the absorption peak and trough measurements are taken nearly simultaneously, so that the β 's and α 's remain constant in time, and if these coefficients do not change significantly over the spectral interval $\lambda_1 - \lambda_2$, then S and S' can be taken to be zero.^{49,52,62} Therefore, making these assumptions, Eq. 2.4:7 reduces to:

$$\bar{N}_T = \frac{1}{2\Delta\sigma\Delta R} \ln \left[\frac{\frac{P_T(R, \lambda_1)}{P_T(R, \lambda_2)}}{\frac{P_T(R + \Delta R, \lambda_1)}{P_T(R + \Delta R, \lambda_2)}} \right], \quad (2.4:10)$$

or,

$$\bar{N}_T = \frac{\ln(1 + \Delta F_T)}{2\Delta\sigma\Delta R}, \quad (2.4:11)$$

where,

ΔF_T = the fractional change in the ratio of ratios of the received signals.

As can be seen from Eq. 2.4:11, the sensitivity of pollutant detection is improved by:

1. the ability of the instrumentation to detect smaller changes in ΔF_T ,
2. increasing the sampling length, ΔR (at a cost of decreasing spatial resolution), and
3. a large resonance absorption cross section, σ_{λ_1} , and a small off-

resonance cross section, σ_{λ_2} .

2.4.4.2 Evaluation of Required System Parameters for Detection of NO₂

2.4.4.2.1 Received Signal Requirements

Assuming a relative change in the ratio of ratios of received signals of 5 percent, a range of 1000 m, minimum spatial resolution of 100 m, and taking the absorption cross sections from Fig. 2.4:1 as $\sigma_{\text{ABS}}(4478.5 \text{ \AA}) = 6.38 \times 10^{-19} \text{ cm}^2$ and $\sigma_{\text{ABS}}(4500 \text{ \AA}) = 3.5 \times 10^{-19} \text{ cm}^2$ (the curve in Fig. 2.4:1 was run with a resolution of 5 Å which matches the typical laser bandwidth used), the minimum detectable pollutant concentration, \bar{N}_p , equal to 0.315 ppm is obtained.

In order to obtain maximum difference in absorption cross sections, and hence achieve better detection sensitivity, laser wavelengths of $\lambda_1 = 4480 \text{ \AA}$ (peak) and $\lambda_2 = 4497 \text{ \AA}$ (trough) were chosen. It should be noted that for narrow filters such as is required in the system described, manufacturers encounter difficulty producing filters exactly to the specifications, and the above was the closest fit that could be obtained.

The received signal power in this DASE LIDAR system is the elastically backscattered fraction of the outgoing laser beam. Since this received power, and therefore the effective range of the system, is determined by the fraction of the power that is reflected, this aspect is considered next.

A detector is dark current limited if²

$$2q \left(\frac{B}{n} \right) \left(\frac{S}{N} \right)_{\min} < i_d, \quad (2.4:12)$$

where,

q = the electronic charge,

B = the electronic bandwidth of the detection system,

n = the number of pulses,

$\left(\frac{S}{N}\right)_{\min}$ = the minimum acceptable signal to noise ratio, and

i_d = the detector dark current.

For photon limited detection the opposite of Eq. 2.4:12 is true. Inserting the values of the detector used, Amprex type 56AVP, ($B = 3$ MHz, $i_d = 15$ nA) into Eq. 2.4:12, it is found that the system is dark current limited for an acceptable signal to noise ratio of 10.

The minimum detectable signal power, $P_{r,\min}$, for dark current limited detectors is given by:²

$$P_{r,\min} = \frac{[2q(B/n)(S/N)_{\min}i_d]^{1/2}}{S_D} \quad (2.4:13)$$

where,

S_D = the detector sensitivity.

For the system described, $P_{r,\min}$ is found to be equal to 6.32×10^{-9} W. The minimum detectable change, ΔP_{\min} , relative to the signal power, P_r , at the detector is given by the following relationship:²

$$\frac{\Delta P_{\min}}{P_r} = \left[\frac{4qB(S)}{nS_D P_r (N)_{\min}} \left(1 + \frac{i_d}{S_D P_r} \right) \right]^{1/2} \quad (2.4:14)$$

Using Eq. 2.4:14 and the parameters for the system ($S_D = 60 \times 10^{-3}$ A/W), a minimum acceptable signal to noise ratio of 10, and a minimum detectable change of 5 percent, it is found that for single pulse operation a received power, P_r , of 0.25 uW is required.

2.4.4.2.2 Transmitted Power Requirements

It is useful at this stage to get an idea of the power requirements

for the laser transmitter for a system of this type.

Assuming an NO₂-polluted-free atmosphere up to the sampled region, ΔR, solving Eq. 2.4:4 for the transmitted power yields:

$$P_0(\lambda) = \frac{P_r(R + \Delta R, \lambda)}{\frac{ct_p [B_R(R + \Delta R, \lambda) + B_M(R + \Delta R, \lambda)]}{2}} \times \frac{1}{\frac{KA}{(R + \Delta R)^2} \exp\{-2[\bar{\alpha}_{SC}(\lambda)(R + \Delta R) + \sigma_{ABS}(\lambda)\bar{N}_r \Delta R]\}}, \quad (2.4:15)$$

where,

$\bar{\alpha}_{SC}(\lambda) = \bar{\alpha}_R(\lambda) + \bar{\alpha}_M(\lambda)$, the total atmospheric volume scattering coefficient without absorption, averaged over R + ΔR, and

\bar{N}_r = the average pollutant concentration over ΔR.

An average pollution concentration of 0.315 ppm of NO₂ over the sampled region of 100 m, a range of 1000 m, a visibility of 10 km, and a received signal power of 0.25 uW for each outgoing wavelength (to give a fractional change of ratio of ratios of received powers of 5 percent), yield the on-line and off-line transmitted powers as 0.0395 MW (9.88 mj) and 0.0375 MW (9.38 mj) respectively.

Increasing the output energies of each line to 1/2 j, the received power increases to 15.9 uW off-line and 15.8 uW on-line, which corresponds to a minimum detectable pollution concentration of 0.029 ppm.

2.4.4.2.3 Pump Depletion

The foregoing discussion considered the Rayleigh and Mie return assuming an NO₂-polluted-free atmosphere up to the sampled region. It is still necessary to consider the problem of pump depletion if the

pollutant is at a density of, say, 0.315 ppm over the entire 1000 m range. Since 100 m cause approximately a 10 percent reduction in received signal power (and approximately a 5 percent reduction in ΔF_r), 1000 m will cause a reduction by a factor of $\exp(-1.08) = 0.34$. The received signal will be down approximately 34 percent of its original value of 5.41 uW off-line and 5.37 uW on-line, and it would be possible to detect a minimum concentration of 0.051 ppm, which corresponds to a 0.45 percent change in ratio of ratios. Thus, a laser pulse energy of 1/2 j per line is sufficient to detect a change of NO₂ concentration of 0.051 ppm averaged over 100 m at a range of 1000 m even when pollution concentrations as high as 0.315 ppm exist along the entire probe beam path.

If the range is decreased to 100 m, a minimum concentration as low as 1.6 ppb could be detected (corresponding to a change in the ratio of ratios of 2.6×10^{-2} percent), with the same optics and output power described above.

2.4.5 Resonance Fluorescence

2.4.5.1 Basic Theory

This scheme determines the pollution concentration at a distance r in space by measuring the fluorescence backscatter induced by the probe beam as it is absorbed by the polluted species. This is shown schematically in Fig. 2.4:4.

2.4.5.2 Evaluation of Required System Parameters for Detection of NO₂

The backscattered fluorescence intensity from range r observed by

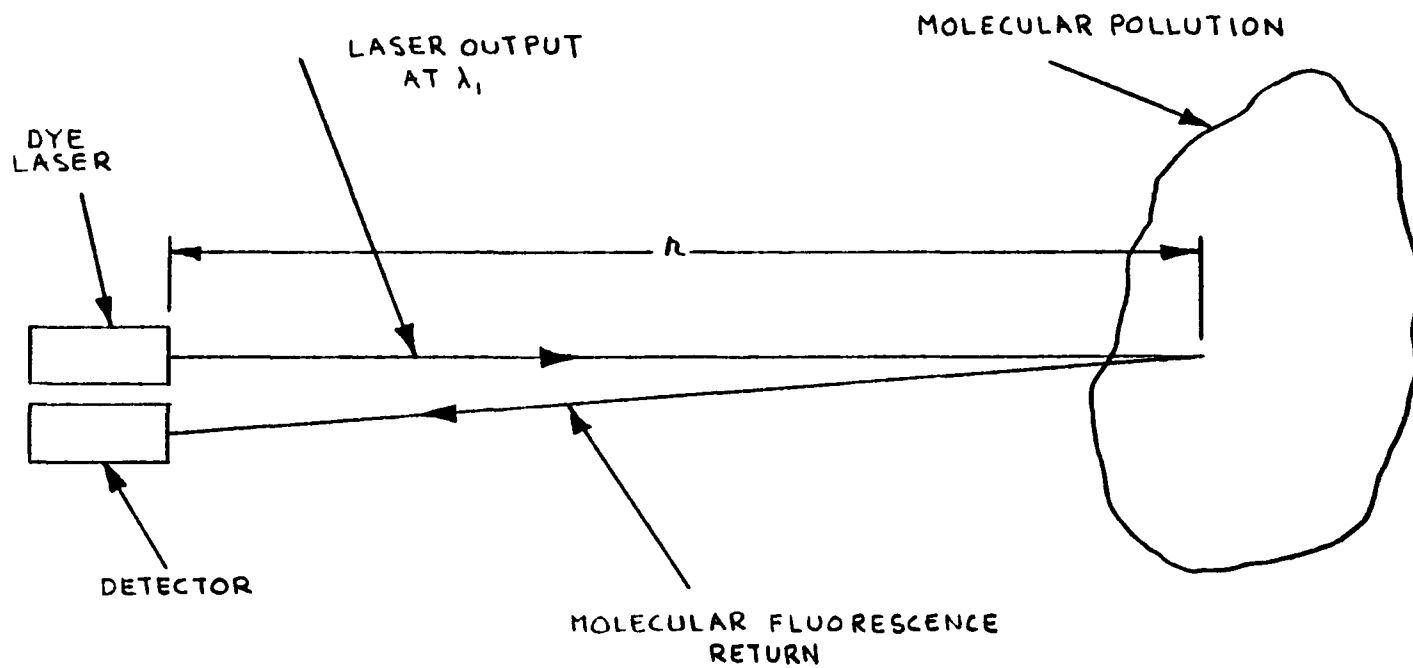


FIGURE 2.4:4 THE RESONANCE FLUORESCENCE SCHEME

a LIDAR system with collinear transmitting and receiving axes is given by Eq. 2.4:1 with the effective reflectivity $\frac{\rho}{\pi}$ given as:²

$$\frac{\rho}{\pi} = \frac{ctN_r\sigma_F}{8} \quad (2.4:16)$$

where,

$$\sigma_F = \sigma_{ABS}(\lambda)Q, \text{ and} \quad (2.4:17)$$

$$Q = \frac{1}{1 + \frac{\tau_{SP}(\frac{1}{Z})}{\tau_{COL}(\frac{1}{Z})}} \approx \frac{\tau_{COL}Z}{\tau_{SP}} \quad (2.4:18)$$

where,

$\frac{1}{Z}$ = the probability of quenching per collision,

τ_{COL} = the collision time, and

τ_{SP} = the spontaneous decay time.

Substituting these terms into Eq. 2.4:1 and assuming an NO₂-polluted-free atmosphere up to the sampled region, ΔR , yields:

$$P_r(R) = KP \frac{0.0ct\sigma_{ABS}(\lambda)\bar{N}_r QAF}{2 \cdot 4\pi R^2} \exp[-2\bar{\alpha}_{SC}(\lambda)R - \sigma_{ABS}(\lambda)\bar{N}_r\Delta R], \quad (2.4:19)$$

where,

F = the fraction of the total fluorescence detected by the receiver,

\bar{N}_r = the average pollutant concentration over the sampled region, ΔR , and

$\bar{\alpha}_{SC}(\lambda) = \bar{\alpha}_R(\lambda) + \bar{\alpha}_M(\lambda)$, the atmospheric volume scattering coefficient without absorption averaged over R.

For an average pollution concentration of 0.029 ppm across the sampled region, a range of 1000 m, a depth resolution of 100 m, and a received

signal of 6.32×10^{-9} W (the minimum detectable received power for the detector used) the required transmitted power of 382 MW is obtained. This power is equivalent to 95.5 j for a dye laser with a pulse length of 250 ns.

The discussion above considered nighttime operation, that is, the entire backscattered spectrum ($F = 1$) was detected. In daytime operation the noise attributed to background radiation must be blocked. This has the effect of reducing the observed fluorescence backscattered signal. Therefore, to detect 0.029 ppm for daytime operation ($F = 0.1$) a transmitted energy of 955 j is required.

These energy requirements are, of course, only to be used as a relative basis for a comparison among the other LIDAR schemes presented. For realistic power requirements, a range of 100 m, a sampled depth of 100 m, an average pollution concentration of 0.1 ppm of NO_2 , yields for nighttime operation a required transmitted power of 3.52×10^5 W (8.80×10^{-2} j). For daytime operation, the required transmitted power increases to 3.52×10^6 W (8.80×10^{-1} j).

To summarize, the resonance fluorescence backscatter scheme has the following disadvantages:

1. Daytime operation severely limits detection sensitivities, resulting from the blockage of background radiation.
2. The fluorescent backscattered signal at the receiver is dependent upon the concentration of the pollutant in the region being probed.

2.4.6 Raman and Resonance Raman

2.4.6.1 Basic Theory

The Raman scheme determines the concentration of the pollutant at an arbitrary point in space by measuring the Raman backscattered intensity induced as the probe beam interacts with the polluted atmosphere. This is shown schematically in Fig. 2.4:5.

2.4.6.2 Evaluation of Required System Parameters for Detection of NO₂

The backscattered Raman intensity at the receiver due to the pollutant is of the same form as that for the resonance fluorescence scheme, but with the effective reflectivity term $\frac{\rho}{\pi}$ given as:¹⁸

$$\frac{\rho}{\pi} = \frac{ctN_p\sigma_{RAM}(\lambda)}{8}, \quad (2.4:20)$$

where,

σ_{RAM} = the Raman scattering cross section.

Substituting this relation into Eq. 2.4:1 and assuming an NO₂-polluted-free atmosphere up to the sampled region, ΔR , yields for the received power:

$$P_r(R) = KP_0 \frac{ct\sigma_{RAM}(\lambda)\bar{N}_p AF}{2 \cdot 4\pi R^2} \exp[-2\bar{\alpha}_{SC}(\lambda)R - \sigma_{ABS}(\lambda)\bar{N}_p \Delta R]. \quad (2.4:21)$$

For an average pollution concentration of 0.029 ppm across the sampled region, a range of 1000 m, a depth resolution of 100 m, and a received power of 6.32×10^{-9} W (the minimum detectable received power), the required transmitted power of 1.77×10^8 MW (4.43×10^7 J) is obtained.

To reduce the transmitted power requirements, this LIDAR scheme can be run in the resonance Raman mode. This has the effect of increasing the received backscattered Raman intensity by increasing the Raman scat-

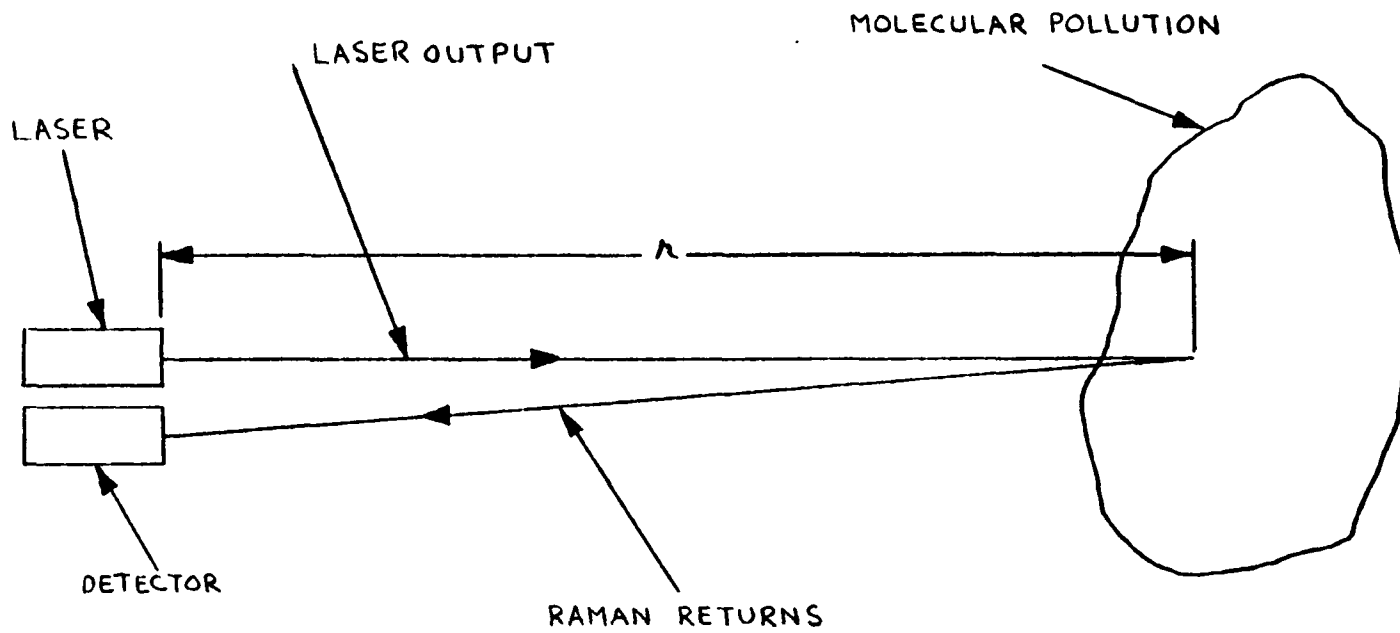


FIGURE 2.4:5 THE RAMAN SCHEME

tering cross section as:²

$$\left(\frac{d\sigma^{\text{RAM}}}{d\Omega}\right)_{\text{RES}} \sim \left(\frac{d\sigma^{\text{RAM}}}{d\Omega}\right)_{\text{NONRES}} \frac{\nu_0^2}{(\nu_1 - \nu_0)^2 + (\Delta\nu/2)^2}, \quad (2.4:22)$$

where,

ν_1 = the laser pump frequency,

ν_0 = the electronic transition frequency, and

$\Delta\nu$ = the linewidth of the electronic transition.

For NO_2 , $\nu_1 = 6.69 \times 10^{14}$ HZ, $\nu_0 = 6.69 \times 10^{14}$ HZ, and $\nu = 2.24 \times 10^{12}$ HZ, Eq. 2.4:22 yields $\left(\frac{d\sigma^{\text{RAM}}}{d\Omega}\right)_{\text{RES}} = 1.21 \times 10^{-23}$ cm^2 . Inserting the

value for the resonance Raman backscattering cross section into Eq. 2.4:21 and evaluating the expression for the same conditions as for the Raman case, 504 MW (126 j) is obtained for the required transmitted power.

Thus far, it has been assumed that the entire backscattered Raman signal was detected. Actually, since the laser probe beam is both Stokes and anti-Stokes shifted, that part of the Raman return signal that the elastic backscatter interferes with must be rejected. Also, since the Raman effect is not a selective process, the backscattered signal consists of many Raman returns from different species of molecules present in the atmosphere. Therefore, the signal of interest must be distinguished from the other Raman returns. This in effect increases the transmitted energy requirement by approximately 10 percent.¹⁸

The energy requirements for both the Raman and resonance Raman schemes, as for the case of resonance fluorescence, are of course only

to be used in a comparison among the LIDAR schemes presented. The magnitude of the nonresonance Raman backscattering coefficient limits the range of this type of LIDAR system to less than 50 m for any practical transmitted energy requirements for monitoring pollution levels present in ambient conditions (0.01 to 5 ppm), and limits the range to less than 75 m for the resonance Raman scheme.²

The disadvantages of the Raman and resonance Raman schemes are summarized below:

1. The Raman backscattering cross sections are 10 to 10^3 smaller than the Rayleigh and Mie backscattering cross sections.
2. The strength of the Raman and resonance Raman returns depend upon the concentration of the pollutant present in the atmosphere. This dependency is the main factor in limiting detection sensitivities. Even though for NO_2 detection, the resonance Raman backscattering cross section is larger than the sum of the Rayleigh and Mie backscattering cross sections ($1.21 \times 10^{-23} \text{ cm}^2$ as compared to $3.21 \times 10^{-28} \text{ cm}^2$ respectively), the backscattering coefficient which is a function of pollutant concentration in the resonance Raman (and Raman) case, and a function of air in the elastic (Rayleigh and Mie) case, determines the strength of the return signal.
3. The Raman and resonance Raman returns that are anti-Stokes shifted are interfered with by the Rayleigh and Mie backscatter. It is therefore necessary to reject that part of the Raman return as well as the elastically backscattered signal, which results in a decrease of detected signal power at the

receiver.

4. In the resonance Raman scheme, since Raman returns are induced by probing approximately with an absorption frequency, and the fluorescence frequency shift for molecules is of the same order as the Raman shift, discrimination problems exist at the receiver. Finally, the magnitude of the backscattered fluorescence intensity may be larger by orders of magnitude than the resonance Raman intensity.²

2.4.7 Long Path Absorption

2.4.7.1 Basic Theory

In this technique, the average pollution concentration along the probe beam, Fig. 2.4:6, is determined from measurements of the relative attenuation along the length of the probed path, R , of two collinear laser beams at close-lying wavelengths, λ_1 and λ_2 , respectively on and off a resonance absorption peak of the pollutant in question. This scheme has the disadvantages of needing a remote detector or reflective target to receive the transmitted beam, and lacks depth resolved measurements. The advantages of this scheme are its good sensitivity and the use of low power light sources.

Since monostatic LIDAR schemes are the ones of interest, two types of long path absorption schemes are considered, namely:

1. long path absorption utilizing a retroreflector, and
2. long path absorption utilizing a topographical target.

The received power at the detector is given by Eq. 2.4:1 with the appropriate effective reflectivity terms inserted. For absorption meas-

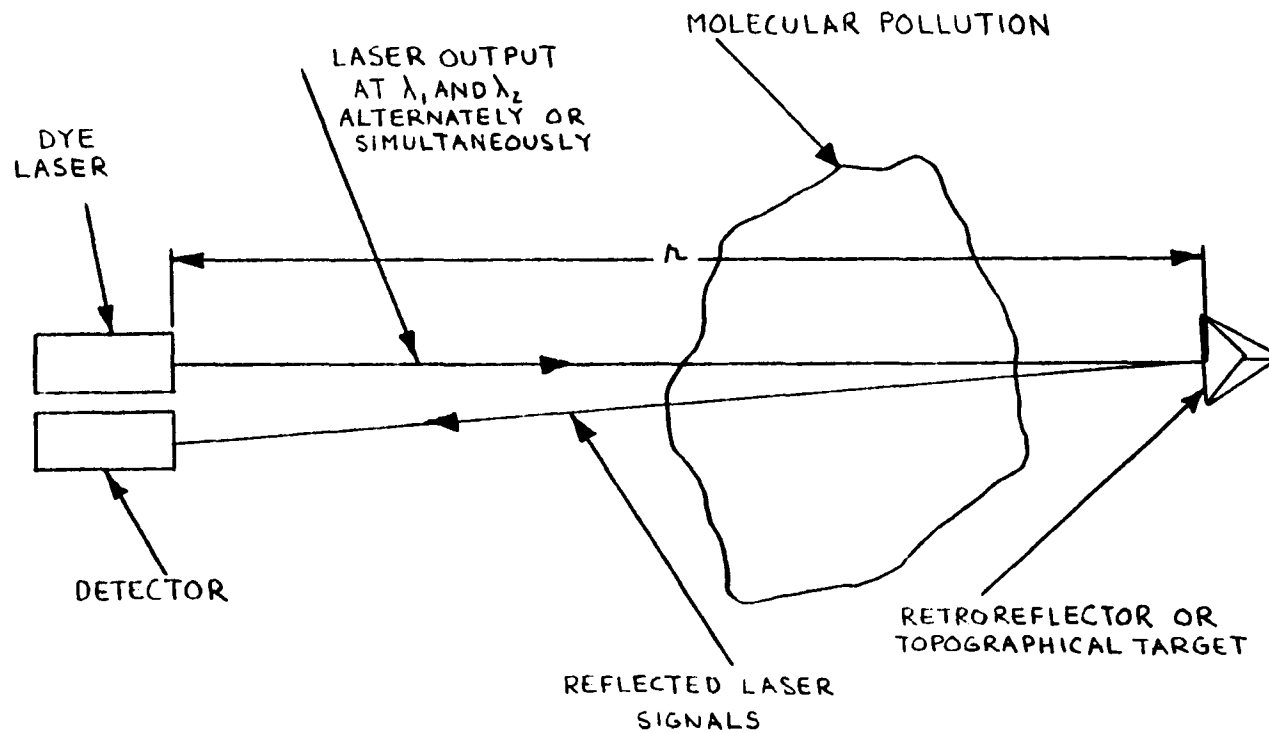


FIGURE 2.4:6 THE LONG PATH ABSORPTION SCHEME

measurements with a retroreflector and a collimated transmitted beam, the range-squared dependence is effectively cancelled. Thus, all the transmitted power is collected except for a collection efficiency factor, ξ , which is near unity, and the effective target reflectivity is orders of magnitude better than for a Lambertian scatterer. The effective reflectivity term for such a case is given by:¹⁸

$$\left(\frac{P}{\pi}\right)_{\text{RETRO}} = \frac{R^2 \xi}{A} . \quad (2.4:23)$$

For long path absorption by scattering from topographical targets:

$$\left(\frac{P}{\pi}\right)_{\text{TOPOG}} = \frac{P}{\pi} , \quad (2.4:24)$$

where,

$$p \approx 0.1 \text{ for visible and u.v. wavelengths.}^{18}$$

An expression for the average pollutant concentration over R can be obtained by taking the difference between the logarithms of the received powers from the off-line and on-line wavelengths respectively:

$$\begin{aligned} \ln P_R(R, \lambda_2) - \ln P_R(R, \lambda_1) &= \ln P_0(\lambda_2) - \ln P_0(\lambda_1) + \\ &2[\bar{\alpha}_{SC}(\lambda_1) - \bar{\alpha}_{SC}(\lambda_2)]R + \\ &2[\sigma_{ABS}(\lambda_1) - \sigma_{ABS}(\lambda_2)]\bar{N}_R R, \end{aligned} \quad (2.4:25)$$

where,

$$\bar{\alpha}_{SC}(\lambda) = \bar{\alpha}_R(\lambda) + \bar{\alpha}_M(\lambda), \text{ the total atmospheric volume scattering coefficient without absorption averaged over R, and}$$

$$\bar{N}_R = \text{the average pollutant concentration over R.}$$

Solving for the average pollutant concentration yields:

$$\bar{N}_R = \frac{1}{2\Delta\sigma R} \left[\frac{\ln P_0(\lambda_1)}{P_0(\lambda_2)} - \frac{\ln P_R(R, \lambda_1)}{P_R(R, \lambda_2)} + S'' \right], \quad (2.4:26)$$

where,

$$S'' = -2[\bar{\alpha}_{SC}(\lambda_1) - \bar{\alpha}_{SC}(\lambda_2)]R, \text{ and}$$

$\Delta\sigma = \sigma_{ABS}(\lambda_1) - \sigma_{ABS}(\lambda_2)$, the difference in absorption cross sections.

In order to evaluate Eq. 2.4:26 exactly, it is necessary to know the magnitude of the S'' term. This quantity is, in general, unknown.

As in the DASE scheme, if the peak and trough measurements are taken nearly simultaneously, so that the α 's remain constant in time, and if these coefficients do not change significantly over the spectral interval, $\lambda_1 - \lambda_2$ (which is true for the case for close-lying wavelengths), then S'' can be taken to be zero.^{49,52,62} Therefore, Eq.

2.4:26 reduces to:

$$\bar{N}_r = \frac{1}{2\Delta\sigma R} \ln \left[\frac{\frac{P_0(\lambda_1)}{P_0(\lambda_2)}}{\frac{P_r(R,\lambda_1)}{P_r(R,\lambda_2)}} \right], \quad (2.4:27)$$

or,

$$\bar{N}_r = \frac{\ln(1 + \Delta F_r)}{2\Delta\sigma R}, \quad (2.4:28)$$

where,

ΔF_r = the fractional change in the ratio of ratios of the on-line and off-line transmitted and received powers respectively.

To make a comparison between the long path absorption and the other LIDAR schemes mentioned, an average pollution concentration of 0.029 ppm of NO_2 along a probed path of 1000 m are assumed. The required on-line and off-line transmitted powers are then found.

2.4.7.2 Evaluation of Required System Parameters for Detection of NO₂

For both the long path absorption methods, utilizing a retroreflector and a topographical target, the received power at the detector is given by Eq. 2.4:1 with the proper effective reflectivity terms inserted for each case. Solving Eq. 2.4:1 for the transmitted power for the topographical target case yields:

$$P_0(\lambda) = \frac{P_r(R, \lambda)}{\frac{0.1KA}{\pi R^2} \exp\{-2[\bar{\alpha}_{SC}(\lambda) + \sigma_{ABS}(\lambda)N_r]R\}} \quad (2.4:29)$$

Inserting the appropriate values into Eq. 2.4:29 yields the on-line and off-line transmitted powers as 1.22×10^5 W (3.05×10^{-2} j) and 1.17×10^5 W (2.93×10^{-2} j) respectively.

The use of a specular retroreflector has the effect of cancelling out the R^2 dependence. This is seen by the reduced on-line and off-line transmitted power requirements, which are 4.44×10^{-4} W (1.11×10^{-10} j) and 4.23×10^{-4} W (1.06×10^{-10} j) respectively.

As can be seen from the above results, the long path absorption scheme offers required sensitivities needed to monitor pollutant concentrations found in urban areas (.01 to 5 ppm). This is done with more than conservative transmitted power requirements. Unfortunately, this is accomplished at the expense of losing depth-resolved measurements.

2.5 Summary

A tabulated summary showing the relative merits for each LIDAR system considered in the comparison is given in Table 2.4:1. The compari-

son was made by first calculating the operating characteristics for the DASE system: an assumed minimum detectable change of received powers of 5 percent, the received power needed to observe the minimum detectable change (0.25 μ W for each on-line and off-line wavelengths), an assumed range of 1000 m, and a depth resolution of 100 m. These conditions led to the attainable sensitivity of 0.029 ppm of NO_2 with moderate transmitted energy requirements of 9.88 mJ (on-line) and 9.38 mJ (off-line). Then, the required received powers were calculated for the above parameters, assuming output energies of 1/2 j in each lasing line.

Since the Raman, resonance Raman, and resonance fluorescence schemes require orders of magnitude higher output energy levels than the long path absorption and DASE methods, the received power was assumed to be equal to the minimum detectable power for our system, namely, 6.32×10^{-9} W. This was done in order to show that under optimum operating conditions, these systems still fall short to the long path absorption and DASE output energy requirements to detect the same pollutant concentration of NO_2 (0.029 ppm).

As can be seen, the long path absorption schemes require the least output energies to monitor a given pollutant concentration, or equivalently the best sensitivity for a given output energy. Unfortunately, this is accomplished at the expense of losing depth-resolved measurement capabilities. The DASE scheme, therefore, combines the spatial resolution offered in the Raman, resonance Raman, and resonance fluorescence schemes, with the greater attainable sensitivities of the long path absorption schemes.

LIDAR Meth.	Range (m)	Res. (m)	Concen. NO ₂ (ppm)	Received Power		Required Transmitted Power		Required Transmitted Energy	
				On-Line (W)	Off-Line (W)	On-Line (MW)	Off-Line (MW)	On-Line (J)	Off-Line (J)
Raman	1000 *	100 *	0.029 *	*	6.32×10^{-9} *	*	1.77×10^9 *	*	4.43×10^8 *
Reson. Raman	1000 **	100 **	0.029 **	6.32×10^{-9} **	**	5.04×10^3 **	**	1.26×10^3 **	**
Reson. Fluor. (night)	1000 (100)	100 (100)	0.029 (0.1)	6.32×10^{-9} (6.32×10^{-9})		3.82×10^2 (3.52×10^{-1})		9.55×10^1 (8.80×10^{-2})	
Reson. Fluor. (day)	1000 (100)	100 (100)	0.029 (0.1)	6.32×10^{-9} (6.32×10^{-9})		3.82×10^3 (3.52)		9.55×10^2 (8.80×10^{-1})	
Long Path Abs. Topog.	1000	1000	0.029	15.8×10^{-6}	15.9×10^{-6}	1.22×10^{-1}	1.17×10^{-1}	3.05×10^{-2}	2.93×10^{-2}
Long Path Abs. Retro.	1000	1000	0.029	15.8×10^{-6}	15.9×10^{-6}	4.44×10^{-10}	4.23×10^{-10}	1.11×10^{-10}	1.06×10^{-10}
DASE	1000	100	0.029	15.8×10^{-6}	15.9×10^{-6}	2.00	2.00	5.0×10^{-1}	5.0×10^{-1}

(): For realistic power requirements

*: Limited to less than 50m for detection of ambient pollution levels

** : Limited to less than 75m for detection of ambient pollution levels

TABLE 2.4:1 TABULATED COMPARISON OF MONOSTATIC LIDAR SCHEMES

CHAPTER 3 THE LIDAR SYSTEM

3.1 Introduction

The basic LIDAR system consists of a flashlamp-pumped dye-laser transmitter, and an optical receiver.⁶³ Figs. 3.1:1a and b show a schematic for the combination. Two arrangements and modes of operation are possible. In one mode, signals at the "on" and "off" resonance absorption wavelengths were generated and detected sequentially. In the other mode they were generated and detected simultaneously. The arrangement shown in Fig. 3.1:1a is for sequential operation and that shown in Fig. 3.1:1b is for simultaneous.

3.2 Optical Receiver

The primary lens of the optical receiver is an acrylic Fresnel lens (purchased from Fresnel II, Inc.) mounted on a light-tight steel frame which was designed for the purpose. This lens is basically a flat thin piece of a plastic on which a series of concentric stepped zones extending from the center to the edge are molded. Fig. 3.2:1 illustrates the geometric relationship between the zones on the Fresnel lens and the surface of an ordinary lens. Each zone refracts the incident light so that the combined action of each refracting facet focuses light essentially in the same manner as a conventional lens.

The lens used has a focal length of 24 inches, a diameter of 15 inches, and a thickness of 1/8 inch. With concentric zones spaced approximately 125 grooves per inch, the lens is capable of forming a sharp image for objects near the optical axis. This is appropriate,

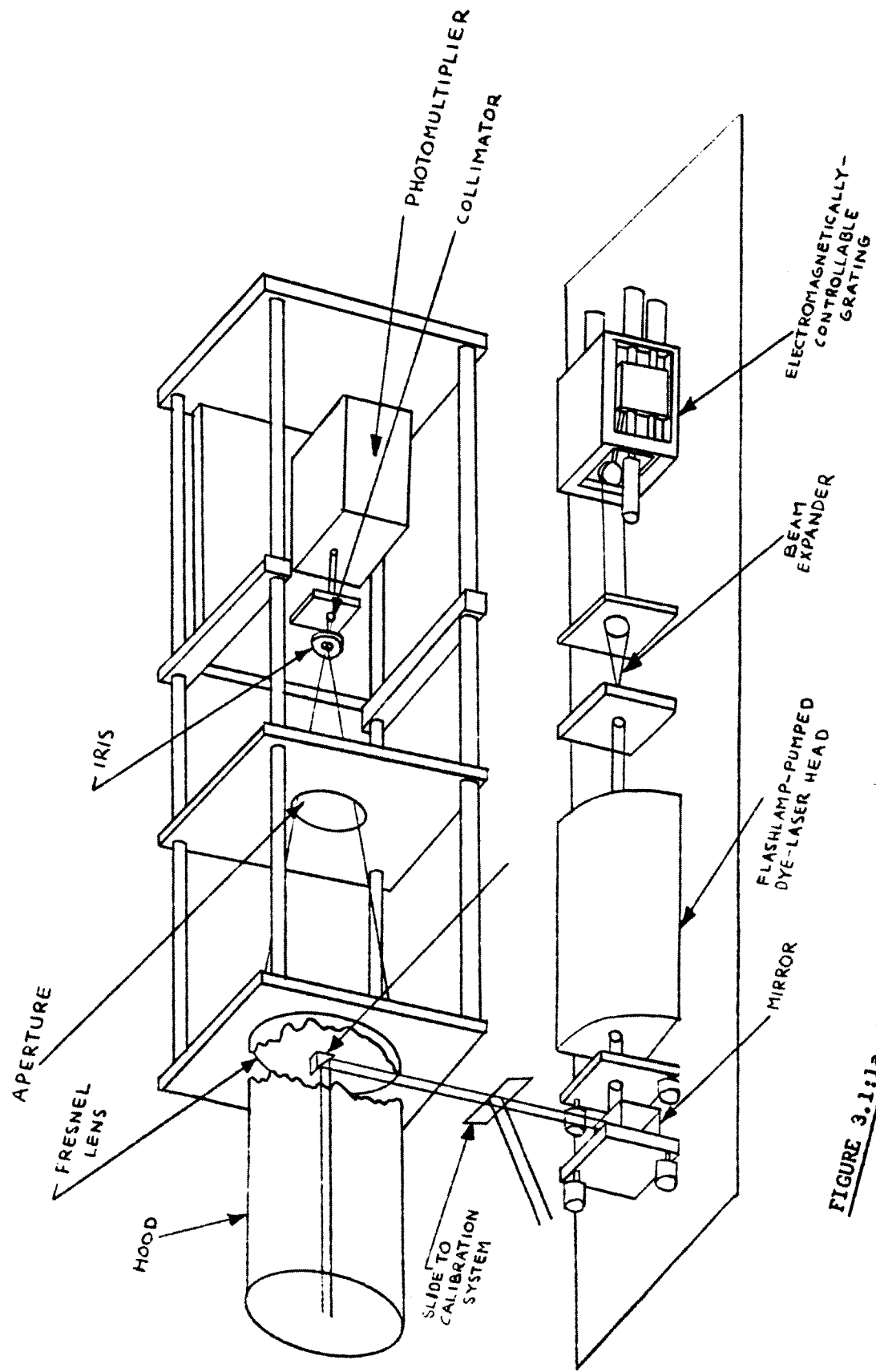


FIGURE 3.1:1a THE LIDAR SYSTEM FOR SEQUENTIAL OPERATION



FIGURE 3.1:1b PHOTOGRAPHS OF THE LIDAR SYSTEM FOR SIMULTANEOUS OPERATION

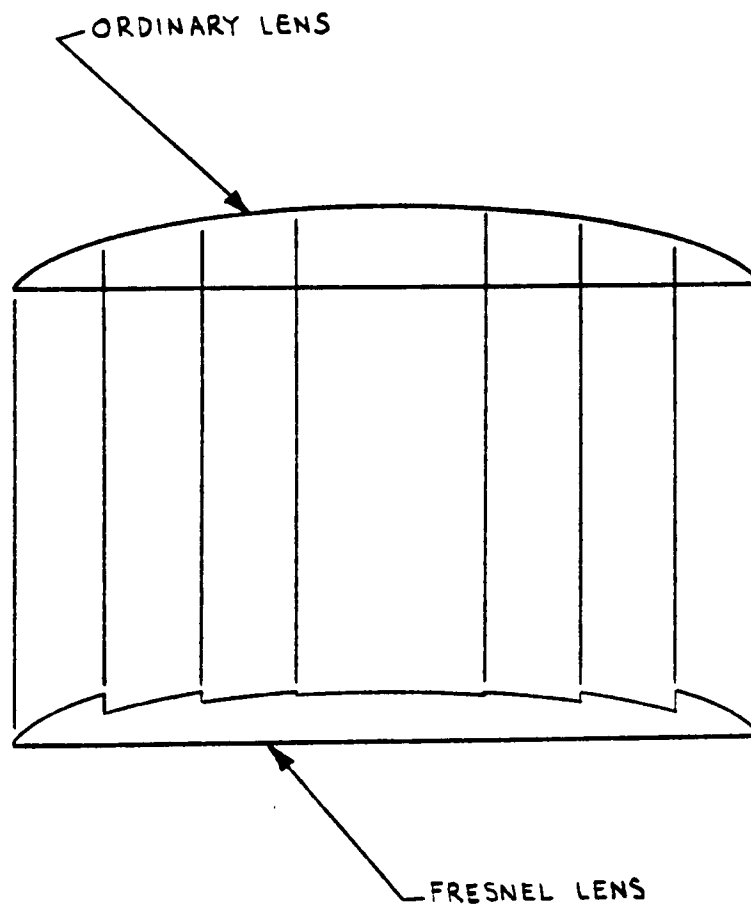


FIGURE 3.2:1 FRESNEL LENS

since a LIDAR receiver does not require a wide field of view for collecting the backscattered light from the region scanned.

For this Fresnel lens, the circle of least confusion for collimated light directed parallel to the optical axis was measured and found to be approximately one centimeter. In the plane containing the circle of least confusion, the spatial distributio of the collected light is a bright spot of the above diameter with the surrounding area weakly illuminated by light spuriously scattered at the edges of the concentric zones of the Fresnel lens. To eliminate the spurious light, an iris was placed in the plane containing the circle of least confusion. Since LIDAR receivers do not require a wide field of view, this remedy does not pose a problem. The Fresnel lens used in this system costs far less than a comparable parabolic mirror, yet its quality is certainly acceptable for our LIDAR application.

The backscattered light collected by the Fresnel lens is then collimated by a 1.5 inch diameter lens, and for the sequential mode of operation, passes through a 58 \AA bandwidth three-period filter onto an Amperex 56 AVP photomultiplier. The center wavelength of the filter and its bandwidth are such that the "on" and "off" resonance absorption wavelengths are both passed by it. To further reduce spurious light pick-up, a three foot cylindrical lens hood is mounted on the front of the receiver.

In the simultaneous wavelength mode of operation, the collimated light entering the receiver is split by means of a partial reflector into two beams. Each of these beams is then directed to a separate photomultiplier covered with a narrow filter of the appropriate fre-

quency. The photomultipliers used are Amperex type 56 AVP. See Figs. 3.2:2a and b. The interference filters have measured half bandwidths of 8.3 \AA and 7.7 \AA centered at 4478.5 \AA and 4500 \AA respectively. See Spec. Sheet 3.6:1.

The photomultiplier outputs, corresponding to the backscatter return signals are displayed on Tektronix type 549 oscilloscopes and recorded photographically.

3.3 The Dye Laser

3.3.1 The Laser Head

The basic laser system consists of a flashlamp-pumped organic-dye laser. The laser head is constructed in a coaxial arrangement in which the flowing dye is uniformly excited by an annular discharge surrounding the active medium. See Figs. 3.3:1a and b. The laser head, model DL2100B, and discharge circuitry was purchased from the Phase-R Company, and was chosen for maximum energy output and shortest possible pulse width. Fig. 3.3:1b shows the laser head situated in the LIDAR system, and Fig. 3.3:2 shows a typical output pulse.

The organic dye, 7-diethylamino-4-methyl coumarine, dissolved in ethanol was used as the lasing medium. A concentration of $3 \times 10^{-5} \text{ M/l}$ was found to give maximum output energy consistent with a laser linewidth that was less than the halfwidth of the absorption peak of NO_2 to be measured, i.e., less than approximately 10 \AA for the 4478.5 \AA absorption peak. In this manner, it was possible to maximize the return signal, thereby increasing range, and still retain the maximum difference between absorption peak and trough, and thus attain the sen-

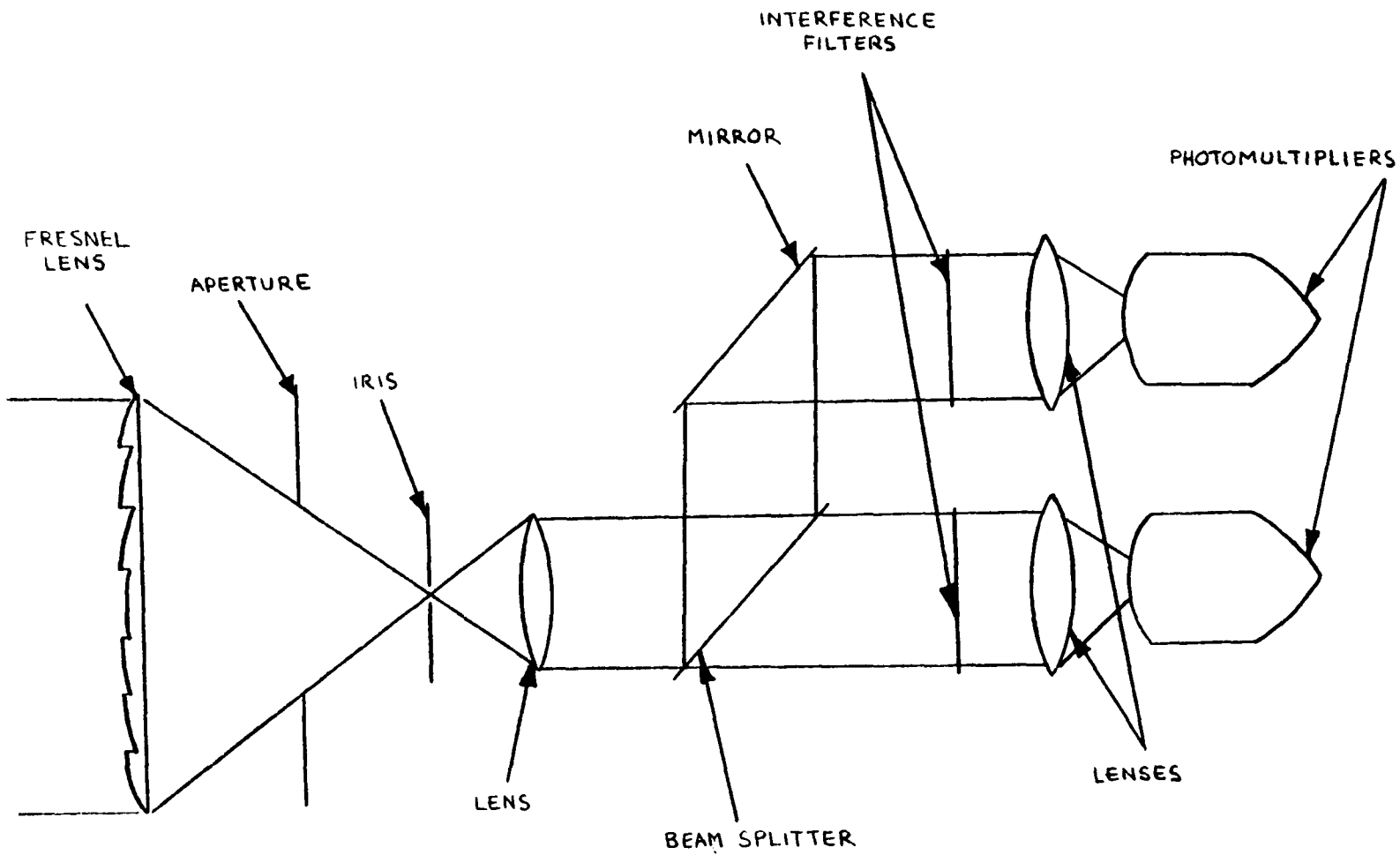


FIGURE 3.2:2a THE OPTICAL RECEIVER SYSTEM FOR SIMULTANEOUS OPERATION

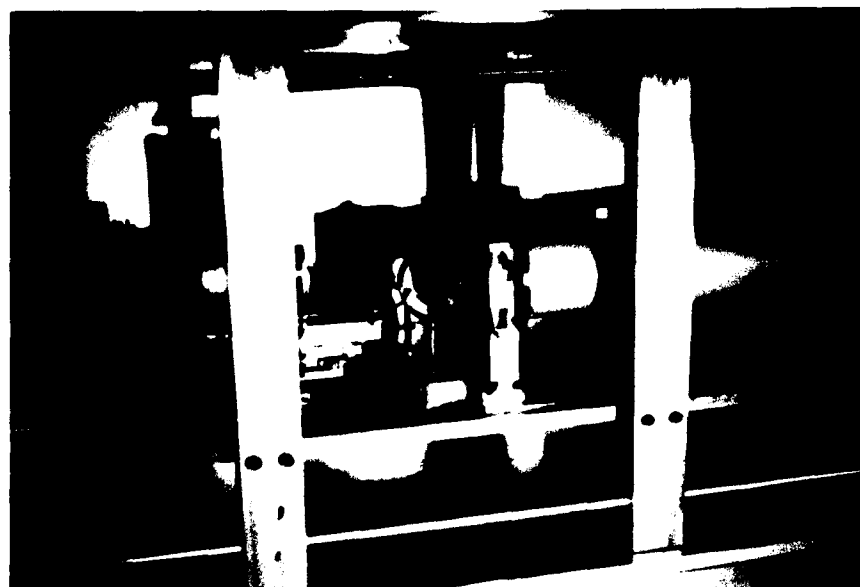


FIGURE 3.2:2b PHOTOGRAPHS OF THE OPTICAL RECEIVER SYSTEM FOR
SIMULTANEOUS OPERATION

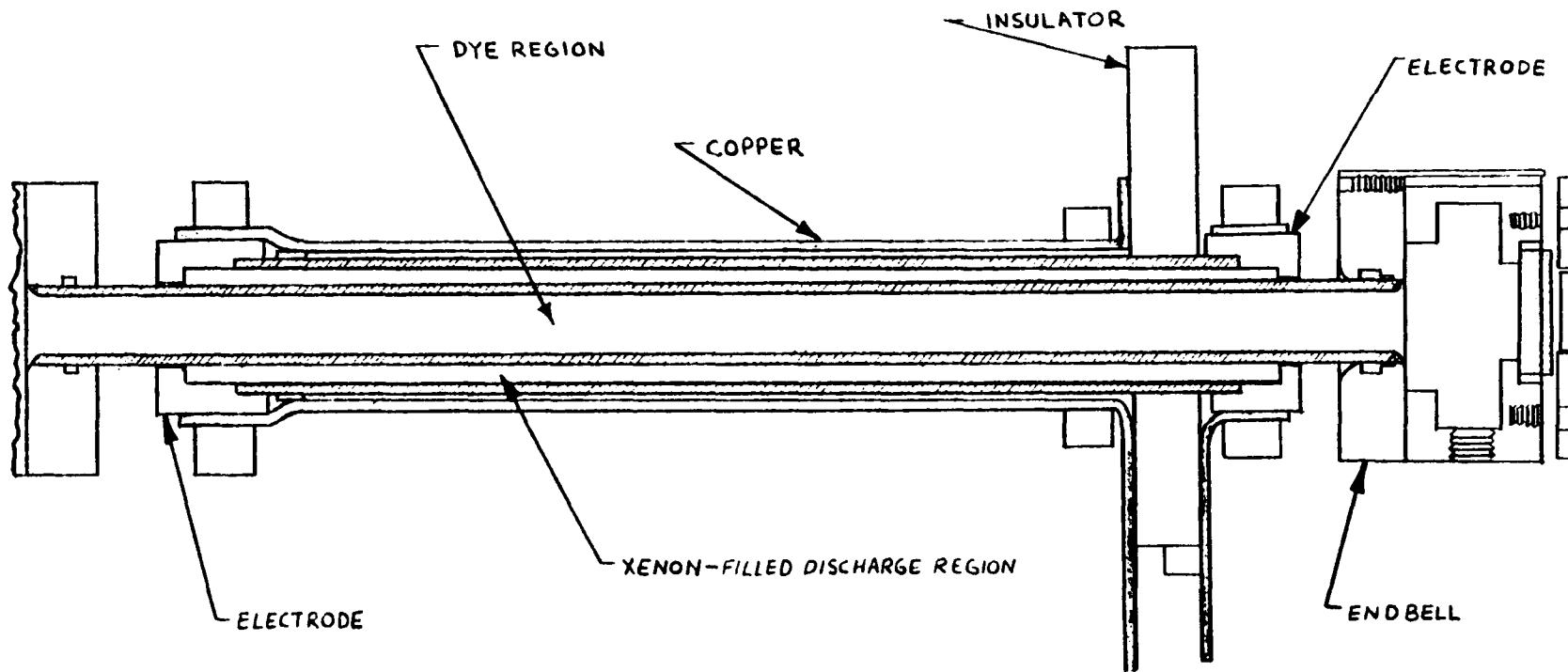


FIGURE 3.3:1a COAXIAL ARRANGEMENT OF THE FLASHLAMP-PUMPED DYE-LASER HEAD

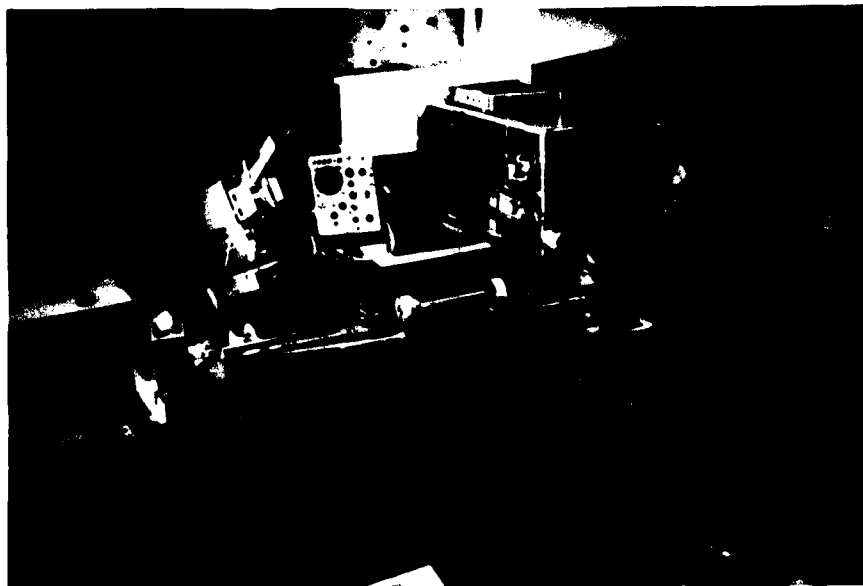


FIGURE 3.3:1b PHOTOGRAPHS OF THE LASER HEAD SITUATED IN THE LIDAR
SYSTEM

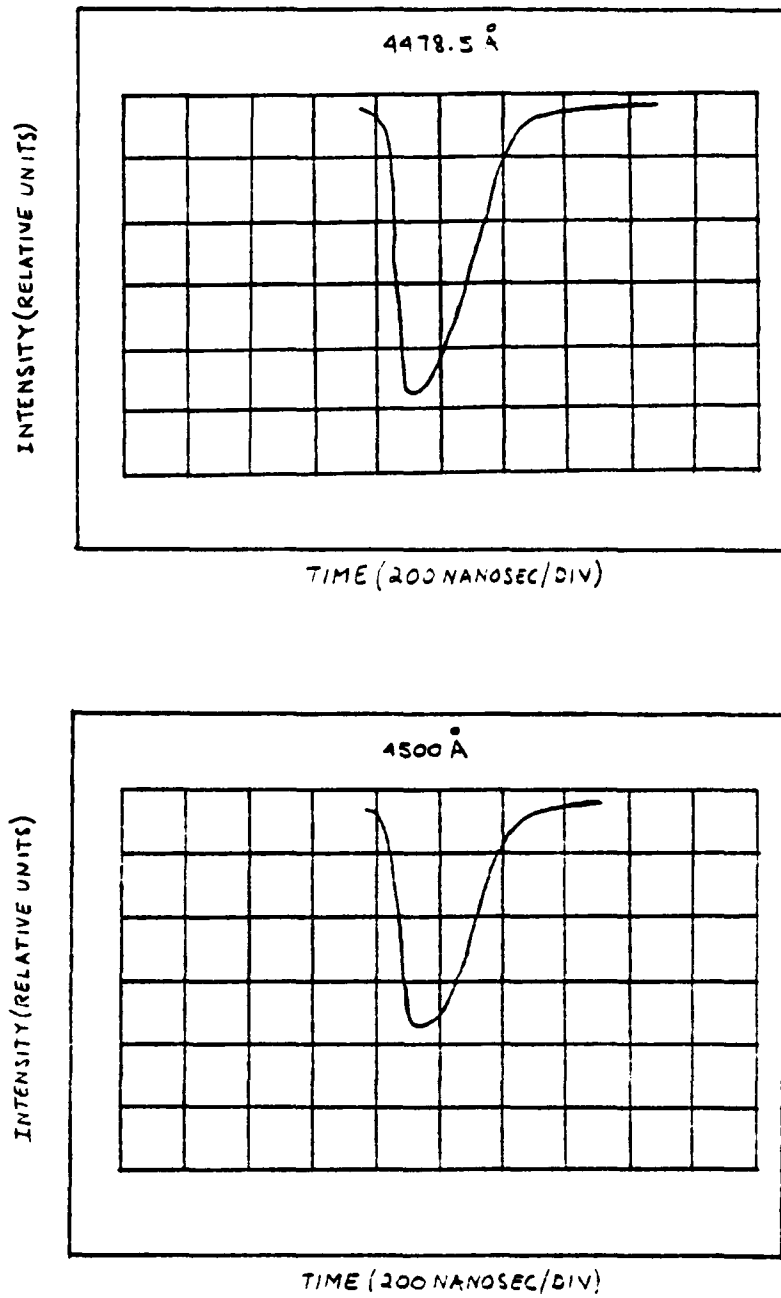


FIGURE 3.3:2 TYPICAL FLASHLAMP-PUMPED DYE-LASER OUTPUT PULSE

sitivities that the system is capable of.

3.3.2 Dye Laser Mechanism--Brief Description

Organic molecules possess a lowest excited singlet state, $^1S_0^*$, and fluorescsnce when it occurs, originates from this state. In making a fluorescent transition the molecule reverts back to its ground state, 1S_0 , while simultaneously emitting radiation.

The spectrum of the fluorescent radiation from an organic dye often has more than one maximum, and it usually spans a region no less than several hundred angstroms wide. The reason for this large bandwidth is that the radiation is actually made up of hundreds of components, corresponding to transitions originating from various sublevels of the first excited singlet state and terminating at various sublevels of the ground state. These sublevels are associated with specific vibrations of the molecule as a whole. See Fig. 3.3:3. Since some of the vibrational sublevels of the ground state may be high enough in energy so that they are normally unoccupied, a population inversion sufficient for laser action can be established between the states from which fluorescence originates and some of the higher vibrational levels of the ground state.

Once threshold conditions are reached, the laser light that is produced has frequencies centered about one of the broad fluorescence peaks. The bandwidth of such broadband operation can range up to 200 Å for flashlamp-pumped dye lasers.

To reduce the naturally large bandwidth of the flashlamp-pumped dye laser output, a tuning element such as a diffraction grating can be

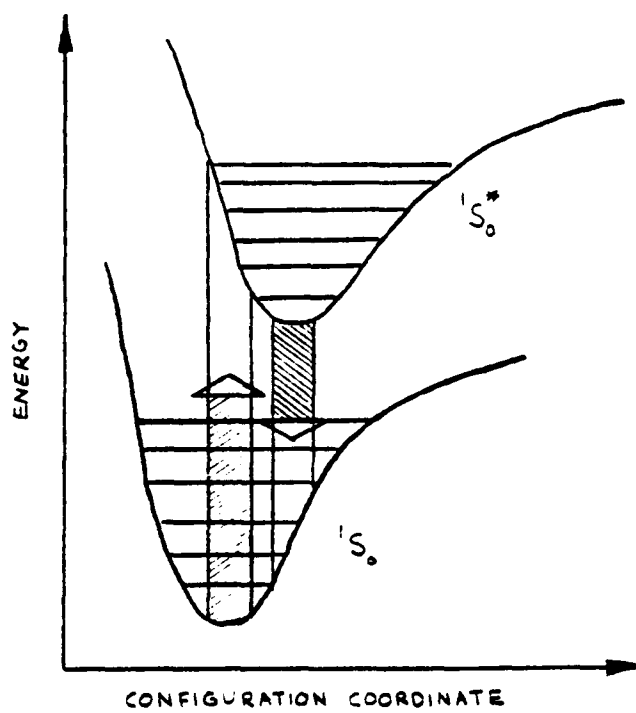


FIGURE 3.3:3 ENERGY LEVELS OF ORGANIC DYE MOLECULES

placed in the laser cavity. With the proper choice of grating characteristics, such as blaze wavelength, grooves per millimeter, and power-density handling capabilities, etc., the desired laser frequency and bandwidth are attainable, and may be chosen to match the absorption peak and troughs for NO_2 .

3.3.3 Intra-Cavity Grating for Wavelength Selection

To obtain laser outputs at the required wavelengths, 4478.5 \AA and 4500 \AA , and linewidths, a grating with the specifications given in Spec. Sheet 3.6:1 was chosen, tested, and found suitable. In both sequential and simultaneous modes of operation, gratings are used in the Littrow configuration with the Blaze angle in the first order. In this manner, all the other orders extinguish and the diffracted energy is concentrated in the first order (at the wavelength desired).

Gratings have different efficiencies (percentage of light incident on a grating that is diffracted into the desired order) for light that is polarized perpendicularly or in parallel to the groove profile. For the gratings used, perpendicularly polarized light gives the better efficiency. See Spec. Sheet 3.6:1. Since a polarizing element is inserted intra-cavity for the simultaneous mode of operation, this factor must be taken into account.

For both modes of operation the bandwidth of the laser lines obtained are determined by the dispersion of the grating and the effective aperture created by the geometry of the lasing medium, which in turn depends upon the distance of the grating from the laser head. This is readily seen in Fig. 3.3:4. The dispersion of the grating is the angular separa-

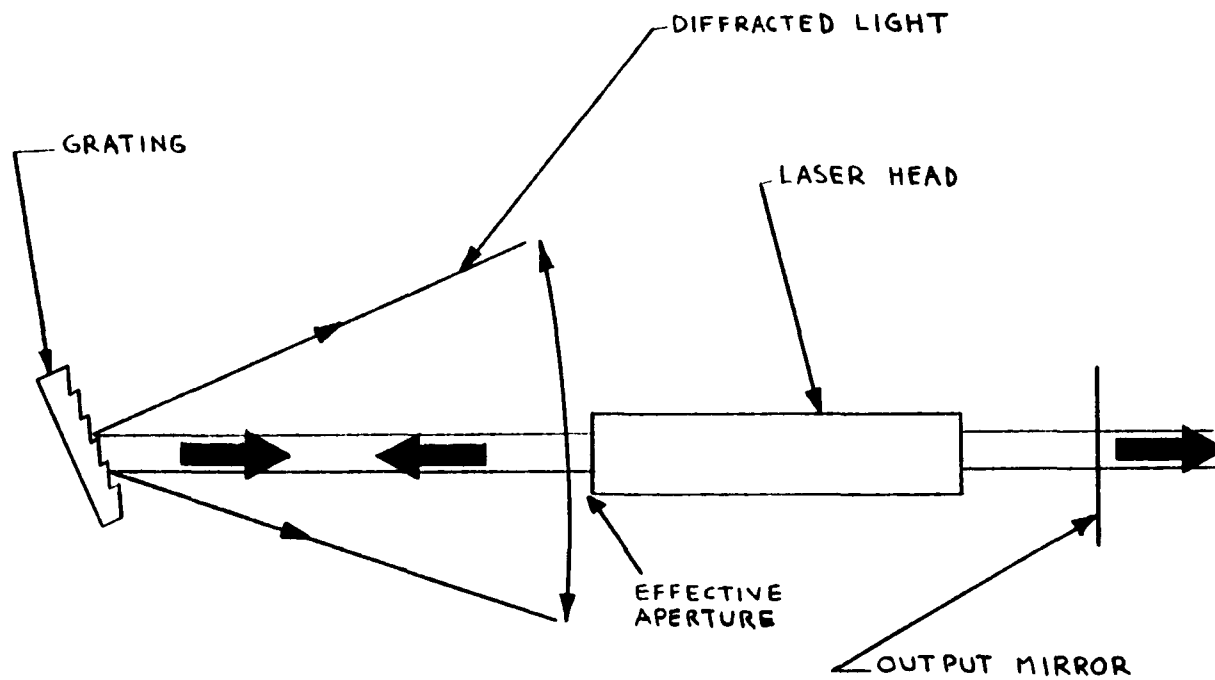


FIGURE 3.3:4 DISPERSION OF GRATING AND EFFECTIVE APERTURE CREATED BY THE LASER HEAD

ration obtained for two different radiations. Therefore, the farther the grating is from the laser head containing the lasing medium the smaller the lasing bandwidth.

3.4 Experimental Arrangement for Sequential Operation

Sequential operation of the dye laser at two desired wavelengths was achieved with the arrangement shown in Figs. 3.3:1 and 3.4:1.

The grating at one end of the laser cavity is used to obtain the desired wavelengths of laser oscillation. With a overall cavity length of approximately 2.5 m, and a 30 percent output mirror, the desired wavelengths at 4478.5 Å and 4500 Å (on and off resonance absorption respectively) are obtained with approximately 5 Å linewidths.

Mechanical stops are adjusted to define the grating orientation at these two wavelengths. The grating is then switched from the setting for one wavelength to the other by means of an electromagnetic drive after each firing of the laser. The time between shots is approximately 5 seconds, the time required for the capacitors to recharge after firing a pulse.

3.5 Simultaneous Two-Wavelength Operation

3.5.1 The Need for Simultaneous Two-Wavelength Operation

Thermal effects and consequent index changes in the atmosphere cause perturbations in both the outgoing and backscattered signals. In addition, particulate drift in existing winds can also cause fairly rapid changes of the scene being scanned by the LIDAR beam. Both these factors argue in favor of the use of simultaneous two-wavelength

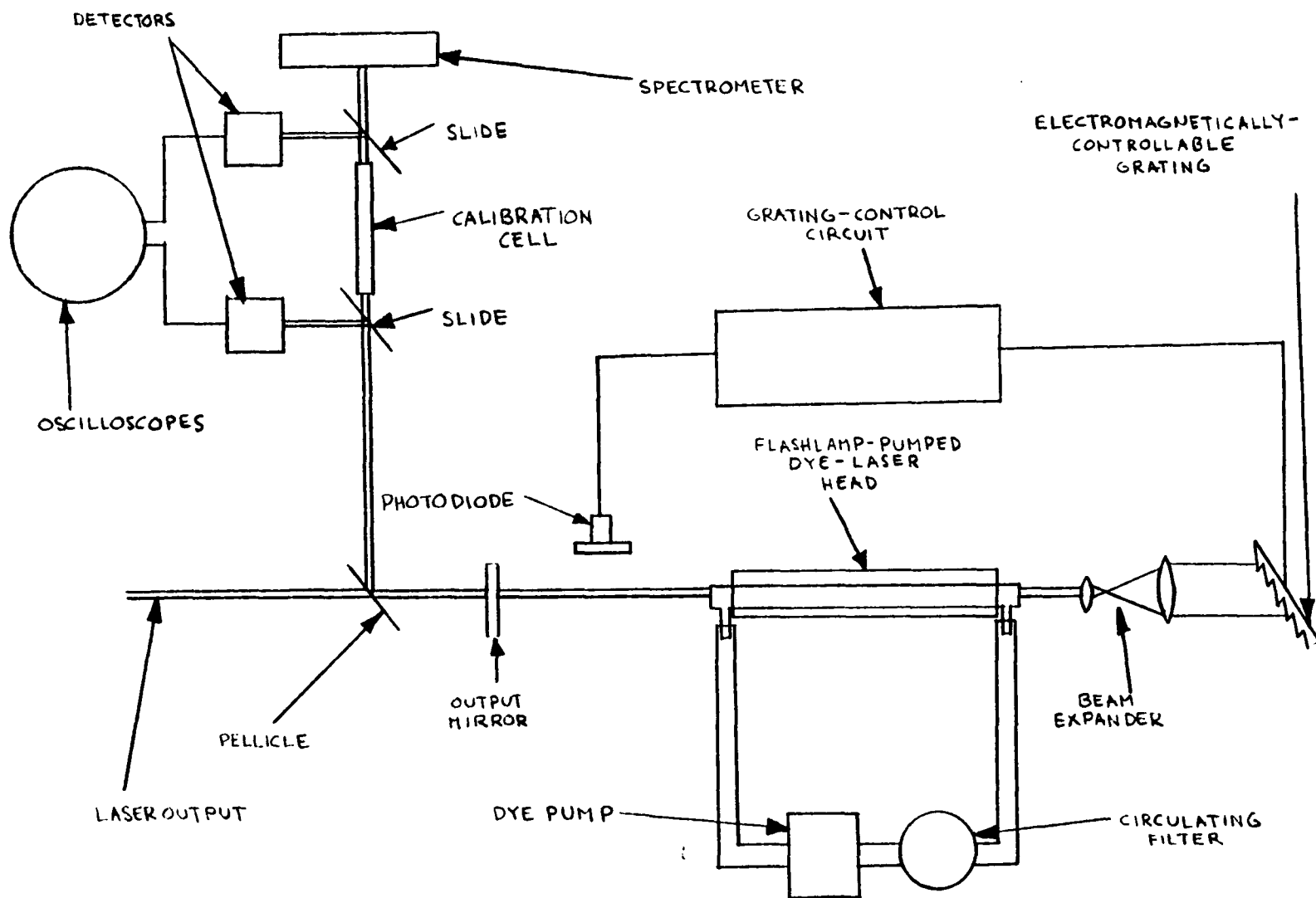


FIGURE 3.4:1 THE OVERALL TRANSMITTING SYSTEM WITH CALIBRATION SETUP FOR SEQUENTIAL OPERATION

LIDAR operating mode.

The thermal factors affecting the signals are summarized below:⁵⁸

1. Beam steering--angular deviation of the beam from the line-of sight path, causing the beam to miss the receiver. See Fig. 3.5:2.
2. Image dancing--variations in the beam-arrival angle, causing the focus to move in the image plane.
3. Beam spreading--small angle scattering, increasing the beam divergence and causing a decrease in spatial power density at the receiver. See Fig. 3.5:1.
4. Beam scintillation--small scale destructive interference within the beam cross section, causing variations in the spatial power density at the receiver. See Fig. 3.5:3.

The effects of scintillation on laser beam propagation have been studied both experimentally and theoretically.^{62,64} However, atmospheric scintillation effects involving 180-degree backscatter have received relatively little attention either theoretically or experimentally.

A recent survey article by Lawrence and Strohbehn demonstrates that under most conditions the power spectrum of intensity fluctuations for one-way propagation decreases above approximately 100 HZ, and is quite small above 1000 HZ.⁶⁴ In the absence of data for two-way propagation, it is reasonable to assume that the high-frequency power spectra for one-way and two-way propagation are the same. Hence, the atmosphere can perhaps be considered stable insofar as scintillation is concerned for time intervals smaller than 1 ms.⁶²

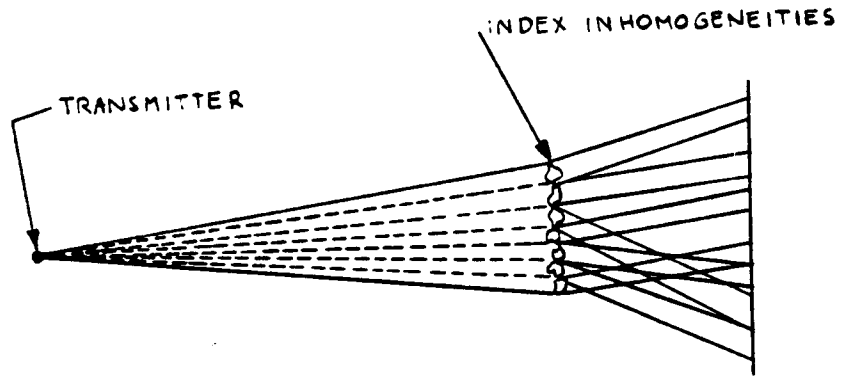


FIGURE 3.5:1 BEAM SPREADING

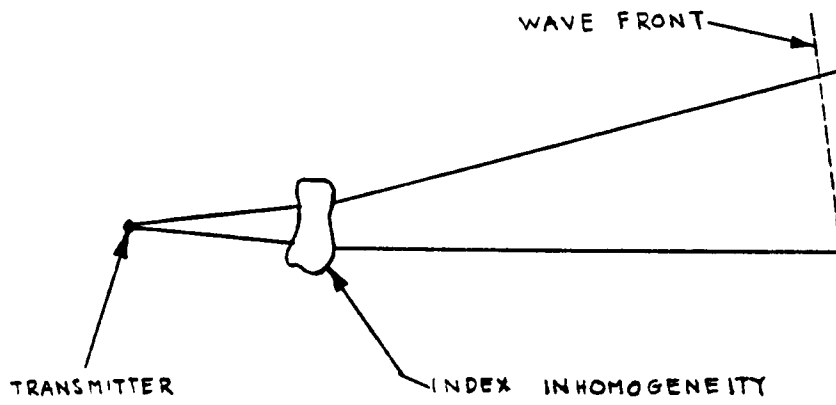


FIGURE 3.5:2 BEAM STEERING

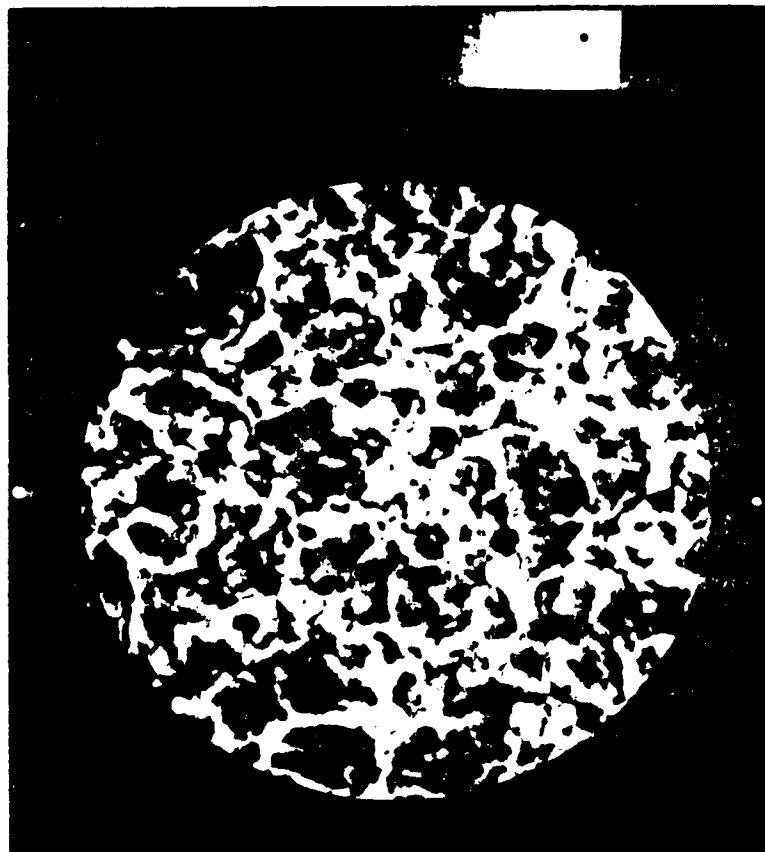


FIGURE 3.5:3 BEAM SCINTILLATION ⁵⁸

Therefore, to be unaffected by scintillation the differential absorption measurement must be completed within this time interval. The optimum manner to meet this requirement is to emit two pulses (of slightly differing wavelengths) simultaneously. Spatial fluctuations within each sampled depth will be averaged out for each pulse, and in any case variations from one sampled depth to another will be the same for both wavelengths, and therefore will not affect the results.

3.5.2 Cavity Design

3.5.2.1 Introduction

To obtain laser action at the two wavelengths simultaneously, the arrangement shown in Figs. 3.5:4a and b, with a polarizing beam-splitting prism in the laser cavity, was evolved and used successfully.^{65,66} With the prism splitting the light into two beams polarized at right angles to each other, each of the two wavelengths lases along one of the polarizations. Competition, in the form of bandwidth changes, between the two wavelengths is observed and is discussed in Sect. 3.6.

Two types of polarizing beam splitters were tested for this application:

1. a polarizing beam-splitting cube utilizing dielectric coatings,
and
2. an air-spaced Glan-Taylor prism.

While both provided simultaneous laser action for close-lying wavelengths in the 4500 Å spectral region, it was found that each suffered some drawbacks. Both types of beam splitters are examined further below.

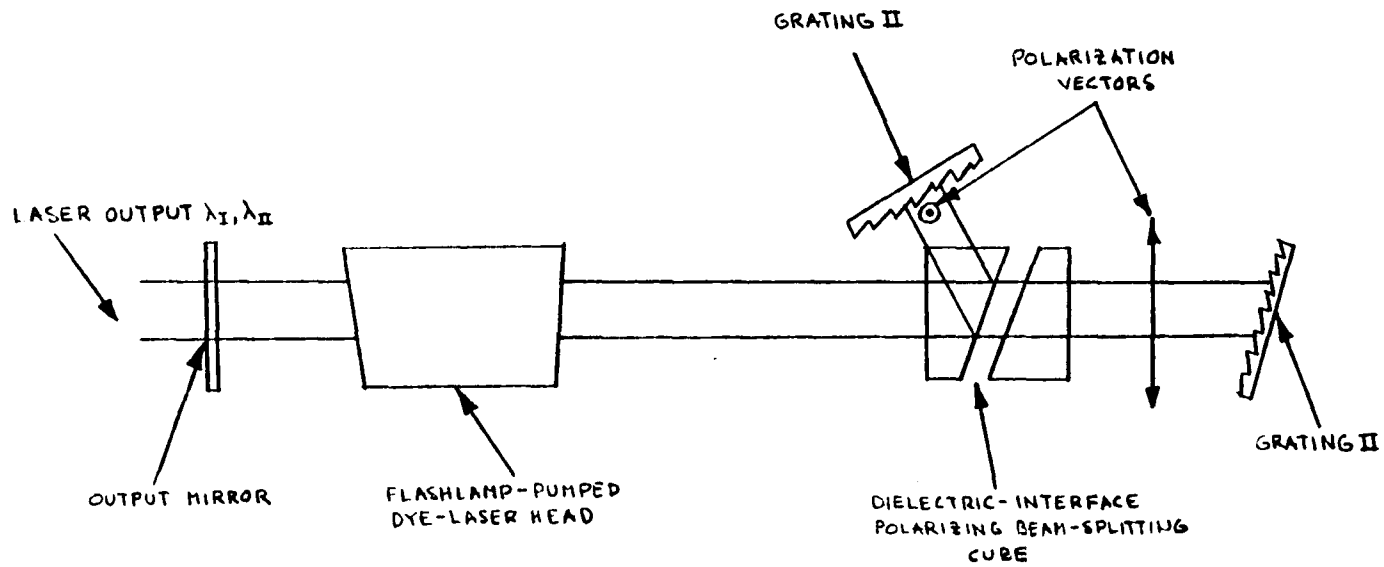


FIGURE 3.5:4a OPTICAL ARRANGEMENT FOR SIMULTANEOUS TWO-WAVELENGTH OUTPUT



FIGURE 3.5:4b PHOTOGRAPHS OF THE OPTICAL ARRANGEMENT FOR SIMULTANEOUS
TWO-WAVELENGTH OUTPUT

3.5.2.2 Dielectric-Interface Polarizing Beam-Splitting Cube

The principle of this device is that it is always possible to find an angle of incidence so that the Brewster condition for an interface between two materials of differing refractive index is satisfied. When this occurs, the reflectance for the parallel-plane (p) of polarization vanishes. Perpendicularly-polarized (s) light is partially reflected and transmitted. To increase the s-reflectance, retaining the p-transmittance at or very near unity, the two materials are then made into a multilayer stack. The layer thicknesses are quarter-wave optical thicknesses at the appropriate angle of incidence.

When the Brewster angle for normal thin-film materials is calculated, it is found to be greater than 90 degrees referred to air as the incident medium. In other words, it is beyond the critical angle for the materials. This presents a problem which is solved by building the multilayer filter into a glass prism so that the light can be incident on the multilayer at an angle greater than critical. The type of arrangement is shown in Fig. 3.5:5.

The dielectric-interface polarizing beam-splitting cube tested was found to have an acceptance angle of up to 5 degrees, a passband extending from approximately 2245 Å to 6739 Å, and whose center wavelength is approximately 4490 Å. The entrance and both exit faces were polished to $\lambda/10$, and were antireflex coated for 4490 Å.

Utilizing the dielectric-interface polarizing beam-splitting cube, simultaneous two-wavelength operation was readily achieved. Fig. 3.5:6 is a picture taken from a 1/2 m Jarrell-Ash scanning spectrometer, and shows the two beams of close-lying wavelengths (the signal to the right is



FIGURE 3.5:6 SPECTROMETER PHOTOGRAPH OF THE SIMULTANEOUS
TWO-WAVELENGTH OUTPUT UTILIZING THE DIELECTRIC-
INTERFACE POLARIZING BEAM-SPLITTING CUBE

centered at 4478.5 \AA and to the left at 4500 \AA) operating in the simultaneous mode, and obtained using the dielectric-interface polarizing beam-splitting cube. Both beams have output energies of approximately 100 mj, and bandwidths of 5 \AA .

3.5.2.3 Air-Spaced Glan-Taylor Prism

The power handling capabilities of the air-spaced Glan-Taylor prism far exceed that of the dielectric-interface prism, since the medium sandwiched between the two prisms is air rather than a delicate dielectric coating. This prism is in fact comprised of two linearly birefringent calcite ($\text{CaO} \cdot \text{CO}_2$) prisms separated by the air gap.

In each prism the optic axis is perpendicular to the incident beam and to the lateral faces. The operation of the device may be readily understood in view of Fig. 3.5:7. This shows the air-spaced prism, its optic axis, and the incident unpolarized beam. When an unpolarized laser beam is incident upon the input face, two refracted orthogonally linearly-polarized beams are produced. The E-ray, the refracted beam whose polarization direction is parallel to the optic axis, experiences no change in index as it propagates through the prism-air-gap-prism combination.

The O-ray, the refracted beam whose polarization direction is perpendicular to the optic axis, experiences a large change in index at the calcite-air-gap interface and is thus totally internally reflected.

Use is made of both the E and O-rays to simultaneously obtain laser action on beams polarized at right angles to each other with gratings terminating the laser cavities beyond each prism. The optical arrange-

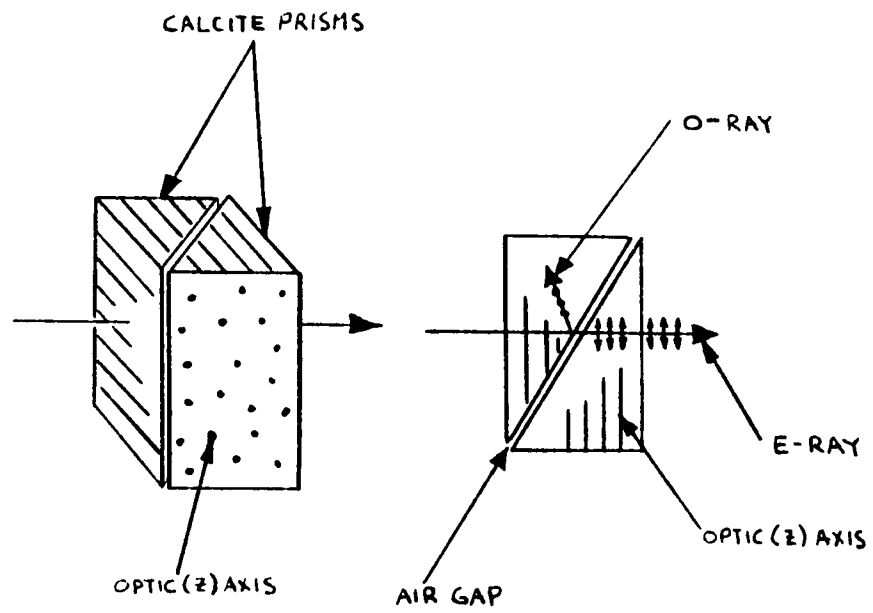


FIGURE 3.5:7 AIR-SPACED GLAN-TAYLOR PRISM

ment is shown in Fig. 3.5:4.^{65,66}

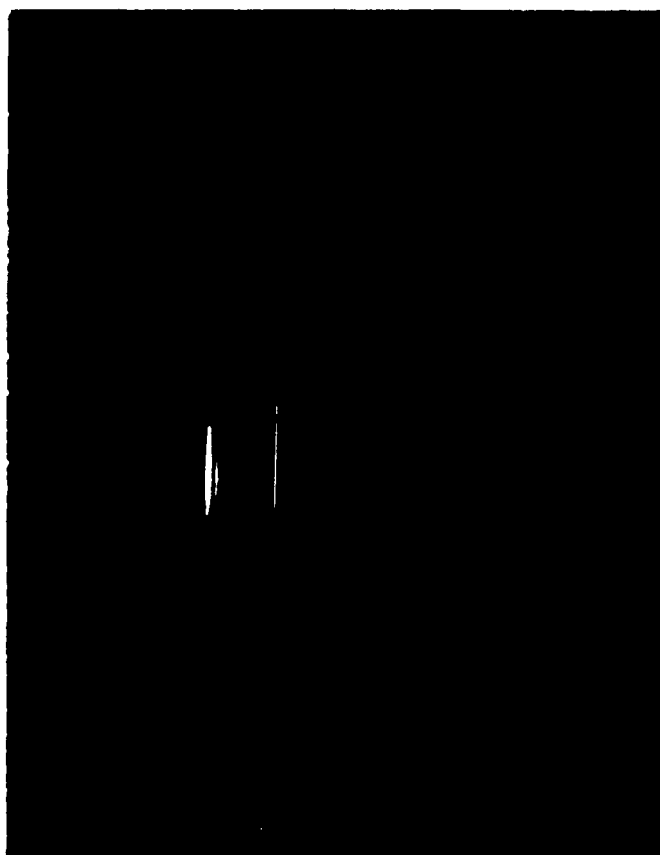
In the manufacture of the air-spaced prism it was only possible to polish the input face and the axial output face to within $\lambda/4$ because of the crystal structure. The lateral faces are perpendicular to the optic axis, and since calcite belongs to the hexagonal crystallographic system, attempts to polish these faces to better than $\lambda/4$ would result in hexagonal pitting, giving rise to large scattering losses.

The high losses on the lateral face meant that for geometrically identically optical arrangements the low-loss axial resonator dominated, and laser action was restricted to it. When the axial resonator was blocked however, laser action was also obtainable in the lateral resonator.

By greatly reducing the off-axial resonator length it was possible to obtain laser action simultaneously in both resonators. Under these conditions, competition effects were clearly observed between the two resonators. Fig. 3.5:8 shows simultaneous two-wavelength operation as displayed in the spectrometer using the air-spaced Glan-Taylor prism.

Thus, when the axial resonator was blocked the output energy of the lateral resonator increased and vice versa. Similar competition effects were previously reported.⁶⁵⁻⁶⁹ The interaction between the two laser beams of perpendicular polarizations in the amplifying medium is possible because the orientation relaxation time of the dye molecule (approximately 300 ps in ethanol) in the solvent is much shorter than the lifetime of the first excited singlet state (approximately 5 ns).^{70,71}

Because of the high losses associated with the lateral faces, it was found that when conditions were arranged to obtain equal energies



FROM LEFT TO RIGHT : LASER LINES, 4500 Å, 4478.5 Å; HG LINES, 4358 Å, 4078 Å,
AND 4047 Å

FIGURE 3.5:8 SPECTROMETER PHOTOGRAPH OF THE SIMULTANEOUS TWO-
WAVELENGTH OUTPUT UTILIZING THE AIR-SPACED GLAN-
TAYLOR PRISM

and equal linewidths from both resonators simultaneously, the output energies were too low to be useful. See Fig. 3.5:9.

Thus, in spite of the higher power-density handling capabilities of the air-spaced prism, it was decided to abandon its use in favor of the dielectric-interface prism.

With this prism simultaneous two-wavelength outputs of approximately 100 mj were obtained at 4478.5 Å and 4500 Å with linewidths of approximately 5 to 6 Å. Fig. 3.5:6 shows the simultaneous outputs displayed on the spectrometer. It was with the dielectric-coated prism that the field experiments described in later sections were carried out.

3.6 Calibration

3.6.1 The Need for Calibration

In order to obtain accurate pollution measurements, it is necessary that we know from shot to shot what the absorption cross section is for a given pollutant for the actual laser bandwidth emitted. In performing the experiment to achieve simultaneous laser action, it was noticed that the output bandwidths varied from shot to shot. These variations in bandwidths depend upon:

1. The bias voltage applied to the charging circuit, i.e., the energy discharged in each flash.
2. The length of time between shots.
3. The degradation of the dye molecules due to repeated exposure to the pump source.

Two experiments were performed to determine:



FROM LEFT TO RIGHT: LASER LINES, 4500 Å, 4478.5 Å; HG LINES, 4358 Å,
4078 Å, AND 4047 Å

FIGURE 3.5:9 SPECTROMETER PHOTOGRAPH OF THE SIMULTANEOUS TWO-
WAVELENGTH OUTPUT UTILIZING THE AIR-SPACED GLAN-
TAYLOR PRISM FOR EQUAL OUTPUT ENERGIES IN EACH
LASING LINE

1. If any frequency pulling occurs between the two lasing wavelengths.
2. The extent of any laser bandwidth variations and frequency shifts from shot to shot for the simultaneous mode of operation. The purpose of this experiment was to determine whether a calibration system was needed to monitor each of the outgoing wavelengths.

The experimental setup is shown in Figs. 3.6:1a and b. The laser is set for simultaneous operation. The two perpendicularly polarized beams are diverted by a beam-steering mirror mount through a variable polarizer, a variable neutral density filter, and a 1 m focal length lens which focuses it onto a Corning 3850 filter and diffusion plate. Following the diffusion plate is a 1/2 m Jarrell-Ash scanning spectrometer whose input and output slits are set at 10 μ each. A camera attachment is used and the results are recorded photographically.

To observe any frequency shifts, the laser lines were compared with known Hg lines: 4047 \AA , 4078 \AA , and 4358 \AA . The Hg lines were initially exposed onto the film by directing the output of an Hg lamp into the spectrometer through the 3850 Corning filter which blocked out any unwanted harmonics. The laser lines were then superimposed onto the film which remained stationary during both exposures.

In the first experiment, an investigation was made of whether frequency shifts occur between the cases where each wavelength lases separately and when both lase simultaneously (with the same grating settings naturally).

To carry out the experiment, the laser was allowed to lase simul-

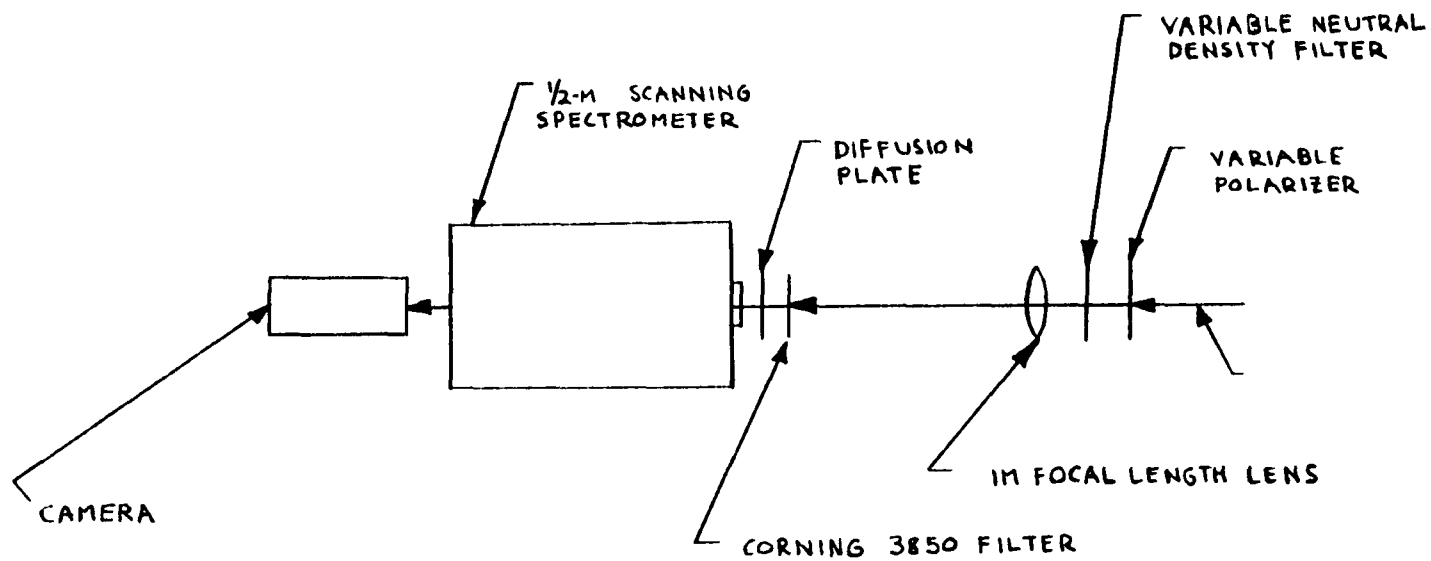


FIGURE 3.6:1a EXPERIMENTAL SETUP FOR MONITORING LASER FREQUENCY SHIFTS AND BANDWIDTH CHANGES



FIGURE 3.6:1b PHOTOGRAPHS OF THE EXPERIMENTAL SETUP FOR MONITORING
LASER FREQUENCY SHIFTS AND BANDWIDTH CHANGES

taneously, but only one polarization was allowed to pass through the variable polarizer and onto the film. The exposed film was then compared to another exposure from a sequential lase at the same wavelength. Any frequency shifts would be obtained by observing the relative changes, if any, from the Hg lines to which both films were exposed. Figs. 3.6:2, 3,4, and 5 show respectively the 4478.5 \AA line lasing sequentially then simultaneously, and the 4500 \AA line lasing sequentially then simultaneously. There were no frequency shifts noted between the lines when lasing sequentially as to compared to when they lased simultaneously, but bandwidth changes did however occur, i.e., there was a change in laser bandwidth (along with a monotonic change in output energy) when the system lased sequentially as opposed to simultaneously. As can be Figs. 3.6:2 through 3.6:5 the simultaneous-mode bandwidths and energies of the 4478.5 \AA and 4500 \AA lines are less than those for the sequential mode. They are: 4478.5 \AA : sequential 10 \AA , 200 mj; simultaneous 7 \AA , 100 mj; 4500 \AA : sequential 7 \AA , 100 mj; simultaneous 4 \AA , 50 mj.

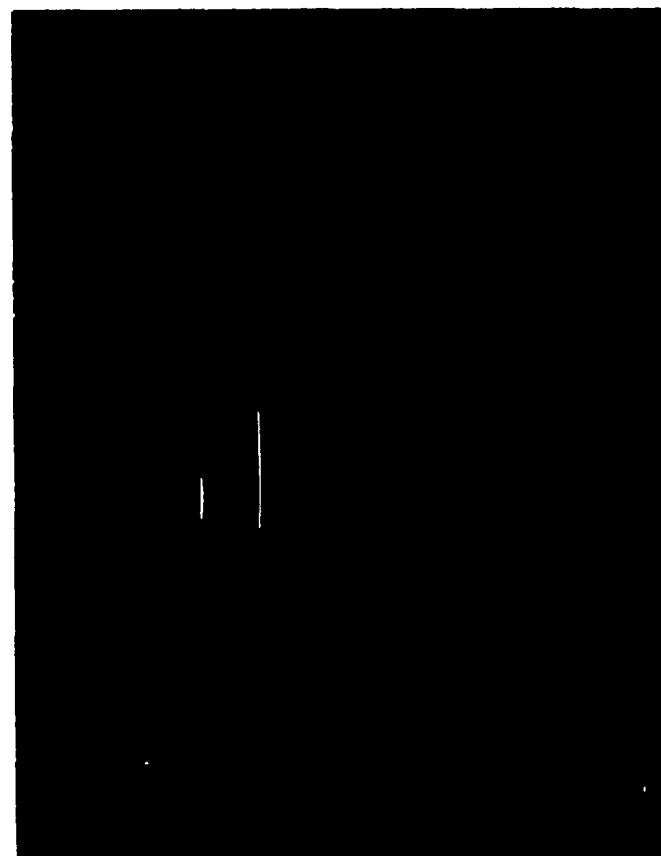
In the second experiment, lasing occurred simultaneously. Any frequency and bandwidth changes were observed in the same manner as above. Figs. 3.6:6a through 1 are photographs that show no frequency shifts existed but bandwidth changes did occur from shot to shot. The bandwidth changes depend upon:

1. bias voltage, i.e., the energy discharged in each flash,
2. time between pulses, and
3. degradation of the dye molecules due to repeated exposure to the pump source.

As can be seen from the photographs the bandwidths varied as much as 43



FROM LEFT TO RIGHT: 4478.5 Å, 4358 Å, 4078 Å, AND 4047 Å
FIGURE 3.6:2 SPECTROMETER PHOTOGRAPH OF THE 4478.5 Å LASER LINE FOR SEQUENTIAL OPERATION



FROM LEFT TO RIGHT: 4478.5 Å, 4358 Å, 4078 Å, AND 4047 Å
FIGURE 3.6:3 SPECTROMETER PHOTOGRAPH OF THE 4478.5 Å LASER LINE FOR SIMULTANEOUS TWO-WAVELENGTH OPERATION



FROM LEFT TO RIGHT: 4500 Å, 4358 Å, 4078 Å, AND 4047 Å
FIGURE 3.6:4 SPECTROMETER PHOTOGRAPH OF THE 4500
Å LASER LINE FOR SEQUENTIAL
OPERATION



FROM LEFT TO RIGHT: 4500 Å, 4358 Å, 4078 Å, AND 4047 Å
FIGURE 3.6:5 SPECTROMETER PHOTOGRAPH OF THE 4500
Å LASER LINE FOR SIMULTANEOUS TWO-
WAVELENGTH OPERATION



FROM LEFT TO RIGHT: 4500Å, 4418.5Å, 4358Å, 4078Å, AND 4047Å
FIGURE 3.6:6a SPECTROMETER PHOTOGRAPH OF THE
SIMULTANEOUS TWO-WAVELENGTH OUTPUT,
BIAS VOLTAGE = 20 KV, FIRST SHOT



FIGURE 3.6:6b BIAS VOLTAGE = 20 KV, SECOND SHOT



FIGURE 3.6:6c BIAS VOLTAGE = 20 KV, THIRD SHOT

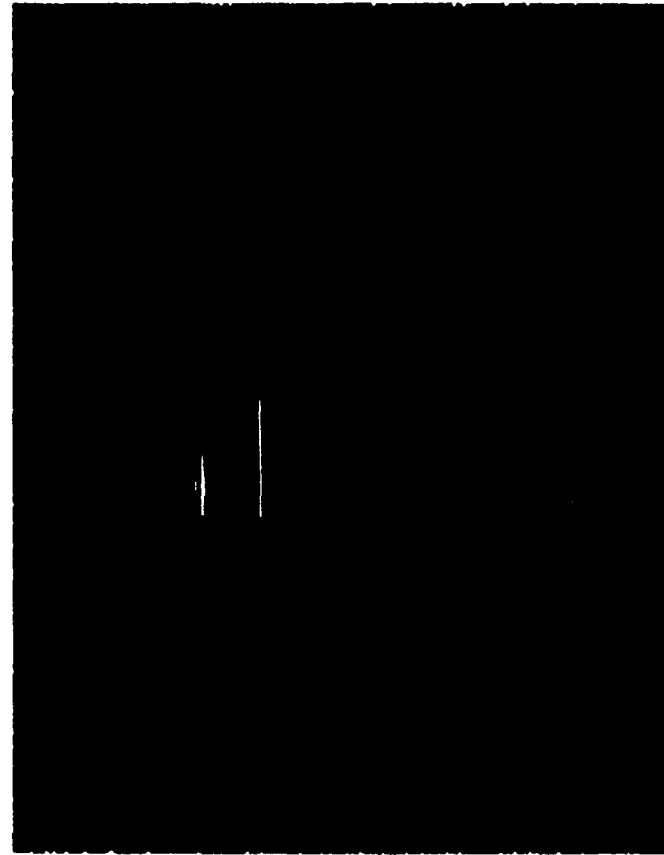


FIGURE 3.6:6d BIAS VOLTAGE = 20 KV, FOURTH SHOT

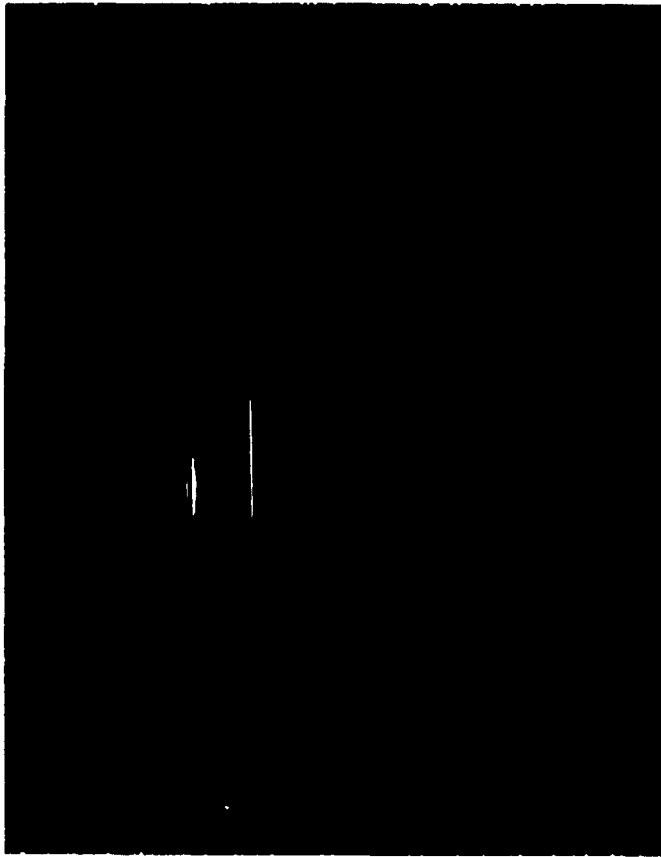


FIGURE 3.6:6e BIAS VOLTAGE = 19 KV, FIRST SHOT



FIGURE 3.6:6f BIAS VOLTAGE = 19 KV, SECOND SHOT

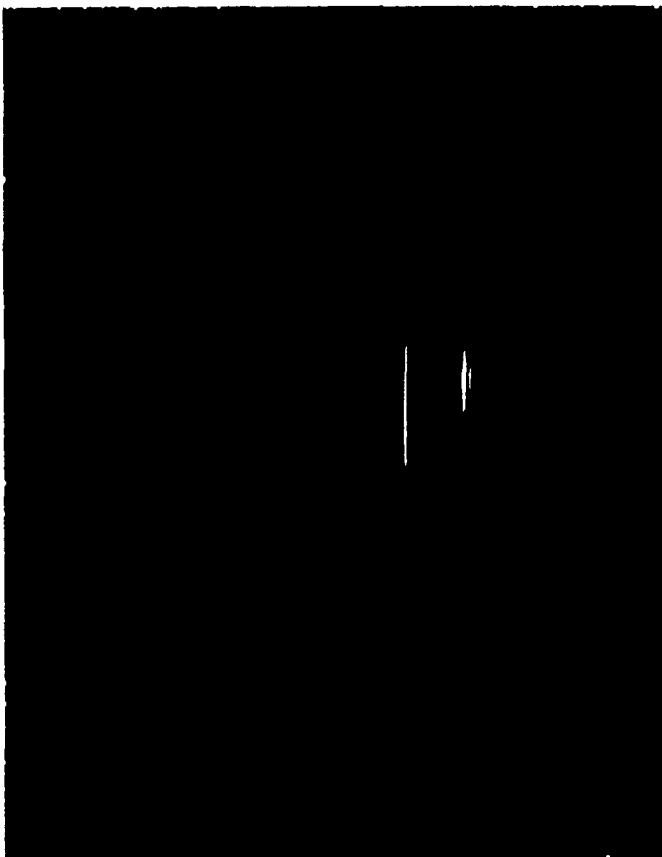


FIGURE 3.6:6g BIAS VOLTAGE = 19 KV, THIRD SHOT



FIGURE 3.6:6h BIAS VOLTAGE = 19 KV, FOURTH SHOT



FIGURE 3.6:6i BIAS VOLTAGE = 18 KV, FIRST SHOT

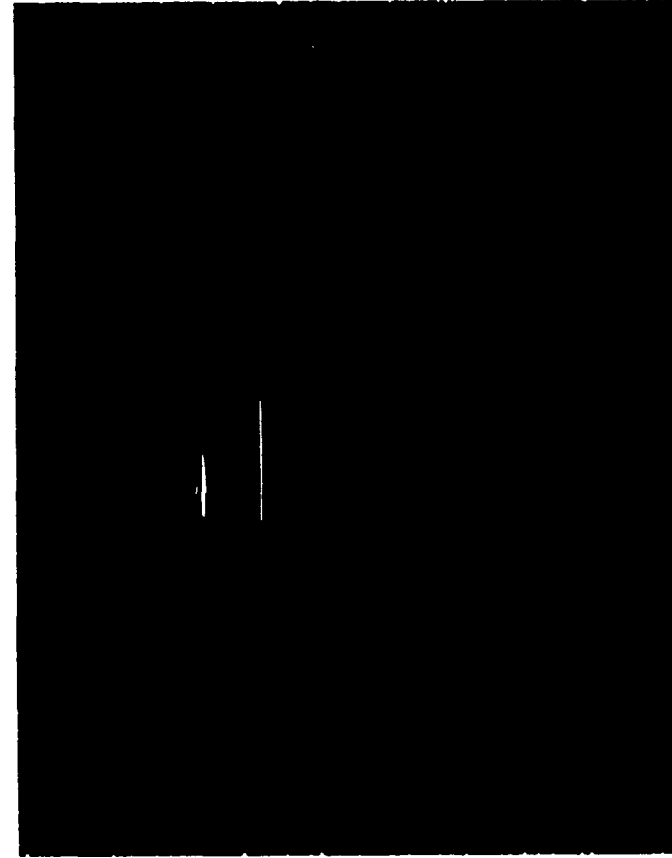


FIGURE 3.6:6j BIAS VOLTAGE = 18 KV, SECOND SHOT



FIGURE 3.6:6k BIAS VOLTAGE = 18 KV, THIRD SHOT

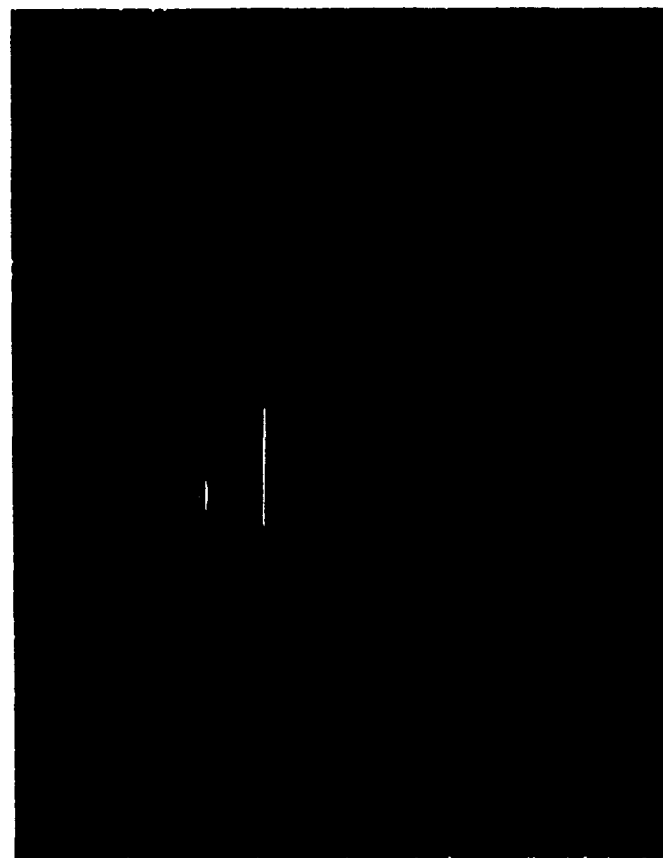


FIGURE 3.6:6l BIAS VOLTAGE = 18 KV, FOURTH SHOT

percent.

As a result of these experiments, it was therefore concluded that since significant bandwidth changes did occur from shot to shot during simultaneous operation, a calibration system must be used in the LIDAR system in order to allow for these changes. The next two sections describe the calibration system devised for this purpose, and tuning techniques used to obtain bandwidths and center-frequency requirements.

3.6.2 The Calibration System

To ensure accurate results which are independent of variations in laser operation which occur from shot to shot, and which affect bandwidth, a calibration system was devised. This is shown schematically in Figs. 3.6:7a and b. This calibration system analyses both output beams simultaneously and permits the effective NO_2 absorption cross sections to be calculated from the data obtained.

Operationally, two beams of mutually-orthogonal polarizations at the close-lying wavelengths λ_1 (4478.5 \AA) and λ_2 (4500 \AA) enter the shielded encasement through the variable iris. Both beams impinge upon an air-spaced Glan-Taylor prism by which the beams are spatially separated. The perpendicularly polarized beam, λ_1 , is directed through slide #1 by a beam-steering mirror. 4 percent of that beam is tapped off by slide #1 and is focused by the 15-cm focal-length lens #1 onto an RCA IP39 vacuum-tube photodiode through neutral density filters and diffusion plate #1. The remaining portion of the beam passes through a $1/2 \text{ m}$ glass cell in which flows 609 ppm of NO_2 in N_2 at just above atmospheric pressure. The beam is then focused onto RCA IP39 photo-

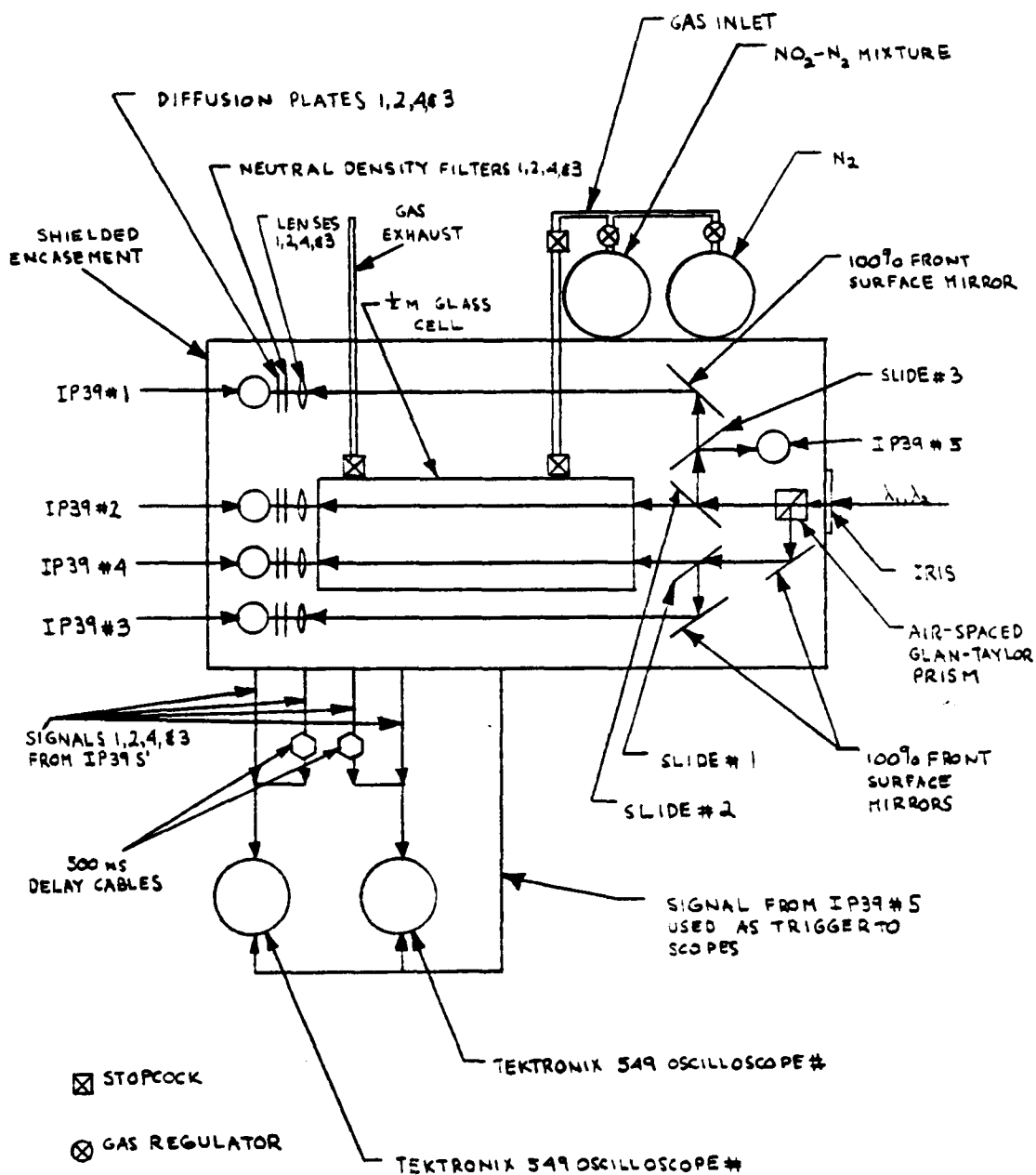


FIGURE 3.6:7a THE CALIBRATION SETUP

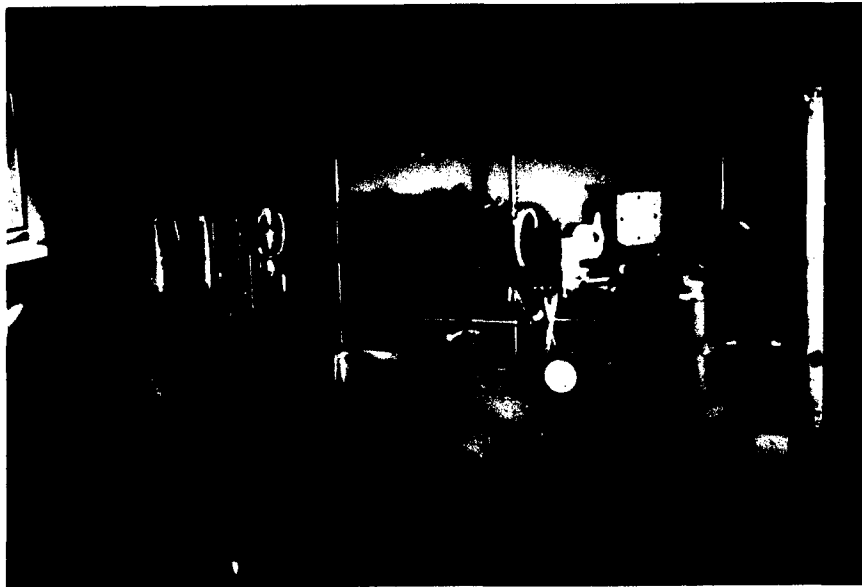
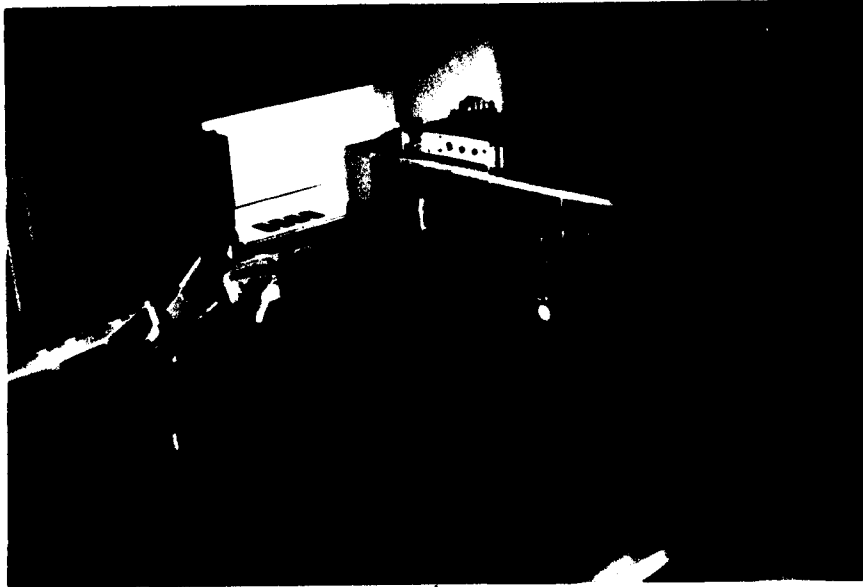


FIGURE 3.6:7b PHOTOGRAPHS OF THE CALIBRATION SETUP

diode #2 through neutral density filters and diffusion plate #2.

The same type of configuration applies to the parallel-polarized beam, λ_2 , which uses component numbers 3 and 4. A portion of the parallel-polarized beam is tapped off by slide #3 onto RCA IP39 photovacuum diode #5, whose signal acts as a trigger to two Tektronix type 549 storage oscilloscopes. The signals corresponding to the portion of the beams that propagate through the cell are delayed in time by two 500 ns delay cables. The signals are then displayed on the two storage scopes along with the signals corresponding to the reference beams that bypassed the cell.

The type of data obtained in this manner and the method of calculating the effective NO_2 absorption cross sections for each lasing line from shot to shot are described below:

1. Four signals, two of which are displayed on each storage scope, are obtained.
2. The two signals on the first scope correspond to the 4478.5 \AA laser line. The first signal on storage scope 1 is used for normalizing for any power fluctuations that may occur from shot to shot. This allows relative measurements to be made. The second signal, which is delayed approximately 500 ns, is partially absorbed by the $\text{NO}_2\text{-N}_2$ mixture in the cell.
3. The two signals on storage scope 2 correspond to the 4500 \AA laser line. As before, the first signal is used for normalization. The delayed signal is partially absorbed by the $\text{NO}_2\text{-N}_2$ mixture, but not as much as the 4478.5 \AA laser line.
4. To calculate the percent absorption and therefore the effective

NO₂ absorption cross section for each laser pulse for each laser line, it is necessary to what losses are attributed to the NO₂ in the mixture and what losses are attributed to the cell itself. It is for this reason that an initial reading is necessary for each lasing wavelength when only N₂ is flowing through the cell.

5. To calculate the percent absorption for each wavelength (which is related to the effective absorption cross section) only relative measurements are required. The percent absorption is calculated using Eq. 3.6:1 below:

$$\% \text{ absorption} = 1 - \frac{A|_W}{A|_{W/O}}, \quad (3.6:1)$$

where,

$A/B|_W$ = the ratio of the signal that propagates through the cell containing the NO₂-N₂ mixture (the delayed signal) divided by the signal that bypasses the cell.

$A/B|_{W/O}$ = the ratio of the signal that propagates through the cell containing only the N₂ (the delayed signal) divided by the signal that bypasses the cell. This is done for each of the lasing wavelengths.

6. To obtain the percent transmission of each lasing wavelength from shot to shot, each $A/B|_W$ reading from each scope obtained during each shot is normalized by the initial $A/B|_{W/O}$ reading.

To obtain the percent absorption the ratio of the above ratios is subtracted from unity.

7. The effective absorption cross section is related to the percent absorption by:

$$\sigma_{\text{EFF}} = \frac{-\ln(1 - \% \text{ absorption})}{Nl} \text{ (cm}^2\text{)}, \quad (3.6:2)$$

where,

N = the concentration of NO_2 in the cell (cm^{-3}), and

l = the length of the cell (cm).

Figs. 3.6:8a, b, 3.6:9a, and b show curve traces of photographs of the signals from the storage scopes in the calibration system. Figs. 3.6:8a and b correspond to the readings without NO_2 but with N_2 in the cell for the lines centered about 4478.5 \AA and 4500 \AA respectively. Figs. 3.6:9a and b correspond to the readings with the $\text{NO}_2\text{-N}_2$ mixture in the cell for these lines. The effective absorption cross sections for the lines centered about 4478.5 \AA and 4500 \AA for this particular set of measurements are $6.36 \times 10^{-19} \text{ cm}^2$ and $3.54 \times 10^{-19} \text{ cm}^2$ respectively.

Knowing the calibrated values of the effective NO_2 absorption cross sections for each of the simultaneous laser wavelengths for each laser firing, permits allowance to be made for any variations of laser bandwidths which occur from shot to shot.

3.6.3 Tuning Technique

For operation of the LIDAR system, it is necessary that:

1. The center frequencies of both laser lines coincide with the

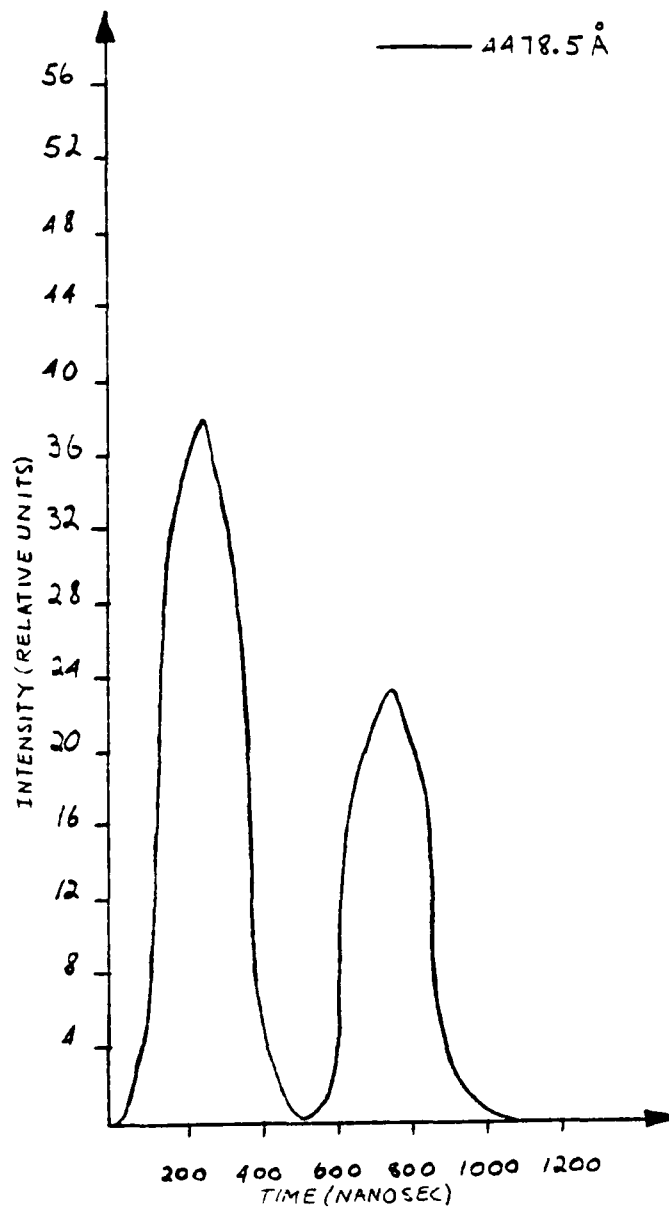


FIGURE 3.6:8a CALIBRATION SIGNALS FOR SIMULTANEOUS TWO-WAVELENGTH OPERATION FOR THE 4478.5 Å LASER LINE WITH N₂ IN THE CALIBRATION CELL

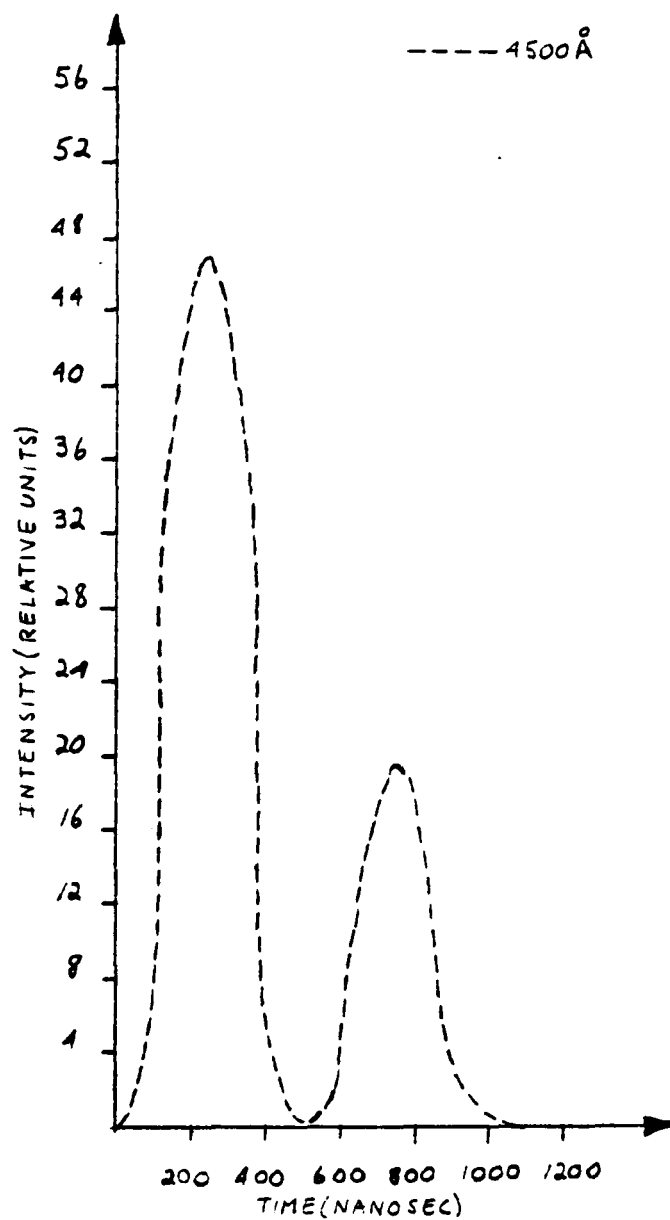


FIGURE 3.6:8b CALIBRATION SIGNALS FOR SIMULTANEOUS TWO-WAVELENGTH OPERATION FOR THE 4500 Å LASER LINE WITH N₂ IN THE CALIBRATION CELL

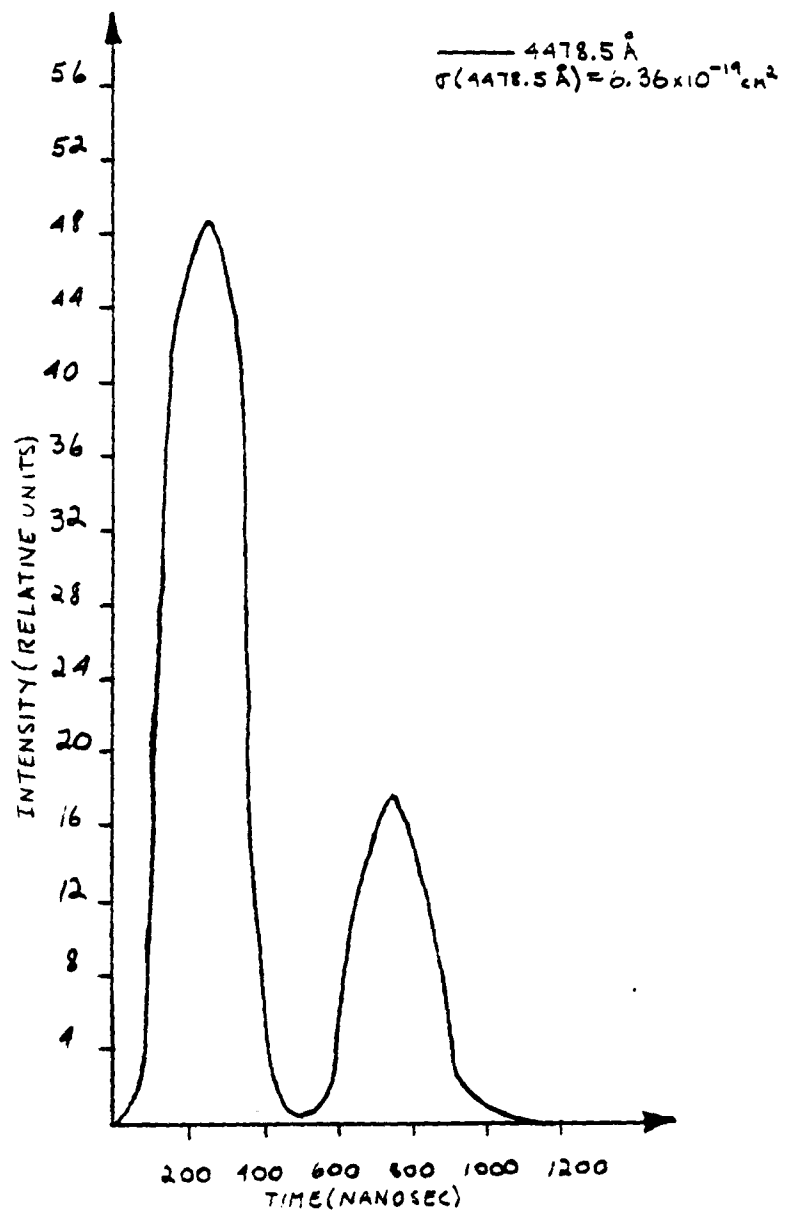


FIGURE 3.6:9a CALIBRATION SIGNALS FOR SIMULTANEOUS TWO-WAVELENGTH OPERATION FOR THE 4478.5 Å LASER LINE WITH NO₂-N₂ MIXTURE IN THE CALIBRATION CELL

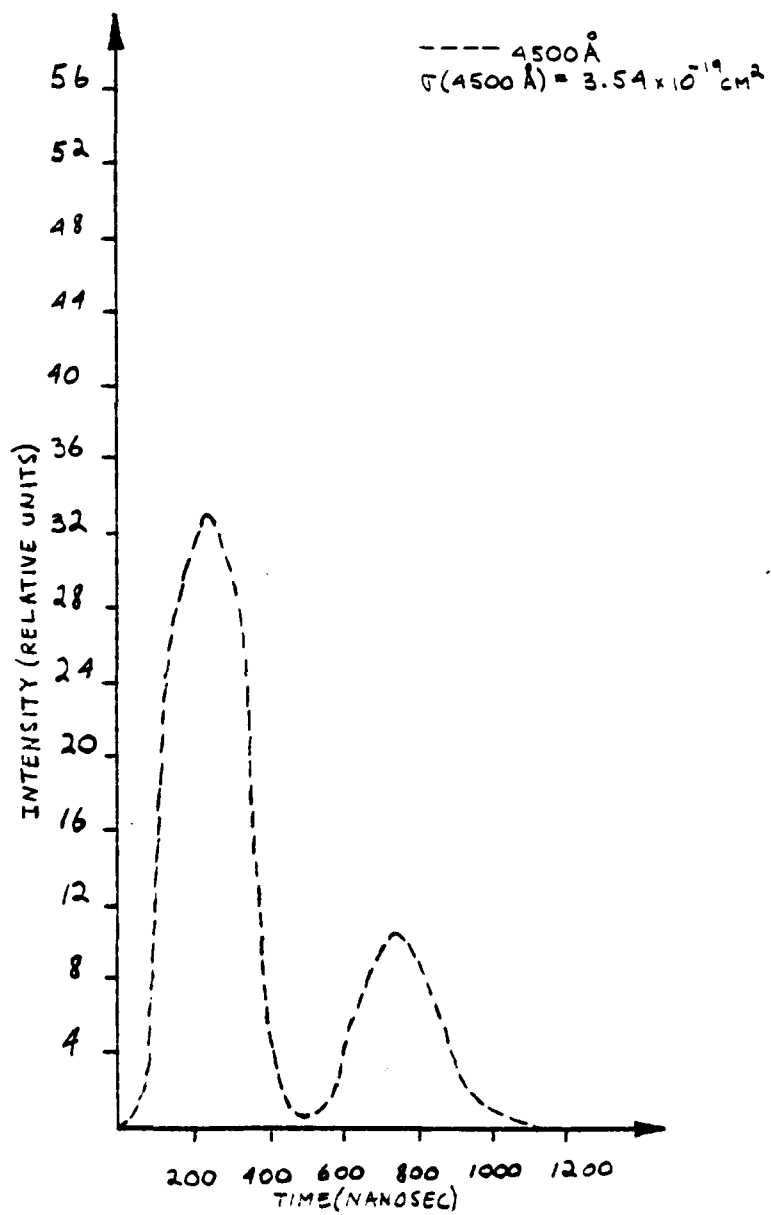


FIGURE 3.6:9b CALIBRATION SIGNALS FOR SIMULTANEOUS TWO-WAVELENGTH OPERATION FOR THE 4500 Å LASER LINE WITH NO₂-N₂ MIXTURE IN THE CALIBRATION CELL

center frequencies of the two interference filters in the receiver.

2. The bandwidths of both laser lines must be less than the bandwidths of the respective interference filters.

3. Any increase in laser bandwidths must result in bandwidths that remain less than the bandpass of the interference filters.

If the laser bandwidths are larger than the bandpass of the filters, erroneous readings would result, i.e., the data obtained from the calibration system corresponds to the actual effective absorption cross sections, whereas the receiver would be detecting only a certain portion of the laser-signal spectrum.

The operating characteristics of the receiving system could have been designed so as to require both lasing bandwidths to be much larger than the interference filter bandpass. This would eliminate the need for a calibration system in the following manner. If both laser-line bandwidths were larger than the filter bandpass, then known spectral quantities would be detected and determined exactly by the filter bandpass. The exact effective absorption cross sections would then be known and would not vary since they were determined by the filter characteristics.

There are three reasons why this approach was not used. First, when operating a LIADR system, it is desirable to obtain readings from useful ranges (up to 10 km). When detecting only a portion of the laser backscatter, the signal is reduced and the attainable range is decreased. Second, the signal to noise ratio for a given range decreases, since the signal is decreased. Third, in dye-laser systems,

the dye lasing medium degrades due to repeated exposure to the pump source. This has the effect of monotonically decreasing the laser bandwidth over a period of time. Therefore, there is a difficulty in maintaining laser output signals whose bandwidths are much larger than those of the receiver interference filters.

The tuning scheme was therefore developed to achieve:

1. Laser-line center-frequency and filter-bandpass coincidence.
2. Desirable laser bandwidths.
3. Laser bandwidth fluctuations that continue to keep bandwidths below the bandpass of the interference filters.

Fig. 3.6:10 shows the experimental setup used to check the system. With the laser operated in the simultaneous mode, fractions of both beams of mutually-orthogonal polarizations were tapped off by slide #1 and were directed through variable polarizer #1, variable neutral density filter #1, and lens #1 (1 m focal length). The beams were then focused onto diffusion plate #1, neutral density filter #1, and were detected by an RCA 6217 photomultiplier attached to a 1/2 m Jarrell-Ash scanning spectrometer. The input and output slits were set at 10 μ each to give a detectable resolution of 0.16 \AA . To compensate for any laser power fluctuations, the signal obtained through the spectrometer was normalized by a signal from a RCA IP39 vacuum-tube photodiode used as the trigger source in the calibration system. A portion of the main beam was tapped off with a pellicle and directed into the calibration system where it was detected by the IP39 photodiode. Signals from the spectrometer and the IP39 were recorded photographically on two Tektronix type 549 storage oscilloscopes.

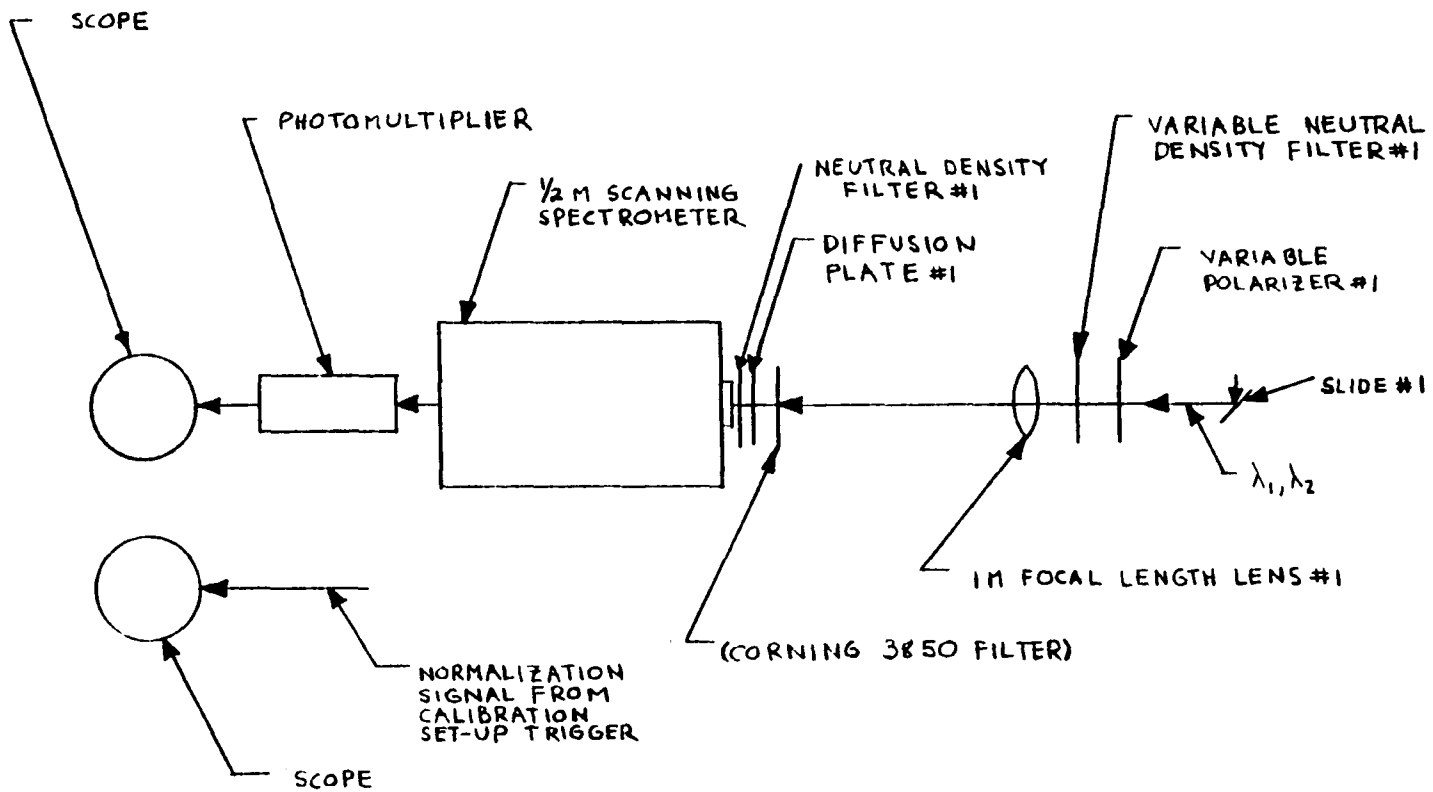


FIGURE 3.6:10 EXPERIMENTAL SETUP USED FOR FINE FREQUENCY TUNING

The spectrometer was initially calibrated using an Hg lamp and was then manually set to detect the 4478.5 \AA line. With the laser operating in the simultaneous mode, both beams were tapped off, but only the line desired to lase at 4478.5 \AA was allowed to pass through variable polarizer #1 initially. The laser line was initially sighted by eye through the view port on the spectrometer. Coarse tuning was accomplished by observing the spectral shift while the grating's rotational position was changed. Once having achieved the desired spectral center-line frequency, within visual approximation, the desired laser bandwidth, approximately 5 \AA , was sought. As mentioned earlier, the bandwidths must be less than the bandpass of the interference filters. If the laser bandwidths were initially set at 5 \AA with the bias voltage set at the maximum to be used, and knowing that the bandwidths monotonically decrease due to repeated exposure of the lasing medium to the pump source, the laser bandwidths would be ensured to always be within the bandpass of the filters.

Initially, the laser bandwidths were adjusted for maximum width, approximately 20 \AA , by setting the grating positions as close as possible to the polarizing prism. To obtain the desired 5 \AA bandwidths, the distance of the gratings need only be increased relative to the polarizing prism. To check the bandwidths each time the grating positions were moved, a camera was attached to the view port on the spectrometer, and the laser spectral widths were recorded photographically. Initial exposure of the film to an Hg lamp through a Corning 3850 filter and the spectrometer served as a calibration check on the bandwidth readings. The resolution obtained on the film was 16 \AA/mm . Initially, the

two laser lines might partially overlap since the bandwidths were originally set at approximately 20 \AA . Therefore, variable polarizer #1 was set to allow only one polarization to pass into the spectrometer initially. Through repeated adjustments of the gratings' axial positions, the desired bandwidths were obtained with the center-line frequencies set visually at 4478.5 \AA and 4500 \AA . Figs. 3.6:11a through i show the run to obtain the 5 \AA bandwidths for each of the simultaneous laser frequencies.

Having obtained the desired bandwidths, the next step was to finely adjust the laser frequencies using the tuning technique described earlier in the section. The gratings' rotational positions were finely adjusted using micrometers and the normalized readings of the scopes were maximized. Figs. 3.6:12a, b, 3.6:13a, and b show the first and final scope readings for fine center line adjustment for the simultaneous laser frequencies 4478.5 \AA and 4500 \AA respectively. Fig. 3.6:14 shows the desired simultaneous output with each line approximately 5 \AA wide and the center-line frequencies set at 4478.5 \AA and 4500 \AA .

In conclusion, the results of the experiments to determine whether frequency shifts and bandwidth changes occur from shot to shot during LIDAR operation, definitely show the necessity for a calibration system. If meaningful pollution readings are to be obtained, calibrated output signals must be used.

In the following chapter, calibrated LIDAR returns are interpreted and pollution concentrations at various ranges from the LIDAR site are given.



FROM LEFT TO RIGHT: 4478.5 Å, 4358 Å, 4078 Å, AND 4047 Å
FIGURE 3.6:11a SPECTROMETER PHOTOGRAPH OF THE SIMUL-
TANEOUS TWO-WAVELENGTH OUTPUT TO GET
5 Å BANDWIDTHS IN EACH LINE--4478.5 Å

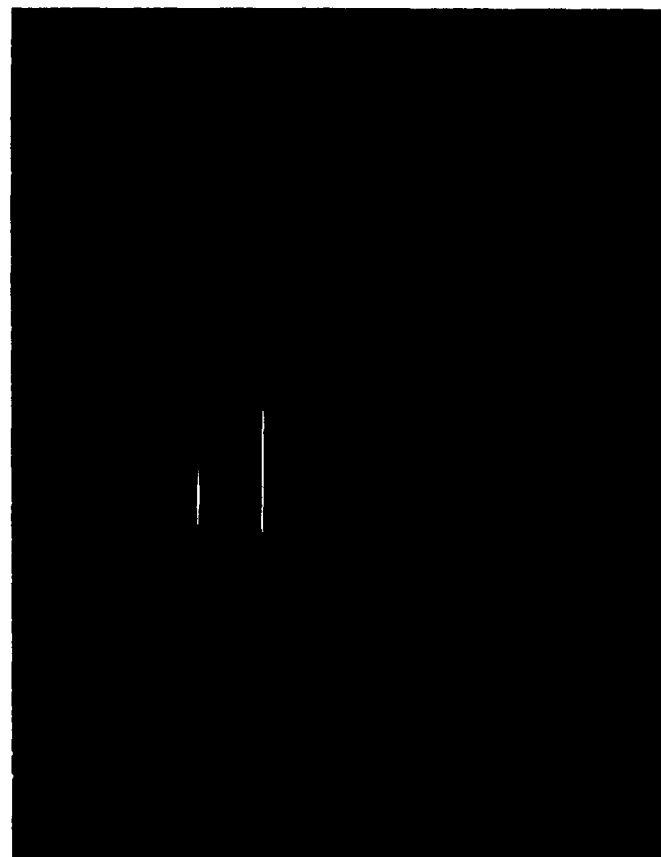
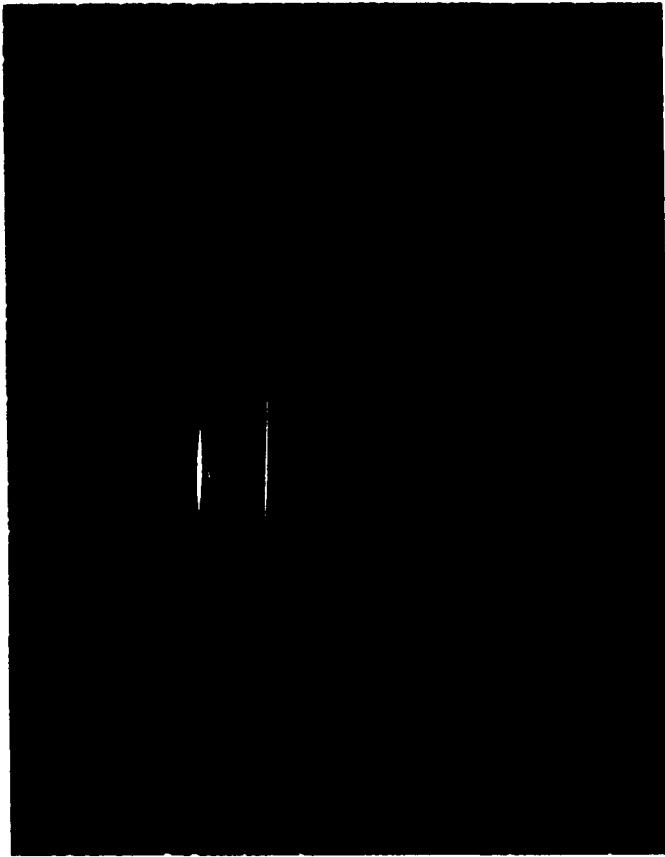


FIGURE 3.6:11b --4500 Å



FROM LEFT TO RIGHT: 4500 Å, 4478.5 Å, 4358 Å, 4078 Å, AND 4047 Å
FIGURE 3.6:11c --THE 4478.5 Å AND 4500 Å LASER
LINES

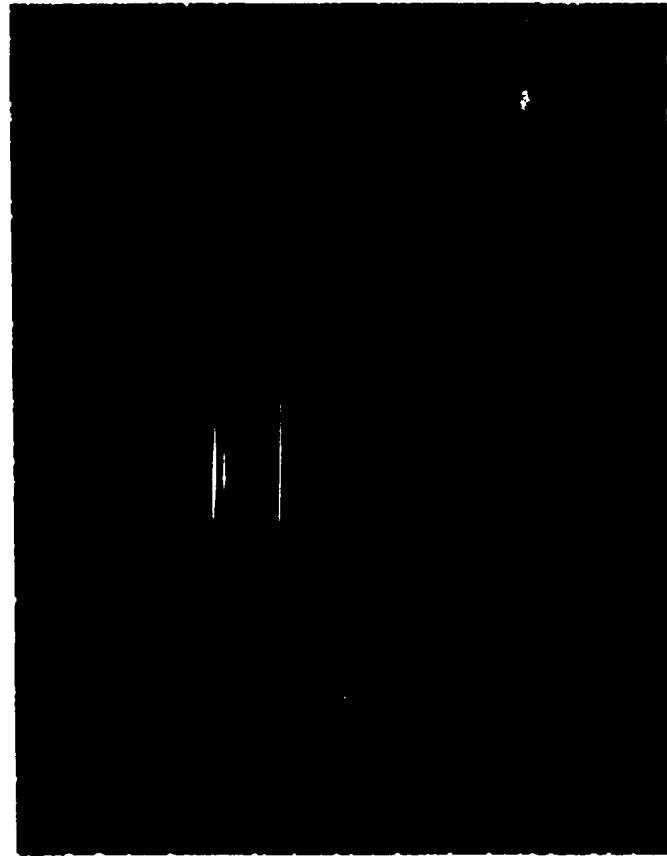


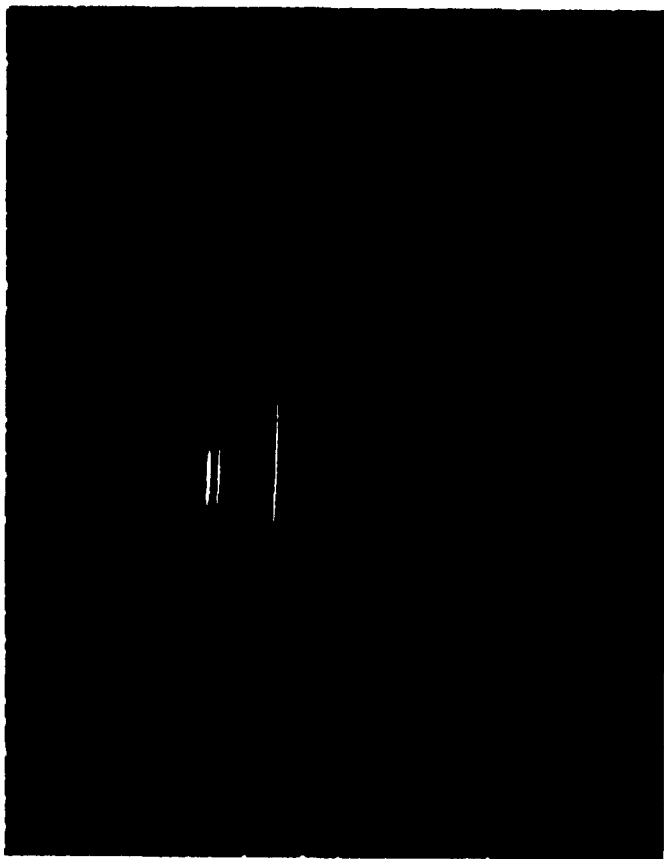
FIGURE 3.6:11d --THE 4478.5 Å AND 4500 Å LASER
LINES



FIGURE 3.6:11e --THE 4478.5 Å AND 4500 Å LASER
LINE



FIGURE 3.6:11f --THE 4478.5 Å AND 4500 Å LASER
LINE



5
2700A

FIGURE 3.6:11g --THE 4478.5 Å AND 4500 Å LASER
LINE



FIGURE 3.6:11h --THE 4478.4 Å AND 4500 Å LASER
LINE

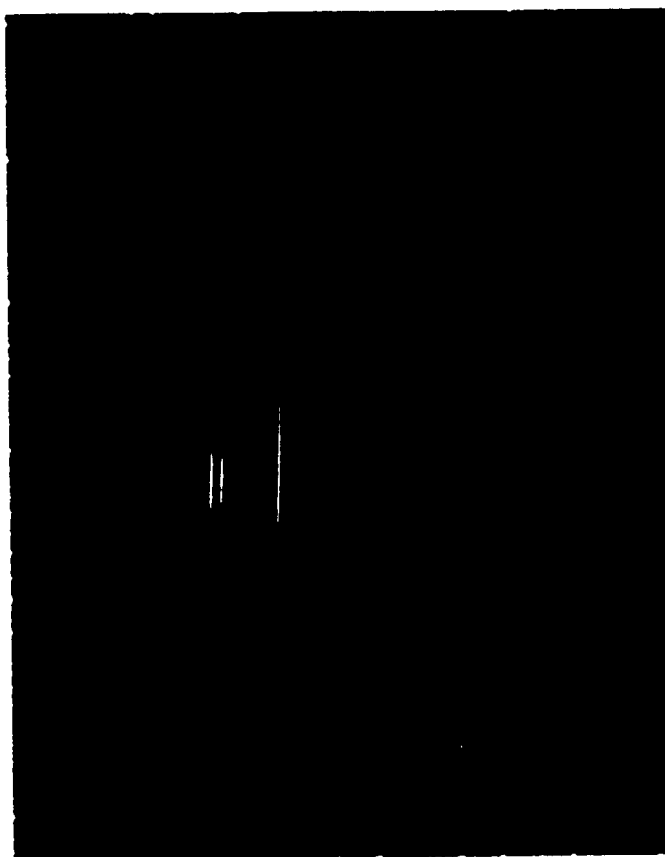


FIGURE 3.6:111 --THE 4478.5 Å AND 4500 Å LASER LINE

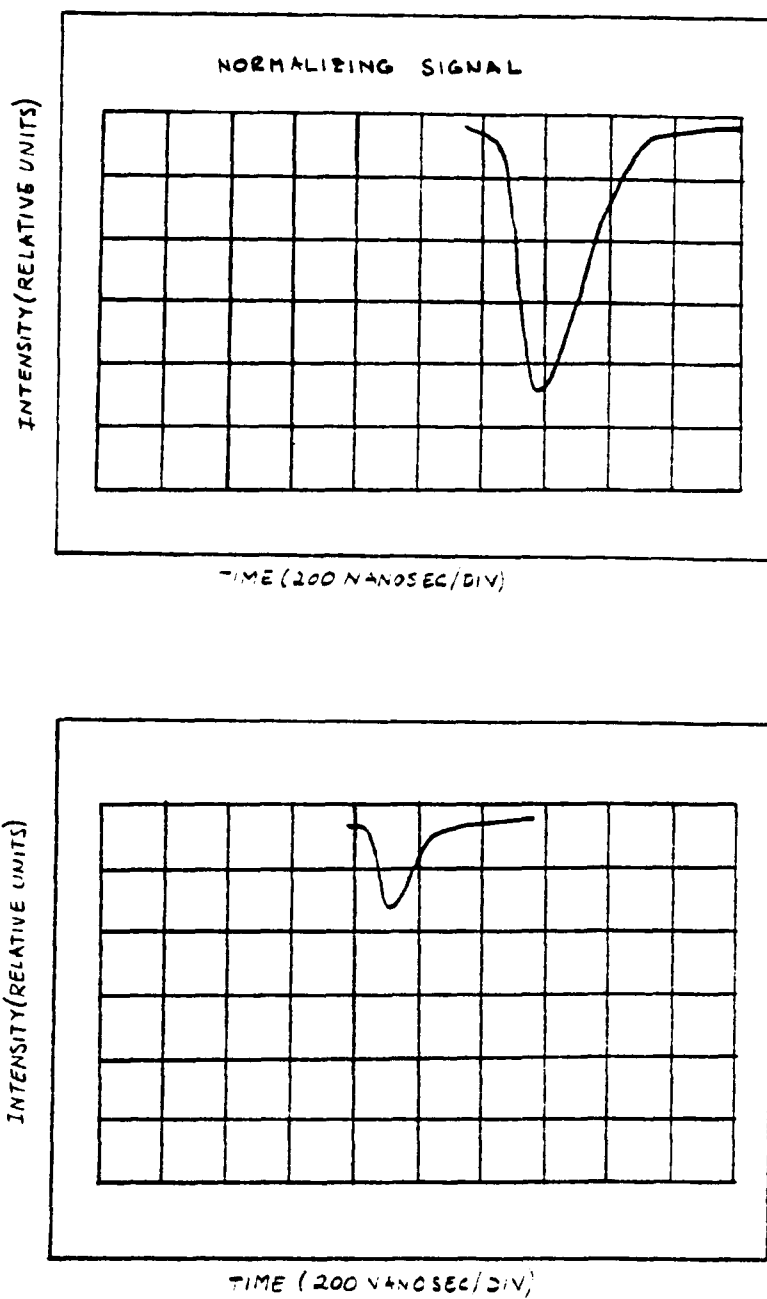


FIGURE 3.6:12a THE INITIAL FINE TUNING SIGNALS FOR SIMULTANEOUS TWO-WAVELENGTH OPERATION FOR OBTAINING FREQUENCY COINCIDENCE FOR THE 4478.5 Å LASER LINE

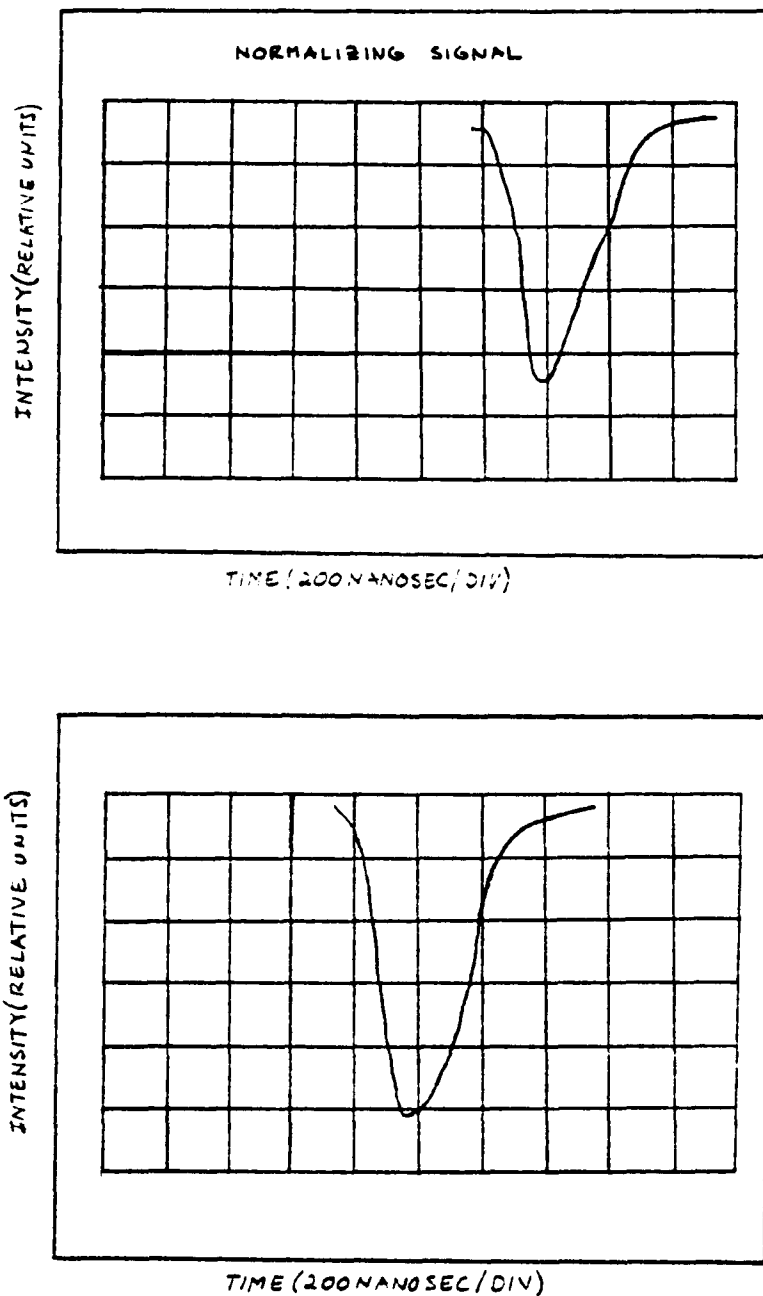


FIGURE 3.6:12b THE FINAL FINE TUNING SIGNALS FOR SIMULTANEOUS TWO-WAVELENGTH OPERATION FOR OBTAINING FREQUENCY COINCIDENCE FOR THE 4478.5 Å LASER LINE

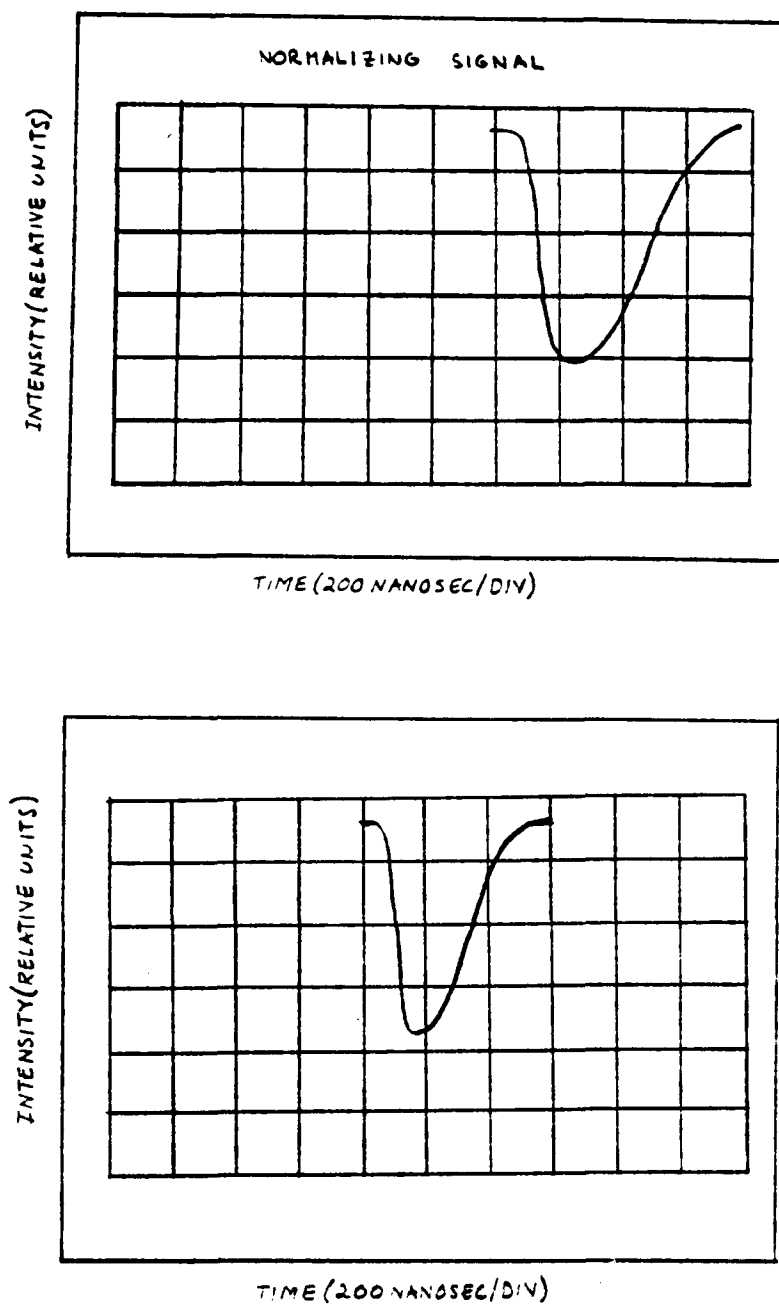


FIGURE 3.6:13a THE INITIAL FINE TUNING SIGNALS FOR SIMULTANEOUS TWO-WAVELENGTH OPERATION FOR OBTAINING FREQUENCY COINCIDENCE FOR THE 4500 Å LASER LINE

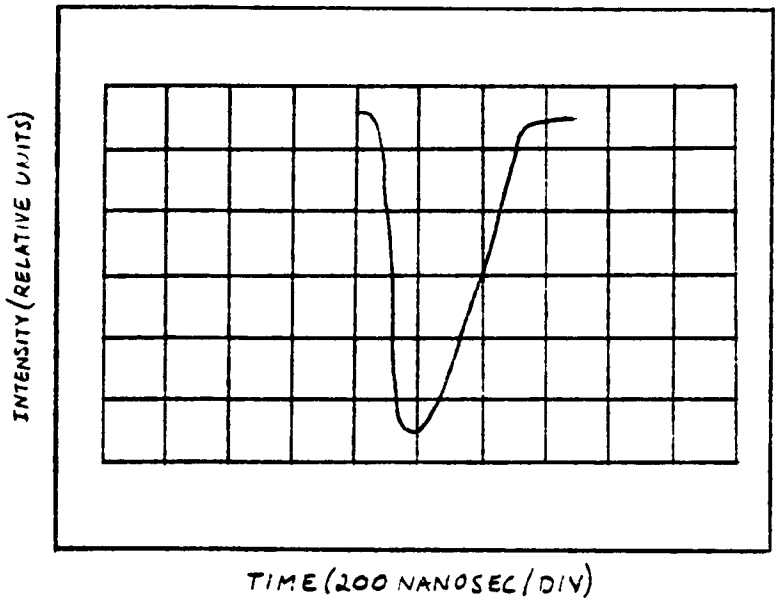
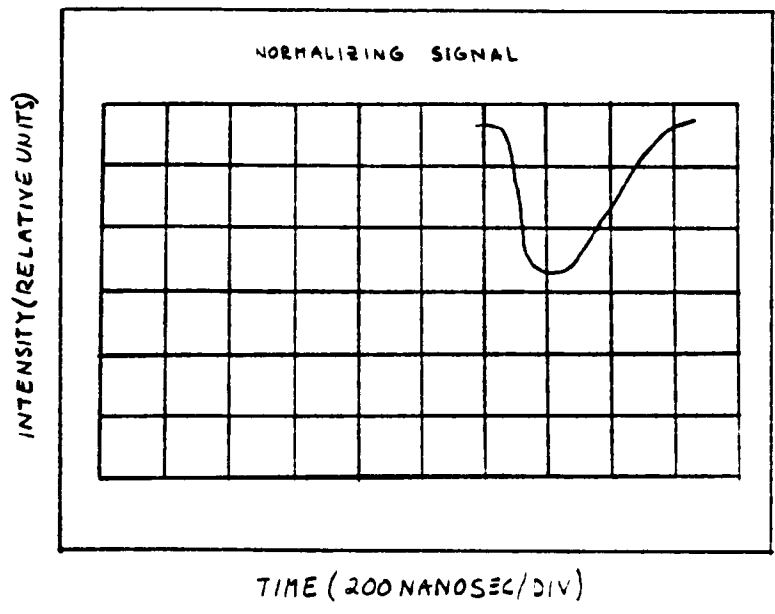
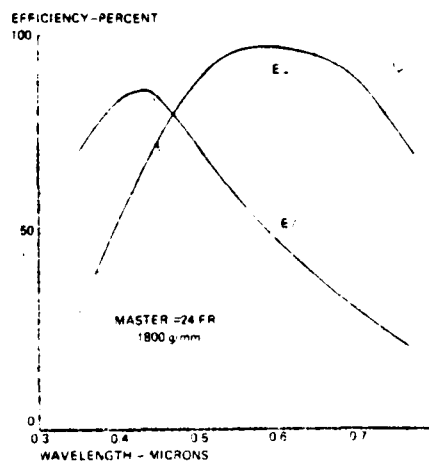


FIGURE 3.6:13b THE FINAL FINE TUNING SIGNALS FOR SIMULTANEOUS TWO-WAVELENGTH OPERATION FOR OBTAINING FREQUENCY COINCIDENCE FOR THE 4500 Å LASER LINE



FROM LEFT TO RIGHT: 4500 Å, 4478 Å, 4358 Å, 4078 Å, AND 4047 Å

FIGURE 3.6:14 SPECTROMETER PHOTOGRAPH OF THE SIMULTANEOUS
TWO-WAVELENGTH OUTPUT WITH LASER FREQUENCIES
FINE TUNED TO 4478.5 Å AND 4500 Å WITH APPROX-
IMATELY 5 Å BANDWIDTHS

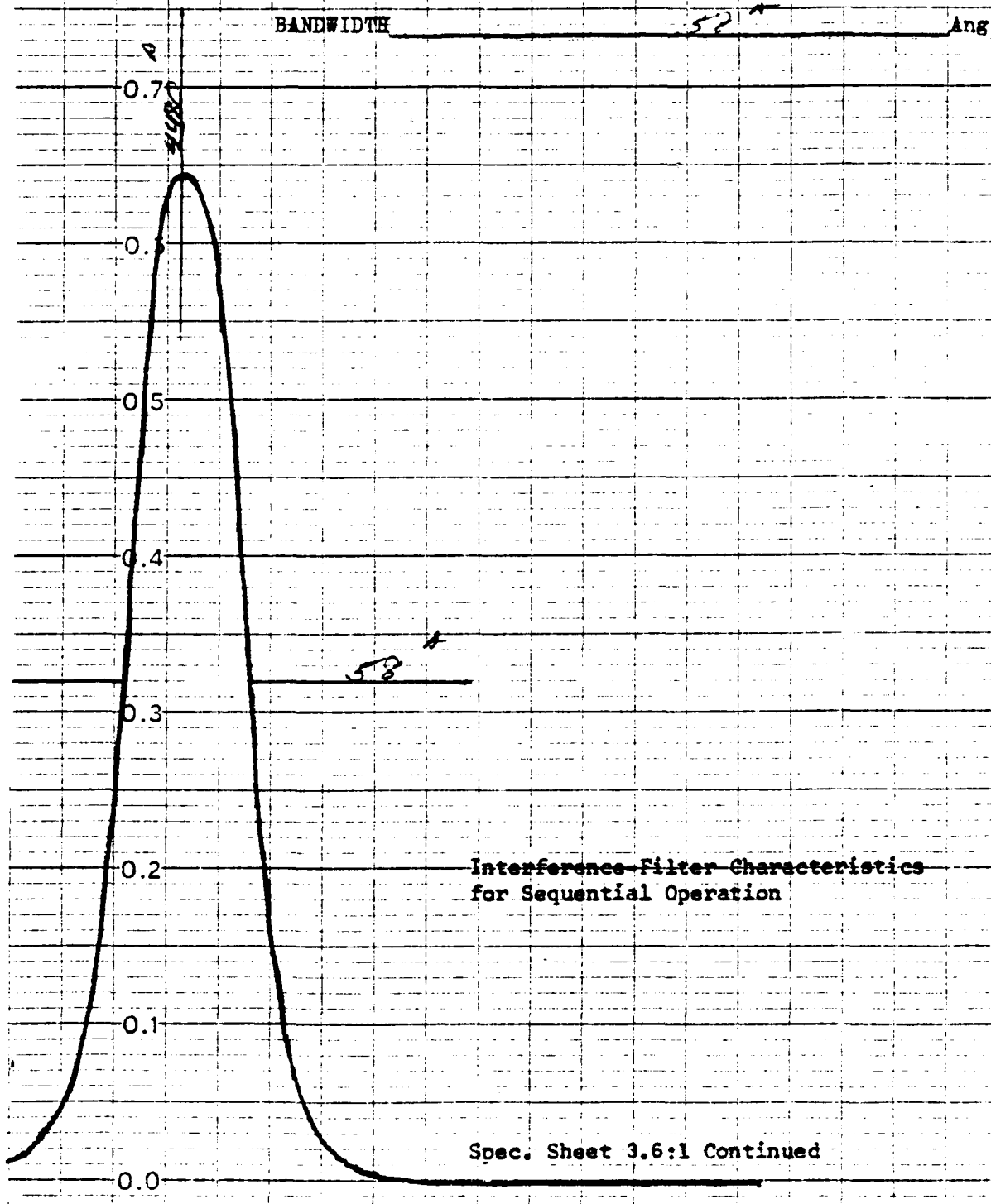


GRATING TYPE	LASER POWER CONTINUOUS	LASER POWER PULSED	MAXIMUM TEMPERATURE
Replica on pyrex aluminum coating	50 W/cm ²	2 MW/cm ² on 20 - 30 ns	100°C

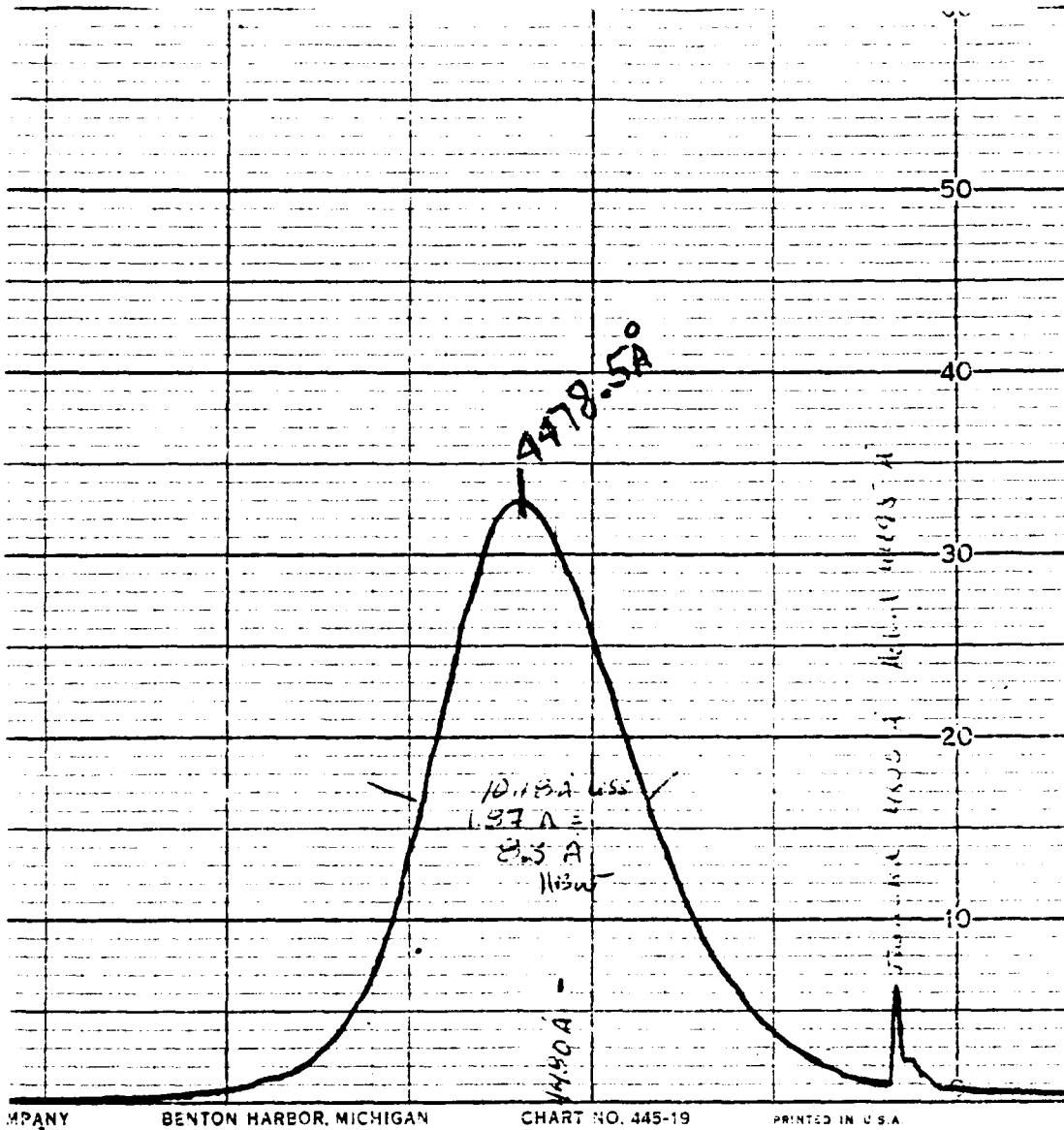
Grating Characteristics

FIGURE 3.6:15 SPEC. SHEET 3.6:1

TEST INSTRUMENT C-20-14
 DATE 11/26/74 TECHNICIAN JDP
 AMBIENT TEMP. _____ °C CHART SPEED 20 Ang/Div.
 CALIBRATION CORRECTION FACTOR _____ Ang
 PEAK WAVELENGTH 4480 Ang
 BANDWIDTH 58 Ang

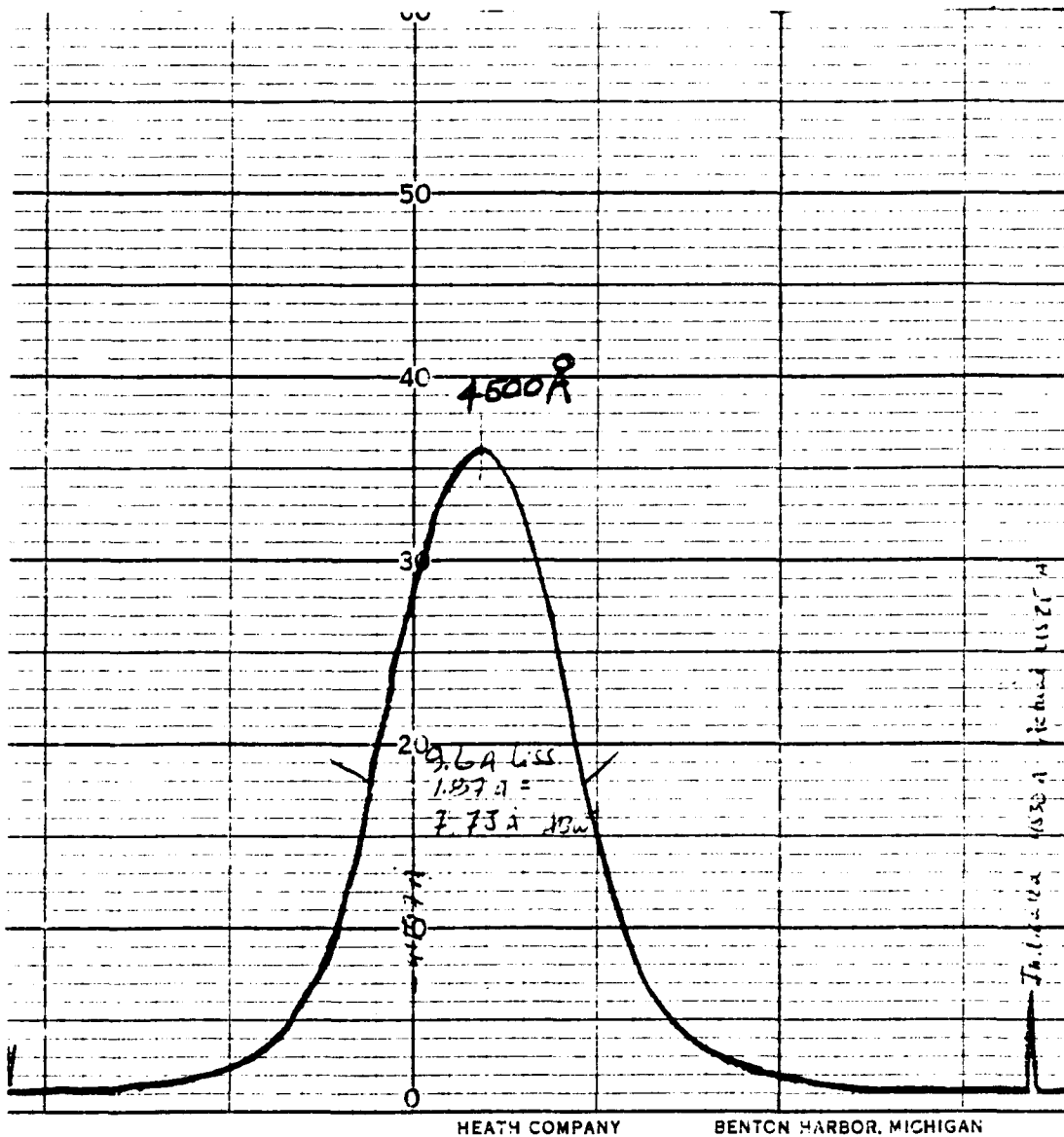


Interference Filter Characteristics
 for Sequential Operation



Interference-Filter Characteristics for Simultaneous Two-Wavelength Operation

Spec. Sheet 3.6:1 Continued



Interference-Filter Characteristics for Simultaneous Two-Wavelength Operation

Spec. Sheet 3.6:1 Continued

CHAPTER 4 NO₂ MEASUREMENTS

4.1 Introduction

Measurements on NO₂ were carried out using laser outputs at 4478.5 Å and 4500 Å. These were optimized using the procedure described in Sect. 3.6.3.

Alignment of the outgoing laser beam with the receiver telescope was carried out by using a water tower on top of a building over 2 km away as a target, and adjusting the alignment of the receiver telescope to obtain the maximum return signal from it. The outgoing beam goes out eastwards from a corner window in our laboratory, and passes over upper Manhattan and the East River.

4.2 Results of Field Tests

4.2.1 Sequential Measurements

Measurements were carried out in the sequential mode of operation with pulses fired at intervals of approximately 5 seconds. These were fired in trains of three pulses: on-peak, off-peak, and on-peak. Measurements were only considered valid when the first and the third pulse returns were nearly identical, indicating that no substantial scene change had occurred between pulses.

With the LIDAR system pointing out of the laboratory window, measurements of the LIDAR backscatter returns at 4478.5 Å and 4500 Å were carried out. The return signal, the output of the photomultiplier tube in the receiver system, was displayed on the oscilloscope and recorded photographically.

Fig. 4.2:1 shows a curve trace from an oscilloscope photograph of a typical return signal. The peak occurring at 16 us represents the reflection from a water tower on top of a building some 2400 m away from the LIDAR site.

Fig. 4.2:2 shows the trace of the return signal when a number of chimneys below the beam path were emitting smoke.

Fig. 4.2:3a and b show respectively two curves plotted from oscilloscope photographs of the returns at 4478.5 \AA and 4500 \AA , and the calibration signals obtained for these readings. As can be seen from the curves, the signal at 4478.5 \AA , which is on the absorption peak, was clearly attenuated more than the signal at 4500 \AA , which is off the absorption peak.

The different attenuations may be noticed immediately by looking at the reflection peaks from the building 2400 m (16 us) away.

The relative attenuation is largest over a 450 m region extending from a range of approximately 1050 to 1500 m. Below the LIDAR beam in that region are several avenues with heavy traffic. NO_2 densities over that region are calculated from the curves to be approximately 0.46 ppm.

The overall average density to the building and back is approximately 0.09 ppm. Measurements of this type show a correlation within 30 percent of the sample measurements made at the fixed-site Department of Air Resources monitoring station situated near the area.

4.2.1.1 Factors Affecting Accuracy

In the initial field tests, the laser beam was paraxial with the optical receiver axis. This arrangement was used to avoid local scat-

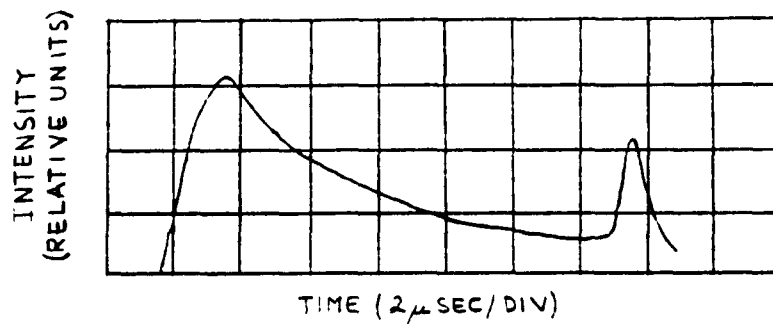


FIGURE 4.2:1 TYPICAL LIDAR RETURN SIGNAL

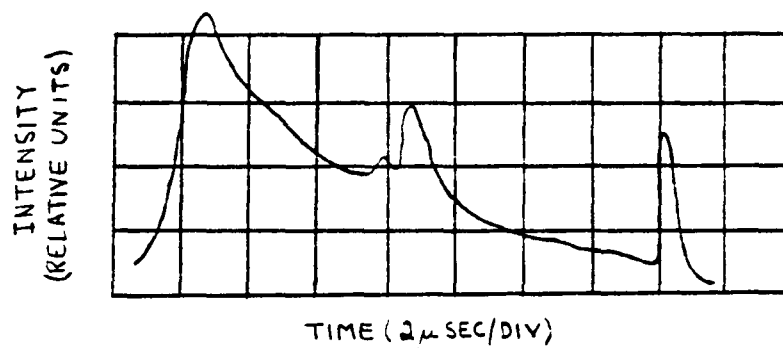


FIGURE 4.2:2 TYPICAL LIDAR RETURN SIGNAL WITH CHIMNEYS BELOW BEAM
PATH

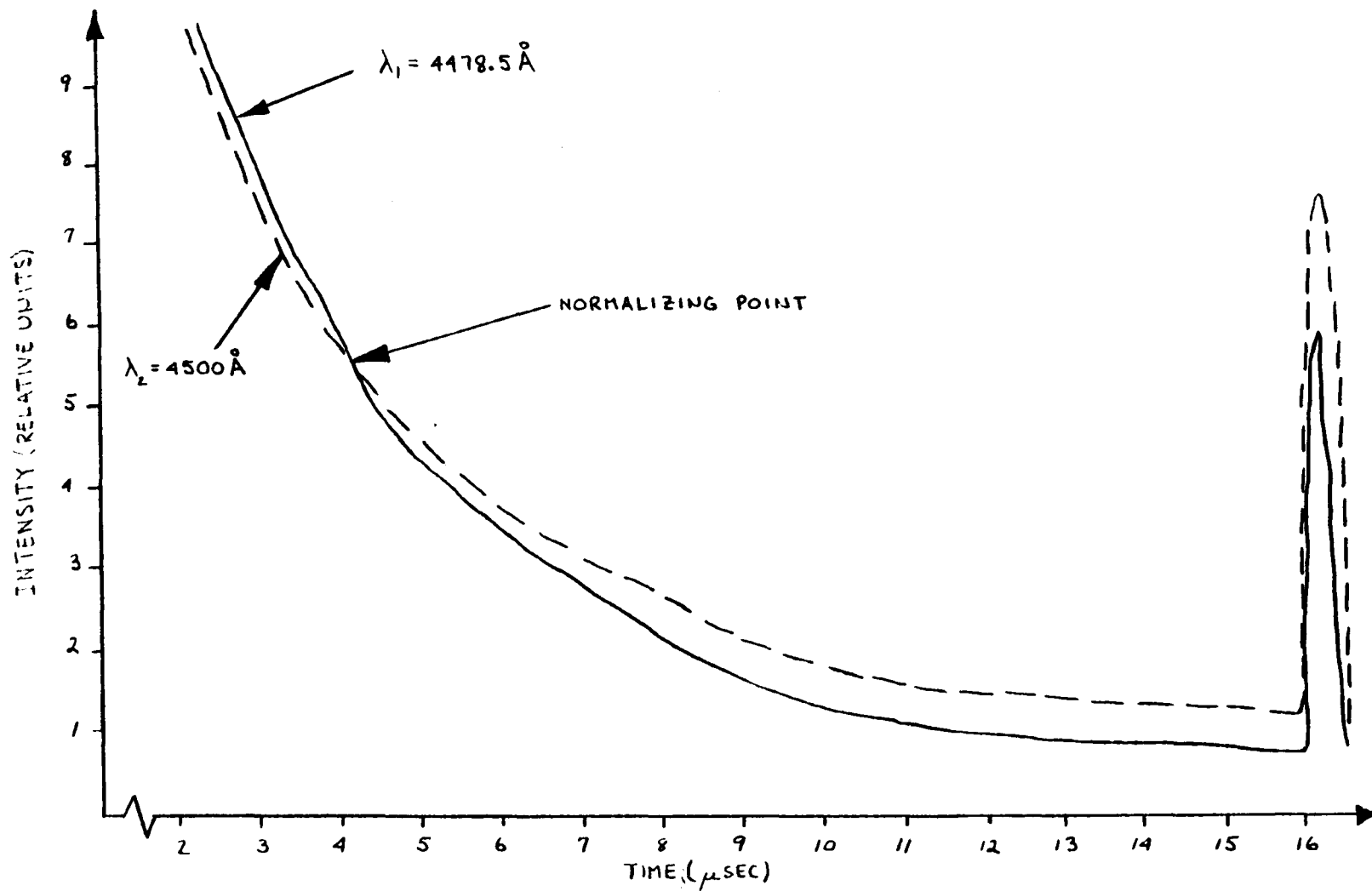


FIGURE 4.2:3a SEQUENTIAL LIDAR RETURN SIGNALS AT 4478.5 Å AND 4500 Å

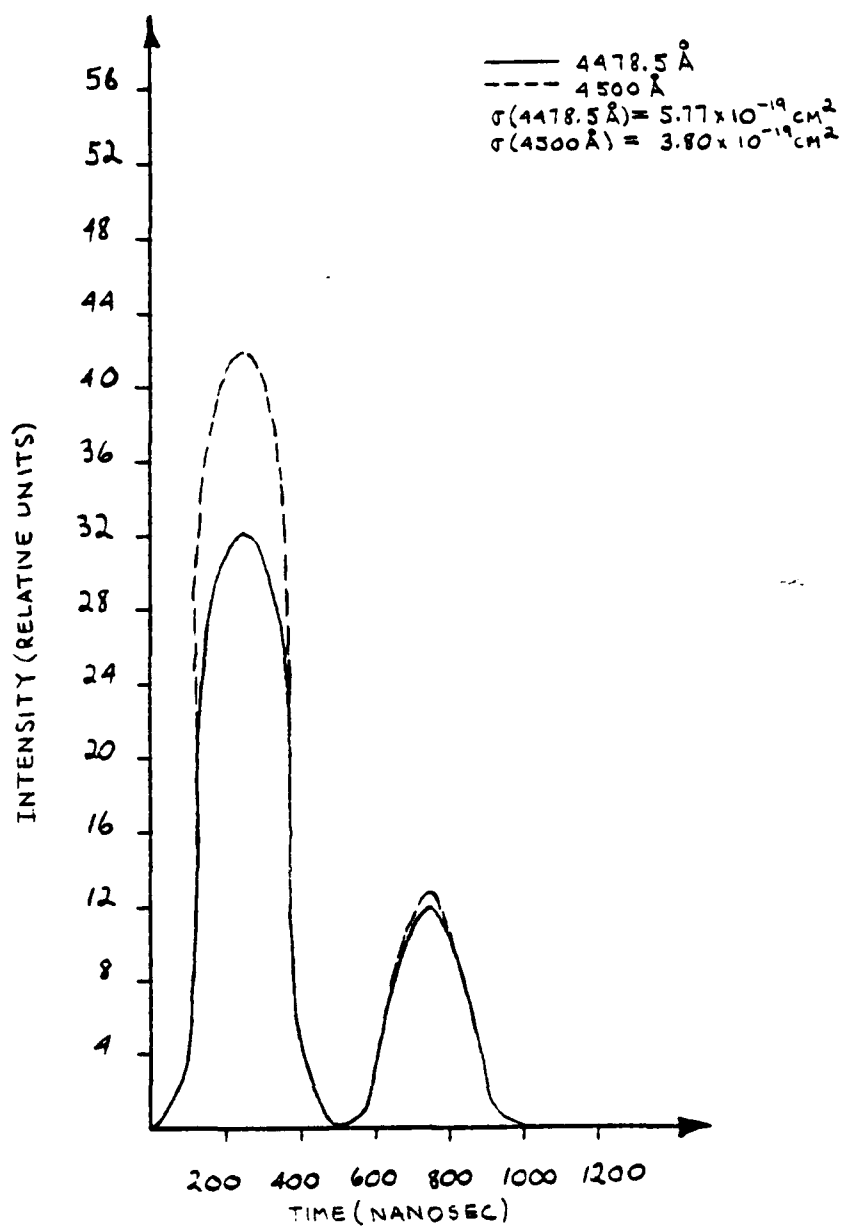


FIGURE 4.2:3b SEQUENTIAL CALIBRATION SIGNALS AT 4478.5 Å AND 4500 Å

tering from the outgoing beam into the receiver. This scattering problem was overcome with a redesigned optical arrangement with the outgoing beam collinear with the optical receiver axis. This permitted the use of a much more collimated output beam along with a smaller acceptance angle for the optical receiver field of view. This has resulted in improved signal to noise ratios as well as reducing the importance of shot to shot repeatability of the geometric intensity distribution of the laser output pulse.

Other factors were also found to affect the accuracy of measurements. With sequential operation, changes in the region probed by the laser beam in the time interval between shots obviously cause errors.

Changes are of two types:

1. Scintillation effects, which cause rapid changes in the transmission of the beam and backscattered signal through the atmosphere.
2. More gradual changes due to particulates and pollutants being blown by wind.

Scintillation effects are particularly bad when there are large temperature gradients across the beam path.

To check that neither of these effects is causing substantial errors when sequential measurements are being made, the laser is operated in groups of three pulses, with the first pulse being off-resonance, the second on-resonance, and the third pulse off-resonance again, to ensure no substantial changes with the first. It is found that these conditions prevail particularly when there are no patches of particulates, e.g., smoke drifting across the scene being viewed, and when

there are no strong temperature gradients causing scintillation effects. The curves of Figs. 4.2:1 and 4.2:3a were obtained under such conditions.

For conditions where the scene or optical path is changing rapidly, which is frequently the case, there appears to be no remedy but to use simultaneous wavelength operation, so that both wavelengths are traversing the same optical path at the same time.

4.2.2 Simultaneous Two-Wavelength Measurements

A series of field tests were carried out operating the laser in the simultaneous two-wavelength mode of operation. For this purpose, the arrangement described in Sect. 3.5.2 and Figs. 3.5:4a and b was used, as well as the calibration cell arrangement described in Sect. 3.6.2 and Figs. 3.6:7a and b.

Figs. 4.2:4a through o each show typical pairs of curves plotted from oscilloscope photographs of the LIDAR returns and the calibration signals at 4478.5 \AA and 4500 \AA for various times during the day.

During the field tests it was noted that the readings from the calibration system indicated that there was a monotonic narrowing in laser bandwidth with the number of laser firings. This can readily be seen in view of Figs. 4.2:4b, d, f, h, j, l, and n. These curves show that the difference in effective absorption cross sections increased with the number of times the laser was fired.

The effective NO_2 absorption cross sections therefore varied from $5.43 \times 10^{-19} \text{ cm}^2$ and $4.17 \times 10^{-19} \text{ cm}^2$ to $6.36 \times 10^{-19} \text{ cm}^2$ and $3.54 \times 10^{-19} \text{ cm}^2$ for the 4478.5 \AA and 4500 \AA lines respectively. This effect was expected, and as explained in Sect. 3.6 is due to solarization of

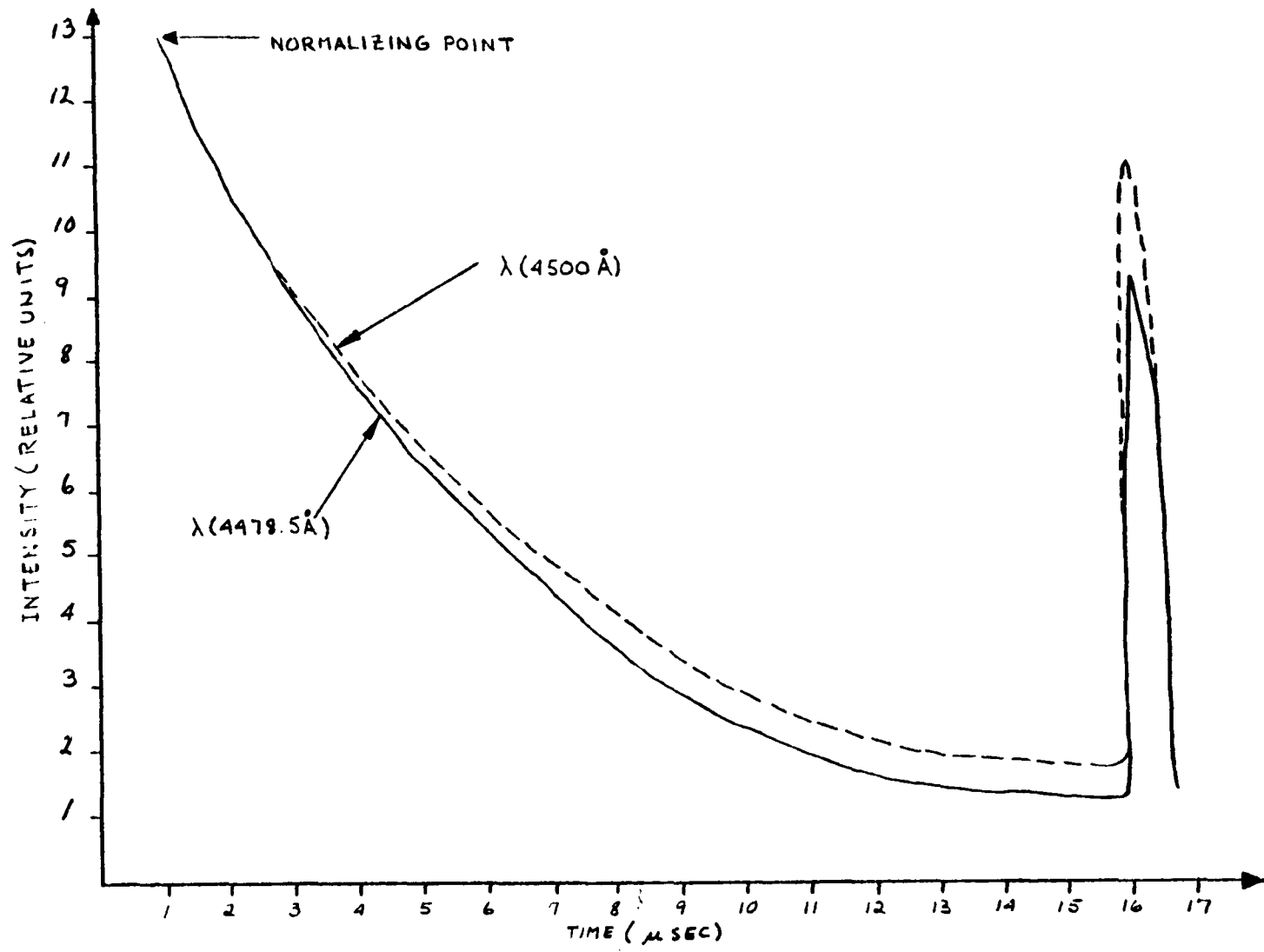


FIGURE 4.2:4a SIMULTANEOUS LIDAR RETURN SIGNALS AT 4478.5 Å AND 4500 Å, TIME: 8:45 A.M.

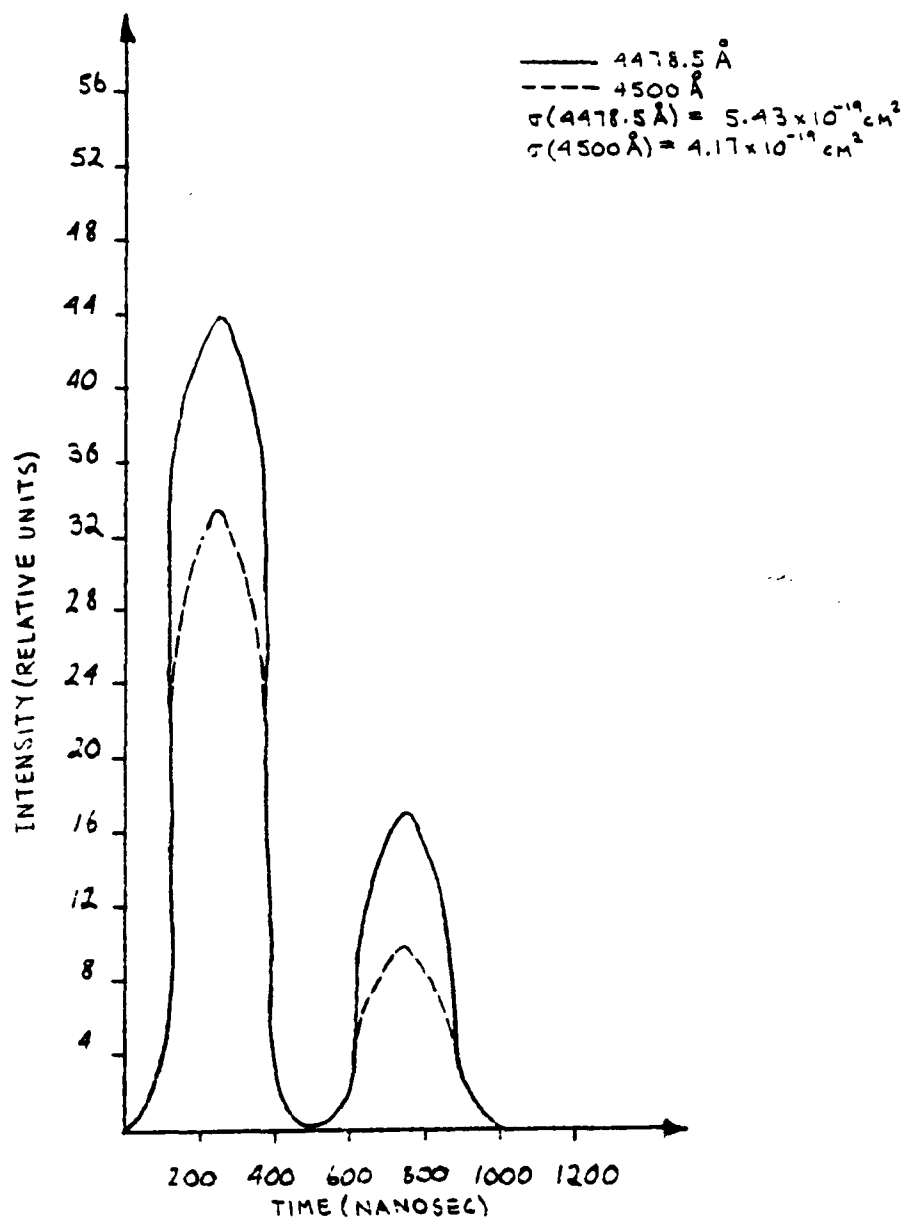


FIGURE 4.2:4b SIMULTANEOUS CALIBRATION SIGNALS FOR 4478.5 Å AND 4500 Å, TIME: 8:45 A.M.

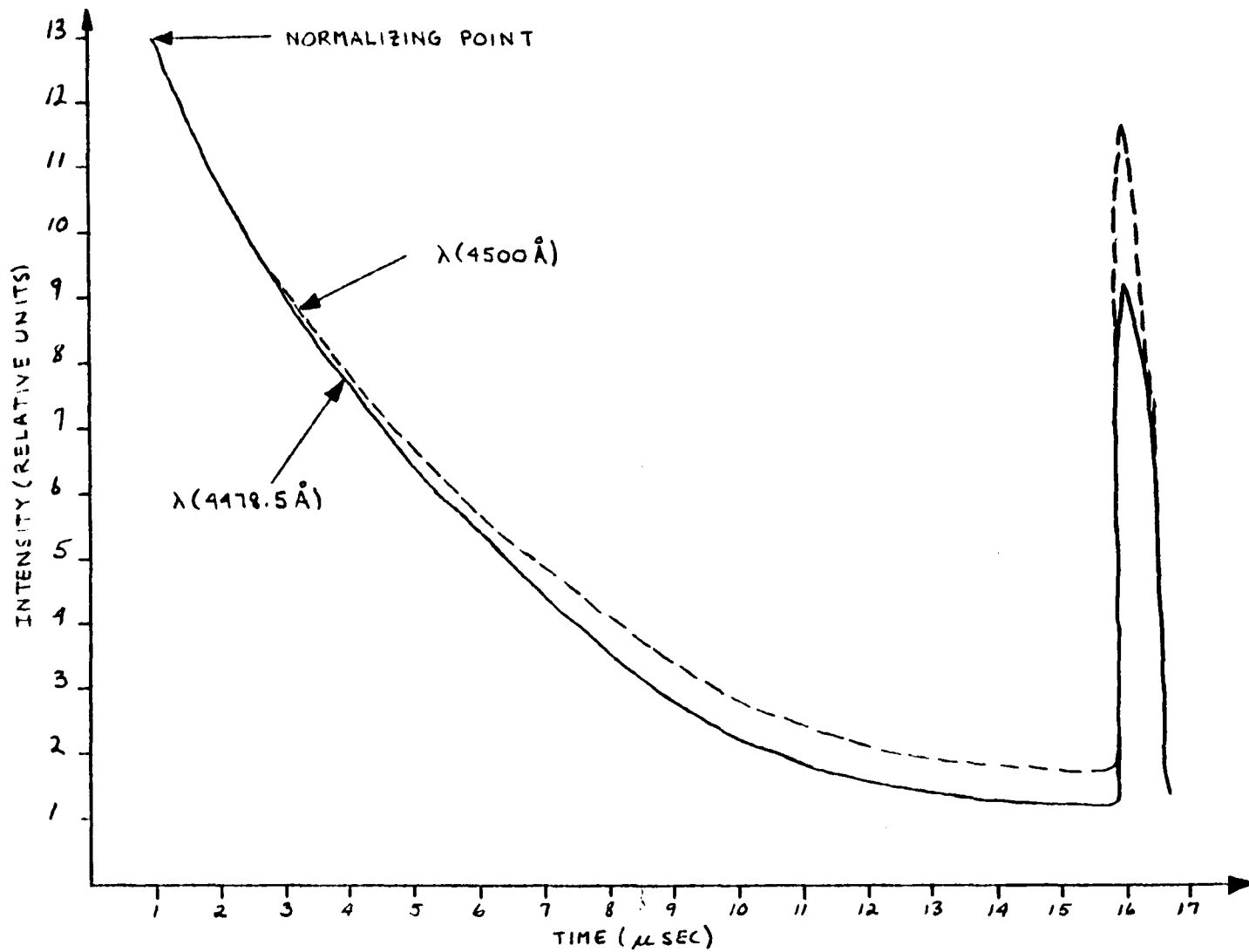


FIGURE 4.2:4c SIMULTANEOUS LIDAR RETURN SIGNALS AT 4478.5 Å AND 4500 Å, TIME: 9:00 A.M.

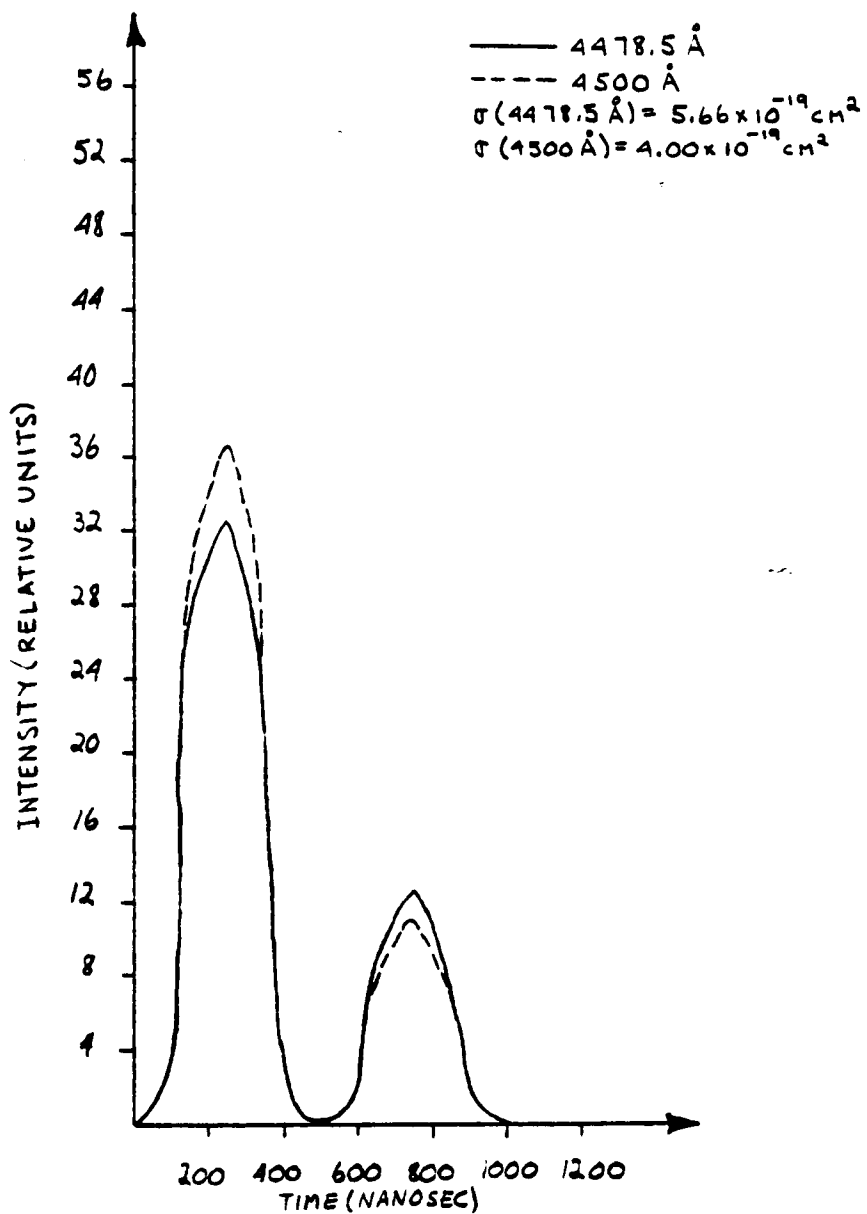


FIGURE 4.2:4d SIMULTANEOUS CALIBRATION SIGNALS FOR 4478.5 Å AND 4500 Å, TIME: 9:00 A.M.

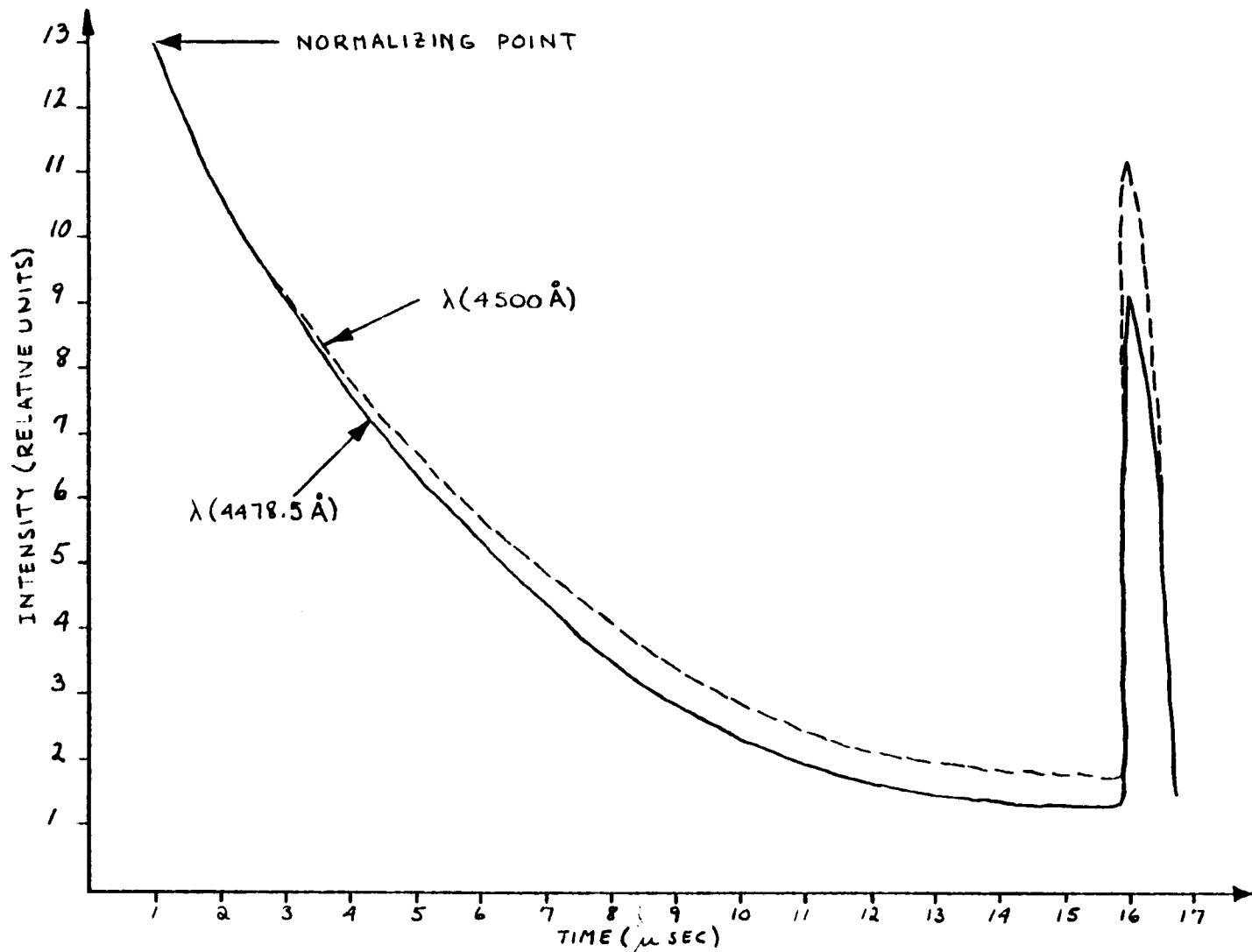


FIGURE 4.2:4e SIMULTANEOUS LIDAR RETURN SIGNALS AT 4478.5 \AA AND 4500 \AA , TIME: 9:30 A.M.

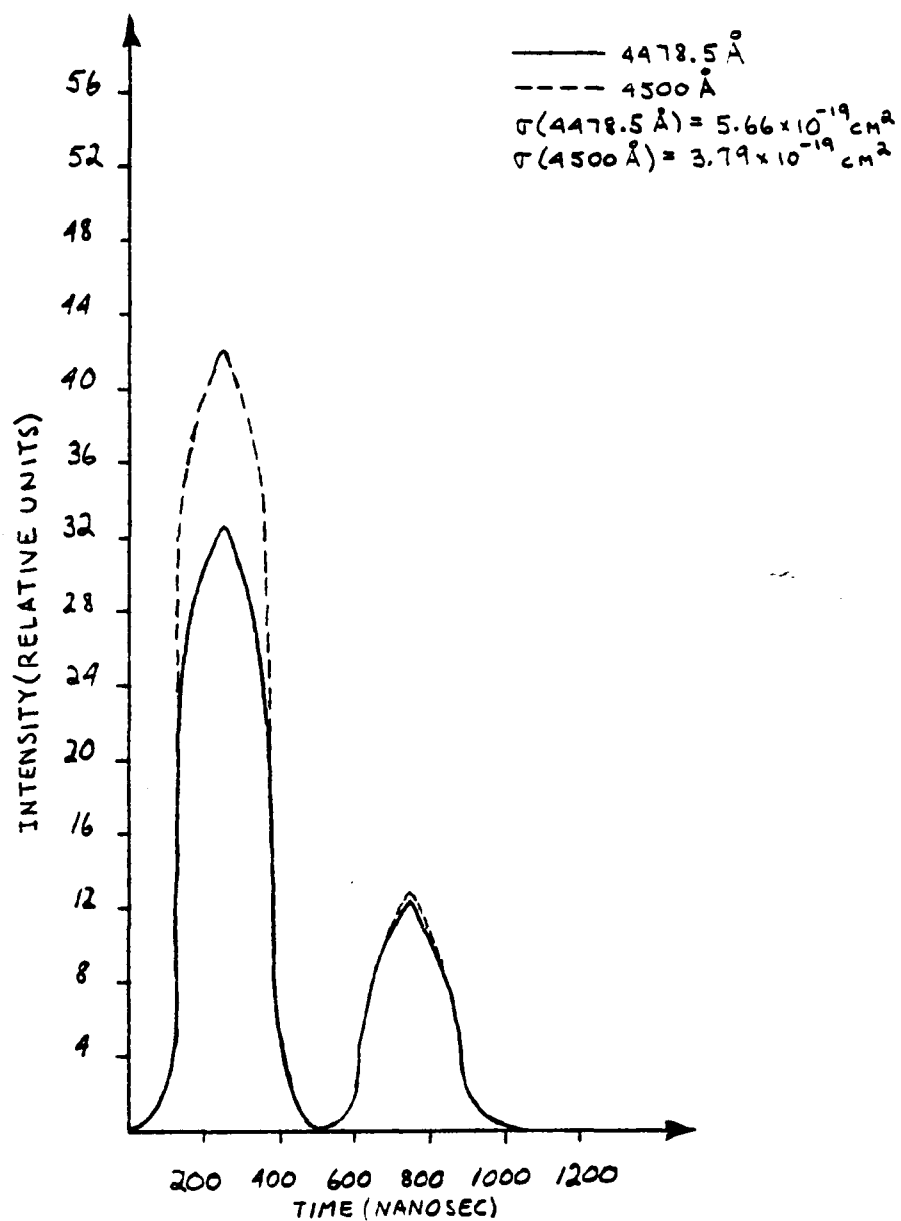


FIGURE 4.2:4F SIMULTANEOUS CALIBRATION SIGNALS FOR 4478.5 Å AND 4500 Å, TIME: 9:30 A.M.

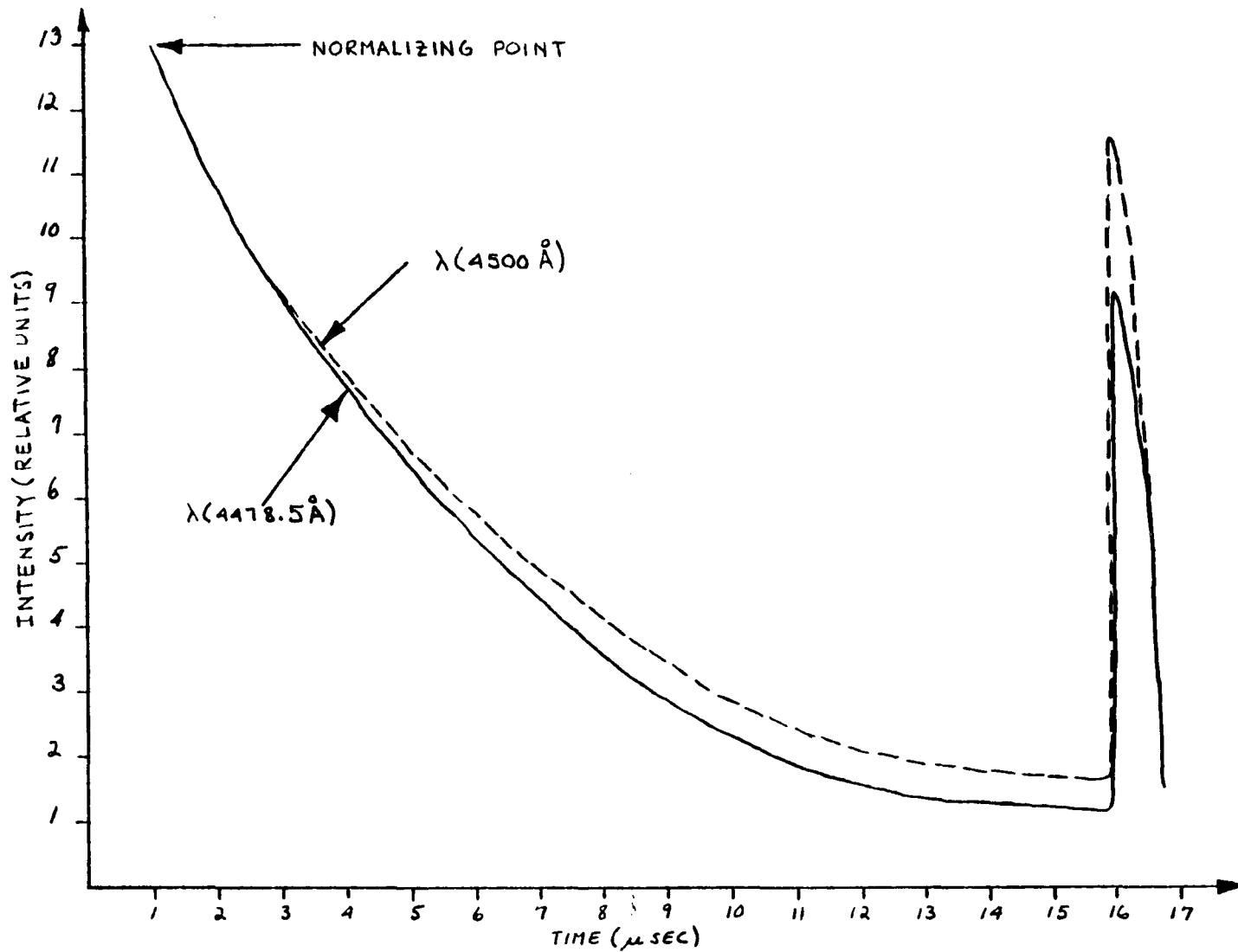


FIGURE 4.2:4g SIMULTANEOUS LIDAR RETURN SIGNALS AT 4478.5 Å AND 4500 Å, TIME: 5:30 P.M.

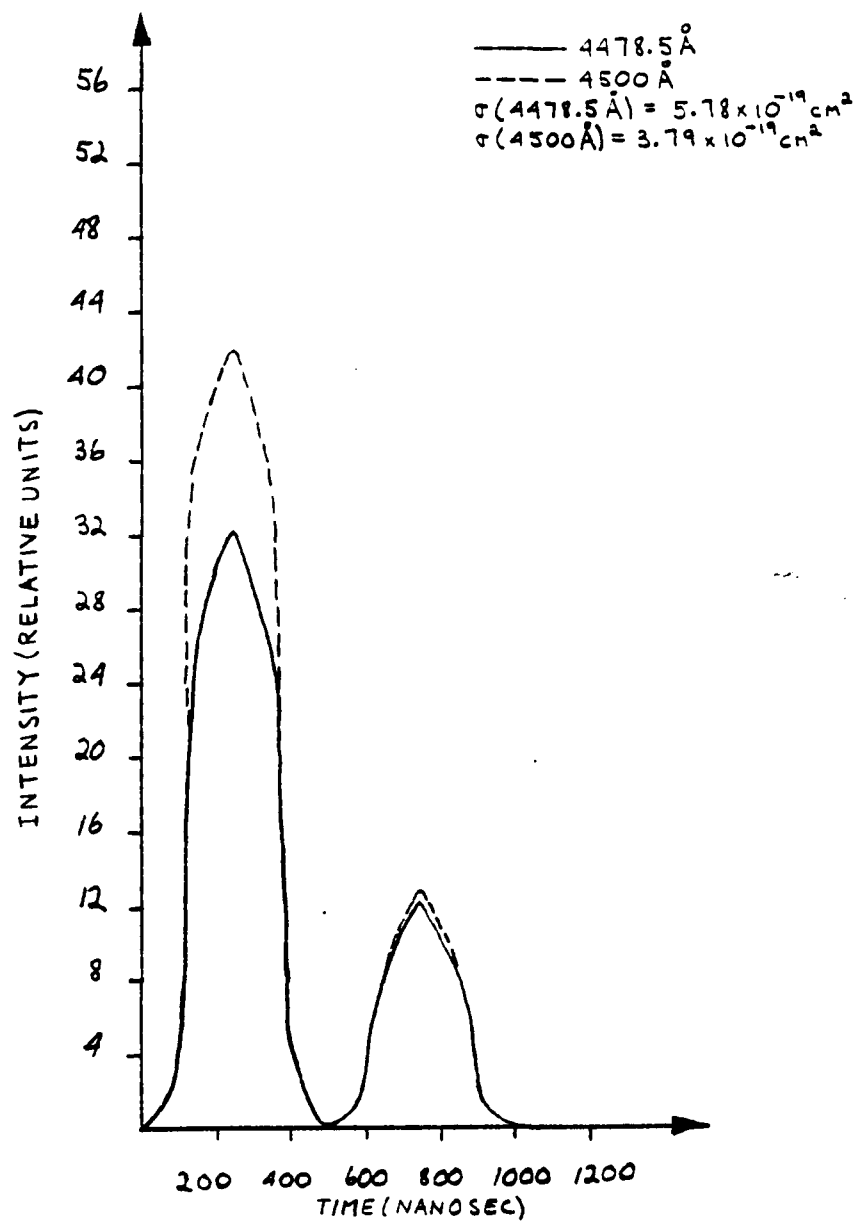


FIGURE 4.2:4h SIMULTANEOUS CALIBRATION SIGNALS FOR 4478.5 Å AND 4500 Å, TIME: 5:30 P.M.

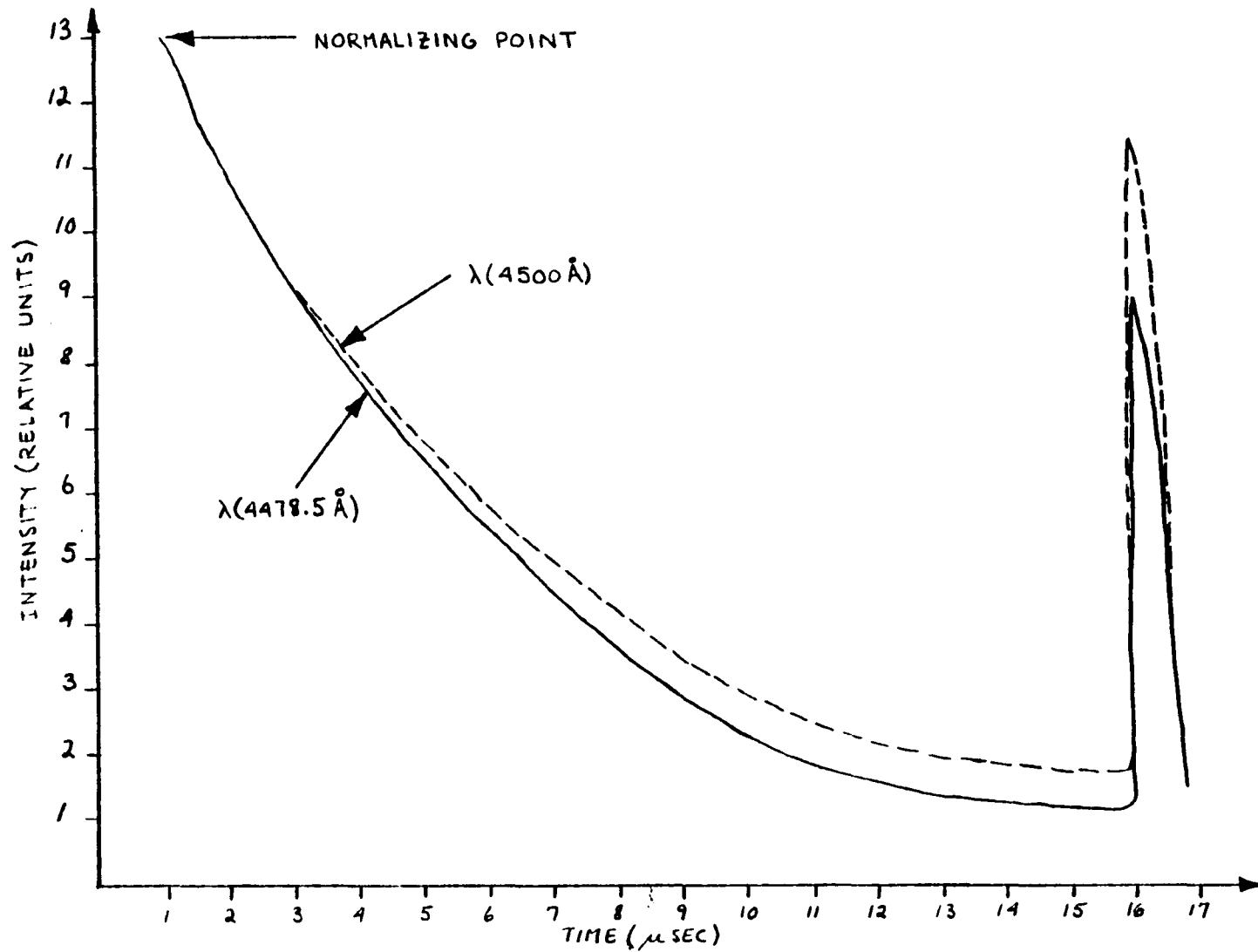


FIGURE 4.2:4i SIMULTANEOUS LIDAR RETURN SIGNALS AT 4478.5 Å AND 4500 Å, TIME: 6:00 P.M.

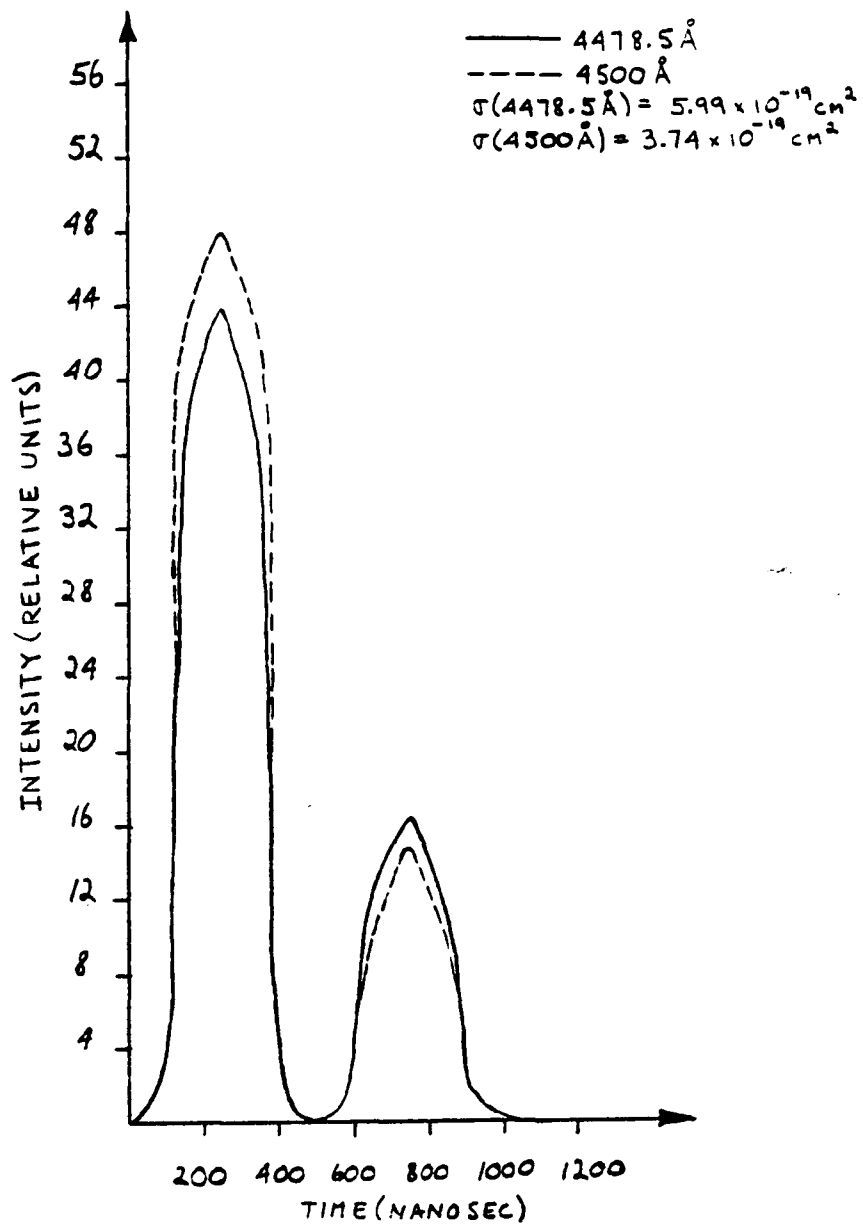


FIGURE 4.2:4j SIMULTANEOUS CALIBRATION SIGNALS FOR 4478.5 Å AND 4500 Å, TIME: 6:00 P.M.

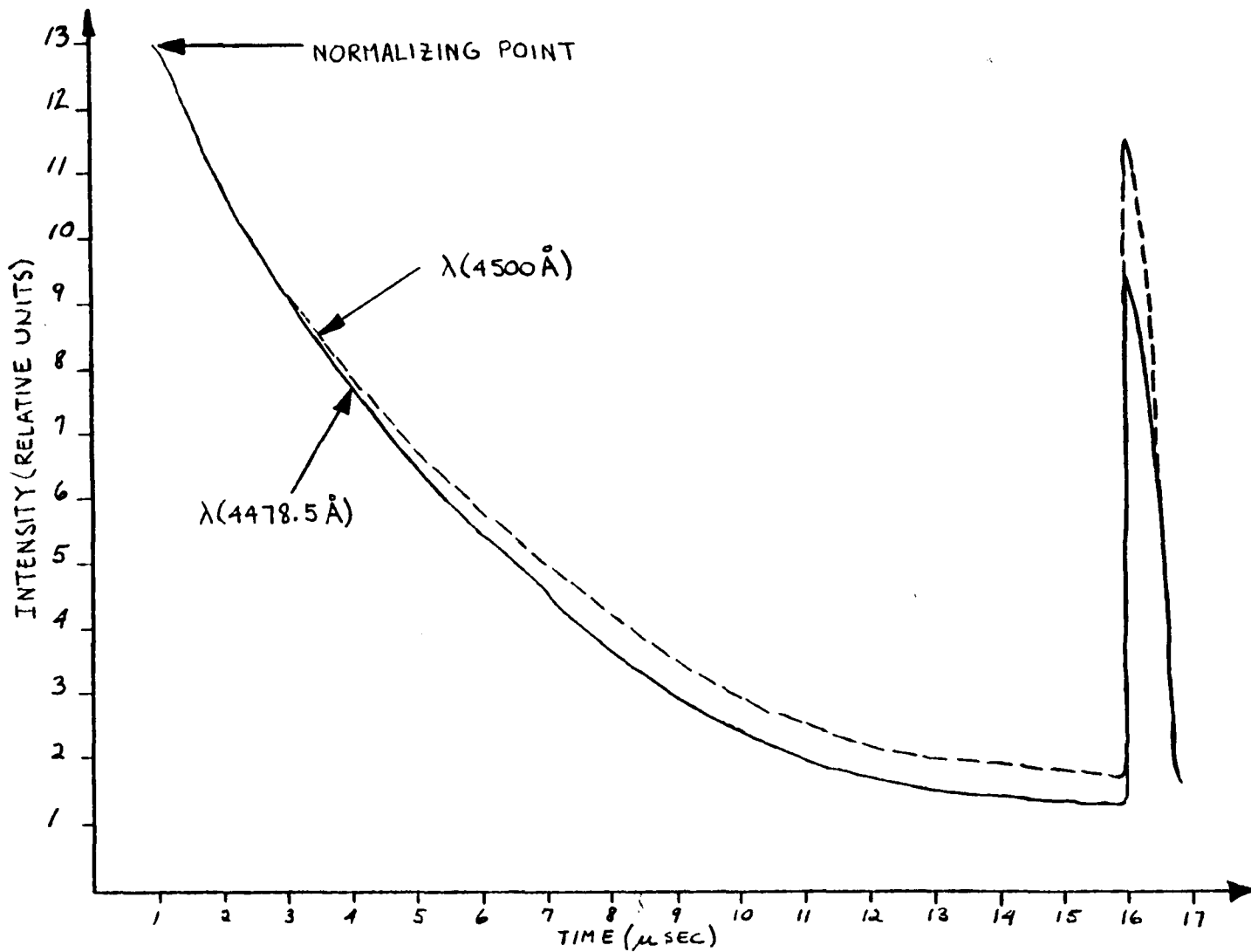


FIGURE 4.2:4k SIMULTANEOUS LIDAR RETURN SIGNALS AT 4478.5 Å AND 4500 Å, TIME: 6:30 P.M.

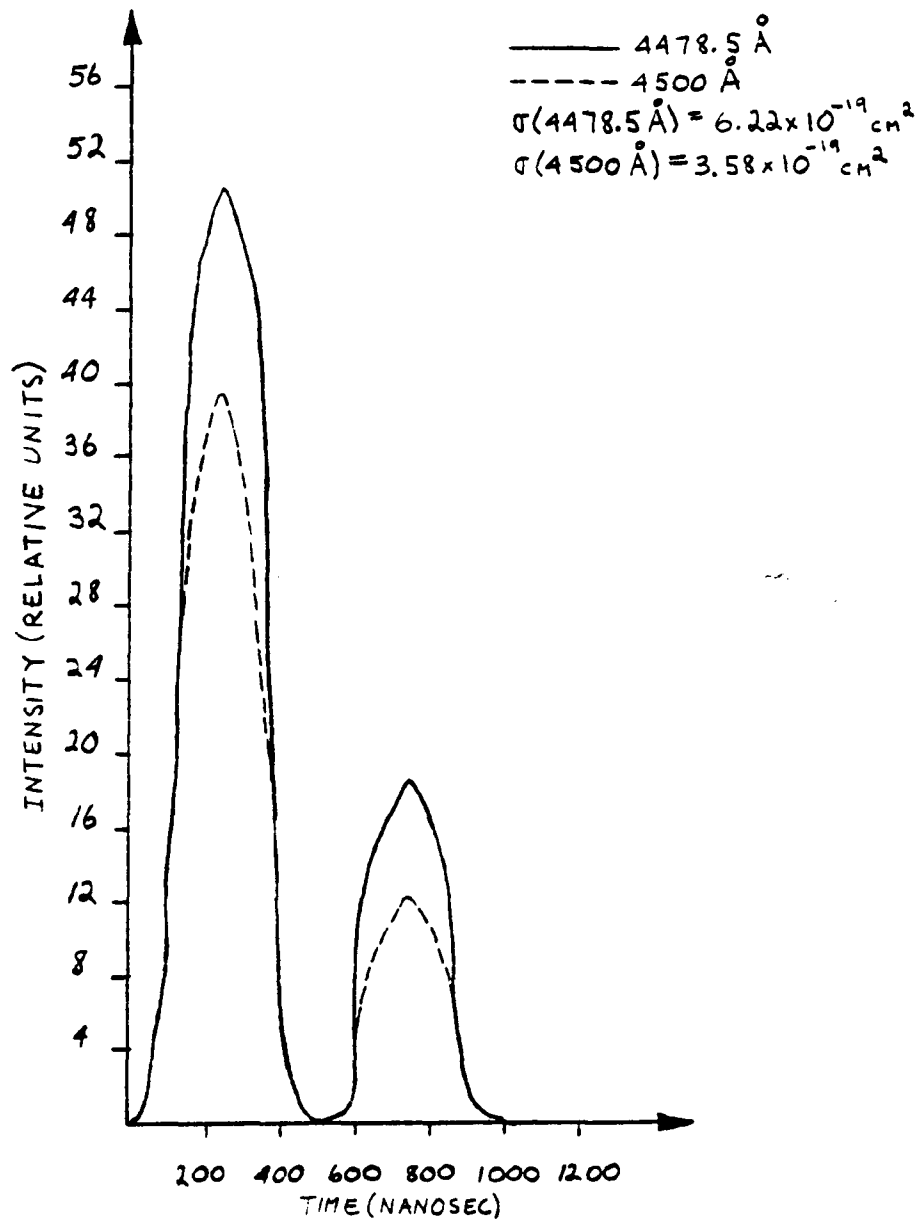


FIGURE 4.2:41 SIMULTANEOUS CALIBRATION SIGNALS FOR 4478.5 Å AND 4500 Å, TIME: 6:30 P.M.

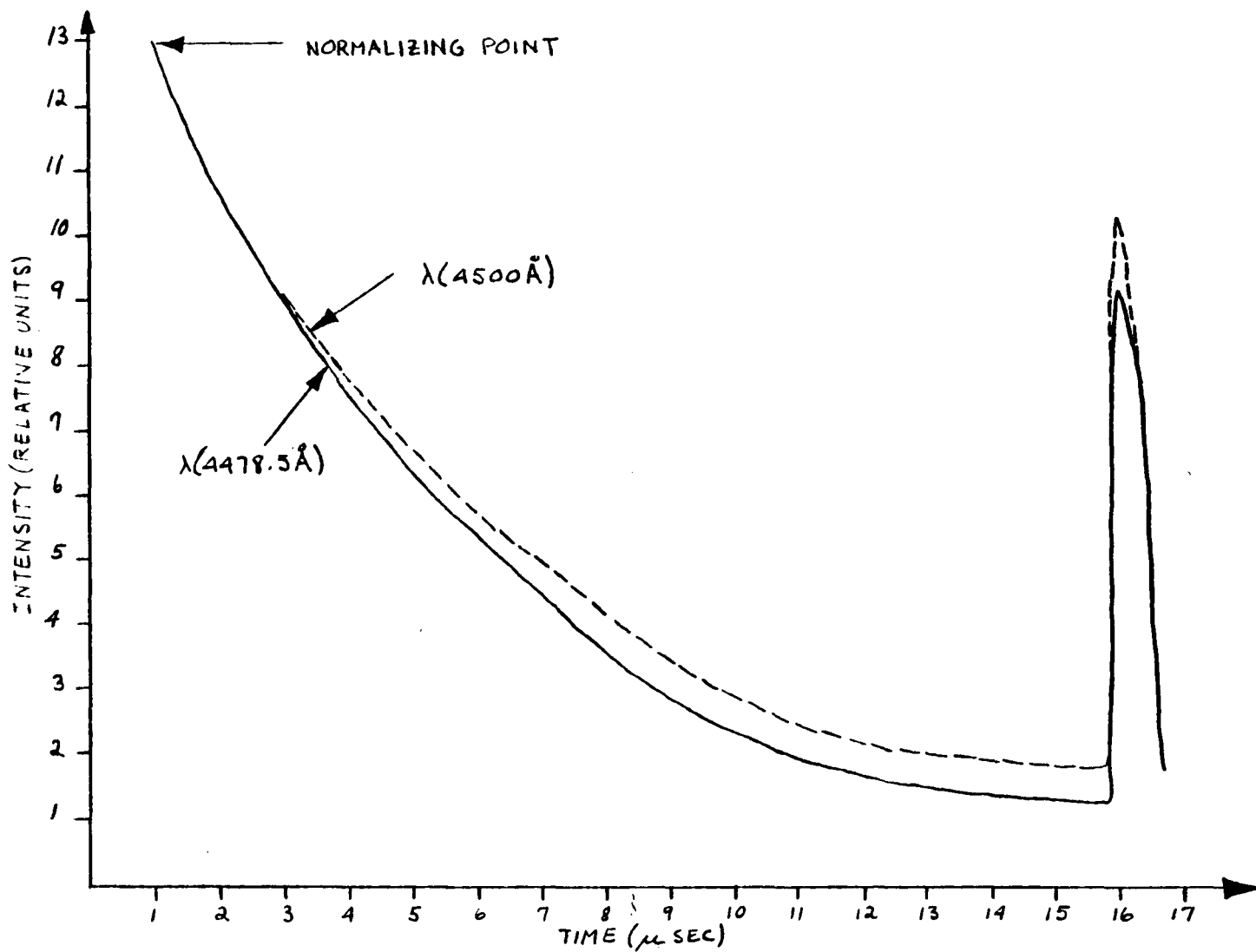


FIGURE 4.2:4m SIMULTANEOUS LIDAR RETURN SIGNALS AT 4478.5 Å AND 4500 Å, TIME: 8:00 P.M.

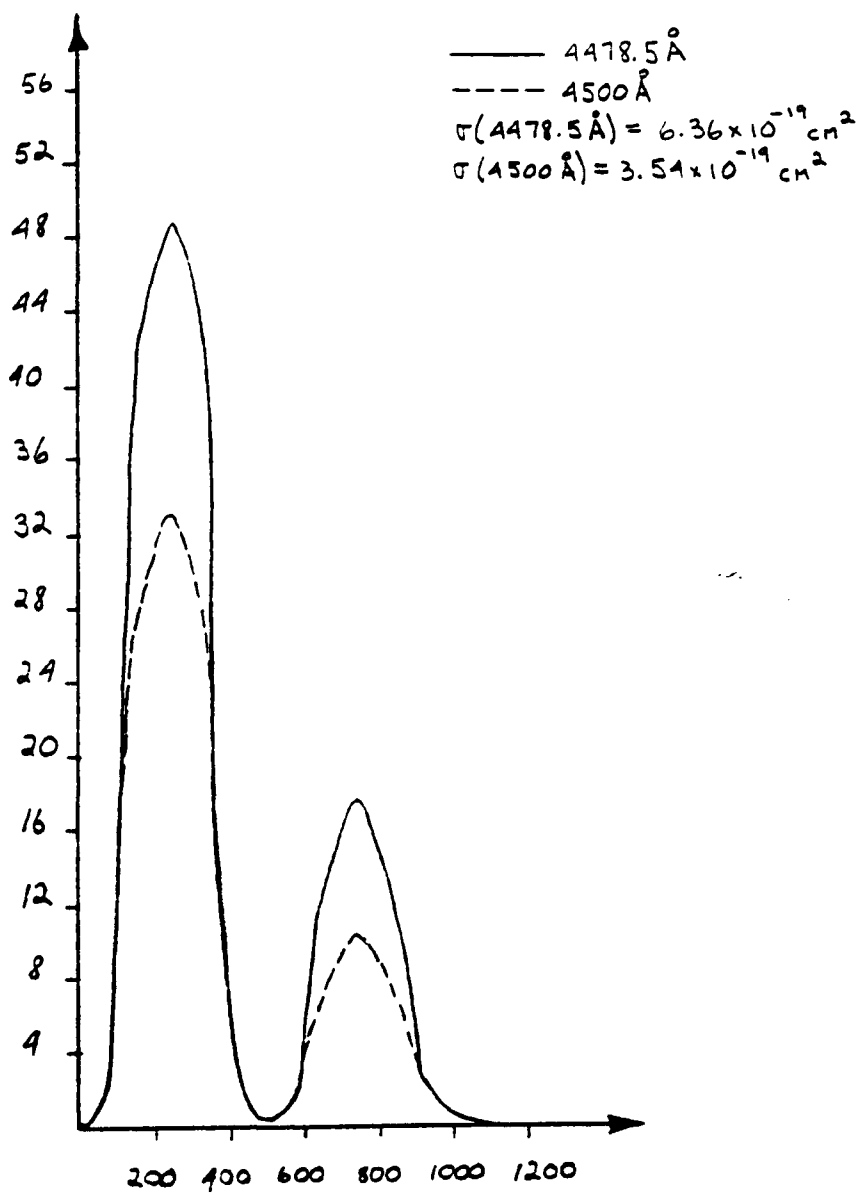


FIGURE 4.2:4n SIMULTANEOUS CALIBRATION SIGNALS FOR 4478.5 Å AND 4500 Å, TIME: 8:00 P.M.

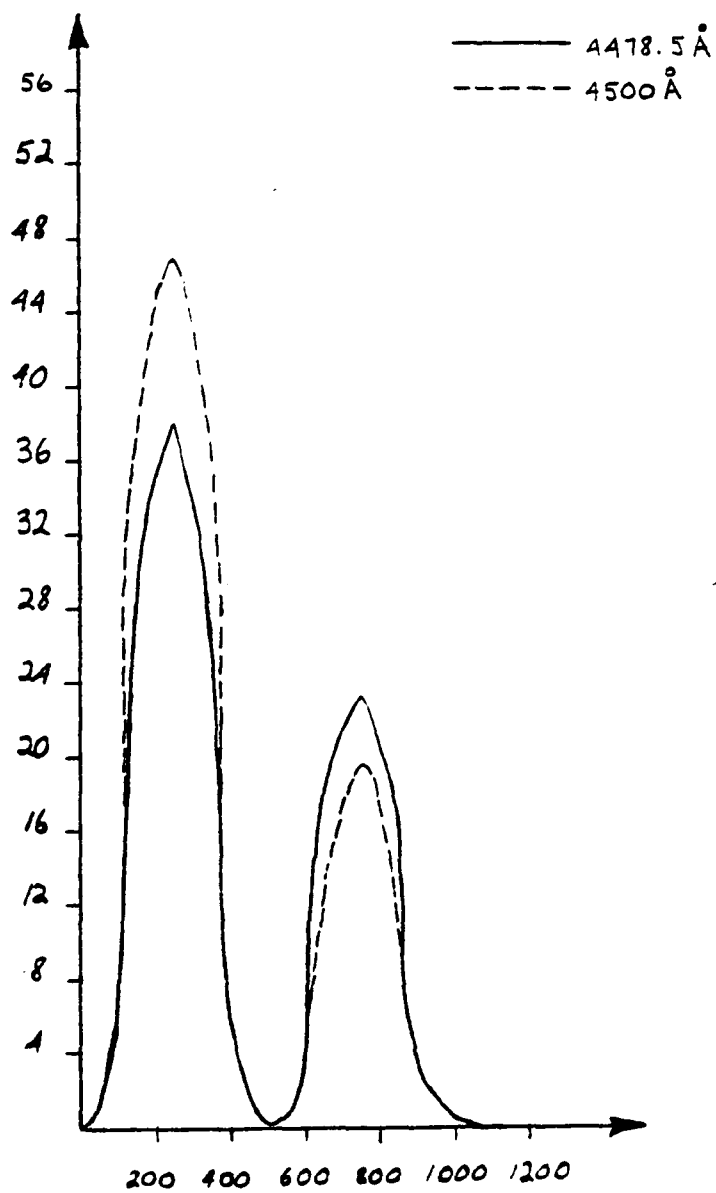


FIGURE 4.2:40 SIMULTANEOUS CALIBRATION SIGNALS FOR 4478.5 Å AND 4500 Å FOR NORMALIZATION (WITH N₂ IN THE CALIBRATION CELL)

r (m)	r (m)	Time	NO ₂ Concentration (ppm)	Uncertainty (ppm)
1050	450	8:45 A. M.	0.29	0.05
		9:00 A. M.	0.31	
		9:30 A. M.	0.21	
		5:30 P. M.	0.26	
		6:00 P. M.	0.24	
		6:30 P. M.	0.15	
		8:00 P. M.	0.14	
750	300	8:45 A. M.	0.31	0.07
		9:00 A. M.	0.22	
		9:30 A. M.	0.22	
		5:30 P. M.	0.19	
		6:00 P. M.	0.15	
		6:30 P. M.	0.16	
		8:00 P. M.	0.11	
FROM LIDAR SITE TO BLDG.	2400	8:45 A. M.	0.11	0.009
		9:00 A. M.	0.11	
		9:30 A. M.	0.09	
		5:30 P. M.	0.09	
		6:00 P. M.	0.08	
		6:30 P. M.	0.06	
		8:00 P. M.	0.06	

TABLE 4.2:1 RANGE, RESOLUTION, NO₂ POLLUTION CONCENTRATION,
AND UNCERTAINTIES FOR VARIOUS TIMES DURING THE DAY

the dye and degradation of gain following many laser firings during the course of the day.

From the traces of the LIDAR returns, Figs. 4.2:4a, c, e, g, i, k, and m, it is seen that in each case the relative attenuation is largest over a 450 m region extending from a range of approximately 1050 m to 1500 m. This result corresponds well with the fact that over that region the LIDAR beam crosses over several avenues with heavy traffic.

Table 4.2:1 lists the pollution concentration measured at various times during a typical day. The region of particular interest to observe pollution changes during rush hours is located approximately 1200 m from the LIDAR site (the region where areas of heavy traffic exist). Table 4.2:1 shows that the readings obtained at the range of 1050 m and depth resolution of 450 m do in fact evidence peaks in pollution levels during the morning and evening rush hours, while dropping lower thereafter. From 8:45 a.m. to 9:00 a.m. the pollution level remained approximately the same (0.29 ppm to 0.31 ppm respectively), then declined to 0.21 ppm at 9:30 a.m.. During the evening rush hours the peak NO₂ concentration reached 0.26 ppm at 5:30 p.m. then declined to 0.24 ppm at 6:00 p.m.. Thereafter, the level of NO₂ pollution reduced steadily from 0.15 ppm at 6:30 p.m. to 0.14 ppm at 8:00 p.m.. The overall average NO₂ density observed from the building (2400 m or 16 us away) to the LIDAR site ranged from 0.11 ppm to 0.06 ppm from 8:45 a.m. to 8:00 p.m. respectively.

These average density results were generally found to be within 30 percent of the values measured by the New York City Department of Air Resources fixed-site monitoring station situated a short distance to the south of the LIDAR beam trajectory.

4.3 Error Analysis

For the practical interpretation of the LIDAR pollution measurements it is useful to know the uncertainty that is associated with the measurement. Towards this end, an experiment was performed in which a known concentration of NO_2 was monitored by the LIDAR system.

The experimental setup is shown in Fig. 4.3:1. The simultaneous laser output passed through a 1/2 m sample cell which contained 609 ppm of NO_2 in N_2 . The output was then directed into the atmosphere and the backscattered returns were monitored by the receiving system. Each output pulse was monitored by the calibration system and the signals obtained from detectors 1 and 3 in the calibration setup served as the before-cell signals for both the calibration and sample cells. The experiment was performed on a windy clear night such that clear-air conditions existed, and that the output signals would not be further attenuated by ambient levels of NO_2 .

By knowing the before cell readings and the signals backscattered from the atmosphere, the pollutant concentration in $\text{ppm} \cdot \Delta r(\text{m})$ was obtained for a series of 5 shots. The mean value of the deviations from the known concentration in the cell (609 ppm in 1/2 m = $304.5 \text{ ppm} \cdot \Delta r(\text{m})$), was calculated to be $21 \text{ ppm} \cdot \Delta r(\text{m})$ or $0.021 \text{ ppm} \cdot \Delta r(\text{km})$. Fig. 4.3:2 shows the results of the experiment.

Knowing the uncertainty associated with a given depth resolution, Δr , the corresponding values were calculated for the pollution readings and are shown in Table 4.2:1.

In conclusion, the results obtained from the LIDAR field measurements were what were expected. The NO_2 pollution level peaked at rush

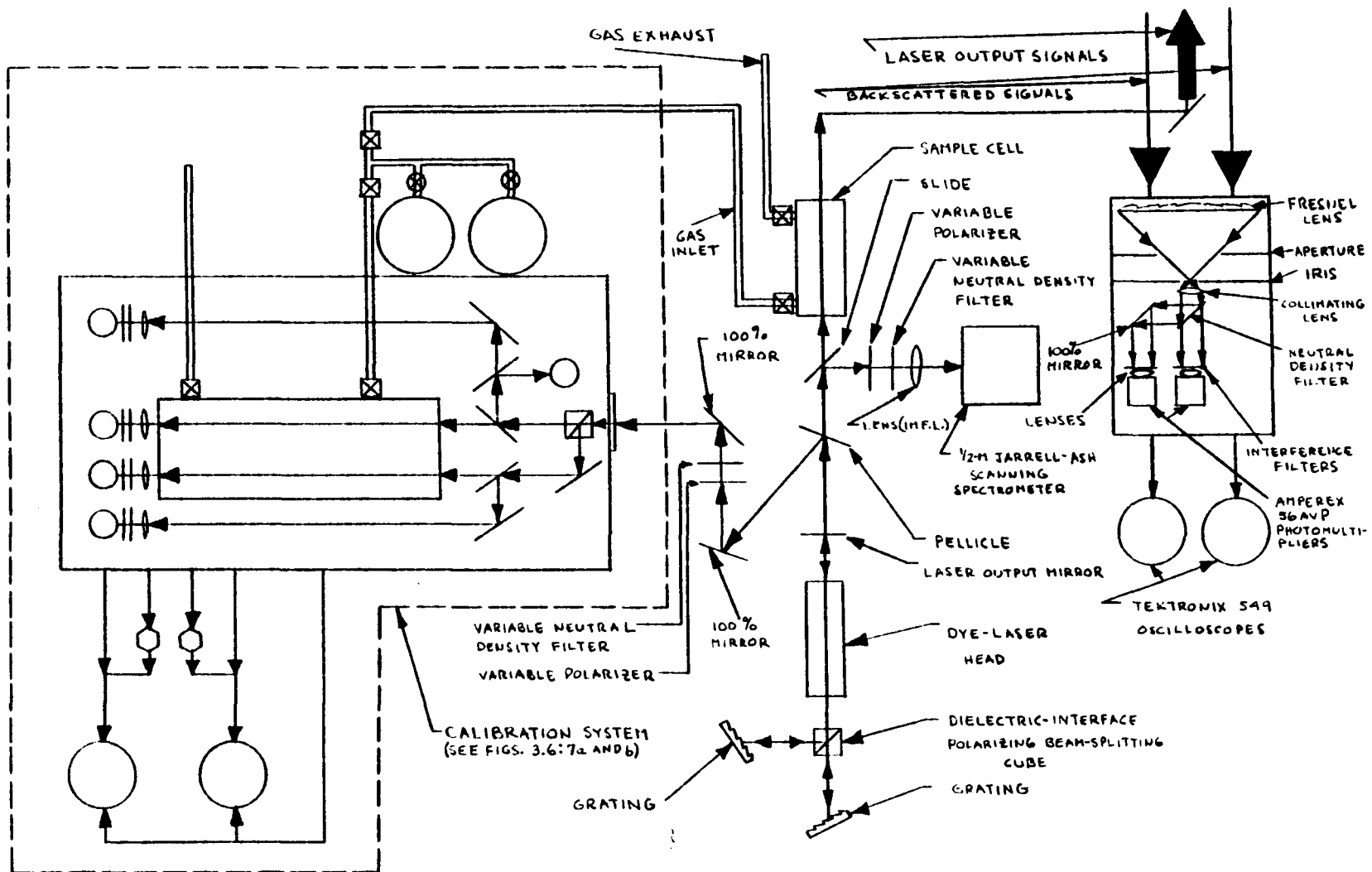


FIGURE 4.3:1 EXPERIMENTAL SETUP FOR DETERMINATION OF LIDAR-READING UNCERTAINTIES

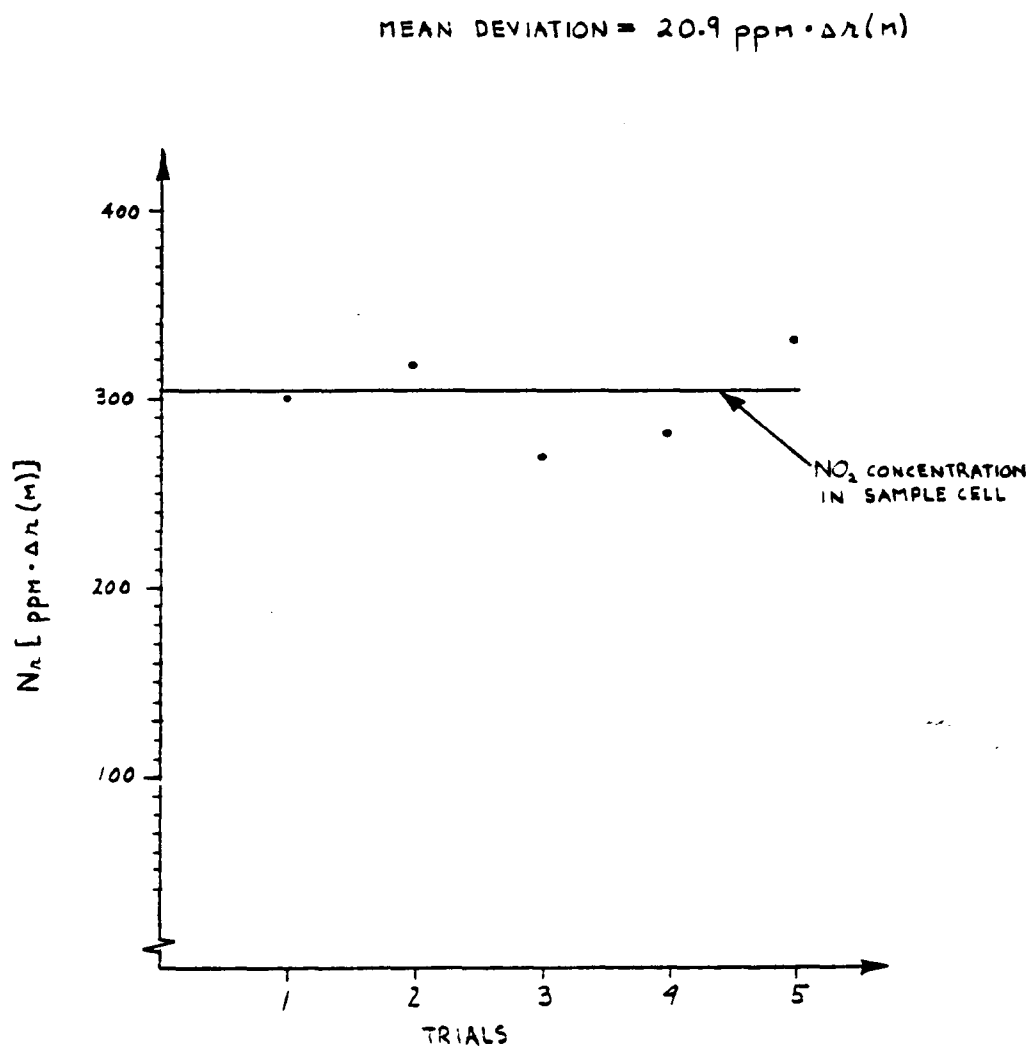


FIGURE 4.3:2 ERROR PLOT FOR DETERMINATION OF LIDAR-READING
UNCERTAINTIES

hour times and leveled off thereafter. The pollution levels calculated from the returns are typical of the levels found at intersections and avenues of heavy traffic.

An experiment was performed to obtain quantitative uncertainties associated with each pollution reading obtained in the simultaneous mode of operation. The variations in the readings obtained by the LIDAR system in monitoring the known concentration of NO_2 were primarily attributed to ambient levels of NO_2 present during the time of the experiment.

CHAPTER 5 SIMULTANEOUS MULTIWAVELENGTH OUTPUTS FROM ENERGY-TRANSFER
DYE-MIXTURE LASERS

5.1 Introduction

In a second generation LIDAR system it would be desirable to have the capability of monitoring several pollutants simultaneously. This can be accomplished by lasing simultaneously in the spectral regions necessary to monitor the pollutants of interest.

Thus, though the work being reported here centered primarily on the detection of NO_2 , an experimental program was carried out on dye mixtures for the purpose of:

Obtaining simultaneous outputs at two pairs of wavelengths, one in the 4500 \AA spectral region (for monitoring NO_2) and the other in the 6200 \AA spectral region. (The outputs in the 6200 \AA region could then be used, in conjunction with frequency doubling, for monitoring SO_2 and O_3 in the 3100 \AA spectral region.)

The program carried out was successful and simultaneous laser operation was obtained at two and even three wavelengths (in the three primary colors) for the first time.⁷⁷

To achieve these results, use was made of energy transfer processes in organic dye mixtures. Energy transfer processes in organic dyes have received some consideration in the past.⁷⁴⁻⁸⁹ The results of the experiments described below conclusively demonstrate that:

1. In a mixture of two or more dyes in a solution, excitation energy may be very efficiently transferred from an excited molecule of one species to another, and that the process may be repeated

successively to a third dye with the excitation energy being efficiently cascaded to still longer wavelengths.

2. Furthermore, simultaneous outputs at several widely separated spectral regions may be obtained from a dye-mixture laser.
3. Dye mixtures can be used to reduce the required concentration of the lasing dye, while still maintaining effective absorption of the pump source radiation. The reduced concentration of the lasing dye reduces self-absorption losses at the laser wavelengths. This in turn reduces threshold upper level population density requirements, and therefore the required pump source intensity.

A second series of experiments was carried out to define the energy transfer processes involved. Possible processes were either radiative or nonradiative resonance transfer or a combination of the two. Two experiments were devised which required only static measurements to be performed.

The next section considers the theoretical background for energy transfer processes that could occur at the concentrations found optimum for simultaneous laser action in dye-mixture lasers.

5.2 Energy Transfer Mechanisms

5.2.1 Introduction

The characteristics of a donor-acceptor system in which intermolecular energy transfer plays the dominant role are illustrated schematically in Fig. 5.2:1. There, the fluorescence emission spectrum of donor molecule D overlaps its own absorption spectrum as well as that of the

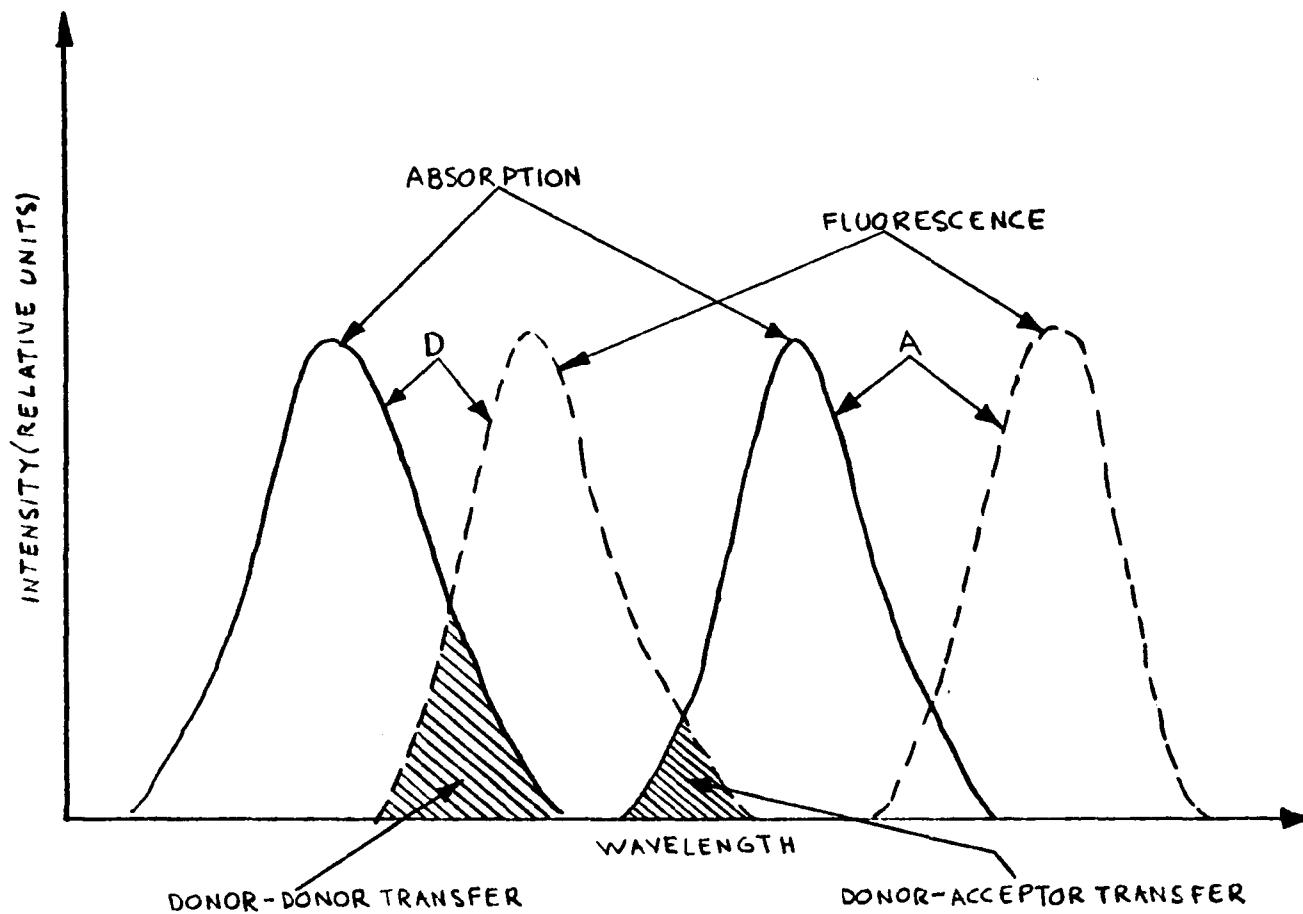


FIGURE 5.2:1 DONOR-ACCEPTOR SYSTEM OF TWO ORGANIC DYES WITH OVERLAPPING FLUORESCENCE AND ABSORPTION BANDS

acceptor molecule A. These spectra indicate an overlap in the energy manifolds of the transitions in D and the absorptive transitions in D and A, thus permitting excitation transfer from D to D and from D to A. Energy transfer along a chain of donor to donor molecules and from donor to acceptor molecules are therefore possible. It is also clear that such a process can be cascaded down through several dyes, e.g., D to A to B to C. This is shown in Fig. 5.2:2.

A second type of dye mixture in which simultaneous emission is possible is illustrated in Fig. 5.2:3. In this case the absorption bands of dyes D and A overlap, while the emission bands are widely separated. Thus, excitation of such a mixture will result in simultaneous excitation of, and emission (and possibly laser emission under the appropriate conditions) from both dyes.

The main mechanisms that can be responsible for the intermolecular energy transfer between the donor-donor pairs and donor-acceptor pair molecules are:^{76,90-92}

1. radiative transfer by means of radiation by the donor dye and reabsorption by the donor and acceptor dyes.
2. singlet-singlet nonradiative transfer between donor and donor molecules and between donor and acceptor molecules due to coulombic interactions (dipole-dipole etc.) and exchange or collision induced nonradiative decay back to 1S_0 (ground state).

5.2.2 Radiative and Nonradiative Energy Transfer

In the case of radiative transfer, excitation transfer rates are related in a relatively straightforward manner by the values of the absorp-

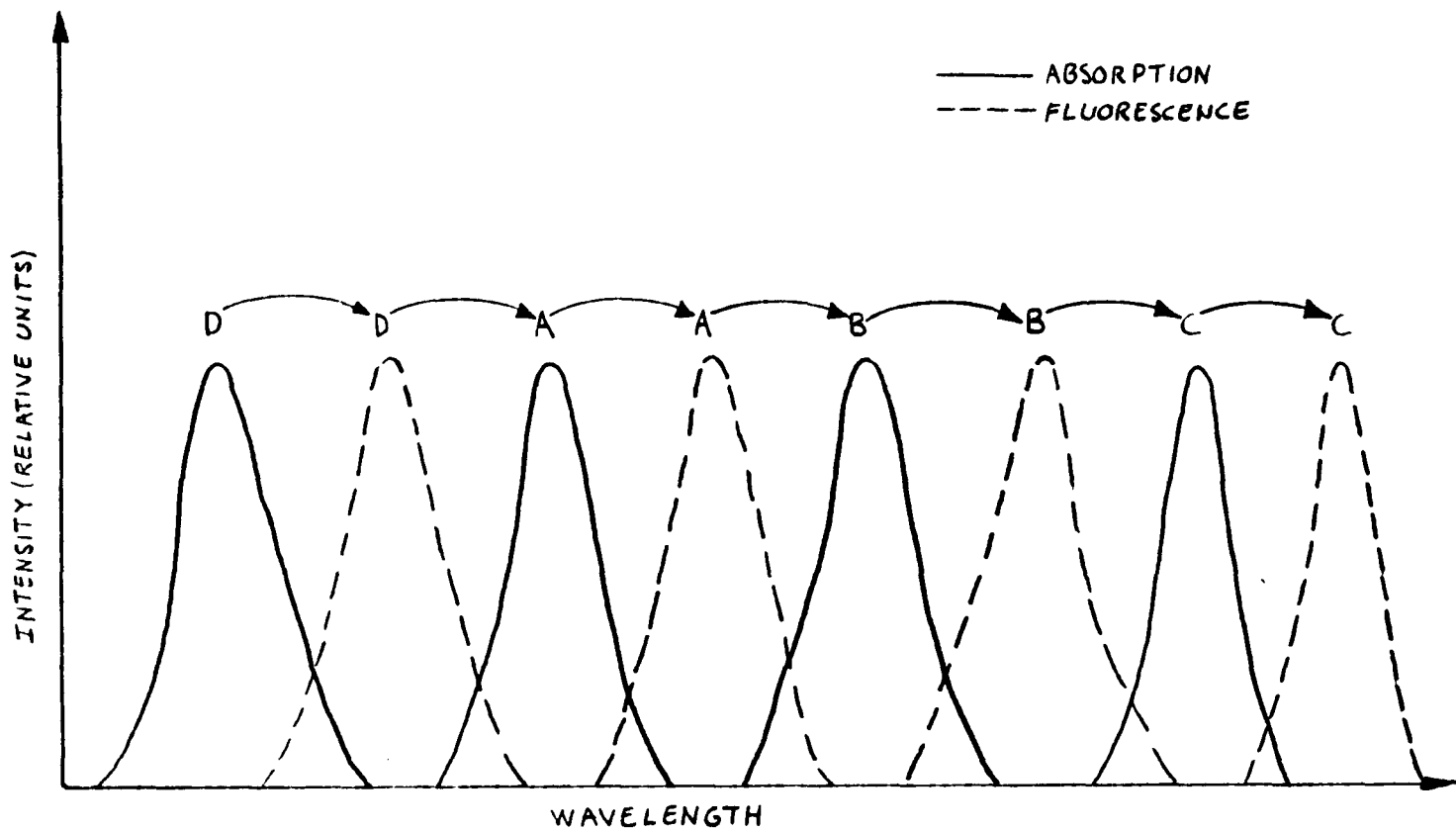


FIGURE 5.2:2 DONOR-ACCEPTOR SYSTEM OF FOUR ORGANIC DYES WITH OVERLAPPING FLUORESCENCE AND ABSORPTION BANDS

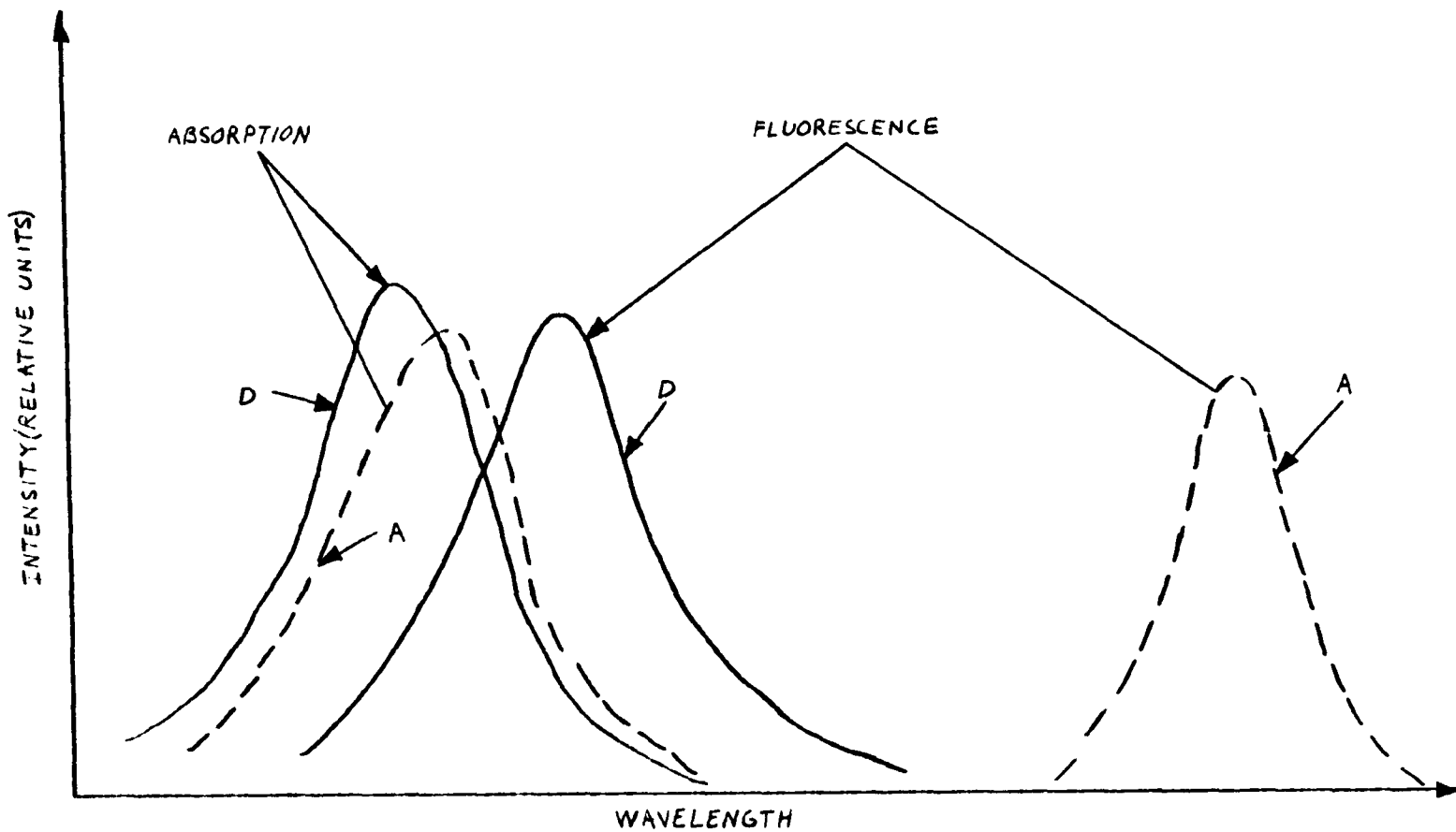


FIGURE 5.2:3 DONOR-ACCEPTOR SYSTEM WITH OVERLAPPING ABSORPTION BANDS

tion and emission cross sections of the acceptor and donor dye and their extent of overlap, and takes place over distances greater than 50 to 100 Å.

Analysis of these factors show that the probability of radiative transfer, $K_{ET}(\text{RAD})$, is given by:⁹⁰

$$K_{ET}(\text{RAD}) \approx \frac{2.303[N_A]l}{Q_D} \int_0^{\infty} f_D(\nu) E_A(\nu) d\nu, \quad (5.2:1)$$

where,

l = the specimen thickness,

f_D = the donor normalized fluorescence spectrum,

E_D = the acceptor absorption coefficient,

$[N_A]$ = the molar concentration of acceptors, and

Q = the quantum efficiency of the donor.

The mechanism of singlet state transfer of energy between donor and acceptor molecules was analyzed by Forster.⁹³ According to Forster, the probability of nonradiative transfer from a donor to an acceptor molecule is proportional to the overlap of the fluorescence band of the donor and the absorption band of the acceptor molecule. This is a resonance transfer mechanism and is illustrated in Fig. 5.2:4. Radiationless transfer due to coulombic interaction takes place over distances less than 50 to 100 Å depending upon the molecules involved in the process. The probability of nonradiative energy transfer, $K_{ET}(\text{NONRAD})$, from an excited fluorescent molecule D to an acceptor molecule A is expressed below:

$$K_{ET}(\text{NONRAD}) = \frac{1}{\tau_0} \left(\frac{R_0}{R} \right)^6, \quad (5.2:2)$$

where,

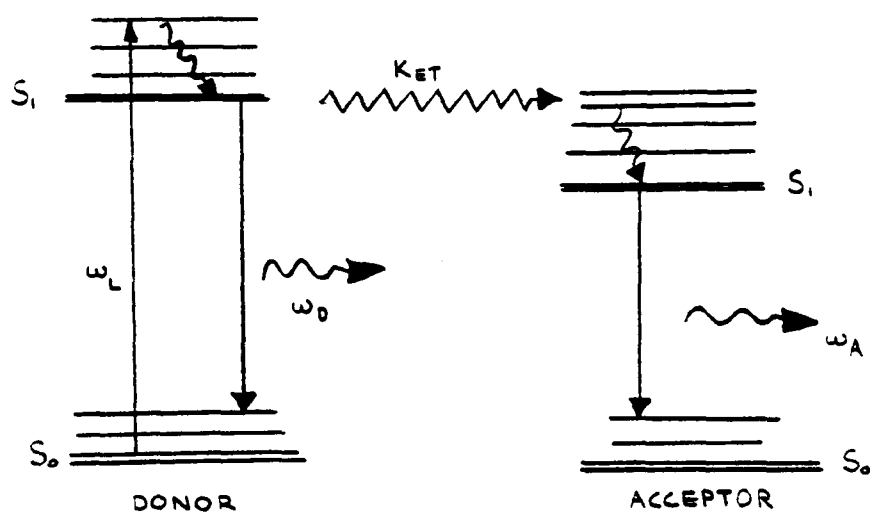


FIGURE 5.2:4 DONOR AND ACCEPTOR ENERGY LEVELS

$$R_0^6 = \frac{(9000 \ln 10) \chi^2}{128(\pi^5)(n^4)N} \int_0^\infty f_D(\nu) E_A(\nu) d\nu, \quad (5.2:3)$$

where,

τ_0 = the fluorescence lifetime of isolated donors,

R = the distance between D and A,

n = the refractive index,

f_D = the normalized fluorescence intensity of D,

E_A = the absorption coefficient of A,

χ = a geometrical factor ($\langle \chi^2 \rangle = 2/3$), and

R_0 = the critical transfer distance at which there is equal probability of radiative or nonradiative resonance transfer to occur.

5.3 Multiwavelength Laser Action in Dye Mixtures--Experimental Results

In the first series of experiments carried out, dye mixtures were chosen from which simultaneous laser outputs at useful spectral combinations could be obtained. 7-diethylamino-4 methyl coumarine, Acriflavine, and Rhodamine B constituted a mixture from which dye laser outputs could be obtained at the three primary colors.⁷⁷

Fig. 5.3:1 shows the absorption and fluorescence spectra of these three dyes. The absorption bands of Acriflavine and Rhodamine are seen to overlap the fluorescence bands of the Coumarine and the Acriflavine respectively. This overlap in the energy gaps of these dyes would permit, in principle, excitation energy transfer from Coumarine to the Acriflavine and from the Acriflavine to Rhodamine B either by radiative or nonradiative resonance transfer.

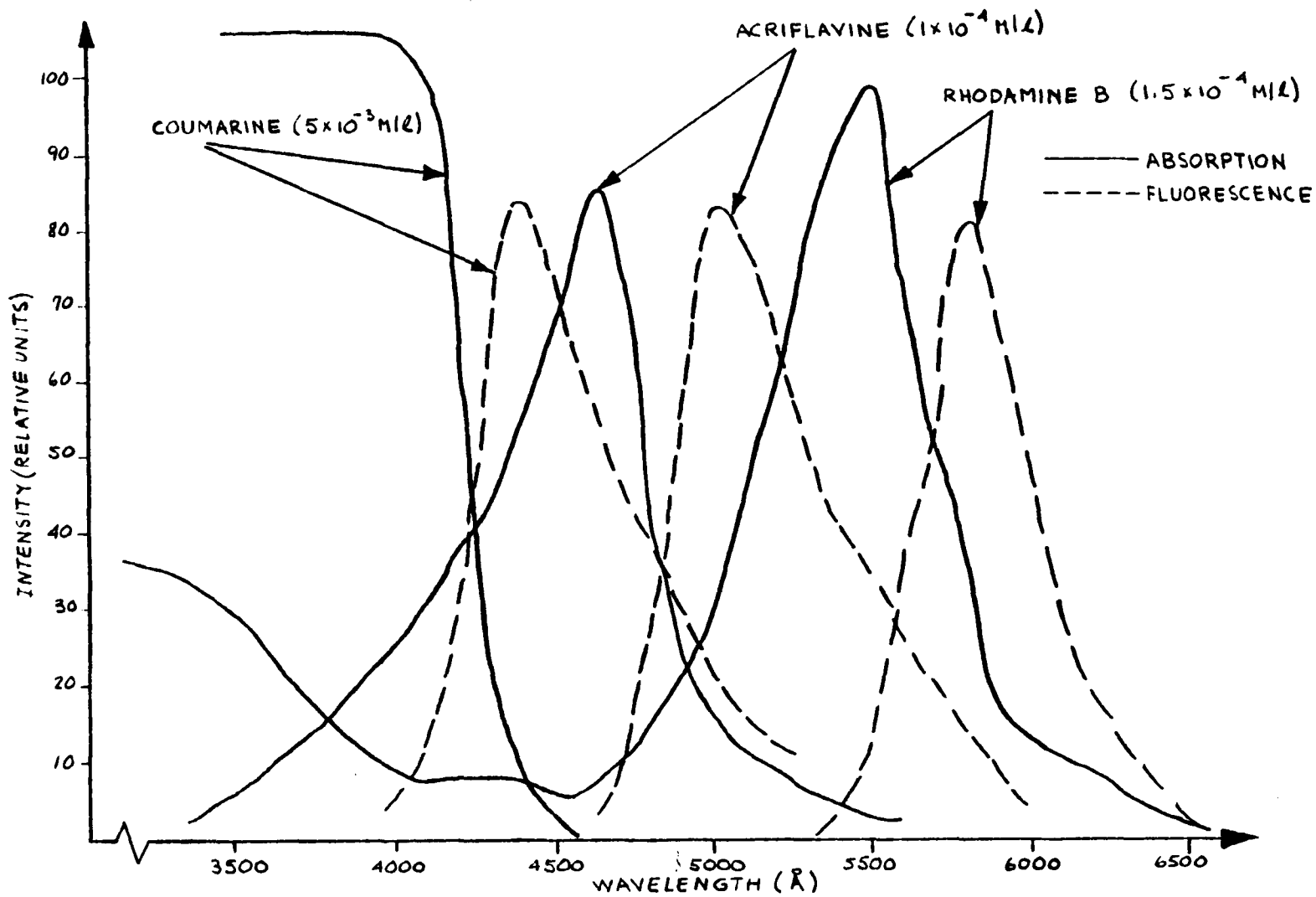


FIGURE 5.3:1 ABSORPTION AND FLUORESCENCE SPECTRA OF THE THREE DYES AT OPTIMUM CONCENTRATIONS FROM WHICH SIMULTANEOUS LASER OUTPUTS WERE OBTAINED IN THE THREE PRIMARY COLORS

It was therefore possible to use the 3371 \AA output of an N_2 laser to excite the Coumarine dye and obtain excitation transfer to, and simultaneous emission (including laser emission) from, all three dyes in a mixture with appropriate concentration ratios.

Fig. 5.3:2 shows the absorption and fluorescence spectrum of this three-dye mixture at concentrations found optimum for three-color laser operation. The absorption curve shown is for a 1.0 mm optical path length, and ethanol was the solvent used. Excitation for the front surface fluorescence measurements depicted in Fig. 5.3:2 was by means of the 3650 \AA output obtained from an Hg discharge lamp. This is absorbed by the Coumarine, which transfers excitation to the Acridine, which in turn transfers excitation to the Rhodamine B. Fig. 5.3:3 shows the experimental setup used to obtain the absorption and emission curves of the dyes.

The different concentrations used for each of the three dyes arises from the fact that the excitation source for laser action in the dye mixture was the 200-kw 30-ns 1-HZ N_2 laser output at 3371 \AA . The absorption of this pump light was therefore predominantly by the Coumarine dye, hence its large concentration requirements relative to the other two dyes. Thus, in this case, the type of dye mixture used would be a combination of the types depicted in Figs. 5.2:1, 2, and 3. With this three dye mixture, laser action was obtained simultaneously at three wavelengths centered at 4400 \AA , 4900 \AA , and 6200 \AA . These outputs could be individually tuned over a range of approximately 15 \AA , as shown in Fig. 5.3:3.

That excitation transfer is the predominant mechanism for exciting

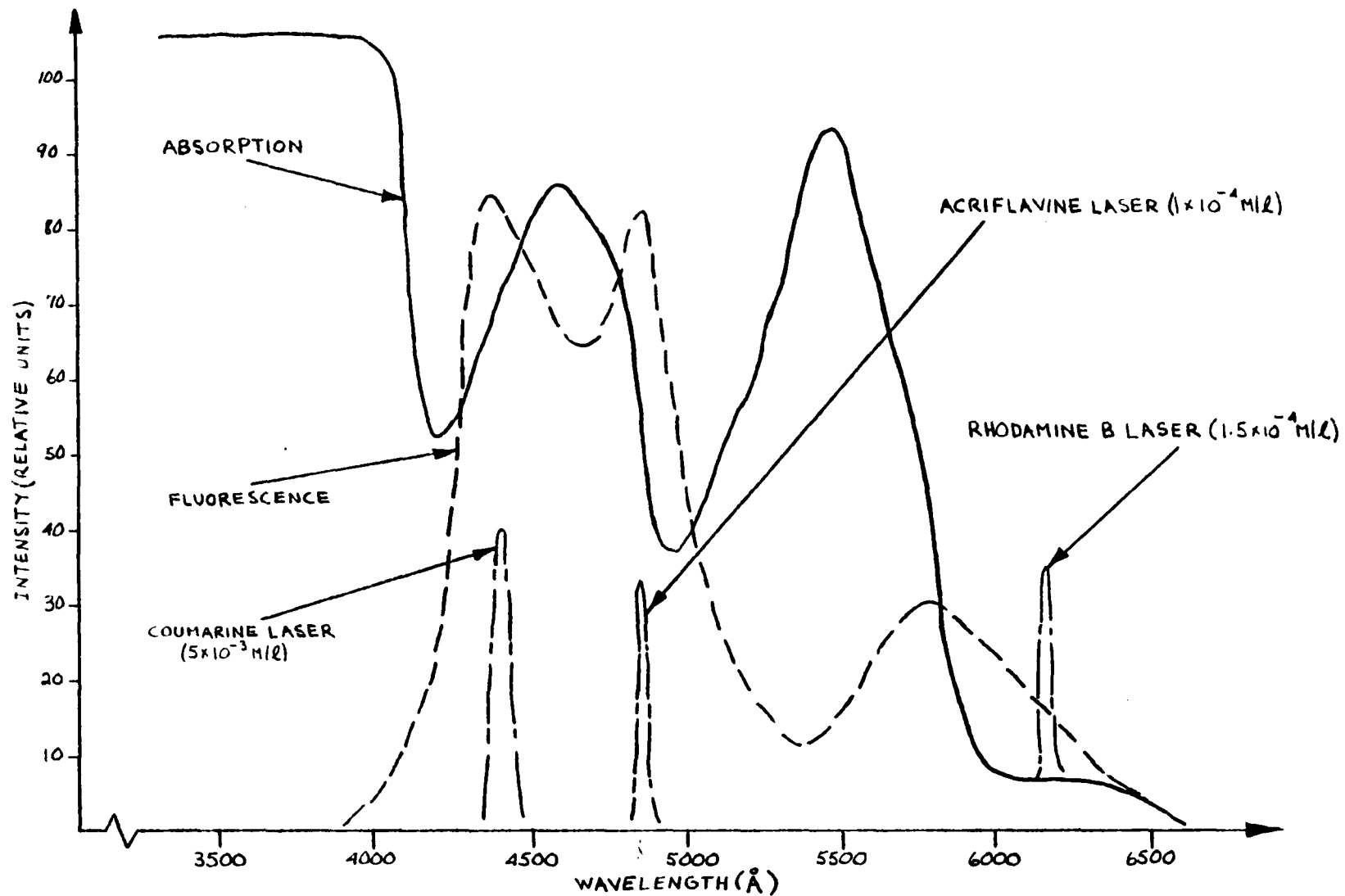


FIGURE 5.3:2 ABSORPTION AND FLUORESCENCE SPECTRA OF THE THREE-DYE MIXTURE AT OPTIMUM CONCENTRATIONS FROM WHICH SIMULTANEOUS LASER OUTPUTS WERE OBTAINED IN THE THREE PRIMARY COLORS

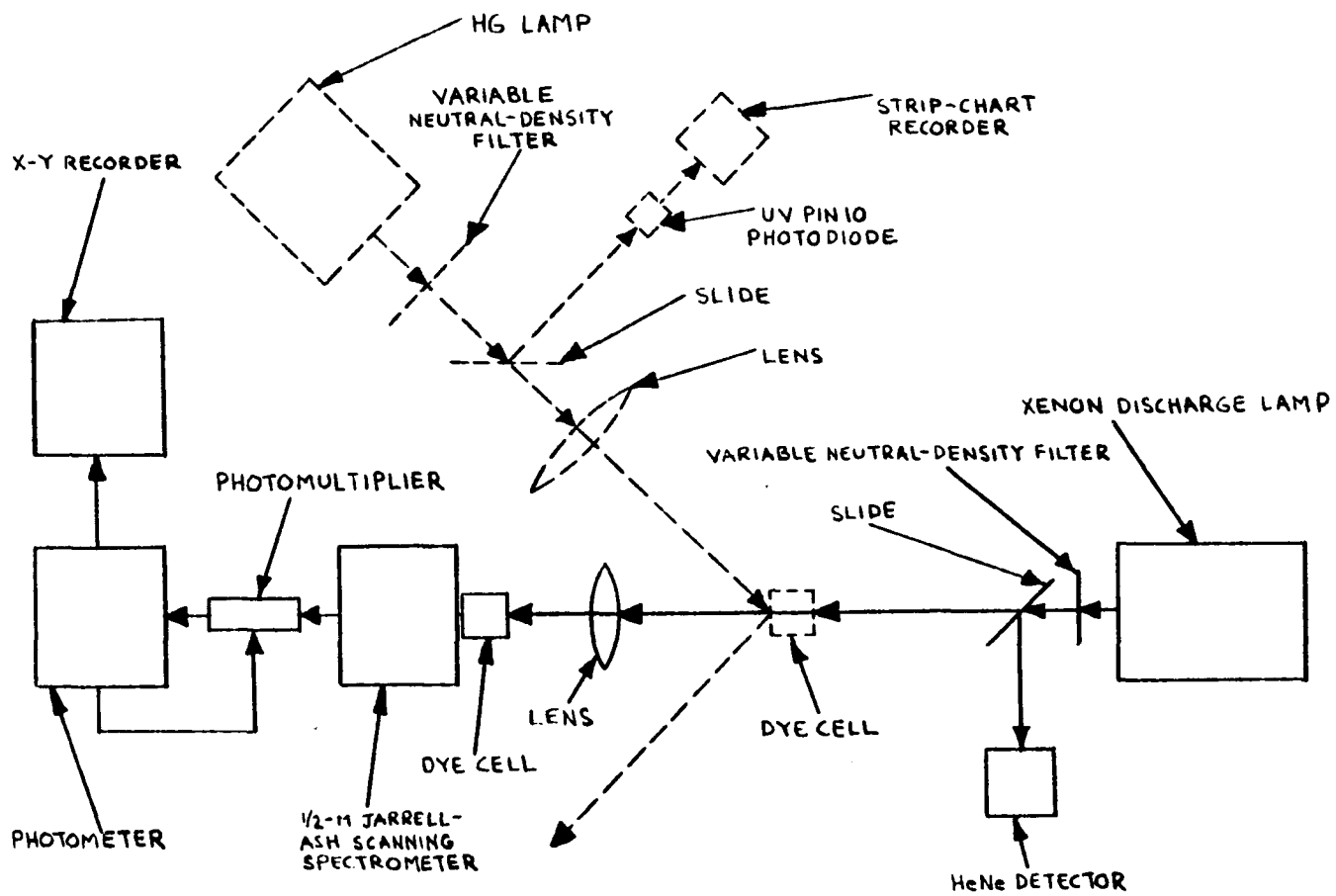


FIGURE 5.3:3 EXPERIMENTAL SETUP FOR OBTAINING FLUORESCENCE AND ABSORPTION SPECTRA

laser action in the Acriflavine and Rhodamine B is confirmed by the fact that it was not possible to obtain laser action from Acriflavine alone, at any concentration, using the 3371 Å N₂ laser output for excitation, while laser action by direct excitation at 3371 Å of Rhodamine B alone was found to require an order of magnitude higher concentration of Rhodamine B with the same optical arrangement used. See Fig. 5.3:4.

For two-wavelength operation in the 4500 Å and 6200 Å region, the concentration of the center dye, Acriflavine, was reduced, and that of the Rhodamine B increased. This resulted in effective laser operation at the desired spectral regions. Fig. 5.3:5 shows the spectrum of the dye mixture for two-wavelength operation. An optical arrangement suitable for getting simultaneous laser action at two pairs of wavelengths in each of the spectral regions of interest is shown in Fig. 5.3:6.

By comparing the fluorescence quantum yield for each of the three dyes alone with the fluorescence quantum yield for the dye mixtures, it was found that the fluorescence quantum yield for the single-step transfer process, Coumarine to Acriflavine, was approximately 90 percent. The yield for the two-step transfer process, Coumarine to Acriflavine to Rhodamine B, was approximately 80 percent.

5.4 Energy Transfer Mechanisms--Experimental Results

5.4.1 Radiative Energy Transfer

If energy transfer were predominantly a radiative process at the concentrations required for simultaneous laser action, the energy

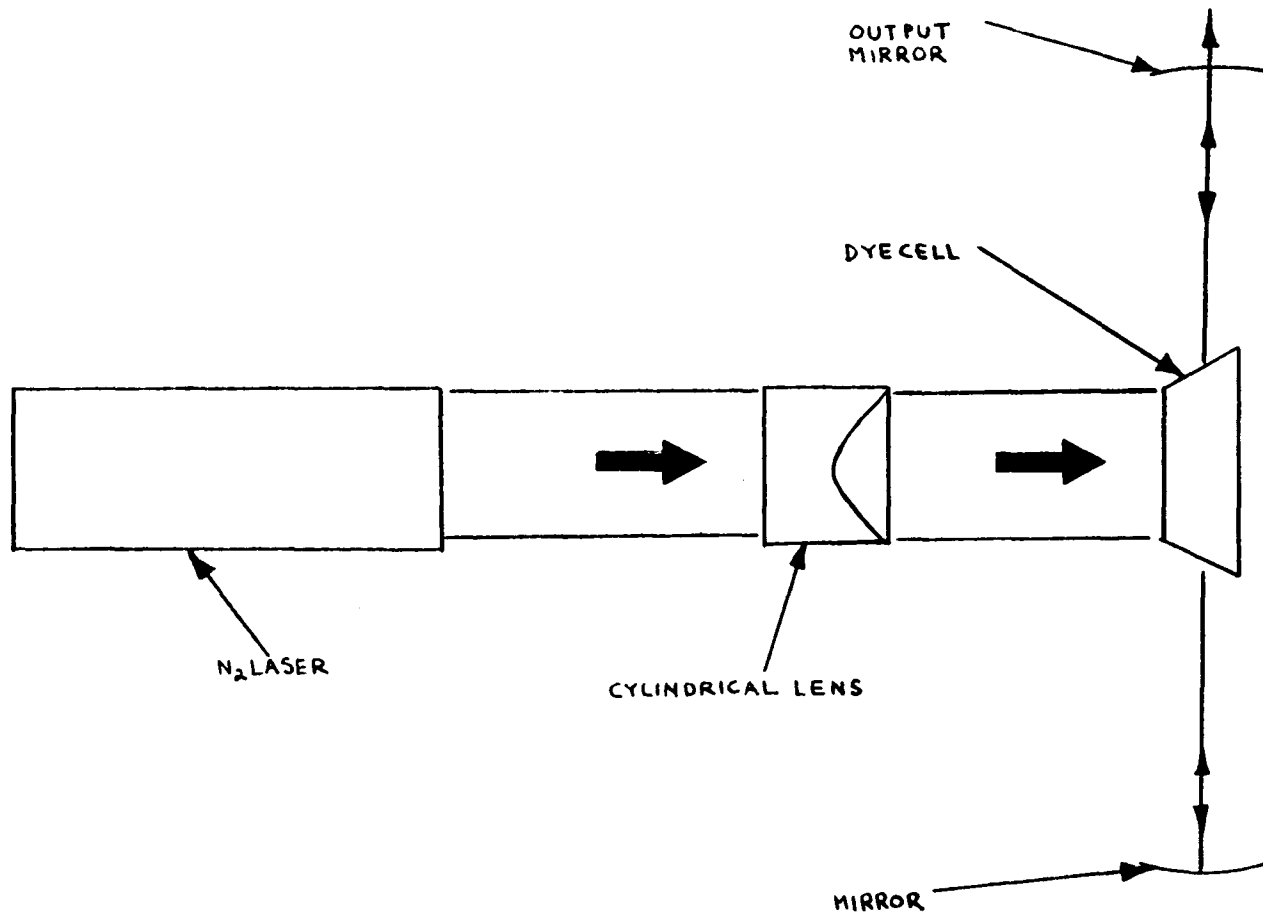


FIGURE 5.3:4 OPTICAL ARRANGEMENT FOR OBTAINING SIMULTANEOUS THREE-COLOR OUTPUTS IN THE THREE PRIMARY COLORS

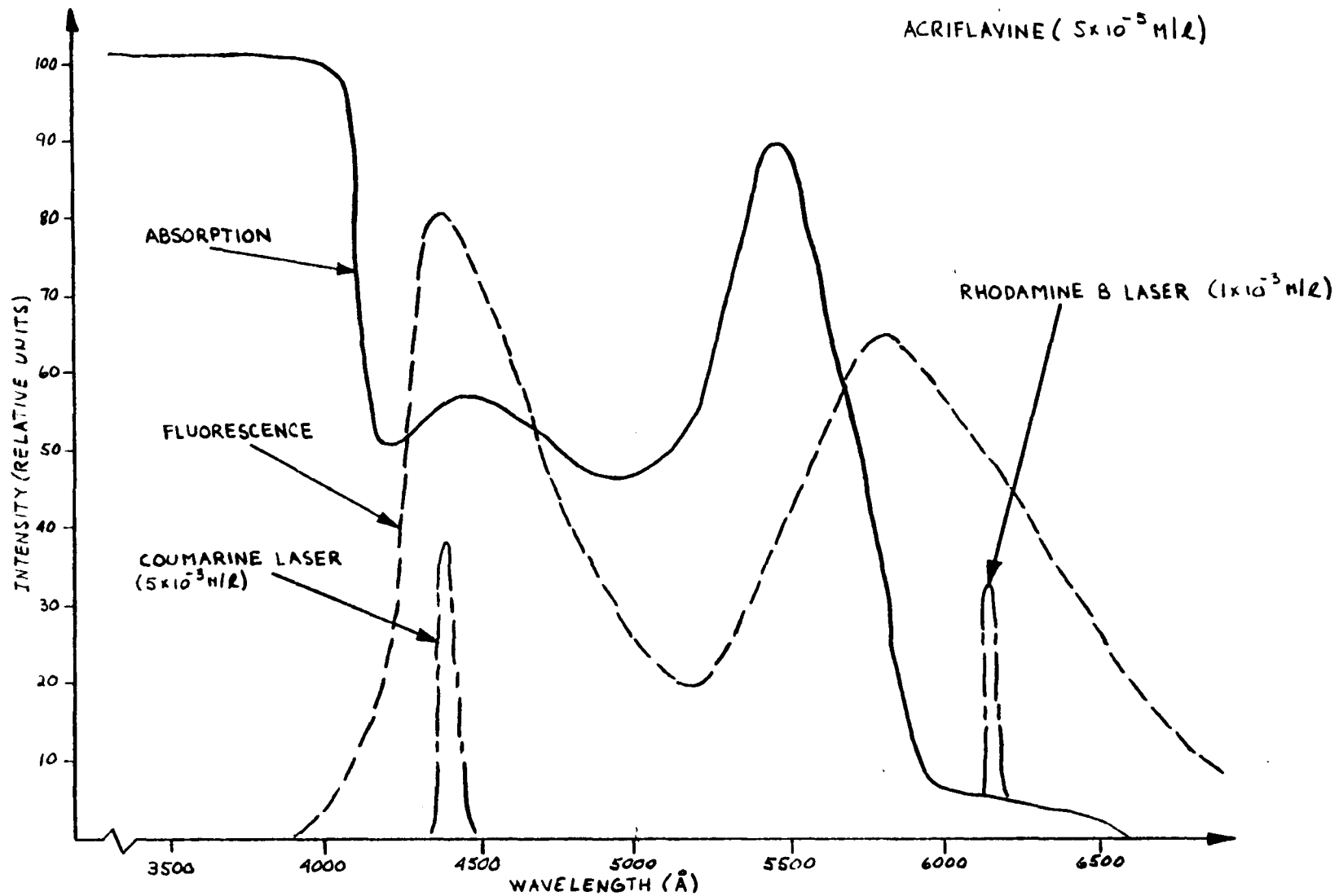


FIGURE 5.3:5 ABSORPTION AND FLUORESCENCE SPECTRA FOR SIMULTANEOUS TWO-WAVELENGTH OUTPUT

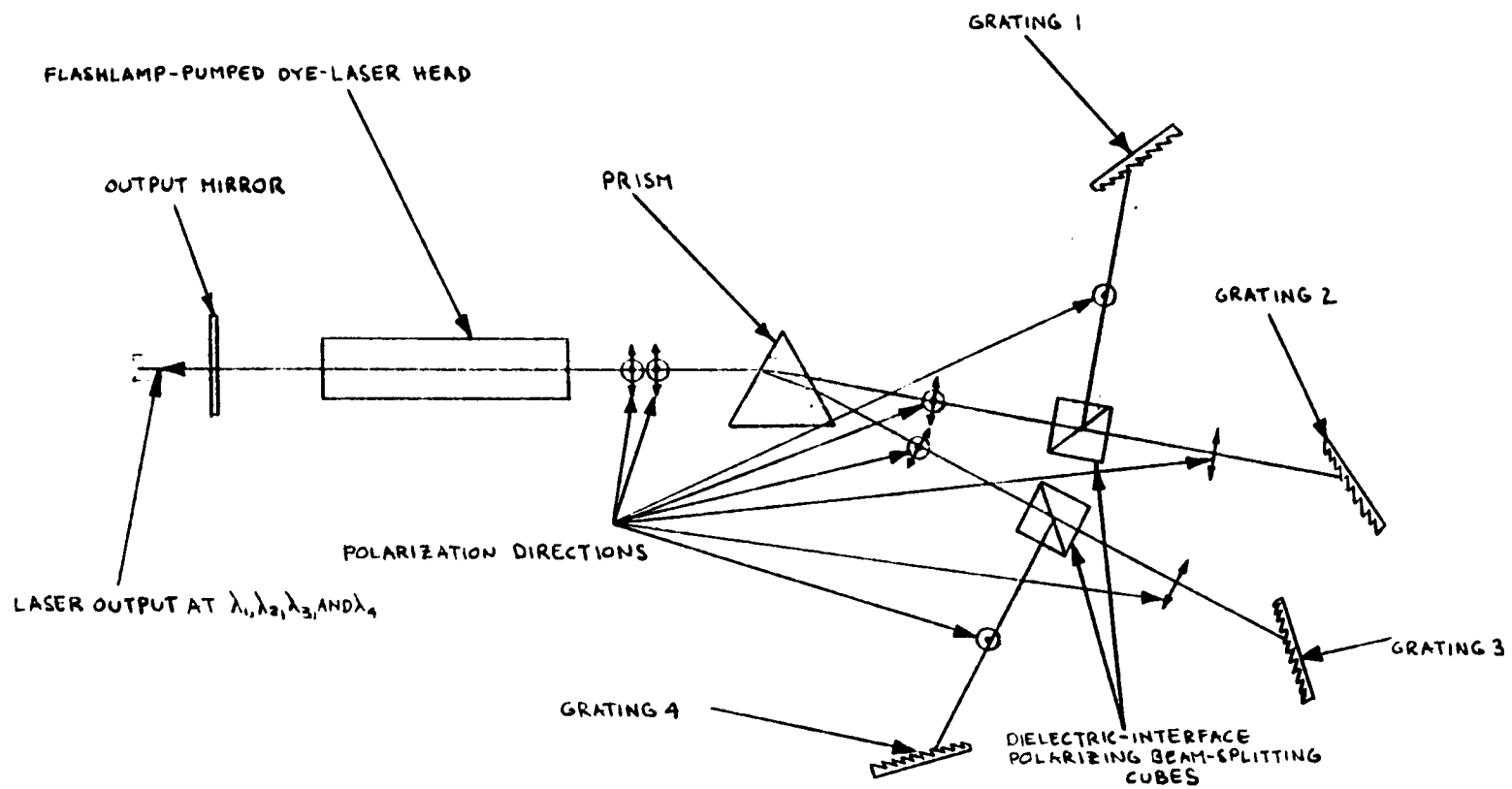


FIGURE 5.3:6 OPTICAL ARRANGEMENT FOR OBTAINING TWO PAIRS OF WAVELENGTHS SIMULTANEOUSLY

transfer rate would be given by Eq. 5.2:1. The energy transfer rate from D to A would be directly proportional to the overlap integral, P, as defined in Eq. 5.2:1. Thus, the emission from the acceptor molecules, A, would be proportional to the product of the quantum efficiency of A and the overlap integral P.

Two pairs of dyes were chosen such that the absorption spectrum of each acceptor dye overlapped the fluorescence spectrum of the same donor dye differently. Relative measurements were made to determine the dominant mechanism for energy transfer in the following manner:

$$\frac{P_1 n_{Q1}}{P_2 n_{Q2}} = \frac{\text{Fluorescence of } A_1 \text{ in mixture 1}}{\text{fluorescence of } A_2 \text{ in mixture 2}}, \quad (5.4:1)$$

where,

A_1 = acceptor dye #1,

A_2 = acceptor dye #2,

$P_{1,2}$ = the overlap integrals of the fluorescence spectrum of donor dye, D, with the absorption spectrum of acceptor dye, $A_{1,2}$, and

$n_{Q1,2}$ = the quantum efficiencies of the acceptor dyes $A_{1,2}$.

If Eq. 5.4:1 holds, it can then be concluded that the dominant mechanism for energy transfer is by the radiative process.

In the experiments performed, Dichlorofluorescein was chosen as the donor, and Rhodamine B and DODC as acceptors. Ethanol was used as the solvent. The exciting line was the 4880 Å output of an argon-ion laser which excited the donor alone. Fig. 5.4:1 shows the experimental set-up used to determine the absorption and front fluorescence spectra of the dyes. The experiment was run with both dyes in both mixtures at

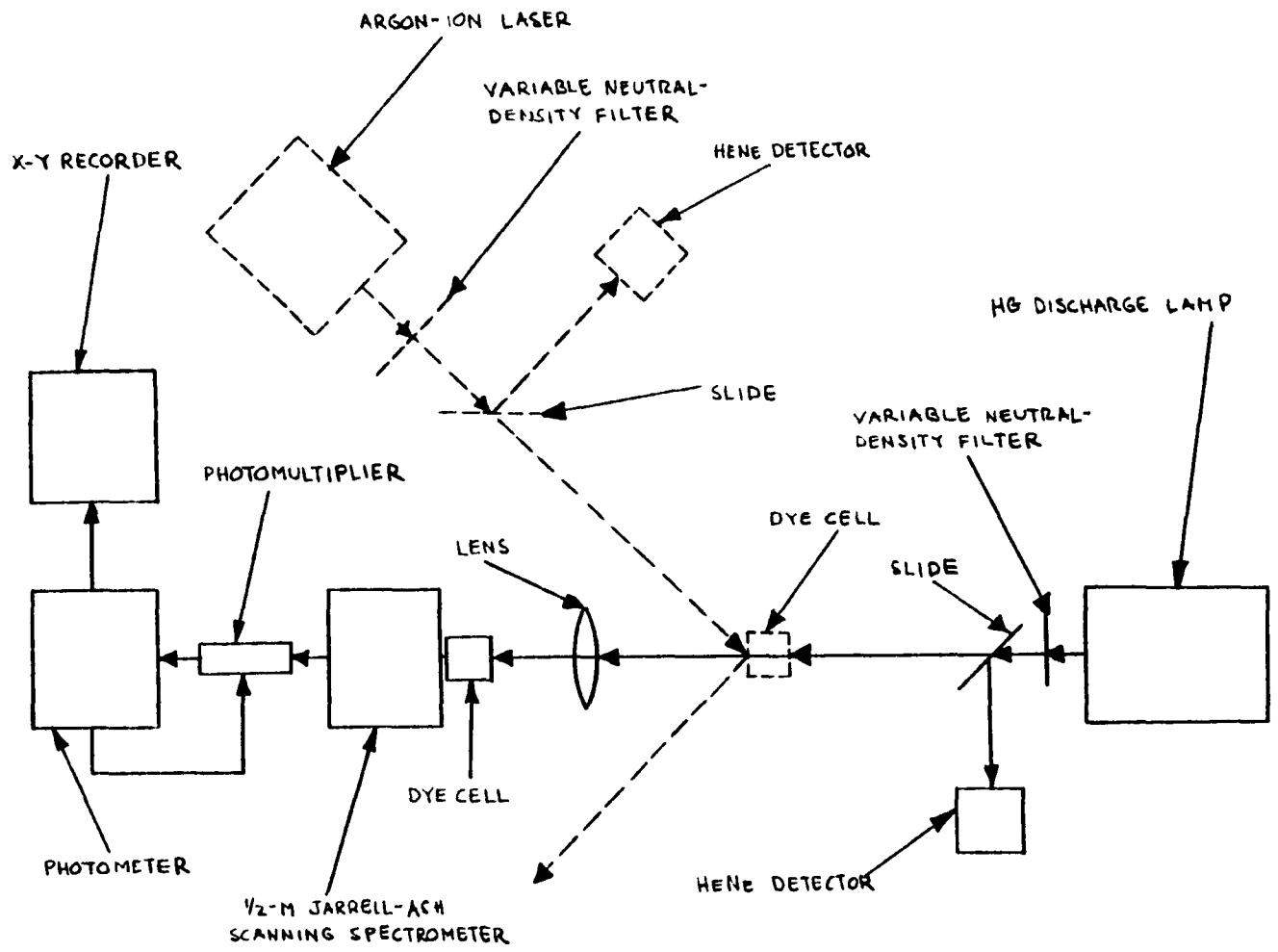


FIGURE 5.4:1 EXPERIMENTAL SETUP FOR OBTAINING FLUORESCENCE AND ABSORPTION SPECTRA

the same concentration. The first mixture consisted of Dichlorofluorescein (2×10^{-2} M/l), donor, and DODC (5.52×10^{-5}), acceptor, in ethanol. The second mixture consisted of Dichlorofluorescein (2×10^{-2} M/l), donor, and Rhodamine B (5.52×10^{-5} M/l) in ethanol.

Figs. 5.4:2 and 3 show the absorption and fluorescence spectra and the overlap integrals of Dichlorofluorescein with DODC and Dichlorofluorescein with Rhodamine B in the concentrations stated above. Figs. 5.4:4 and 5 show the fluorescence spectra of DODC and Rhodamine B in the appropriate mixtures respectively.

Inserting the appropriate terms into Eq. 5.4:1 yields:

$$1.00 \approx 0.92 \quad (5.4:2)$$

This result confirms the fact that, at the concentrations needed for lasing, radiative transfer plays the dominant role in the mixtures used.

5.4.2 Nonradiative Energy Transfer

The next experiment performed was designed to determine at what concentration of donor molecules nonradiative resonance energy transfer would initiate. Energy transfer in dye mixtures takes place at various concentrations of donor and acceptor dyes.

If the acceptor concentration were kept constant and the donor concentration increased--or equivalently the mean distance between acceptor-acceptor, \bar{R}_a , kept constant, between donor-donor, \bar{R}_d , and between donor-acceptor, \bar{R} , varied--there would be a donor concentration reached at which nonradiative energy transfer would initiate. This would be noted by an increase in the normalized fluorescence yield of the ac-

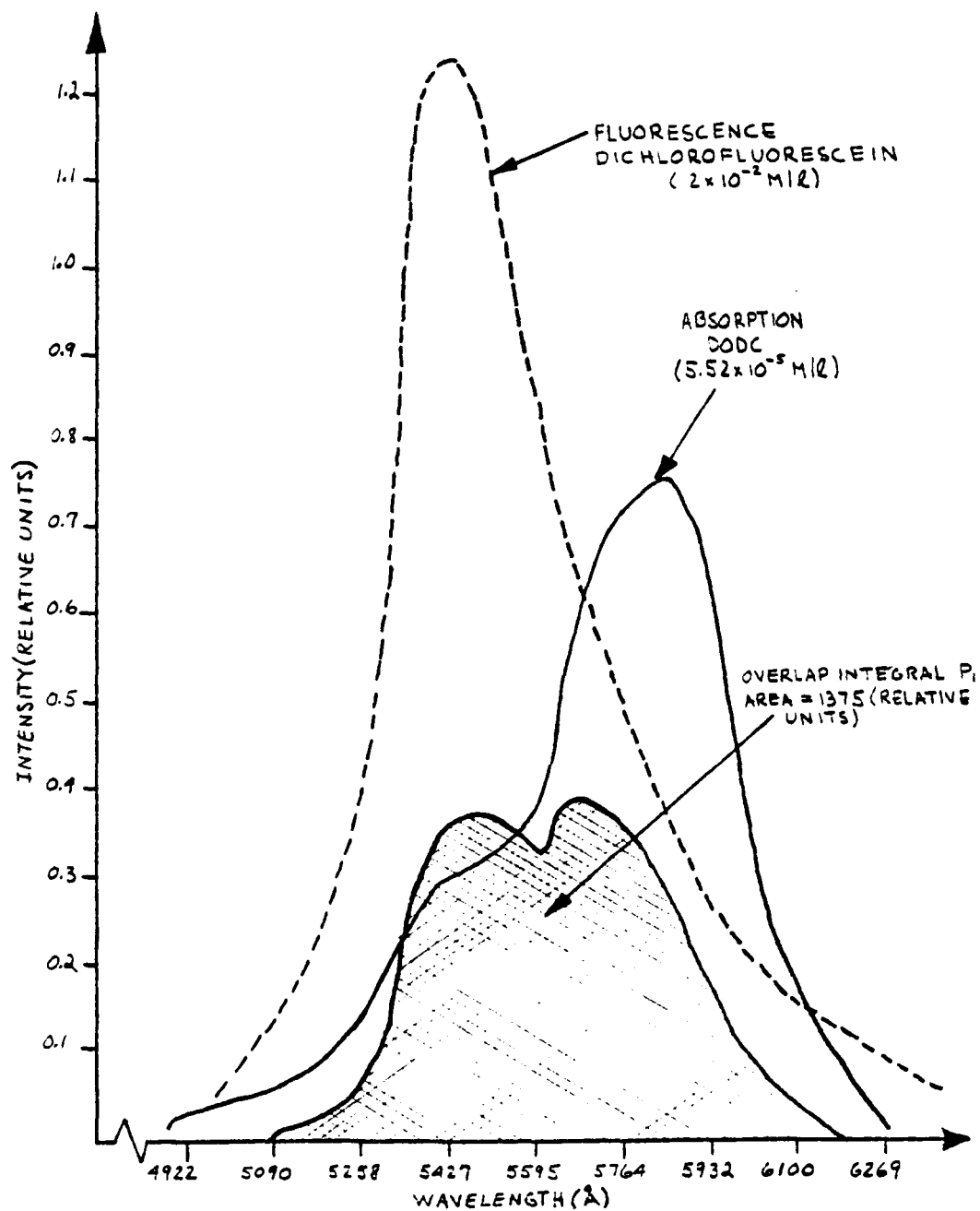


FIGURE 5.4:2 OVERLAP INTEGRAL OF DICHLOROFLORESCEIN (DONOR) AND DODC (ACCEPTOR)

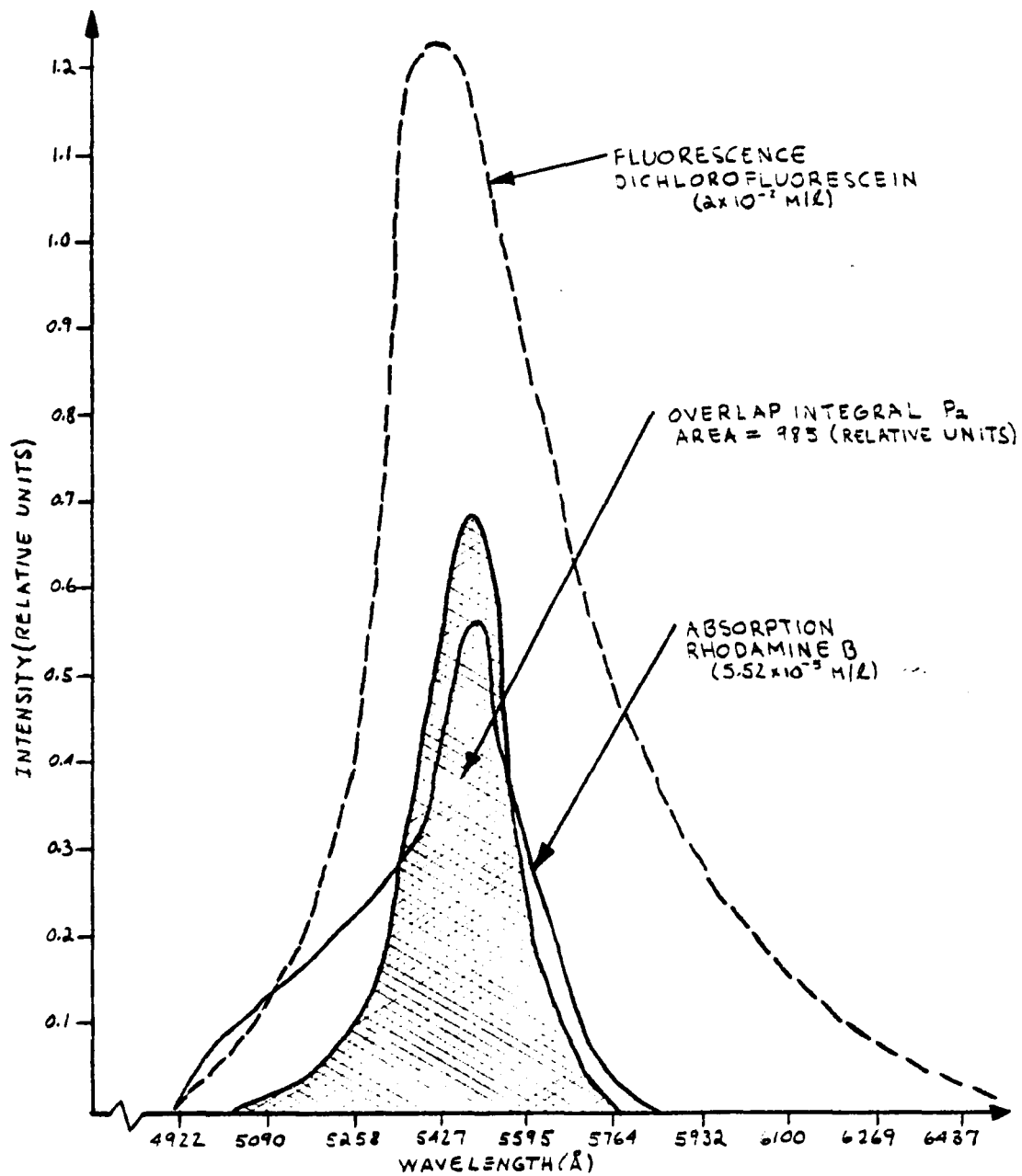


FIGURE 5.4:3 OVERLAP INTEGRAL OF DICHLOROFLUORESCEIN (DONOR) AND RHODAMINE B (ACCEPTOR)

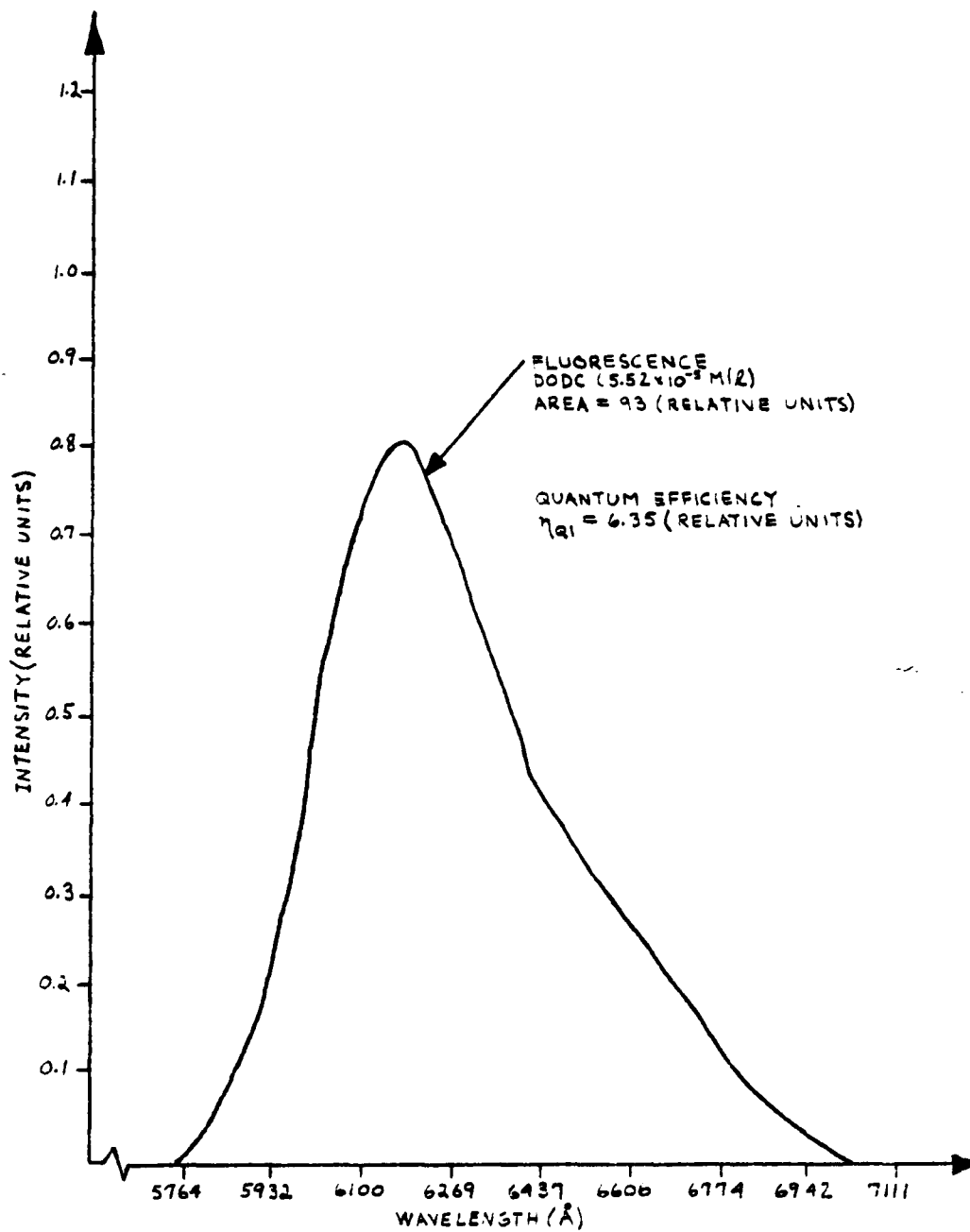


FIGURE 5.4:4 FLUORESCENCE QUANTUM YIELD OF DODC IN THE MIXTURE WITH
DICHLOROFLOURESCIEIN

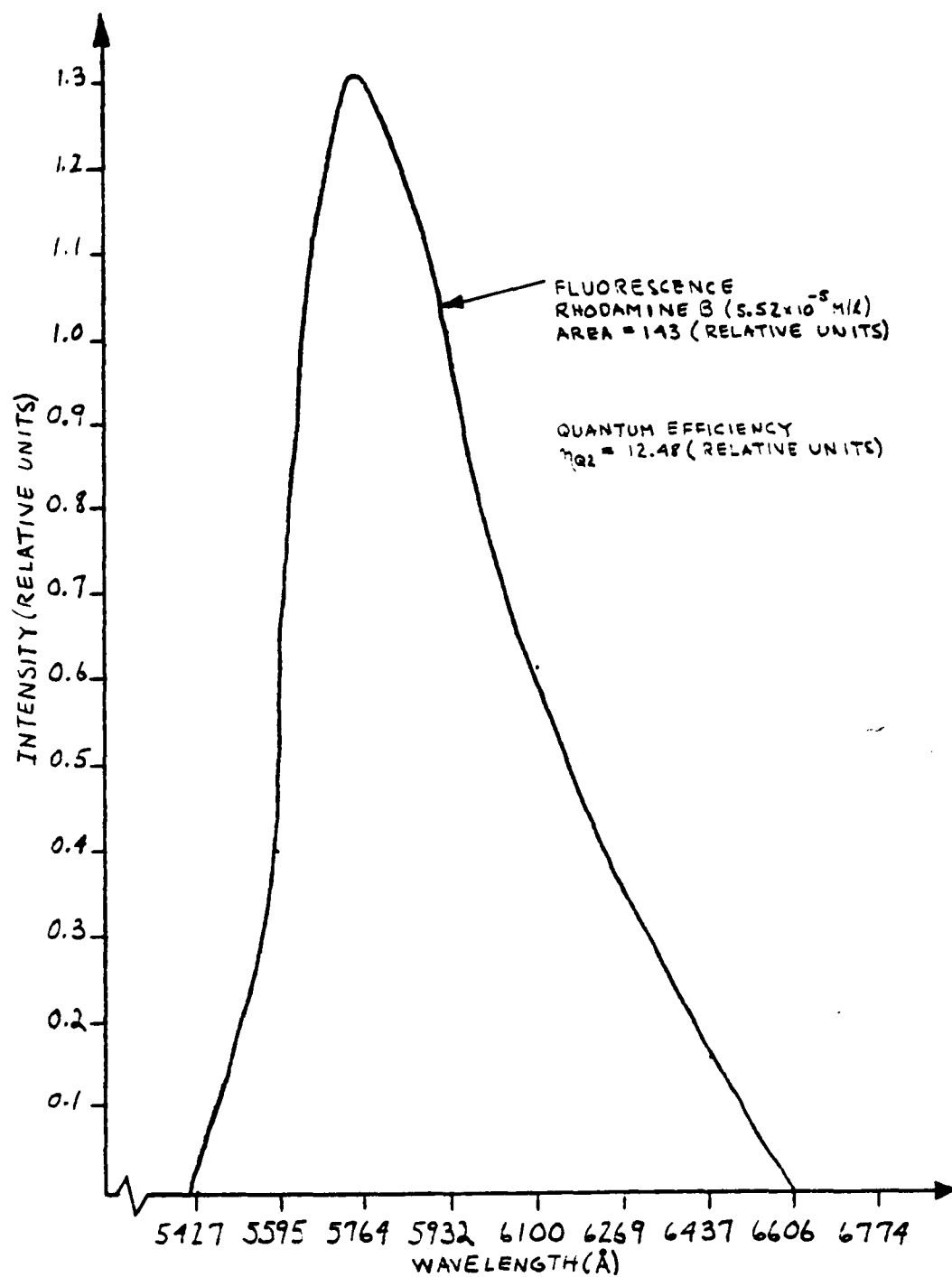


FIGURE 5.4:5 FLUORESCENCE QUANTUM YIELD OF RHODAMINE B IN THE MIXTURE WITH DICHLOROFLOURESCEIN

ceptor relative to the fluorescence of the donor in the same mixture. Before this critical concentration, energy transfer would take place by the radiative process. The emission of the donor would be partially absorbed by the acceptor. As the donor concentration is increased and the mean distance between donors decreases (along with a decrease in donor-acceptor distance), a point will be reached at which the energy transfer flow would take place from donor to donor to donor to... to acceptor. This "hopping" phenomenon is observed during the process of photosynthesis but at concentrations much higher than those used in dye-mixture lasers.

Two organic dyes were chosen such that the fluorescence band of the donor overlapped the absorption band of the acceptor, and that the acceptor would not absorb at the pump wavelength. 7-diethylamino-4-methyl coumarine and DODC were chosen as the donor and acceptor dyes respectively. Ethanol was used as the solvent throughout. The acceptor concentration was kept constant at 1×10^{-4} M/l ($\bar{R} = 158 \text{ \AA}$), while the donor concentration varied from 1×10^{-4} M/l ($\bar{R} = 158 \text{ \AA}$, $\bar{R} = 126 \text{ \AA}$) to 5×10^{-2} M/l ($\bar{R} = 20 \text{ \AA}$, $\bar{R} = 20 \text{ \AA}$). Fluorescence curves were obtained for the pure donor, and the donor and acceptor in the same mixture. The experimental setup used to obtain the fluorescence curves is shown in Fig. 5.4:6. The pump light, 3700 \AA and 50 \AA bandwidth, was obtained from a xenon-lamp 1/4-m Jarrell-Ash monochrometer combination. The output of the monochrometer went through a variable neutral density filter and was then focused onto a 1 cm quartz cell containing the dye solutions. The cell was pointed at such an angle that the reflection of the pump light from the front surface of the cell would not be picked up by the detection system. The detection system used to monitor the

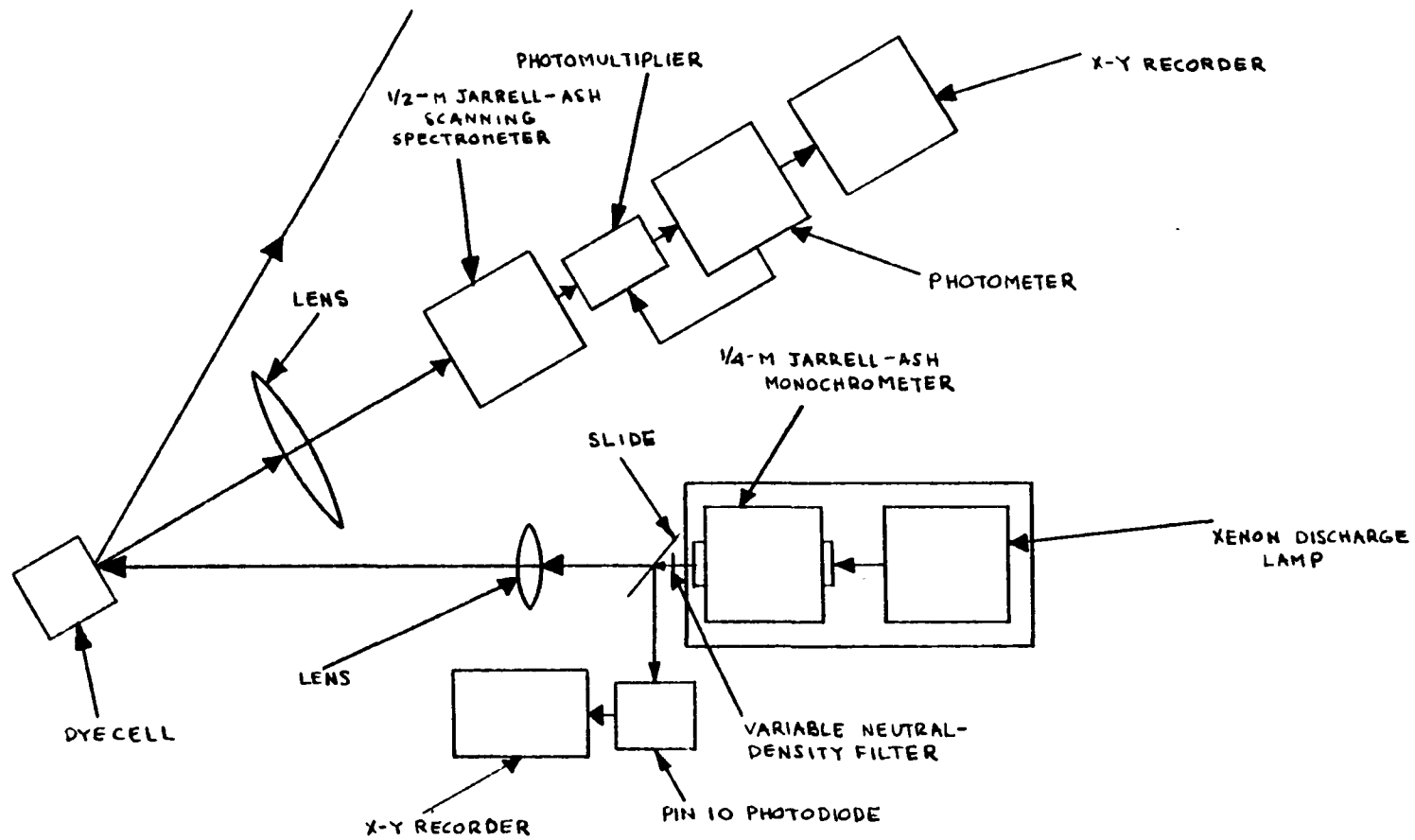


FIGURE 5.4:6 EXPERIMENTAL SETUP FOR OBTAINING FLUORESCENCE SPECTRA

front surface fluorescence of the mixtures consisted of a 1/2-m Jarrell-Ash scanning spectrometer whose light output was detected by an RCA 6217 photomultiplier. The output of the photomultiplier went to a photometer, the output of which went to an x-y recorder.

The results of the experiment are shown in Figs. 5.4:7 through 11. Fig. 5.4:7 shows the effect of concentration quenching of pure solutions of the donor dye, 7-diethylamino-4 methyl coumarine.^{90,94} Fig. 5.4:8 shows the quantum yield of the donor in mixtures with the acceptor dye, DODC. The slope in Fig. 5.4:8 is steeper than in Fig. 5.4:7 indicating energy transfer to the acceptor.^{90,94} For dilute concentrations of the donor, the energy transfer is due to the radiative process.⁹⁰ This can be seen in Fig. 5.4:11, which is the quantum yield of the acceptor dye normalized with respect to the fluorescence of donor dye in the same mixtures. The flat portion of the curve extending from donor concentration of 1×10^{-4} M/l to 2×10^{-3} M/l is due predominantly to the radiative process. As the donor-donor distance decreases still further there is an increase in the relative quantum yield of the acceptor. If the radiative process were the dominant energy transfer mechanism in this region, 2×10^{-3} M/l to 5×10^{-2} M/l, the curve would have remained flat. The increase in the quantum yield starting at 2×10^{-3} M/l is therefore due to the nonradiative process. At the donor concentration of 5×10^{-2} M/l the nonradiative process is the dominant energy transfer mechanism.

Hence, the dominant energy transfer mechanisms found for various regions of donor-donor concentrations are as follows:

1. radiative transfer for the region extending from 1×10^{-4} M/l to

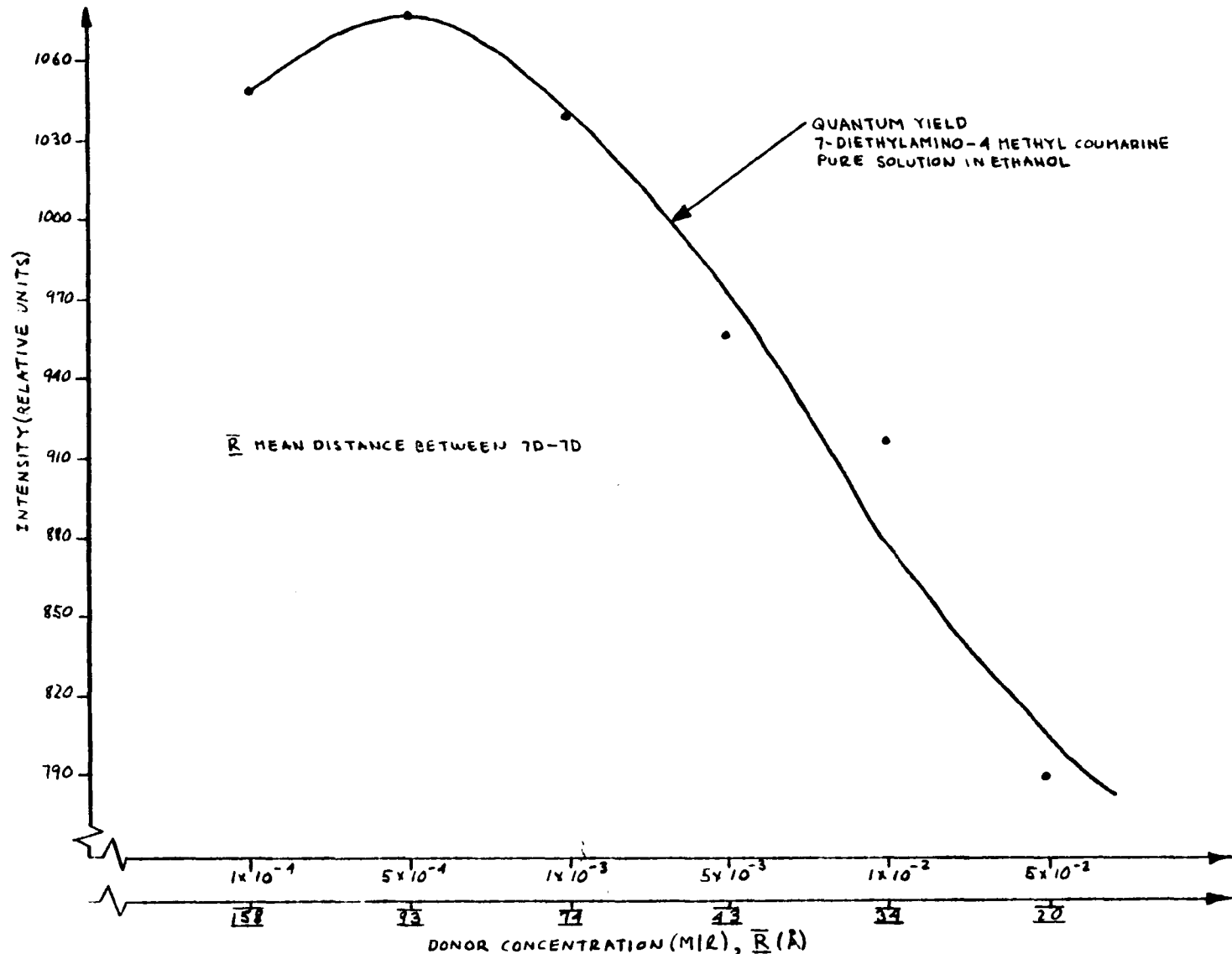


FIGURE 5.4:7 FLUORESCENCE QUANTUM YIELD OF 7-DIETHYLAMINO-4 METHYL COUMARINE VERSUS CONCENTRATION

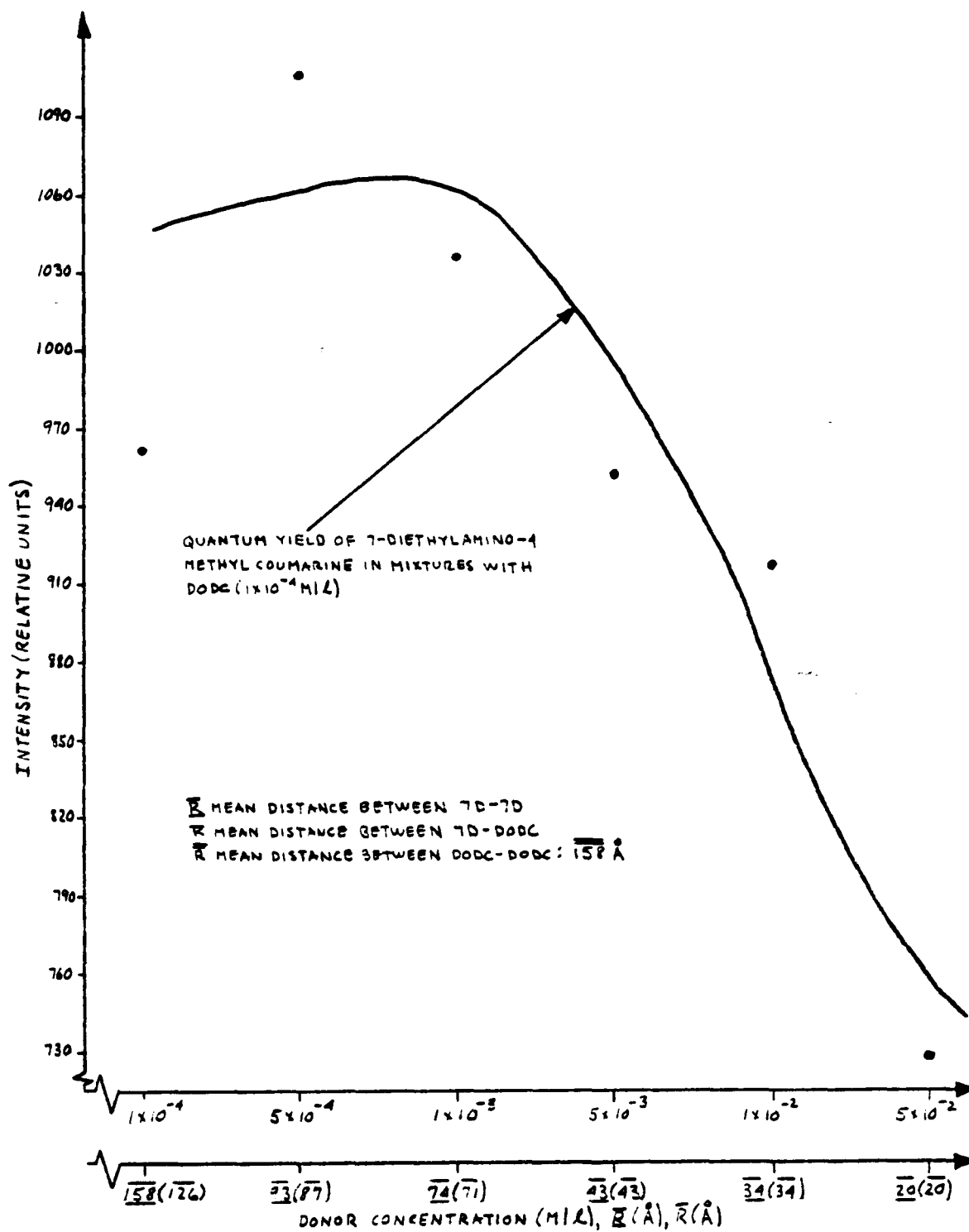


FIGURE 5.4:8 FLUORESCENCE QUANTUM YIELD OF 7-DIETHYLAMINO-4 METHYL COUMARINE (DONOR) IN MIXTURES WITH DODC (ACCEPTOR, 1×10^{-4} M/L) VERSUS DONOR CONCENTRATION

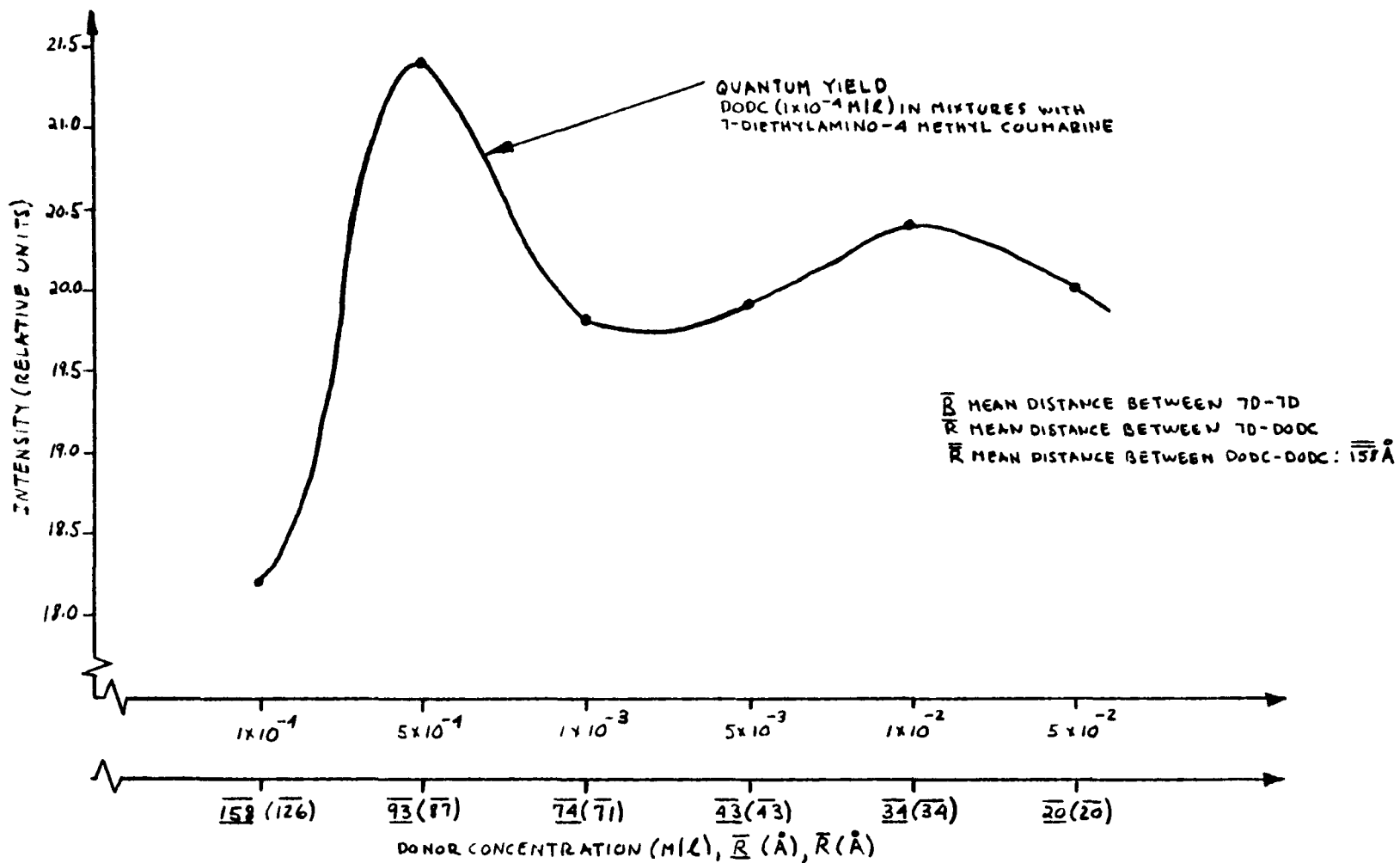


FIGURE 5.4:9 FLUORESCENCE QUANTUM YIELD OF DODC (ACCEPTOR, 1×10^{-4} M/L) IN MIXTURES WITH 7-DIETHYL-AMINO-4 METHYL COUMARINE (DONOR) VERSUS DONOR CONCENTRATION

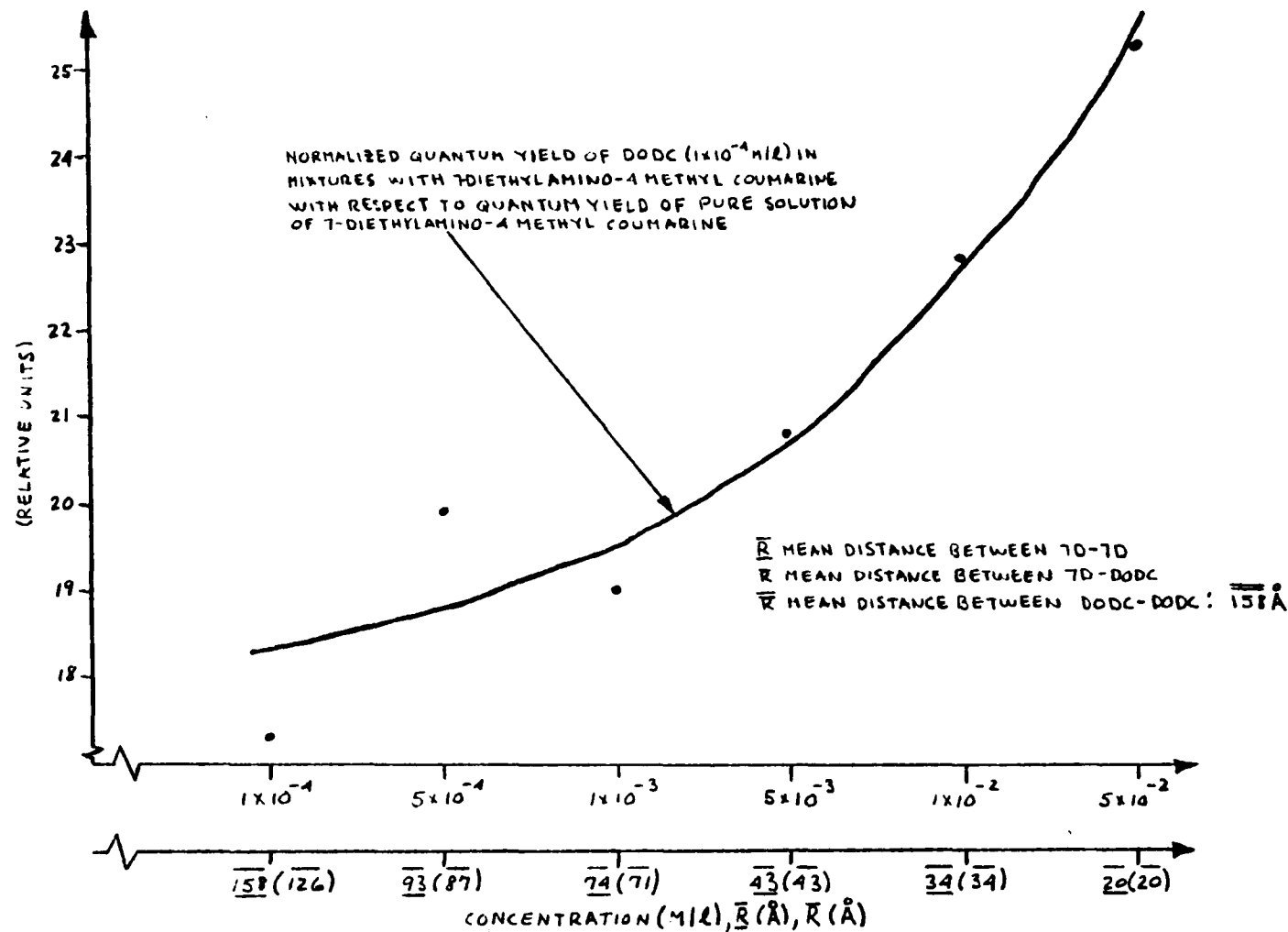


FIGURE 5.4:10 NORMALIZED FLUORESCENCE QUANTUM YIELD OF DODC (ACCEPTOR, 1×10^{-4} M/l) IN MIXTURES WITH 7-DIETHYLAMINO-4 METHYL COUMARINE (DONOR) WITH RESPECT TO THE FLUORESCENCE QUANTUM YIELD OF PURE SOLUTION OF THE DONOR VERSUS DONOR CONCENTRATION

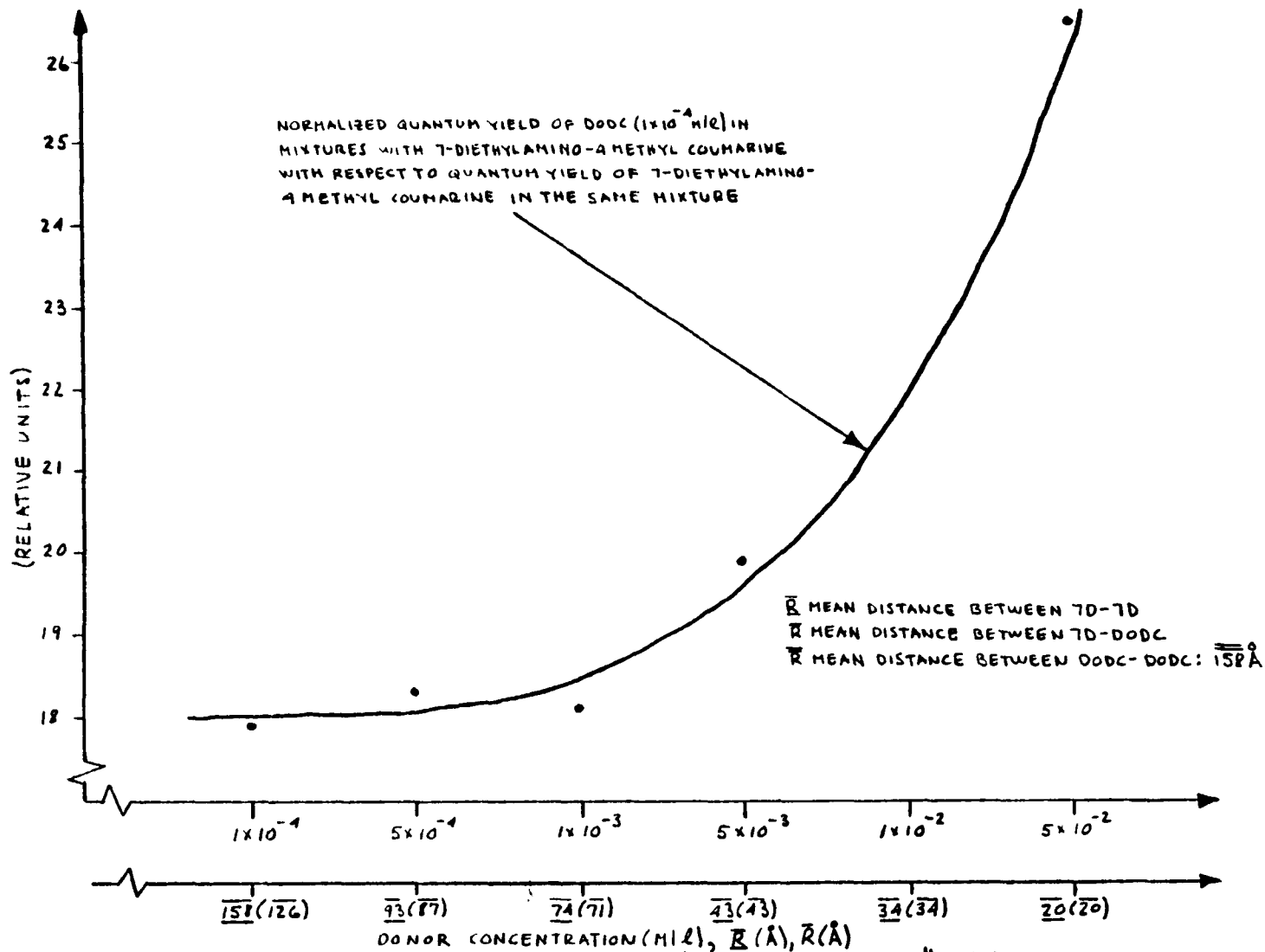


FIGURE 5.4:11 NORMALIZED FLUORESCENCE QUANTUM YIELD OF DODC (ACCEPTOR, 1×10^{-4} M/L) IN MIXTURES WITH 7-DIETHYLAMINO-4 METHYL COUMARINE (DONOR) WITH RESPECT TO THE FLUORESCENCE QUANTUM YIELD OF THE DONOR IN THE SAME MIXTURE VERSUS DONOR CONCENTRATION

2×10^{-3} M/l,

2. the onset of nonradiative resonance transfer at approximately 2×10^{-3} M/l, and
3. nonradiative resonance transfer at 5×10^{-2} M/l.

In conclusion, experiments were designed to obtain simultaneous outputs at two (and three) wavelength regions. The experiments were successful in that multiwavelength dye-mixture lasers were developed in spectral regions necessary to monitor the pollutants of interest, namely, NO_2 , SO_2 , and O_3 .

Investigations of the energy transfer processes in dye-mixture lasers were carried out. Successful determination of the dominant energy transfer mechanisms was achieved.

To explore the dynamic flow of energy transfer in dye-mixture lasers, use would have to be made of time resolved spectroscopy using picosecond laser techniques. By pumping the donor dye with a picosecond laser pulse and observing the rise of the acceptor dye's fluorescence at various acceptor concentrations, the radiative and nonradiative energy transfer rates could be determined. Only static measurements were made in this work. This is suggested as another topic for future studies.

The LIDAR system developed in this work was designed to monitor ambient levels of NO_2 . It would be desirable if the LIDAR system had the capability of simultaneously monitoring several pollutants, for example, NO_2 , SO_2 , and O_3 . Use could be made of the results obtained in achieving simultaneous laser action in dye mixtures and the investigation of the processes involved. The spectral regions obtained in

the dye-mixture lasers that could be used in pollution detection would be at 4500 Å and 6200 Å. The 4500 Å region could be used to monitor NO₂, and the 6200 Å region could be frequency doubled into the ultraviolet to 3100 Å to monitor SO₂ and O₃. This would be an attractive feature of an integrated LIDAR system, and is suggested as another topic for future studies in the LIDAR area.

CHAPTER 6 SUMMARY AND CONCLUSIONS

The basic objective of the work reported was to design, build, and operate a DASE LIDAR system for monitoring NO_2 molecular pollution concentration in the atmosphere. A DASE LIDAR system was designed and successfully used for this purpose in both sequential and simultaneous modes of operation. Simultaneous two-wavelength operation of the LIDAR system, which was the first such operation of a DASE LIDAR system, was found to be the preferred method since it reduces errors resulting from scintillation and other temporal effects.

To minimize the errors associated with the uncertainty of laser bandwidths, which intrinsically vary from shot to shot, a calibration system was developed to automatically allow for these variations. The calibration system determined the effective absorption cross sections for each outgoing laser pulse. The LIDAR system developed by us was the first to incorporate this automatic self-correcting feature, which it is believed will be necessary for any resonance absorption scheme.

Having minimized the sources of error by operating the system in the simultaneous mode and at the same time utilizing the calibration system, pollution readings were obtained. These were found to be generally in reasonable agreement with those obtained by fixed-site monitoring stations operated by the New York City Department of Air Resources. The effect of changing vehicular traffic conditions was also readily evident from the analysis of the LIDAR measurements, demonstrating the practical utility of the system.

Several readings were obtained for various times during the day to observe changes in pollution levels. As expected, the pollution level

of NO_2 peaked during morning and evening rush hours and steadily declined afterwards. The concentration of pollution obtained are typical of those found present in urban areas. The pollution was highest at avenues of heavy traffic located approximately 1 kilometer east of City College.

To examine the potential for second generation LIDAR systems capable of operating simultaneously in two and three spectral regions for the simultaneous monitoring of several pollutants as well as NO_2 , a program of experiments on dye-mixture lasers was carried out. The objective of this was to use energy transfer mechanisms that were considered feasible in dye mixtures to obtain simultaneous laser action at widely separated spectral regions. The program was successful with simultaneous laser action obtained for the first time at widely separated spectral regions, including simultaneous outputs at the three primary colors. Analysis of the experimental results showed that radiative energy transfer was dominant at the concentrations found optimum for simultaneous two and three-wavelength operation in dye-mixture lasers. Nonradiative resonance energy transfer was found to dominate at higher concentrations.

REFERENCES

1. L. B. Lave and E. P. Seskin, *Science*, 169, (1970), pp. 723-731.
2. H. Kildal and R. L. Byer, *Proc. IEEE*, 59, (1971), pp. 1644-1663.
3. T. Kobayashi and H. Inaba, 'Laser Beam Technology for Remotely Sensing Invisible Molecules in the Polluted Atmosphere', 11th Symposium on Electron, Ion and Laser Beam Technology, ed. R. F. M. Thornley, San Francisco Press, Inc., (1971), pp. 385-401; see also S. Nakahara, K. Ito, A. Fuke, S. Komatsu, H. Inaba and T. Kobayashi, *Opto-electronics*, 4, (1972), pp. 169-177.
4. R. T. H. Collins, *Appl. Opt.*, 9, (1970), pp. 1782-1788.
5. C. S. Cook, *Appl. Opt.*, 11, (1972), p. 1742.
6. G. Fiocco and L. D. Smullin, *Nature (London)*, 109, (1963), pp. 1275-1276.
7. M. G. H. Ligada, *Proc. Conf. Laser Tech.*, 1st San Diego, California, U. S. Navy ONR, (1963), p. 62.
8. D. A. Leonard, *Nature*, 216, (1967), pp. 142-143.
9. J. A. Cooney, *Appl. Phys. Letts.*, 12, (1968), pp. 40-42; see also *J. Appl. Meteorology*, 9, (1970), pp. 182-184.
10. S. H. Melfi, J. D. Lawrence, Jr. and M. P. McCormick, *Appl. Phys. Letts.*, 15, (1969), pp. 295-297.
11. H. Inaba and T. Kobayashi, *Nature*, 224, (1969), p. 170; see also *Opto-electronics*, 2, (1970), pp. 45-46.
12. T. Kobayashi and H. Inaba, *Appl. Phys. Letts.*, 17, (1970), pp. 139-141.
13. J. A. Cooney, *J. Appl. Meteorology*, 10, (1971), pp. 301-308.
14. R. G. Strauch, V. E. Derr and R. E. Cupp, *Appl. Opt.*, 10, (1971), pp. 2665-2669.
15. S. H. Melfi, *Appl. Opt.*, 11, (1972), pp. 1605-1610.
16. T. Hirschfeld, E. R. Schildleraut, H. Tannenbaum and D. Tannenbaum, *Appl. Phys. Letts.*, 22, (1973), pp. 38-40; see also T. Hirschfeld and S. Klainer, *Opt. Spect.*, (1970), pp. 63-66.
17. T. Hirschfeld, *Appl. Opt.*, 13, (1974), pp. 1435-1437.
18. R. L. Byer, *Opt. and Quant. Elect.*, 7, (1975), pp. 147-177.
19. G. B. Jacobs and L. R. Snowman, *IEEE J. Quant. Elect.*, QE-3, (1967), pp. 603-605.

20. P. L. Hanst and J. A. Morreal, *J. Air Pollut. Cont. Ass.*, 18, (1968), pp. 754-759.
21. P. L. Hanst, *Appl. Spect.*, 24, (1970), pp. 161-174.
22. S. Zaromb, *Proc. Electro-Optical Systems Design Symposium*, Sept., (1969), p. 609.
23. S. Nakahara and K. Ito, *International Quantum Electronics Conf. Digest Tech. Papers*, Sept., (1970), p. 226.
24. H. Inomata and T. Igarashi, *Trans. Tech. Group on Quant. Elect. of the Inst. Elect. Comm. Engr. (IECE) of Japan*, QE-70-36, Dec.
25. J. A. Hodgeson, W. A. McClenney and P. L. Hanst, *Science*, 182, (1973), p. 248.
26. R. L. Byer and M. Garbuny, *Appl. Opt.*, 12, (1973), pp. 1496-1505.
27. E. D. Hinkley, *Appl. Phys. Letts.*, 16, (1970), pp. 351-354; see also K. W. Nill, F. A. Blum, A. R. Calowa and T. C. Harman, *Appl. Phys. Letts.*, 19, (1971) pp. 79-82.
28. E. D. Hinkley and P. L. Kelley, *Science*, 171, (1971), pp. 635-639; see also I. Melngailis, *IEEE Trans. on Geo. Sci. Elect.*, GE-10, (1972).
29. E. D. Hinkley, *Opto-electronics*, 4, (1972), pp. 69-86.
30. L. R. Snowman. Technical Report R72ELS-15, General Electric Electronic Laboratory, Syracuse, New York, March, (1972).
31. D. O'Shea and L. G. Dodge, *Appl. Opt.*, 13, (1974), pp. 1481-1486.
32. T. Henningsen, M. Garbuny and R. L. Byer, *Appl. Phys. Letts.*, 24, (1974), pp. 242-244.
33. M. R. Bowman, A. J. Gibson and M. C. W. Sandford, *Nature*, 221, (1969), p. 456; see also A. J. Gibson, *J. Sci. Instr.*, 2, (1969), p. 802.
34. M. C. W. Sandford and A. J. Gibson, *J. Atmos. Terr. Phys.*, 32, (1970), pp. 1423-1430.
35. A. J. Gibson and M. C. W. Sandford, *J. Atmos. Terr. Phys.*, 33, (1971), p. 1675.
36. C. J. Schuler, C. T. Pike and H. A. Miranda, *Appl. Opt.*, 10, (1971), pp. 1689-1690.
37. R. D. Hake, D. E. Arnold, D. W. Jackson, W. E. Evans, B. P. Ficklin and R. A. Song, *J. Geophys. Res.*, 77, (1972), p. 6839.

38. J. E. Blamont, M. L. Chanin and G. Megie, *Ann. Geophys.*, 28, (1973), pp. 833-838.
39. V. W. J. H. Kirchoff and B. B. Clemesha, *J. Atm. Terr. Phys.*, 35, (1973), p. 1493.
40. A. J. Gibson and M. C. W. Sandford, *Nature*, 239, (1972), pp. 509-511.
41. F. Felix, W. Keenliside, G. Kent and M. C. W. Sandford, *Nature*, 246, (1973), p. 345.
42. C. M. Penney, W. W. Morey, R. L. ST. Peters, S. D. Silverstein, M. Lapp and D. R. White, Final Report for NASA CR-132363, prepared by General Electric Corporate Research and Development, Schenectady, New York.
43. R. M. Measures and G. Pilon, *Opto-electronics*, 4, (1972), pp. 141-153.
44. S. A. Ahmed and J. S. Gergely, 'Atmospheric Pollution Monitoring Using Tunable Dye Lasers', *Proc. Tech. Prog., Electro-Opt. Systems Design Conf., New York, N. Y., Sept., (1973)*, pp. 275-282.
45. J. A. Gelwachs, M. Birnbaum, A. W. Tucker and C. L. Fincher, *Opto-electronics*, 4, (1972), pp. 155-160.
46. R. M. Schotland, E. E. Chermack and D. T. Chang, *Proc. First International Symp. of Humidity and Moisture*, p. 569 (Reinhart Book Div., New York, N. Y., 1964); see also R. M. Schotland, *Proc. Third Symp. on Remote Sensing of the Environment*, Oct. 14-16, (1964), pp. 215-224, Univ. of Michigan, Ann Arbor, Mich.
47. S. A. Ahmed and J. S. Gergely, 'Laser Radar Study Using Resonance Absorption for Remote Detection of Air Pollutants', *Fifth Conf. on Laser Radar Studies of the Atm.*, June 4-6, (1973), Williamsburg, Va.
48. S. A. Ahmed, *Appl. Opt.* 12, (1973), pp. 901-903.
49. M. L. Wright, E. K. Proctor, L. S. Gasiorek and E. M. Liston, Final Report for NASA CR-132724, Contract NA S1-11657, Stanford Research Institute, Menlo Park, California.
50. T. Igarashi, 'Laser Radar Study Using Resonance Absorption for Remote Detection of Air Pollutants', *Fifth Conf. on Laser Radar Studies of the Atm.*, June 4-6, (1973), Williamsburg, Va.
51. K. W. Rothe, U Brinkmann and H. Walther, *Proc. VIII ICPEAC, Beograd*, July, (1973); see also *Appl. Phys.*, 3, (1974), pp. 115-119.
52. W. B. Grant, R. D. Hake, Jr., E. M. Liston, R. C. Robbins and E. K. Proctor, Jr., *Appl. Phys. Letts.*, 24, (1974), pp. 550-552

53. K. W. Rothe, U. Brinkman and H. Walther, Appl. Phys., to be published.
54. R. Penndorf, J. Opt. Soc. Am., 47, (1957), pp. 176-182.
55. R. F. Begley, A. B. Harvey and R. L. Byer, Appl. Phys. Letts., 25, (1974), pp. 317-390.
56. H. Inaba and T. Kobayashi, Opto-electronics, 4, (1972), pp. 101-123.
57. P. W. Kruse, L. D. McGlauchlin and R. B. McQuistan, 'Elements of Infra-Red Technology', Wiley, New York, (1963).
58. W. K. Pratt, 'Laser Communication Systems', Wiley, New York, (1969).
59. H. Walther and J. L. Hall, Appl. Phys. Letts., 17, (1970), p. 239.
60. R. C. C. Leite, Phys. Rev. Letts., 14, (1965), p. 7.
61. R. C. Damen, Phys. Rev. Letts., 14, (1965), p. 9.
62. R. M. Schotland, J. Appl. Meteorology, 13, (1974), pp. 71-77.
63. G. W. Grams and C. M. Wyman, J. Appl. Meteorology, 11, (1972), pp. 1108-1113.
64. R. S. Lawrence and J. W. Strohbehn, Proc. IEEE, 58, (1970).
65. H. S. Piloff, Appl. Phys. Letts., 21, (1972), pp. 339-340.
66. P. Dezauzier, A. Eranian and O. deWitte, Appl. Phys. Letts., 22, (1973), pp. 664-666.
67. A. A. Friesem, U. Ganiel and G. Neumann, Appl. Phys. Letts., 23, (1973), pp. 249-251.
68. P. Flamont and Y. H. Meyer, Opt. Comm. 13, (1975), pp.13-16.
69. H. Furtumoto and H. Ceccon, Appl. Phys. Letts. 13, (1968), pp. 335-337.
70. K. B. Eisenthal, Accounts of Chem. Res., 8, (1975), pp. 118-124.
71. I. B. Berlman, 'Handbook of Fluorescence Spectra of Aromatic Molecules', Academic Press, New York, (1965).
72. H. J. Bernstein, Paper presented at the 1973 Spring Meeting of the Optical Society of America, New York, N. Y., April 11-13.
73. H. P. Rosen, P. Robrish and O. Chamberlain, 'Feasibility of the Remote Detection of Pollutants Using Resonance Raman Scattering', Lawrence Berkeley Lab., Energy and Environment Div., U. C. Berkeley, California, (1975).

74. P. Bied-Charreton, C. R. Acad. Sci., Paris, 268, (1969), pp. 1377-1380.
75. C. E. Moeller, C. M. Verber and A. H. Adelman, Appl. Phys. Letts., 18, (1971), p. 278.
76. T. Urisu and K. Kajiyama, J. Appl. Phys., 47, (1976), p. 3563.
77. S. A. Ahmed, J. S. Gergely and D. A. Infante, J. Chem. Phys., 61, (1974), p. 1584.
78. T. Urisu and K. Kajiyama, J. Appl. Phys., 47, (1976), p. 3559.
79. J. M. Drake, E. M. Tam and R. I. Morse, IEEE J. Quant. Elect. (Corresp.), QE-8, (1972), pp. 92-94.
80. W. W. Morey, IEEE J. Quant. Elect. (Corresp.), QE-8, (1972), pp. 818-819.
81. D. D. Whawalkar and L. Pandit, IEEE J. Quant. Elect. (Corresp.), QE-9, (1973), pp. 43-46.
82. C. Lin and A. Dienes, J. Appl. Phys., 44, (1973), p. 5050.
83. F. B. Dunning and E. D. Stokes, Opt. Comm., 6, (1972), p.160.
84. E. D. Stokes, F. B. Dunning, R. F. Stebbings, G. K. Walters and R. D. Rundel, Opt. Comm., 5, (1972), p. 267.
85. R. C. Hilborn and H. C. Brayman, J. Appl. Phys., 45, (1974), p. 4912.
86. A. Dienes and M. Madden, J. Appl. Phys., 44, (1973) p. 4161.
87. C. V. Shank, A. Dienes and W.T. Silfvast, Appl. Phys. Letts., 17, (1970), p. 307.
88. O. G. Peterson and B. B. Snavely, Bull. Am. Phys. Soc., 13, (1968), p. 397.
89. J. B. Marling, D. W. Gregg and S. J. Thomas, IEEE J. Quant. Elect., QE-6, (1970).
90. J. B. Birks, 'Photophysics of Aromatic Molecules', edited by J. B. Birks (Wiley-Interscience, New York, 1970).
91. F. Wilkinson, 'Advances in Photochemistry', edited by W. A. Noyes, Jr., G. S. Hammond and J. N. Pitts, Jr. (Interscience, New York, 1964), Vol. III.
92. I. B. Berlman, 'Energy Transfer Parameters of Aromatic Molecules', Academic Press, New York, (1973).

93. Th. Forster, 'Light and Organic Crystals', Modern Quantum Chemistry, Sinanoglu, editor, Academic Press, (1965); Th. Forster, Ann. Phys., 2, (1948), p. 55; Z. Naturforsch, A 4, (1949), p. 32.
94. G. S. Beddard, S.E. Carlin and G. Porter, Chem. Phys. Letts., 43, (1976), pp. 27-32.
95. T. D. Wilkerson, B. Ercoli and F. S. Tomkins, 'Absorption Spectra of Atmospheric Gases', Tech. Note BN-784, Institute for Fluid Dynamics and Applied Mathematics, Feb., (1974).